CEDI

Cost-Effective Drone Interceptor | Final Report
AE3200 Design Synthesis Exercise

Group 16

Anna Bolhuis	5321395	Ariele Malugani	5701031
Stijn Cuppers	5680824	Benjamin Paulis	5752264
Douwe de Jong	5313899	Jan Paul Peters	5292972
Maciej Grajda	5463734	Nicolas Rodriguez Dfouni	5465109
Vincent Maan	5463823	Tim Uijlenhoet	5510295

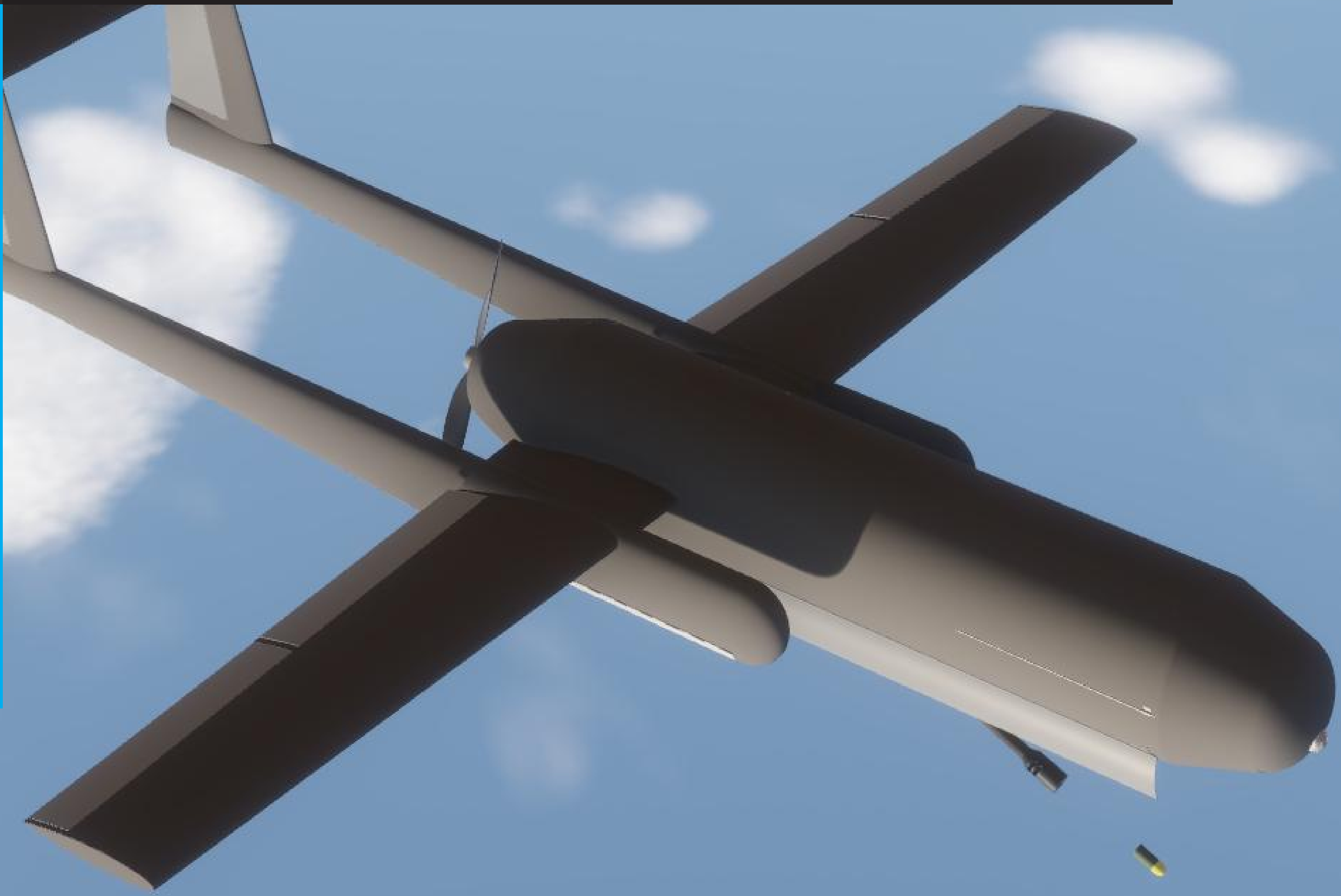

Delft University of Technology

TUDelft

This page is intentionally left blank.

Executive Overview

Project Description

Modern air defense systems face new difficulties as a result of the growing use of cheap, mass-produced loitering munitions and one-way attack drones. Coordinated drone swarms have proven capable of overwhelming conventional ground-based defense systems, which were initially built to fend off more sophisticated cruise missiles or manned military aircraft. These new threats are distinguished by their low cost, ease of manufacture, and capacity to seriously inflict (psychological) damage. Low-cost drones are the most concerning tactical development since the rise of the improvised explosive device, head of the U.S. Central Command K. McKenzie Jr. said in a speech[1].

The objective of this project is to provide a solution to this growing threat, more specifically a system that can reliably sustain a long-term campaign of such cheap loitering munitions being deployed against a country. Therefore, the system need not only succeed in taking down the adversaries, but in doing so, must ensure the defense of the adversary is cheaper than the cost to attack for the enemy. Taking down $50,000 drones with $1,000,000 defenses is not a reliable long-term strategy, as the enemy can simply maintain its attack until the defending country exhausts their financial budget, ultimately leaving them vulnerable.

As the need for reliable, cost-effective defense against loitering munitions is relatively new, many potential solutions remain in early stages of development. In this context, a concept has already been identified and selected through a prior evaluation and scoring process. The purpose of this report is to build on that foundation by presenting the detailed design of the chosen solution, refining its subsystems and components to ensure performance, feasibility, and readiness for further analysis and testing.

The design

A render of the final design is presented in Figure 1 together with the most important specifications in Table 1. The selected aircraft design follows a conventional layout, featuring a single main wing and a rear-mounted propeller that pushes the aircraft forward. The wing is mounted in the centerline of the fuselage making it a mid-wing configuration, with no quarter chord sweep and no dihedral. All fuel is stored within the central wing structure to maximize space and efficiency. To maintain stability and control during flight, the aircraft uses an H-shaped tail design. The entire horizontal stabilizer is capable of rapid movement to allow for greater maneuverability. It is positioned between two vertical tails, each equipped with a rudder for directional control. Twin booms connect the empennage surfaces to the wing. In between the two booms, at the end of the fuselage, a compact yet powerful 225CS, 40BHP, Wankel engine is installed. The engine comes integrated with an alternator to provide power to all the subsystems that require it. To ensure smooth operation of sensitive equipment, a battery is included to regulate power delivery and support high-demand moments.

Table 1: *Main parameters of the Air Vehicle*

Parameter	Value
Span [m]	5.2
Fuselage length [m]	3.2
Total length [m]	5.2
MTOW [kg]	155
Thrust [N]	155
Cruise speed [$\mathrm{m\,s^{-1}}$]	80
Cruise Endurance [h]	2.92
Cruise Range [km]	840
# of intercepts [-]	5
Direct comm. range [km]	133
Direct hit probability [-]	0.9

The main part of the fuselage has an elliptical shape, which fits the weapon system neatly while minimizing surface area to reduce air resistance. The detection system is located at the front of the

---

[1] URL `https://taskandpurpose.com/news/drone-threat-ieds-middle-east-mckenzie/` [cited 01 May 2025]

aircraft, and the engine is positioned at the rear. The Norinco LG5 grenade launcher functions as the primary armament. It was selected due to its ability to fire programmable airburst munitions, ensuring a high reliability of taking down the target, with reduced aiming requirements, due to the airburst nature of the ammunition. The aircraft can carry up to 16 rounds of ammunition and is designed to take down approximately five drones per mission. To enhance its effectiveness, the gun can tilt downward by up to 32 degrees from its default position, giving it a wider firing range.

To ensure that the aircraft can reliably detect and engage threats, a combination of advanced sensing technologies is used. First, a dual visual and infrared camera system is installed. This serves multiple purposes: during peacetime, it can be used for surveillance tasks such as monitoring forest fires, while during combat, it helps track and identify targets. However, cameras alone can be affected by weather and lighting conditions. To overcome this, a laser-based sensing system known as LiDAR is also included. LiDAR is very precise and excels at identifying and tracking nearby threats, making it ideal for aiming the weapon system accurately. Despite their advantages, both the camera and LiDAR have limited range. To provide long-distance detection and tracking capabilities, a radar system is added. By combining these three systems, the aircraft can detect, identify, and track targets effectively across all mission scenarios and environmental conditions.

To make sure the aircraft can handle the physical forces it experiences during flight, a strong internal structure was designed. For the lifting surfaces, wingboxes were designed, alongside ribs and stringers. For the fuselage and the booms, longerons and ribs were designed to carry the loads. The primary material used for these structures is a high-strength aluminum alloy (AL7075-T6), which is both lightweight and durable. For takeoff and landing, the aircraft is equipped with three landing gears. The main landing gear is positioned behind the aircraft's center of gravity and is housed within the rear booms during flight. The front landing gear is slightly off-center to make space for the weapon system and retracts into the main body of the aircraft when not in use.

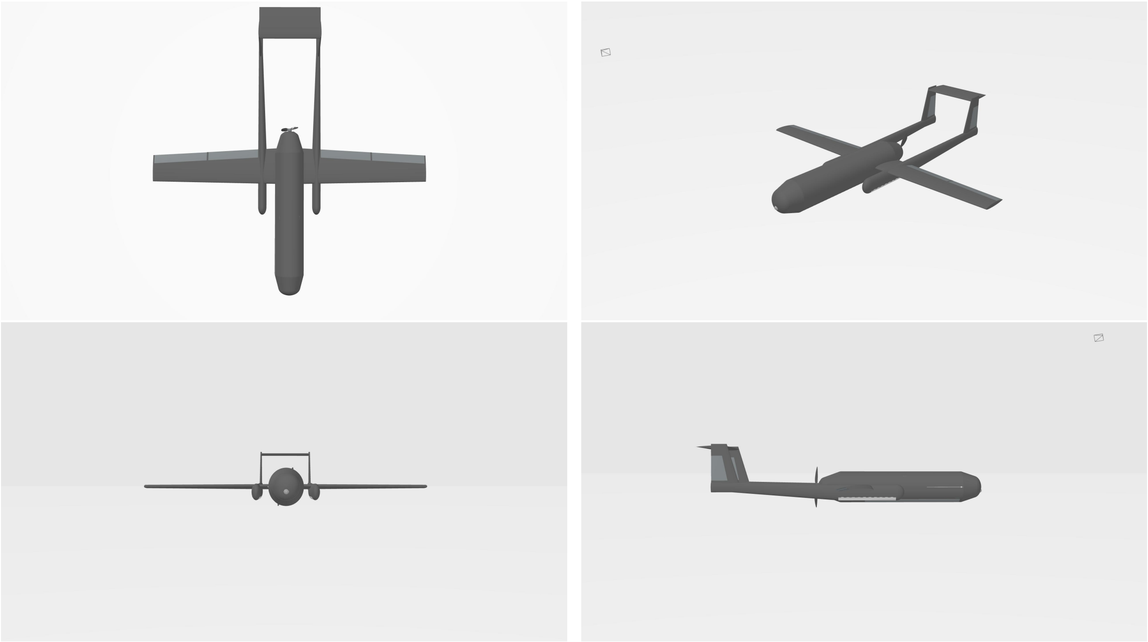

Figure 1: *3-view drawing of the aircraft*

Logistics and Operations

Operationally, the system must integrate seamlessly into the standard NATO operational framework. This means it has to be able to network effectively and share data. This is done through an interface with the so-called NATO C4I (Command, Control, Communications, Computers, and Intelligence) network. What it gains from this is an improved operational picture compared to when operating stand-alone.

The primary mission of CEDI is air defense. CEDI will operate from 10 airfields across the Netherlands, ready to take off within 5 minutes to intercept any threat. A mission begins with C4I issuing a scramble command, after which the system will activate. The air vehicles will take off, and the target information will be shared with them. The vehicles navigate to their assigned targets, locate them, and engage. This process is, of course, more involved: a moving target must be detected under any weather condition; it must be identified as hostile with sufficient certainty; the interceptor must be positioned correctly; gun doors must open; and the shot must be precisely aimed and fired. After a shot is taken, it must be assessed whether the attack was effective. When a successful take-down is performed, the interceptor can move on to the next target or return to base, depending on target availability and ammo levels. When the incoming attack is especially large, an integrated combat turnaround can be performed where the interceptor is refueled and rearmed quickly to take off and continue its mission as soon as possible.

Sustainable Development

While not a primary design driver, environmental sustainability is still considered in the CEDI project, achieved primarily through the drone's reusability, use of low eco-cost and recyclable aluminum, and efficient propulsion to reduce fuel consumption. Additionally, by serving as a potential deterrent to enemy attacks, the system may help avoid the environmental impact of larger-scale defense operations.

Social sustainability is addressed throughout the need of a defense system. It is a powerful deterrent against enemy attacks that lead to social peace of mind. By promoting safety in areas deploying the system, which citizens are expected to value highly, this increases the social acceptability (and therefore also social sustainability) of the system.

To ensure economic sustainability, the design process focused on minimizing the costs of acquisition, operation, and per-target elimination, resulting in a unit cost of approximately €82,000 and total acquisition and yearly operational costs of around €4.26 million and €3.95 million, respectively. The system also meets its budgetary goals with a low estimated marginal cost per elimination of €900, demonstrating strong cost-effectiveness.

Future Outlook

Immediate next steps include validating the use of a large fixed-wing drone with the YOLOv8 model, optimizing controller design and tuning, and analyzing the impact of gun recoil on stability. Additionally, attention should be given to the integration and routing of data logs across avionics systems to ensure reliable operation and effective diagnostics.

Contents

Nomenclature

List of Symbols

Symbol	Definition	Unit
A	Aspect ratio of wing	-
A	Cross-sectional area	$\mathrm{m^2}$
A_h	Aspect ratio of hor. stabilizer	-
A_i	Lifting line intermediate unknowns	-
a	Semi-major axis	m
B	Boom area	$\mathrm{m^2}$
B	Bandwidth	Hz
b	Span	m
b	Length of sheet	m
b	Semi-minor axis	m
b_f	Width of fuselage	m
C_D	Drag coefficient	-
C_{d_c}	Cruise airfoil drag coefficient	-
$\bar{C}_i$	Mean geometric chord of segment	m
C_{L_0}	A/C lift coefficient at α_0	-
C_{L_c}	Wing cruise lift coefficient	-
C_{L_i}	Lift coefficient of component i	-
$C_{L_{max}}$	Wing maximum lift coefficient	-
$C_{L\alpha}$	A/C lift curve slope	$\mathrm{rad^{-1}}$
$C_{L\alpha_i}$	Lift curve slope of component i	$\mathrm{rad^{-1}}$
C_{l_i}	Airfoil cruise lift coefficient	-
$C_{l_{max}}$	Airfoil max lift coefficient	-
C_{l_α}	Lift curve slope of airfoil	$\mathrm{rad^{-1}}$
C_{m_0}	Pitching moment coefficient at zero lift	-
$C_{m_{ac}}$	Pitching moment coeff. about aerodynamic center	-
C_{m_α}	Pitching moment coeff. slope	$\mathrm{rad^{-1}}$
C_p	Power coefficient	-
C_s	Torque coefficient	-
C_t	Thrust coefficient	-
c'/c	Ratio of airfoil chord with flaps to clean chord	-
c	Speed of light	$\mathrm{m\,s^{-1}}$
$\bar{c}$	Mean aerodynamic chord	m
c_{eq}	Damping coefficient	$\mathrm{N\,s\,m^{-1}}$
D	Drag force	N
D_{sp}	Propeller spinner diameter	m
D_P	Propeller diameter	m
E	Young's modulus	Pa
E	Energy	J
e	Oswald factor	-
F_d	Damper force	N

Symbol	Definition	Unit
F_s	Spring force	N
F_{side}	Side force	N
f	Frequency	Hz
GR	Gear ratio	-
G	Gain	dB
G	Shear modulus	GPa
g	Gravitational acceleration	$\mathrm{m\,s^{-2}}$
H	Pitch	m
h	Altitude	m
$\dot{h}$	Climb rate	$\mathrm{m\,s^{-1}}$
h_f	Height of fuselage	m
I	Moment of inertia	$\mathrm{m^4}$
J	Advance ratio	-
K	Column buckling coefficient	-
K_i	Non-dimensional radius of gyration about the i axis	-
K_{wf}	Wing-fuselage interference coeff.	-
K_i	Non-dimensional radius of gyration about the i axis	-
k_b	Boltzmann constant	$\mathrm{J\,K^{-1}}$
k_c	Buckling coefficient for compression	-
k_{eq}	Spring stiffness	$\mathrm{N\,m^{-1}}$
k_s	Buckling coefficient for shear	-
L	Length of column	m
L_{atm}	Atmospheric power loss	dB
L_{FS}	Free space path loss	dB
l_f	Length of fuselage	m
l_h	Distance between wing and tail 1/4-chords	m
M	Mach number	-
M_i	Moment around i axis	$\mathrm{N\,m}$
m	Mass	kg
n_h	Dynamic pressure ratio	-
NP	Noise power	dB
P	Power	W
P_{SL}	Power at sea level	W
P_z	Point load	N
p	Roll rate	$\mathrm{rad\,s^{-1}}$
Q	First moment of area	$\mathrm{m^3}$
q	Shear flow	$\mathrm{N\,m^{-1}}$
q	Pitch rate	$\mathrm{rad\,s^{-1}}$
$\bar{q}$	Dynamic pressure	Pa
R	Range	m
R_E	Earth radius	m

Symbol	Definition	Unit
r	Yaw rate	$\mathrm{rad\,s^{-1}}$
S	Wing surface area	$\mathrm{m^2}$
S_h	Horizontal stabilizer surface area	$\mathrm{m^2}$
SNR	Signal to Noise Ratio	dB
S_s	Projected side surface area	$\mathrm{m^2}$
S_{wf}/S	Flapped-to-clean wing area ratio	-
T	Thrust	N
T	System noise temperature	K
t	Time	h
t	Thickness	m
$\hat{u}$	Dimensionless change in velocity	-
V	Speed	$\mathrm{m\,s^{-1}}$
V_c	Cruise speed	$\mathrm{m\,s^{-1}}$
V_T	Total A/C speed	$\mathrm{m\,s^{-1}}$
$V_{tip,cr}$	Propeller tip velocity at cruise	$\mathrm{m\,s^{-1}}$
$V_{tip,st}$	Propeller tip velocity at $V_c = 0$	$\mathrm{m\,s^{-1}}$
V_w	Crosswind speed	$\mathrm{m\,s^{-1}}$
V_h/V	Tail efficiency	-
V_s	Stall speed	$\mathrm{m\,s^{-1}}$
V_z	Shear distribution	N
W_{ave}	Average weight during cruise	N
W_{TO}	Take-off weight	N
$\bar{x}_{ac}$	Aerodynamic center position of the A/C as % of MAC	-
w_z	Distributed load	N
$\bar{x}_{ac}$	Aerodynamic center position of the A/C as % of MAC	-
$\bar{x}_{ac_i}$	Aerodynamic center position of component i as % of MAC	-
x_{cg}	Center of gravity position from nose of A/C	m
$\bar{x}_{cg}$	Center of gravity position as % of MAC	-
y_{max}	Maximum displacement	m
α	Angle of attack	°
α_0	Zero-lift angle of attack	°
α_i	Effective angle of attack of a segment	°
α_s	Stall angle of attack	°
β	Prandtl–Glauert compressibility correction	-
β	Sideslip angle	°
β	Blade angle	°
$\Delta C_{l_{HLD}}$	Increase in airfoil lift coefficient due to high-lift devices	-
$\Delta C_{l_{max}}$	Increase in airfoil lift coefficient generated by flaps	-
δ	Spring pre-compression	m
$\delta\epsilon/\delta\alpha$	Change in downwash with angle of attack	-
δa	Aileron deflection	°
δe	Elevator deflection	°
δr	Rudder deflection	°
ζ	Damping ratio	
η	Efficiency	-
Γ	Torque	$\mathrm{N\,m}$
γ	Ratio of specific heats	-
γ_R	Specific atmospheric attenuation	$\mathrm{dB\,km^{-1}}$
κ	Camera field of view angle	°
Λ	Sweep angle	°
λ	Wavelength	m
μ_c	Symmetric dimensionless mass	-
μ_b	Asymmetric dimensionless mass	-
ν	Poisson ratio	-
ρ	Air density	$\mathrm{kg\,m^{-3}}$
ρ_0	Air density at sea level	$\mathrm{kg\,m^{-3}}$
σ	Normal stress	$\mathrm{N\,m^{-2}}$
σ	Sidewash angle	°
τ	Shear stress	$\mathrm{N\,m^{-2}}$
ϕ	Roll angle	rad
θ	Lifting line segment angles	°
θ	Pitch angle	°
θ	Elevation angle	°
ω	Angular speed	$\mathrm{rad\,s^{-1}}$

List of Abbreviations

Abbreviation	Definition
BMEP	Brake Mean Effective Pressure
CEDI	Cost Effective Drone Interceptor
CG	Center of gravity
DoD	Department of Defense (USA)
FoV	Field of View
HLD	High Lift Device
IoU	Intersection over Union
MTOW	Maximum Take-Off Weight
MAP	Mean Average Precision
MLG	Main Landing Gear
NLG	Nose Landing Gear
NVM	Normal-Shear-Moment
SFC	Specific Fuel Consumption
TBD	To Be Determined
UAS	Unmanned Aerial System
WOT	Wide Open Throttle
YOLO	You Only Look Once
RHA	Rolled Homogenous Armour
FFD	Functional Flow Diagram
FBS	Functional Breakdown Structure
MP	Mission Process

List of Figures

List of Tables

1

Introduction

The threat of low-cost one-way attack drones becomes ever-greater every day in the 2020s. What started as a niche use-case for a particular conflict has developed into a versatile and vital tool for both aggressors and defenders. This is most prominently seen in the amount of military drones being deployed in recent wars, like the Russo-Ukrainian war as one example, and has already changed warfare as we know it. Even within modern conflicts, their application grows ever broader and more effective. Solutions to the individual aircraft exist, however they are either too costly or underperforming for the threat as a whole[7]. Missile systems such as the Patriot provide the required efficacy, however at a cost of $4 Million per takedown, which is not acceptable to counter $50,000 drones in the long term. FPV-quadcopters are sometimes deployed, which - while being a cheap alternative to conventional SAM-systems - have a limited range, and have limited performance in terms of service ceiling and airspeed, besides being much less adaptable to advancements, and consequentially not every hostile can be reliably taken down this way.

The Cost Effective Drone Interceptor - or CEDI - aims to bridge the gap between these low-cost, but hardly effective and highly effective, but costly systems, providing the required performance to neutralize a wave of 100 enemy drones, more specifically the recently upgraded Shahed-136 or Geran-2 loitering munitions system. The CEDI is a reusable platform specifically designed to take down the Shahed-136, boasting a movable grenade launcher system as well as a fully redundant detection suite including active radar capability, ensuring threat acquisition and takedown are possible even in the event of partial infrastructure failure. By being reusable, it not only contributes to sustainability (both economic and environmental), but also to the military effectiveness of the aircraft, by being able to take down multiple targets before returning to base to refuel and re-arm.

To describe the design of the CEDI as detailed as possible in the current stage of the design process, this report is structured as follows: First, the context and market drive for the project is outlined in Chapter 2. Then, the conceptual design steps to arrive at the top-level architecture of the system are outlined in Chapter 3 and 4. After that, detail design of the CEDI will be synthesized and described, starting in with the Wing and Empennage design in Chapter 5 and Chapter 6. Then, the primary payload systems necessary for operation, namely the Armament, Avionics and Detection subsystems will be described in Chapter 7, Chapter 8 and Chapter 9. Afterwards, the Propulsion, Power and Structural design are detailed in Chapter 10, Chapter 11 and Chapter 12. Then, the Logistics & Operations are discussed in Chapter 13, the Technical Risk Assessment in Chapter 14, the Sustainable Development strategy in Chapter 15, the Future outlook in Chapter 16, and finally the conclusion in Chapter 17.

2

Project Context

In this chapter, the context of the project will be outlined. First, the geopolitical context will be summarized in Section 2.1. Second, the Mission Need Statement and Project Objective Statement will be defined in Section 2.2. Third, the target analysis will be outlined in Section 2.3. Finally, a SWOT analysis will be briefly described in Section 2.4 and the market share will be estimated in Section 2.5.

2.1. Geopolitical Context

The current geopolitical landscape is rapidly evolving: the Russo-Ukrainian war has been going on for over 3 years; tensions are high between India and Pakistan; the Middle East is heating up with missile exchanges, air raids, and drone attacks between Israel and Iran; China is preparing for an invasion of Taiwan. Conflicts are becoming increasingly intense. One of the most significant developments in the midst of all this is the large-scale use of drones. Unmanned air vehicles changed war forever. This can be seen both on the front line and further back. The use of long-range, cheap attack drones, overwhelming air defenses has become a common tactic in recent years.

2.2. MNS and POS

ChatGPT said: The Mission Need Statement and Project Objective Statement define the project objectives.

- **MNS**: Protect an area the size of the Netherlands against the new threat of cheap, large-scale drone attacks overwhelming costly air defenses available in 2024.
- **POS**: Develop a defense system capable of detecting and intercepting an attack of at least 100 drones against an area the size of the Netherlands more cost-effectively than countermeasures available in 2024 by 10 students in 10 weeks.

2.3. Target Analysis

In this section the potential targets are analyzed. A capability gap has been identified in intercepting cheap, long-range loitering munitions that attack deep into friendly territory. Based on this, a selection of possible primary targets is made. Also, some secondary targets like long-range reconnaissance drones are identified and considered, as it might be desirable to also counter these. Short-range loitering munitions are not considered, as they are assumed not to be airborne long enough to be intercepted by a long-range drone interceptor. The primary targets that were identified were:

Figure 2.1: *Main targets*

Loitering Munitions		
Shahed-131/Geran-1	Harpy	Switchblade 600
Shahed-136/Geran-2	Harpy-NG	Hero 900
Shahed-238/Geran-3	mini-harpy	Hero 1250
Gerbera	Harop	Skystriker
Palianytsia	Kub-10E	Samad-3

Reconnaissance Drones
Orlan-10
Orlan-30
Supercam S350
Supercam S450
UJ-22
Eleron-3

General Target Characteristics

The first target characteristic is service ceiling, the interceptor needs to reach the same altitude as the attacking drones to disable them. The typical service ceiling lies between 1 to 5 kilometers, with the Hero loitering munitions reaching 5.5 kilometers [1] and the Samad-3[8] being an outlier with about 8 kilometers.

The second target characteristic is the propulsion type. Most conventional loitering munitions use propellers in pusher configuration, driven by either electric motors or internal combustion engines. Newer additions like the Ukrainian Palianytsia and the Iranian/Russian Shahed-238/Geran-3 use a turbojet engine instead.

The third characteristic is airspeed. This is linked to propulsion type. Most conventional loitering munitions with pusher propellers have a cruise speed of 100 to 200 km/h [9]. The newer turbojet types have a cruise speed of 500 to 600 km/h [2].

The fourth characteristic analyzed is attack pattern, which is closely linked to the survivability of the attack drones. In this analysis, the Russian Shahed-136/Geran-2 attacks in Ukraine are mainly analyzed. Drone warfare is quickly evolving in this theater, it seemed appropriate to analyze the most up-to-date tactics.

The main tactic for these attacks is to attack in large swarms, which saturates air defenses and thus gives each drone a better chance of penetrating. Swarms consist of drones generally flying in very loose formations, with flight paths separated by a couple of kilometers between drones.[3] Traditionally, they flew at low altitudes to avoid radar detection. Ukraine has come up with a solution for this using microphones. From the beginning of 2025, they adapted tactics. Now they fly at 1500 meters over mainland Ukraine and 2000-2500 meters from maritime directions. They then descend to 1000 meters, stabilize the airframe and initiate a dive. Cheaper Gerbera drones are also launched alongside the Shahed-136/Geran-2 drones as decoys to get more lethal drones through air defenses.

The fifth characteristic is evasion. Historically, cheap, loitering munitions have only used passive evasive tactics, such as flying low to avoid radar detection. Recently, active evasion techniques have been used by Russian Zala 421 reconnaissance drones. In a video[4] made by an interceptor FPV, a Zala 421 can be seen dropping altitude when approached from the back. It is speculated that an aft-looking camera using machine vision is used here. The team expects active evasive maneuvers like this to become more widely applied in the future as the tactics used quickly progress.

2.4. SWOT Analysis

In Figure 2.2 below the SWOT analysis diagram is shown. This is a comprehensive overview of the design's strengths, weaknesses, opportunities and threats considering the current market developments. Further market analysis explaining the SWOT points is discussed in subsection 2.5.

---

[1] URL `https://www.designation-systems.net/dusrm/app4/hero-120.html` [Cited 02 May 2025]

[2] URL `https://armyrecognition.com/news/army-news/army-news-2024/leaked-documents-reveal-iranian-new-shahed-238-power-jet-drone-can-intercept-us-mq-9-reaper` [Cited 02 May 2025]

[3] URL `https://odessa-journal.com/alexander-kovalenko-russia-has-changed-its-tactics-of-kamikaze-drone-strikes-on-ukraine` [Cited 01 May 2025]

[4] URL `https://en.defence-ua.com/weapon_and_tech/how_does_russias_automatic_evasion_system_for_uavs_work_and_is_it_effective_video-13112.html` [Cited 01 May 2025]

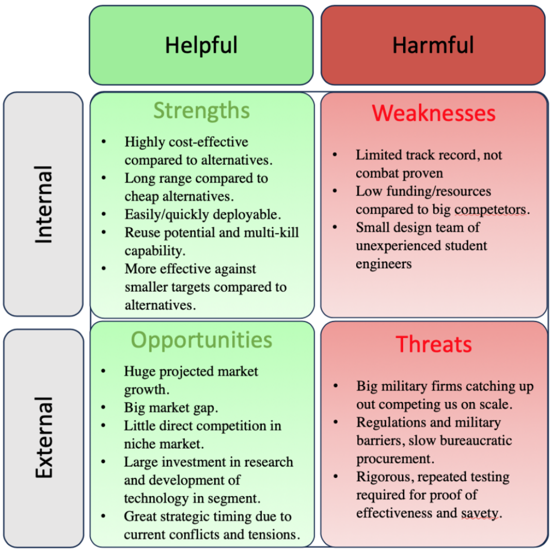

Strengths

- Highly cost-effective compared to alternatives.
- Long range compared to cheap alternatives.
- Easily/quickly deployable.
- Reuse potential and multi-kill capability.
- More effective against smaller targets compared to alternatives.

Weaknesses

- Limited track record, not combat proven
- Low funding/resources compared to big competetors.
- Small design team of unexperienced student engineers

Opportunities

- Huge projected market growth.
- Big market gap.
- Little direct competition in niche market.
- Large investment in research and development of technology in segment.
- Great strategic timing due to current conflicts and tensions.

Threats

- Big military firms catching up out competing us on scale.
- Regulations and military barriers, slow bureaucratic procurement.
- Rigorous, repeated testing required for proof of effectiveness and savety.

Figure 2.2: *SWOT analysis*

2.5. Estimating Market Share

With the emerging threat of military drones and loitering munitions becoming more and more prominent, the global anti-drone market is growing significantly. The total drone defense market is estimated to grow from 2.71 billion USD in 2024 to 11.12 billion USD by 2030 yielding a Compound Annual Growth Rate (CAGR) of 26.5% according to a report by globe newshire with an Anti-drone Market Global Outlook [5]. All over the world governments are making strategic anti-drone system investments into private sector companies in order to acquire the most cutting-edge technologies.

The North American and European markets account for approximately 2/3 of the total global drone defense market, or approximately 7.4 billion USD by 2030, therefore this is the total available allied market for the system being developed. Based on the report by Sejal Akre [6] Leading market players like Dedrone, Droneshield, Precision Hawk , Rafael Advanced Defense Systems Ltd and the Thales Group are greatly investing in research and development of drone defense technologies which will lead to even greater market growth. According to the same report, approximately 60% of the total market is taken up by drone detection and identification, and not direct countermeasures. A large part of the remaining market is expected to be short range low capability systems used against non-hardened targets, such as commercially available quadcopters, or high range high capability systems. This creates a niche market gap for low-cost high-range drone countermeasures capable of neutralizing emerging threats like loitering munitions such as the Shahed 136. Given this market gap and the projected growth of the market right now is a great market entry moment.

Although finding precise information about the market divided by the threat profile has proven to be impossible, it is assumed, based on engineering judgment, that approximately 1/3 of the remaining 40% market share for drone countermeasures is available for low-cost high-range systems. This amounts to a total serviceable market of approximately 1 billion USD by 2030. Considering the fact that little competition is currently active in this regime there exists a huge opportunity for capturing this entire market segment.

---

[5] URL `https://www.researchandmarkets.com/reports/6051069/anti-drone-market-global-outlook-and-forecast?` [Cited 02 May 2025]

[6] URL `https://www.marketresearchfuture.com/reports/drone-defense-system-market-10331` [Cited 02 May 2025]

3

Conceptual Design Work

In this chapter, selected parts of the work done in the baseline[7] and midterm[10] reports to arrive at the selected concept will be presented. First, the user requirements will be outlined in Section 3.1. Second, the concepts considered during the previous design phase will be briefly described in Section 3.2. Third, the previously performed trade-off and concept selection will be summarized in Section 3.3. Finally, the toll used to simulate the system defense will be concisely described in Section 3.4.

3.1. User Requirements

To aid with the understanding of the project User Requirements are provided:

Performance Requirements

The requirements with respect to performance are:

- **USER-PER-1**: The range of the system shall be at least 200 nautical miles.
- **USER-PER-2**: The endurance of the system shall be at least 2 hours.
- **USER-PER-3**: The time to launch of the system shall be less than 5 minutes.
- **USER-PER-4**: The ground speed of the system shall be higher than 200 knots.
- **USER-PER-5**: The landing distance of the system shall be shorter than 500 meters.
- **USER-PER-6**: The take-off distance of the system shall be shorter than 1 kilometer.

Safety And Reliability Requirements

The requirements with respect to safety and reliability are:

- **USER-SAR-1**: The system shall have a kill rate of 95 out of 100 opponents.
- **USER-SAR-2**: The system shall have redundant navigation and communication systems.
- **USER-SAR-3**: The level of autonomy of the system shall be determined by the engineers.

Sustainability Requirements

The requirements with respect to sustainability are:

- **USER-SUS-1**: The flying vehicles shall be reusable after training missions.

Budgeting Requirements

The requirements with respect to budgeting are:

- **USER-BUD-1**: The maximum take-off weight shall be no more than 25 kilograms.
- **USER-BUD-2**: The total system cost shall be less than €10,000,000.
- **USER-BUD-3**: The production cost of the aircraft shall be less than €100,000.
- **USER-BUD-4**: The elimination cost of a single target shall be less than €1000.

Other Requirements

The remaining requirements not fitting into a category are:

- **USER-OTH-1**: A set of likely target loitering munitions shall be identified by the team.
- **USER-OTH-2**: Other use-cases shall be identified by the engineers.

3.2. Concepts Descriptions

A number of options were explored before the current design was selected. 5 final concepts were considered for the trade-off performed in [10].

Final Concepts:

1. **Air mine**, a short-range kamikaze multi-copter with a small rocket motor for the terminal interception stage. Would be placed around the entire perimeter of the area that is to be protected to stop any enemy aircraft from entering friendly airspace.
2. **Pneumatic Gun**, a delta wing medium-performance UCAV, uses bleed air pressure from its turboprop engine to launch projectiles like airburst grenades at attackers. There can be different projectiles for different threats.
3. **High Performance/Missile**, a delta wing with canard high-performance UCAV, uses small, cheap guided missiles for the terminal interception stage. It can cover large distances in a short time and does not have to chase enemies itself as it fires missiles when getting close.
4. **Cost Effective/Gun**, a conventional planform UCAV, optimized for cost, uses an integrated gun to take down attackers. Machine guns in aerial combat are proven technology, and bullets are cheap.
5. **Mothership dropping darts**, a high altitude aircraft carrying guided darts. The mothership intercepts an entire swarm from above, multiple darts are released at once and drop into a steep gliding dive towards their targets while picking up speed, crashing into them, and taking them out.

3.3. Trade-Off and Selection

A trade-off was performed in [10]. A brief summary is provided. The trade-off was performed using Simple Multi-Attribute Rating Technique (SMART) [11]. The chosen trade criteria are Performance, Cost, Resources, and Risk. Each criterion is assigned a weight: Performance 0.35, Cost 0.35, Resources 0.1, and Risk 0.1.

After scoring everything, concept 1 was deemed so inadequate that it wasn't considered any further, the main reason being that too many systems are needed to protect the entirety of the Netherlands. The scores of concepts 2 through 5 are listed in Table 3.1.

Table 3.1: *Summary Trade-Off Table by Criteria*

Criteria	**Weight**	**Concept 2**	**Concept 3**	**Concept 4**	**Concept 5**
Performance	0.35	7.38	7.32	8.6	5.7
Cost	0.35	8.74	4.75	8.58	4.42
Resources	0.20	6.7	5.00	6.85	5.6
Risk	0.10	6	8.6	7.8	7.6
Total	—	7.72	7.46	8.24	5.59

After the trade-off, a sensitivity analysis was performed. This entails assessing the influence of the trade-off methodology and the subsystem selection. It tests whether changing 1 weight slightly or removing 1 criterion would influence the result from the trade-off too drastically. The same is done for the subsystems, checking whether changing only 1 aspect of a design would heavily influence the result from the trade-off. If 1 choice is the best independent of a slightly different design or a slightly different trade-off, there is more certainty about the choice.

3.4. Attack Simulation Tool

During the trade-off extensive use was made of the attack simulation tool as described in the midterm report[10]. This tool simulates and attack and the corresponding response of the system and it was used to quantify the performance of the different systems and to verify their performance metrics. In this report the tool was also used to verify the performance metrics and system architecture as will be explained in the corresponding sections.

4

Design Overview

In this chapter an overview of final design will be presented. First the main parameters and performance metrics are presented in Section 4.1. After, a functional overview will be given in Section 4.2, then the technical resources and various budgets will be presented in Section 4.3. Finally the design will be verified against the user requirements, outlined in Section 3.1, in Section 4.4.

4.1. Design Description

In this section the final design will be described, it is important to realize that an entire system was designed of which the air vehicle is just one part. First the system configuration will be described in Subsection 4.1.1 followed by the air vehicle description in Subsection 4.1.2.

4.1.1. System description

The CEDI system will consist of a total of 52 Air vehicles stationed at 10 existing bases in the Netherlands as can be seen in Figure 4.1. This configuration is presented as one of the possible viable configurations for ensuring a minimum 95% kill rate among the 3 most likely attack scenarios of 100 drones outlined in the midterm report [10]. This viable configuration was reached using the attack simulation tool outlined in Section 3.4. It should be noted that this minimum kill rate is achieved with a minimum of 36 out of 52 deployable vehicles, hence leaving room for inoperative vehicles that would, for example, be grounded for maintenance. An overview of the final system parameters can be seen in Table 4.1.

Figure 4.1: *Base locations of the CEDI system*

Table 4.1: *Overview of system parameters*

Parameter	Value
Initial system cost	€4,264,000
Yearly operational cost	€3,950,000
Cost per vehicle	€82,000
Cost per interception	€900
Total number of vehicles	52
Min. number of op. vehicles	36
Number of bases	10
Minimum kill reliability	95%

4.1.2. Air vehicle Description

In this section, the Air Vehicle design is described. An overview of the Air Vehicle design is given in Figure 4.2, while its main parameters are presented in Table 4.2.

The chosen planform configuration is a conventional configuration with a mid-wing as a primary lifting surface, and a single pusher propeller. It has no quarter chord sweep and no dihedral. All the onboard fuel is stored inside the wingbox. The chosen empennage configuration to ensure stability and controllability is an H-tail configuration. The entire horizontal stabilizer is capable of rapid movement to allow for greater maneuverability. It is encompassed between two vertical tails, both with rudders. Twin booms connect the empennage surfaces to the wing. In between the two booms at the end of the fuselage, the 225CS-40BHP Wankel rotary engine is located. A battery is installed in order to provide the power delivery to components in a smooth manner. This battery can be charged by the generator mounted on the engine, which will also provide direct power to the vital avionics for redundancy.

Table 4.2: *Main parameters of the Air Vehicle*

Parameter	**Value**
Span [m]	5.2
Fuselage length [m]	3.2
Total length [m]	5.2
MTOW [kg]	155
Thrust [N]	155
Cruise speed [$\mathrm{m\,s^{-1}}$]	80
Endurance [h]	2.92
Range [km]	840
# of intercepts [-]	5
Direct comm. range [km]	133
Direct hit probability [-]	0.9

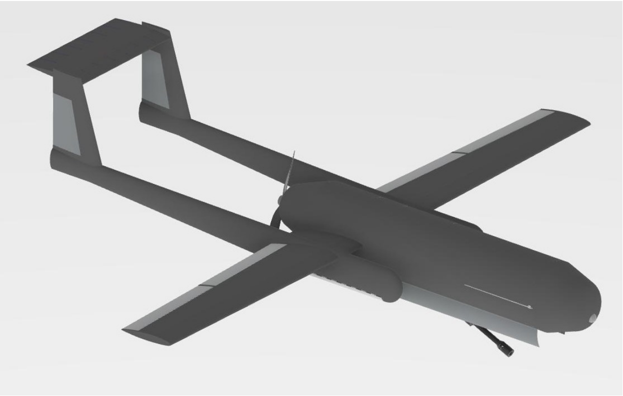

Figure 4.2: *Overview of design*

The main part of the fuselage has an elliptical shape, culminating in the detection suite in the front, and in the engine at the rear. An elliptical shape was selected to best conform to the size of the gun, minimizing the overall surface area and therefore reducing drag. The Norinco LG5 grenade launcher functions as the primary armament. It was selected due to its ability to fire programmable airburst munitions, ensuring a high reliability of taking down the target, with reduced aiming requirements.

It was calculated that a singular airborne system is capable of carrying 16 munitions, and is capable of taking down 5 drones per mission. To further improve the performance of the system, the gun is capable of motion, from a stowed position, down 32°.

To allow for accurate detection, recognition, and tracking, a suite of detection systems is employed. First, a combined visual-IR camera is used. This allows for taking video and monitoring forest fires during peacetime, as well as tracking targets and aiding in target identification during combat missions. While a camera is a very useful system, its performance highly depends on environmental conditions. Therefore, to ensure reliable operations in all environmental conditions, a LiDAR system with high accuracy is employed for short-range detection, recognition and tracking of enemy targets. Finally, neither the camera nor the LiDAR have the range required to ensure reliable interceptions. Therefore, a radar system is employed. Using this suite of sensors allows for reliable detection, identification, and tracking of targets at all operational ranges to ensure reliable mission completion.

Various avionics are included in the design: a Flight Control Unit, an onboard processing unit, an Identification Friend or Foe, and a dual communication system. This includes an antenna for direct ground-to-vehicle communication, as well as one for satellite communication.

In order to ensure that the aircraft is capable of withstanding the loads due to flight operations, a structural support system was designed. For the lifting surfaces, wingboxes were designed, alongside ribs and stringers. For the fuselage and the booms, longerons and ribs were designed to carry the loads. The primary material selected for the structure is AL7075T6. A three piece landing gear has been designed. The main landing gear is positioned behind the center of gravity underneath the booms and retracts into them during flight. The nose landing gear is offset from the centerline to accommodate the gun and is stowed in the fuselage during flight.

4.2. Functional Overview

In this section the functional flow diagram (FFD) and the corresponding functional breakdown structure (FBS) will be presented.

4.2.1. Functional Flow Diagram

The functional flow diagram shows the flow of all functions performed by the system during it's mission and can by seen in the FFD. A distinction is made between mission processes (MP) and functions. Mission processes encapsulate a combination of actions and functions performed during the mission, functions describe the specific technical actions performed by the vehicle's systems and subsystems.

4.2.2. Functional Breakdown Structure

The functional breakdown structure shows a breakdown of all the functions performed by the system and can be seen in FBS. The breakdown starts at the highest level function and ends at the lowest level functions, this shows the grouping of functions per system and subsystem.

4.3. Technical Resources and Budgets

In this section a comparison between the current estimates of the distributions of the cost, weight and power and the budgets set out in[7] will be made. The differences and similarities will be presented and new budgets will be constructed for the future. The current distribution of the the cost, weight, and power can be seen in Figure 4.3, Figure 4.4, and Figure 4.5.

The current total cost estimate of 1 airborne system is 82.000€, and its distribution can be seen in Figure 4.3. This is less than the maximum allowed budget for an airborne system of 100.000€, as set out in the user requirements. By far the largest cost is the armament in the form of the gun. This part was estimated to be approximately 10% of the entire cost, but is currently approximately 46.5%. The 2 other items that also are above the set out budgets are detection and electronics. A large overestimate of the previous budget estimate was the structures estimate. With a previous estimate of 35% and a current estimate of 2.4%, it is clear that the issue needs to be investigated further. An issue arises due to the fact that little literature is available about cost estimation of UAVs. Nevertheless the original budget remains, allowing for the cost to increase by 22% without going overbudget.

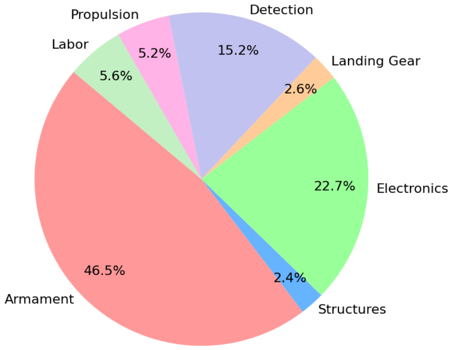

Figure 4.3: *Cost Distribution*

Functional Flow Diagram

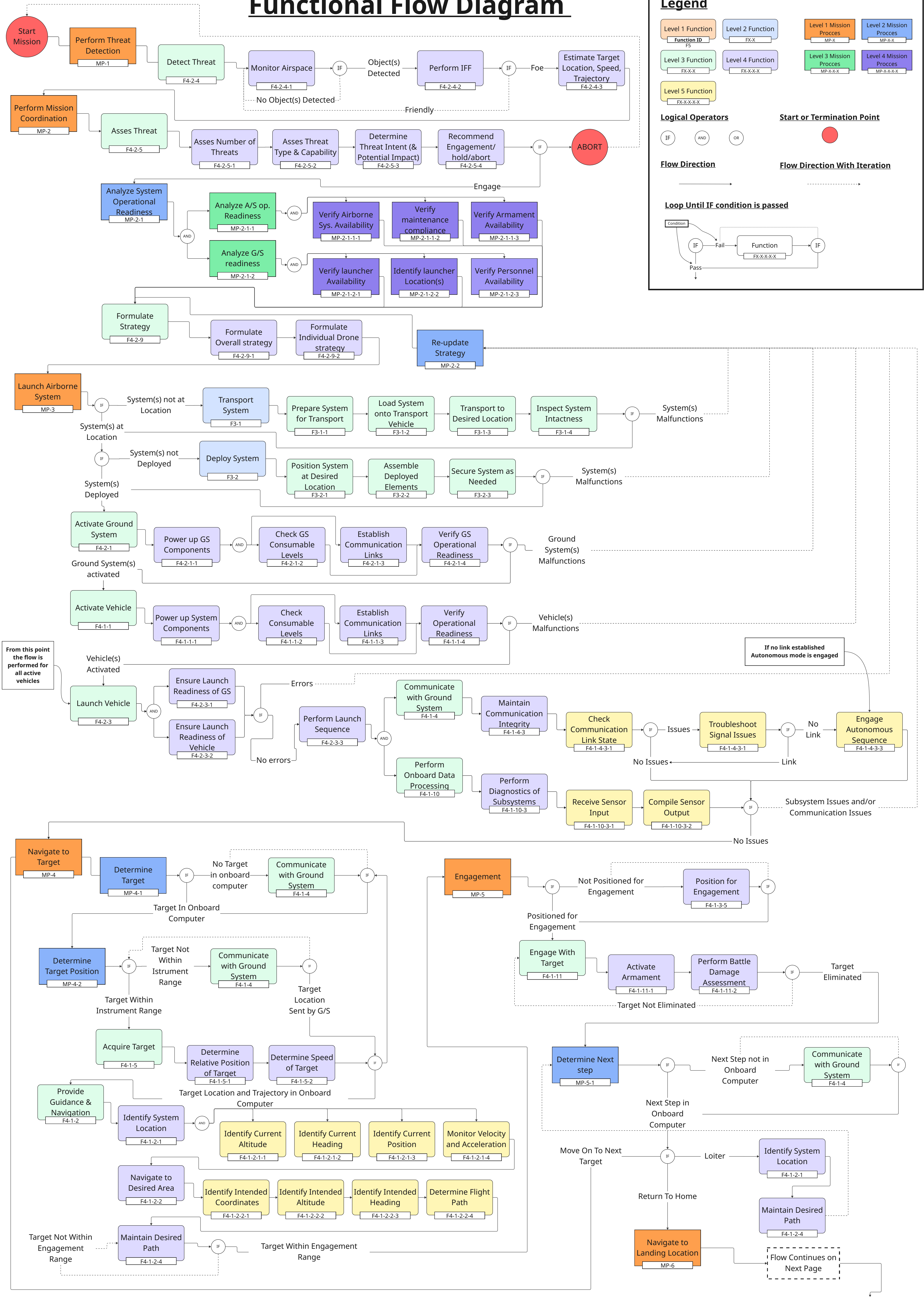

Functional Flow Diagram (Sheet 2/2)

Flow from previous page

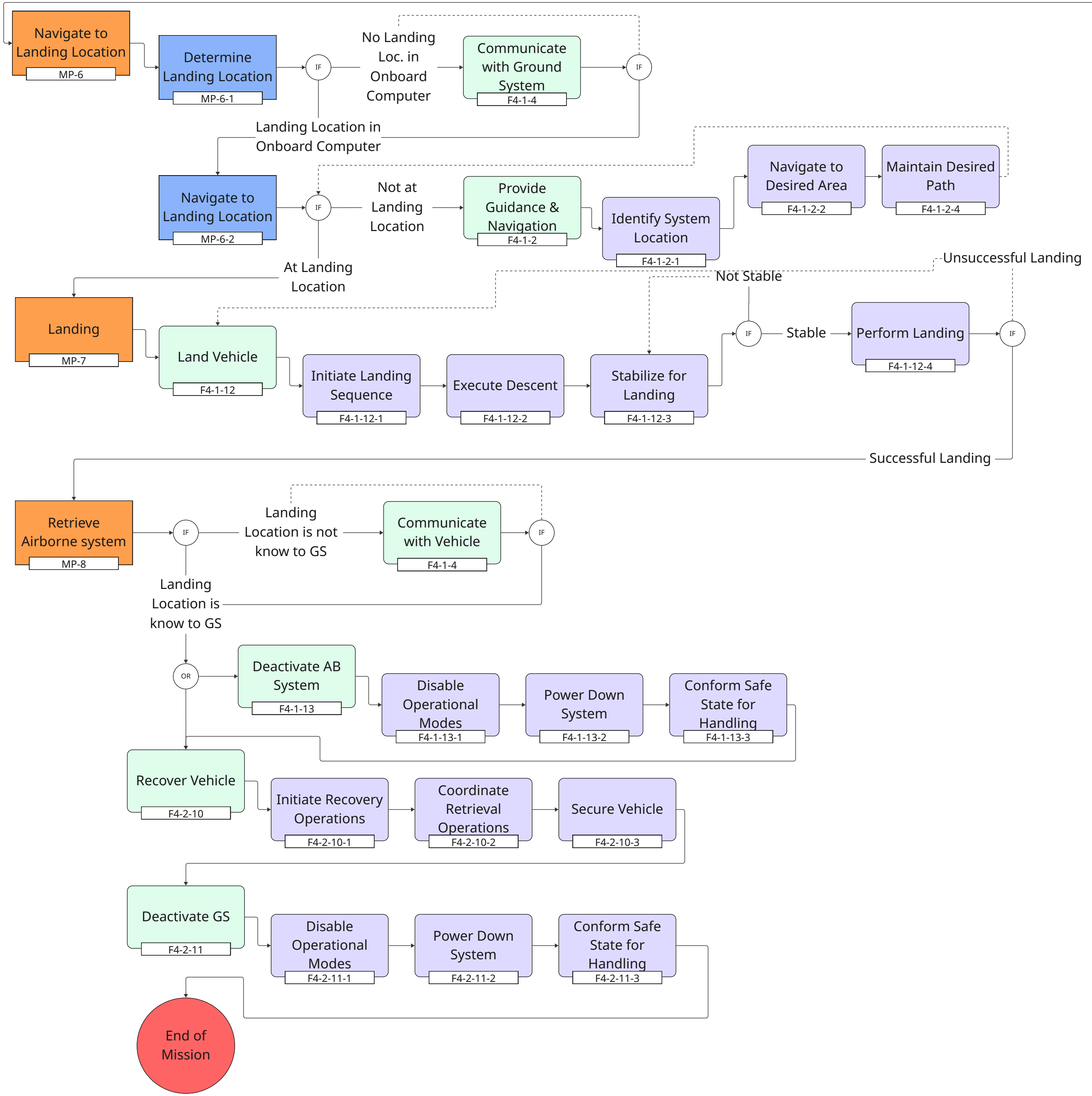

Mission Process Flow Diagram

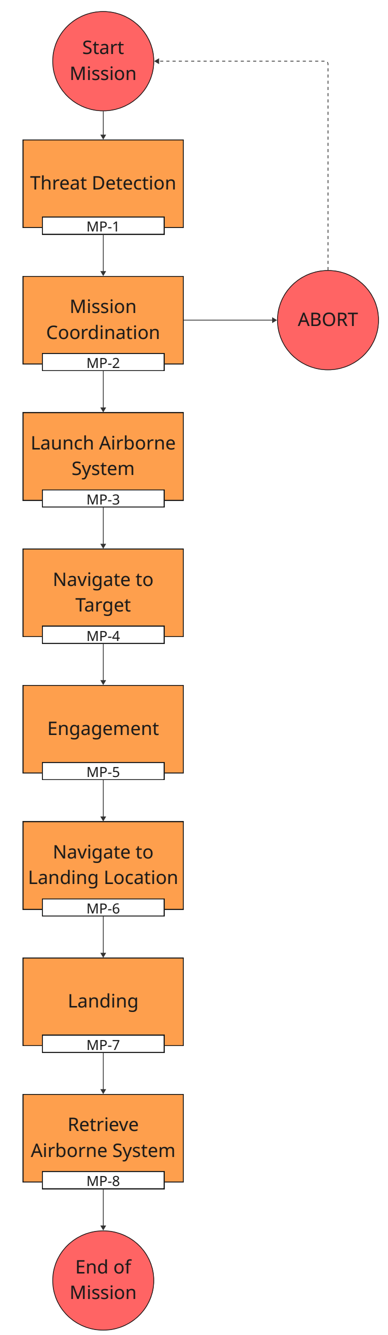

Functional Breakdown Structure

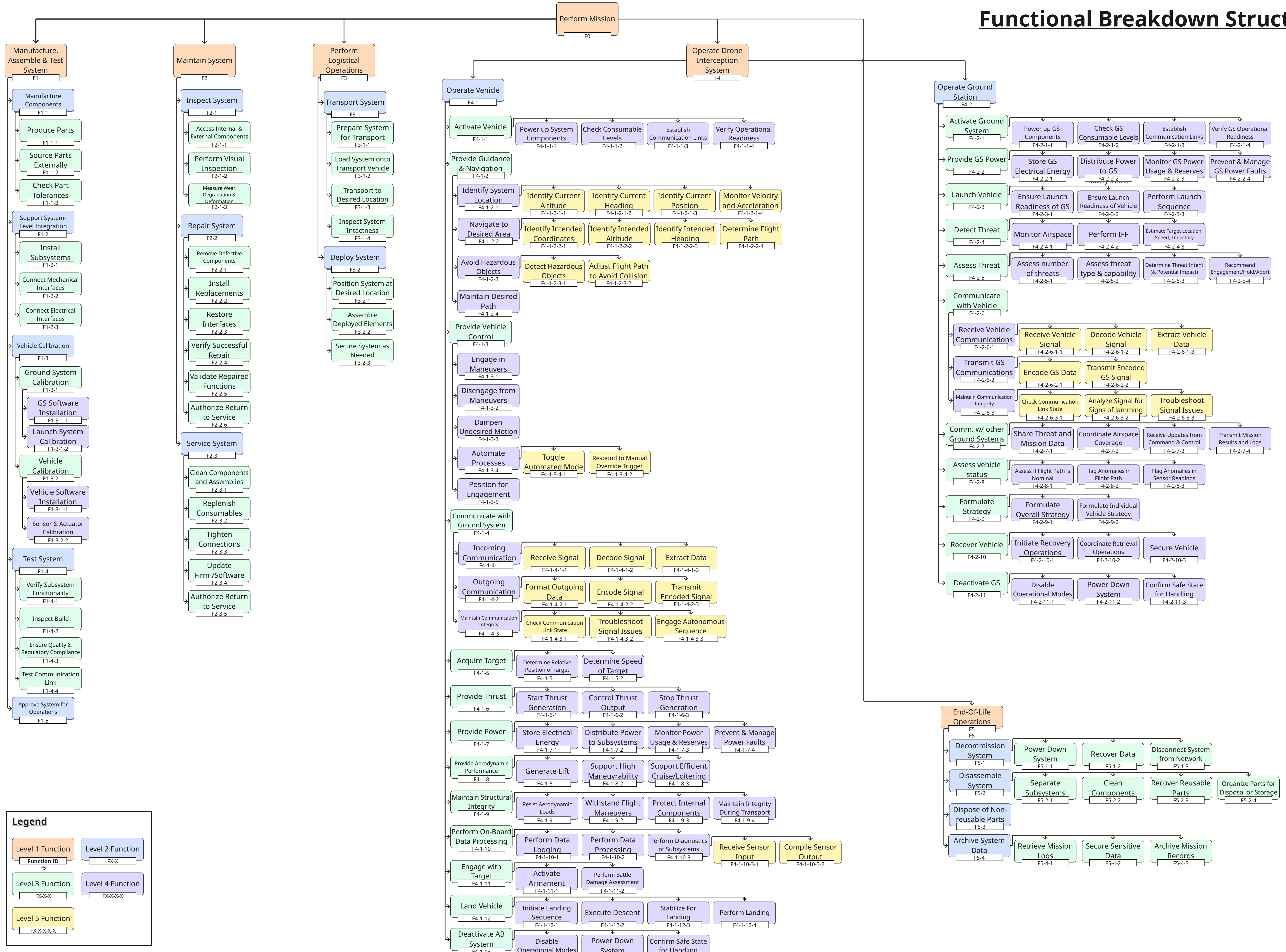

The methodology for obtaining the weight distribution of the aircraft is explained in Subsection 5.2.5, with the distribution visible in Figure 4.4. The current mass estimate of approximately 155 kg is approximately 65 kg larger than the in the mass budget laid out in[7]. When the contingency of the baseline mass budget is considered the new estimates is exactly the mass budget. The largest change is due to the unexpected increase in the mass of the engine and the fuel system, as well as the increase in the weight of the armaments. It is expected that the current mass will not increase but rather it should remain constant or even decrease. Nevertheless, a new margin of 10% is applied leading to a new mass budget of 170 kg.

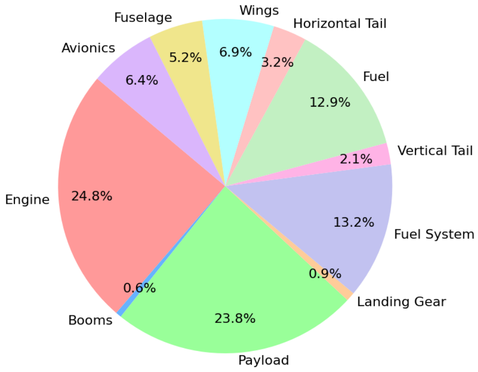

Figure 4.4: *Weight Distribution*

The method for this power budget is explained in Chapter 11. Here, all the power-using components are listed along with their respective power. This distribution is visible in Figure 4.5. This power estimate is assuming a constant power usage of all components, which will not be the case. However, the battery is sized for this just in case. This peak power consumption happens when the linear actuators of the landing gear are being deployed and all control surfaces are active, which could happen shortly after take-off or before landing. This peak power consumption results in a peak of 958 W. Compared to the peak previously outlined in the baseline report [7], 2103 W, it has been managed to half this value. This peak, however, was taking into account maximum contingencies; without the contingencies, a value of 1290 W is obtained, which is in the ballpark of the new value.

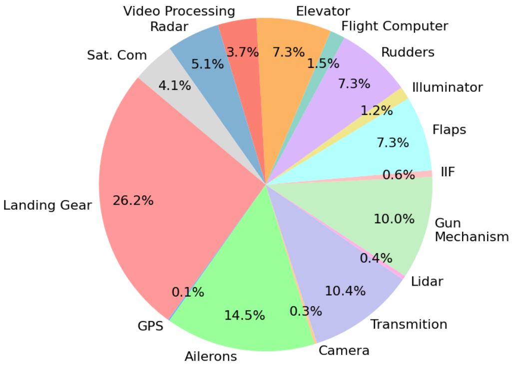

Figure 4.5: *Peak Power Distribution*

As just mentioned, the power consumption will differ between peak usage and cruise usage on a nominal mission. This cruise power distribution is portrayed in Figure 4.6. The power draw is dominated by the continuous operation of core systems such as the flight computer, video processing unit, radar, telemetry transmission, and detection suite.

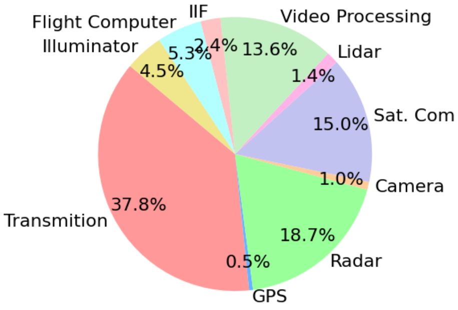

Figure 4.6: *Cruise Power Distribution*

4.4. Verification and Validation

In this section, the requirements compliance of the design with user requirements be presented. The requirement compliance matrix is visible in Table 4.3. As can be observed, USER-PER-6 is not satisfied. The degree to which the requirement is not satisfied, however, means the design can proceed. As a recommendation for the future, a larger high lift device could be considered, or a more accurate method for estimating the landing distance could be used. The requirement is further explored in Chapter 5.

Table 4.3: *User requirements compliance*

Requirement Code	Condition	Result	Met?	How?
USER-PER-1	Range ≥ 200 NM	454 NM	Yes	Section 10.3
USER-PER-2	Endurance ≥ 2 hours	2.9 hour	Yes	Section 10.3
USER-PER-3	Time to launch < 5 min	< 5 minutes	Yes	Subsection 13.3.1
USER-PER-4	Ground speed ≥ 200 knots	155.507 knots	No	Section 10.2
USER-PER-5	Landing distance < 500 m	505	No	Equation 3.12[12]
USER-PER-6	Take-off distance < 1000 m	240 m	Yes	Equation 3.12[12]
USER-SAR-1	Kill rate ≥ 95%	95 %	Yes	Section 3.4 and [10]
USER-SAR-2	Redundant Nav. & Coms.	Dual set-up	Yes	Section 8.3
USER-SAR-3	Level of autonomy	Yes	Hybrid autonomy	Subsection 13.3.1
USER-SUS-1	Air vehicles Reusable	Yes	Yes	Chapter 15
USER-BUD-1	MTOW ≤ 25 kg	155 kg	No	Section 5.3
USER-BUD-2	Total system cost ≤ €10,000,000	€4,264,000	Yes	Section 4.3
USER-BUD-3	Vehicle cost ≤ €100,000	€82,000	Yes	Section 4.3
USER-BUD-4	Single elimination cost ≤ €1000	€900	Yes	Section 15.3
USER-OTH-1	Target loitering munitions should be identified	Figure 2.1	Yes	Section 2.3
USER-OTH-2	Other use cases should be identified	See Subsection 13.3.2	Yes	Subsection 13.3.2

5
Wing Design

In this chapter, the design of the wing subsystem will be outlined. First, the requirements for the wing subsystem will be laid out in Section 5.1. Afterwards, the design process of the wing will be explained in Section 5.2. Then, the final design of the wing will be presented in Section 5.3. Finally, compliance with the requirements will be laid out in Section 5.4.

5.1. Requirements

First, a number of requirements for the design of the wings need to be defined. This has been done for the most part by Bolhuis et al.[7]; however, a number of new requirements are also included. Here, a new list of requirements relevant for the wing design is presented.

- **MIS-01.04**: The airborne part of the system shall be able to perform cruise phases of the mission with the following specifications.
  - **SYS-01.04.08**: The airborne part of the system shall be capable of sustained flight up to an altitude of 5000 meters, in ISA conditions.
    - ◇ **SUB-01.04.08.01**: The wing shall have sufficient lift to fulfill SYS-01.04.08.
  - **SYS-01.04.09**: The airborne part of the system shall be capable of sustained flight down to a ground level of 0 meters.
    - ◇ **SUB-01.04.09.01**: The wing shall have sufficient lift to fulfill SYS-01.04.09.
  - **SYS-01.04.10**: The airborne part of the system shall have a range of no less than 200 NM, in ISA conditions, at cruise altitude, at cruise speed.
    - ◇ **SUB-01.04.10.01**: The wing shall have sufficient fuel volume to fulfill SYS-01.04.10.
  - **SYS-01.04.11**: The airborne part of the system shall have an endurance of no less than 2 h, in ISA conditions, at cruise altitude, at cruise speed.
    - ◇ **SUB-01.04.11.01**: The wing shall have sufficient fuel volume to fulfill SYS-01.04.11.
  - **SYS-01.04.12**: The airborne part of the system shall have a cruise speed, when measured with respect to the ground, of more than 200 kn, in ISA conditions.
    - ◇ **SUB-01.04.12.01:** The wing shall have sufficient lift to fulfill SYS-01.04.12.
- **MIS-01.07**: The airborne part of the system shall be able to approach the target and maneuver with the following specifications.
  - **SYS-01.07.19**: The airborne part of the system shall be capable of withstanding without damage the load factor of at least 4, while maneuvering.
    - ◇ **SUB-01.07.19.01**: The airfoil shall have sufficient volume to fit the structural reinforcements to fulfill SYS-01.07.19.
  - **SYS-01.07.22**: The airborne part of the system shall have a minimum turning radius less than 200 m, in ISA conditions, at all operational flight levels.
  - **SYS-01.07.23**: The airborne part of the system shall have a maximum turn rate of at least $15\,^{\circ}\,\mathrm{s}^{-1}$, in ISA conditions, at all operational flight levels.

  - **SYS-01.07.187**: The airborne part of the system shall comply with military roll requirements.
    - ◇ **SUB-01.19.187.01**: If ailerons are installed, they shall not interfere with other subsystems of the aircraft.
- **MIS-10.19:** The system shall be integrated with a launch system in accordance with the following specifications.
  - **SYS-01.19.188:** The system shall be capable of launching from a runway no longer than 1000 m with onboard propulsion system.
    - ◇ **SUB-01.19.188.01:** The wing shall have sufficient lift to fulfill SYS-01.19.188.
    - ◇ **SUB-01.19.188.02:** If a high lift device is installed to fulfill SYS-01.19.188, it shall not interfere with other subsystems of the aircraft.
- **MIS-01.20**: The system shall be integrated with a recovery system with the following specifications.
  - **SYS-01.19.189:** The system shall be capable of landing on a runway no longer than 500 m.
    - ◇ **SUB-01.19.189.01:** The wing shall have sufficient lift to fulfill SYS-01.19.189.
    - ◇ **SUB-01.19.189.02:** If a high lift device is installed to fulfill SYS-01.19.189, it shall not interfere with other subsystems of the aircraft.

5.2. Design Process

In this section the design process behind the wing planform will be explained. All the tools used to arrive at the final design will be explained, and references will be provided where applicable.

5.2.1. Overview of the Wing Design Process

For the purpose of the design of the aircraft 2 parameters were selected to be minimized, namely drag and weight. A low drag aircraft requires little fuel, and is therefore more environmentally and economically sustainable. Additionally, for the same amount of thrust, a lower drag aircraft can achieve greater speeds, leading to increased performance of the aircraft. Finally, a lighter aircraft requires fewer materials to produce and is therefore also more environmentally and economically sustainable. Assuming all other variables are the same, a lower weight aircraft is also more maneuverable and can accelerate and decelerate faster. It is important to acknowledge that at a certain point the marginal cost of decreasing drag or weight is greater than the cost benefit of doing so. Nevertheless, due to the low complexity of the proposed design, this point should not be reached. Therefore, the recurring costs decrease with decreasing drag and weight.

In order to design and analyze the aircraft, a number of tools needed to be created, these will be described in more detail later on in this chapter. Using them allowed for the creation of a planform deemed most optimal from minimizing the weight and the drag perspective, using an optimization tool described in Subsection 5.2.9.

The design obtained from the minimization function was later tweaked in order to ensure all the requirements were met, and an optimal design was achieved. This amounted to changing the positions of the ailerons and high lift devices, and changing the length of the fuselage to ensure an optimal CG range.

5.2.2. Graph Data Extraction

In order to facilitate the automation process for the design of the wing planform, a new approach was necessary for obtaining data from figures contained in books, such as *Airplane Design Part VI*[1]. The traditional approach of reading data from graphs manually has 3 main problems:

1. Obtained data is highly prone to human errors and inaccuracies.

2. Data can only accurately be obtained for specific values.
3. The process of obtaining the data takes a long time.

Problem 2 can best be understood by looking at Figure 5.1. The values presented are only for 7 configurations of c_f/c, while the design may call for many other options.

To solve all of these problems, a new innovative approach for obtaining the data is proposed, namely approximating the graphs by polynomials, as can be seen in Figure 5.2. To do so, a tool called WebPlotDigitizer[1] was used to aid with extracting the points on the graphs, as can be seen in Figure 5.1. Afterwards, a Python script was used to apply a polynomial of degree best representing the underlying function. Finally, for points between values available on graphs (such as c_f/c for Figure 5.1) linear interpolation was used to find the data in a more structured manner. This approach allows for a greater degree of accuracy, for data to be obtained between values, and greatly speeds up the process of iterations.

It is necessary to point out the problems with this approach. The relationships that are shown on graphs in eg. *Airplane Design Part VI*[1], don't have equations next to them for a reason, namely the relationship is statistical. Furthermore, the process of applying polynomials is somewhat sensitive to the imperfect process of applying points to a curve, though with a large number of points this process is still more accurate than a human reading the data from the figures. The final problem is that when data needs to be extrapolated to a region not covered by the graphs, the accuracy drops, though this problem is not inherent to the chosen approach but exists also when a human reads the graphs to a lesser extent. To minimize this problem, a warning for the user is displayed when extrapolation is used.

For figure 8.13 from [1] extrapolation was used to find values for c_f/c of 0.6. This was done to aid in the analysis of the rudder as explained in Subsection 6.2.3.

Using the approach described above, a total of 49 figures from *Airplane Design Part VI*[1] were automated; these are listed in Table 5.1.

Table 5.1: *Automated figures*

- Figures 4.1-3
- Figure 4.7
- Figure 4.9
- Figure 4.10
- Figure 4.19
- Figure 4.20
- Appendix B Figure 6
- Figures 8.13-15
- Figures 8.31-33
- Figure 8.41
- Figure 8.42
- Figure 8.52
- Figure 8.53
- Figures 10.14-18
- Figures 10.20-26
- Figures 10.28-33
- Figures 10.35-38
- Figures 10.40-46
- Figure 10.48

---

[1] URL `https://automeris.io/wpd/?v=5_2` [Cited 14 June 2025]

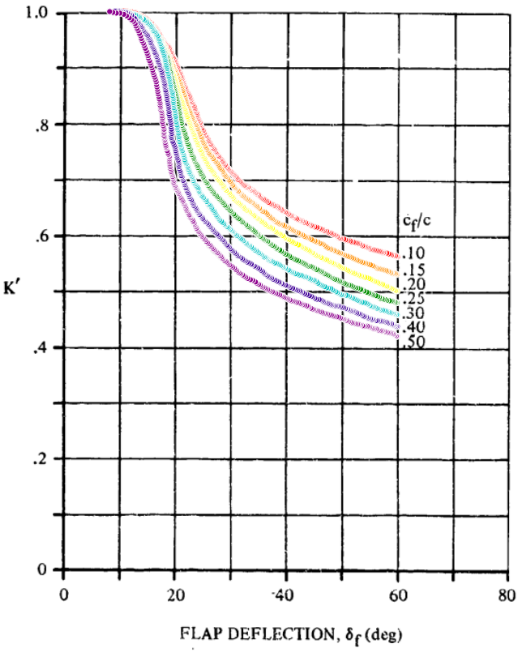

Figure 5.1: *Points used for polynomial approximations of figure 8.13 from Airplane Design Part VI[1], colors represent datasets*

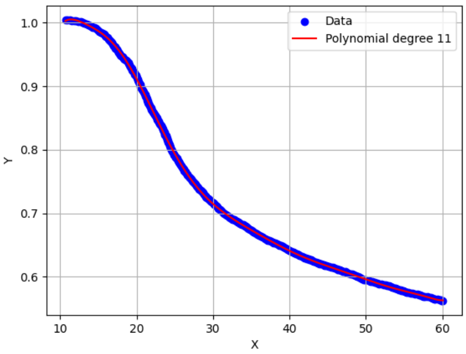

Figure 5.2: *Polynomial approximation of figure 8.13 from Airplane Design Part VI[1],* $c_f/c = 0.10$

5.2.3. Airfoil Selection

In order to proceed with the design of the aircraft, the airfoils for the wing and the empennage surfaces needed to be selected. The goal in choosing the airfoil of the main wing is to minimize the drag during cruise, while having sufficient lift for the take-off and landing conditions. For the horizontal and vertical tail surfaces, the goal is to minimize drag while having sufficient stability and controllability. The process summarized below is adapted from *Aircraft Design A Systems Engineering Approach*[2].

In order to find the ideal wing cruise coefficient, Equation 5.1 (equation 5.10 from [2]) is used. This is then divided by 0.855 to obtain the ideal airfoil cruise coefficient based on equations 5.11 and 5.12 from [2], as can be seen in Equation 5.2. This is the cruise coefficient at which the drag should be as low as possible. In a similar fashion, the maximum required wing lift coefficient can be found using Equation 5.3 (equation 5.13 from [2]). The gross airfoil maximum lift coefficient is then obtained from Equation 5.4 (equations 5.14 and 5.15 from [2]). Finally, the maximum lift coefficient of the airfoil is obtained from Equation 5.5 by subtracting the contribution of high lift devices (equation 5.16 from [2]). It is assumed for now that the contribution of high lift devices is 0.8. This assumption will be verified later in Subsection 5.2.7. The initial data used for selecting the airfoil comes from class 1 analysis performed in [10], with the W_{TO} equal to 125 kg and a surface area equal to 2.23 m^2.

$$C_{L_c} = \frac{2W_{ave}}{\rho V_c^2 S} \tag{5.1}$$

$$C_{l_i} = \frac{C_{L_c}}{0.855} \tag{5.2}$$

$$C_{L_{max}} = \frac{2W_{TO}}{\rho_0 V_s^2 S} \tag{5.3}$$

$$C_{l_{max\_gross}} = \frac{C_{L_{max}}}{0.855} \tag{5.4}$$

$$C_{l_{max}} = C_{l_{max\_gross}} - \Delta C_{l_{HLD}} \tag{5.5}$$

An initial search for airfoil performance data gave unsatisfactory results. An initial attempt at using Airfoil Tools[2] website was thwarted by the website being inaccessible. Further attempts at

---

[2] URL `http://airfoiltools.com/` [Cited 02 June 2025]

using TU Delft Airfoil ClCdCm Database[3] were deemed unsuccessful due to the low amount of data and its poor quality. Therefore, a decision was made to conduct independent analysis of the airfoils.

In order to analyze the airfoils, first airfoil coordinate data needed to be obtained. This was done by utilizing an automation script, obtaining the data for all the airfoils of the TU Delft Airfoil Coordinate Database[4]. Using this tool the coordinates for 1171 airfoils were obtained for further analysis. An initial attempt at analyzing airfoils was performed using XFOIL[5]. A problem quickly arose due to non-convergence of the tool for thicker airfoil, limiting its usefulness. It was therefore decided that Javafoil[6] should be used instead.

Using Javafoil meant that automation could not be set up due to the teams lack of knowledge of the Java coding language. Therefore, a decision was made to choose a representative sample from the total number of airfoils and perform the analysis manually. A low Reynolds number of 10000 was selected for the analysis to aid with the stability of the simulation. The airfoils were then analyzed for the angles of attack of between $-20°$ and $20°$. A stall model of Calcfoil and a transition model of Eppler standard were used. The lift, drag, and moment polars for 369 airfoils were obtained this way. Care was taken to ensure all major airfoil families were represented. As a potential future improvement, the analysis process could be automated to analyze more airfoils or, otherwise, more airfoils could be analyzed manually.

An unfortunate issue arose during the analysis of the moment polar. Due to the numerical nature of Javafoil for certain points, the moment coefficient did not converge, and instead had an infinite value, as can be seen in Figure 5.3. If such a case occurred in between converged values, linear interpolation was used to replace the missing data. In Figure 5.3 there are 2 such cases at about $-17°$ and $-10°$. Otherwise, if such a case occurred on the edge of the dataset, the data for the moment coefficient was cut off at that point. In Figure 5.3 this occurred from 10° onward.

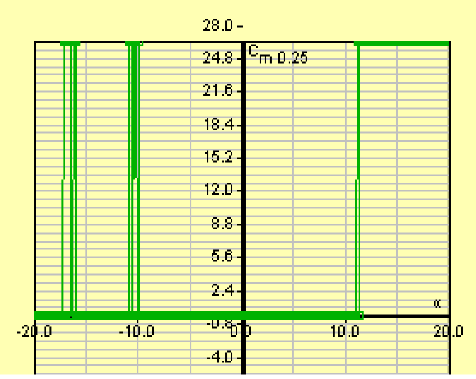

Figure 5.3: *Example of C_m issues in Javafoil*

Using the tools created to analyze all the airfoils, the best performing airfoils for the MTOW and the surface area could be found. The result of the initially selected airfoil using data obtained from Class 1 weight and surface area can be found in Table 5.2 and Figure 5.4. The best performing main wing airfoil of the airfoils analyzed was the NASA/Langley RC12-64 airfoil. It can be seen in Figure 5.5.
As can be seen in Figure 5.4 the selected airfoil exhibits a significant drag bucket, leading to an excellent performance in terms of drag during cruise. It does however complicate the drag analysis, as the typical value of C_{D_0} can no longer be used. Instead, Equation 5.6 (equation 5.8 from [2]) is used to find the drag of the airfoil as a function of the lift coefficient.

Table 5.2: *Airfoil Parameters*

Parameter	Value	Unit
α_s	14	°
C_{l_α}	5.22	rad^{-1}
C_{l_0}	0.09	-
$\alpha_{L=0}$	-0.99	°
C_{m_α}	-0.0524	rad^{-1}
C_{m_0}	-0.0063	-
C_{d_c}	0.01987	-
$C_{l_{max}}$	1.096	-

$$C_d = C_{d_{min}} + K(C_l - C_{l_{min}})^2 \tag{5.6}$$

---

[3] URL https://aerodynamics.lr.tudelft.nl/cgi-bin/afLDM [Cited 02 June 2025]
[4] URL https://aerodynamics.lr.tudelft.nl/cgi-bin/afCDb [Cited 03 June 2025]
[5] URL https://web.mit.edu/drela/Public/web/xfoil/ [Cited 03 June 2025]
[6] URL https://www.mh-aerotools.de/airfoils/javafoil.htm [Cited 03 June 2025]

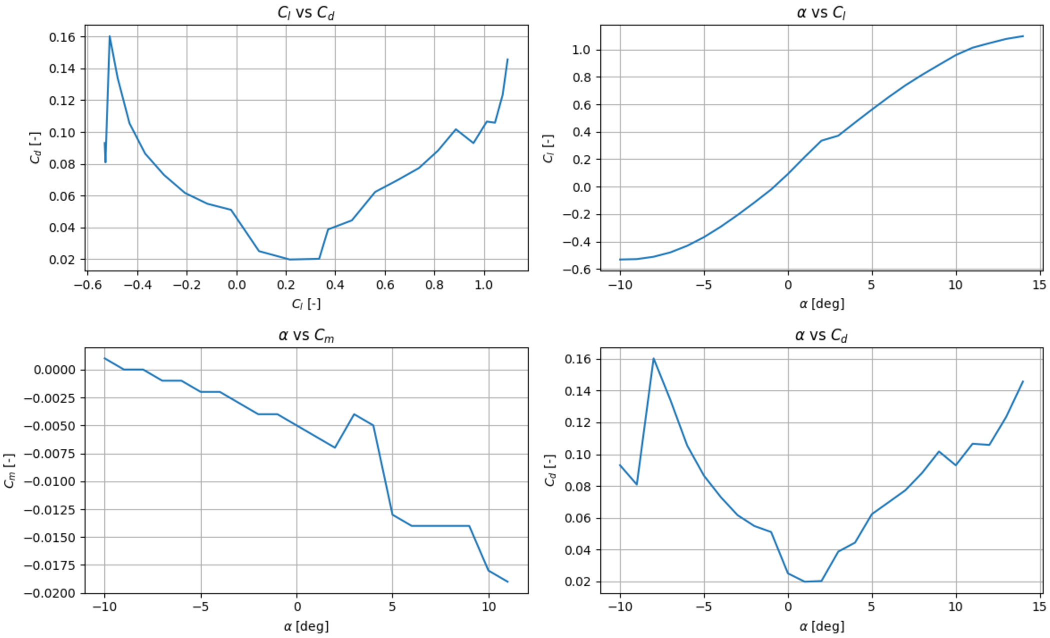

Figure 5.4: *Polars of the initial airfoil of the main wing, NASA/Langley RC12-64C*

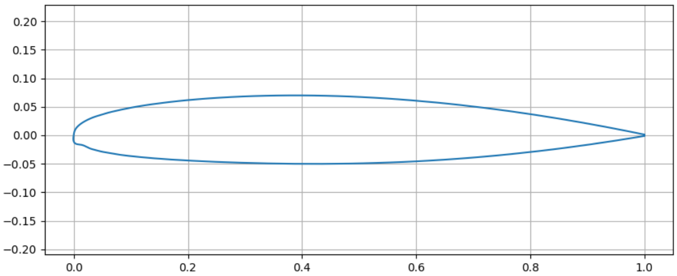

Figure 5.5: *Shape of the initial airfoil of the main wing, normalized to chord = 1*

5.2.4. Lifting Line

In order to more accurately analyze the wing, a wing lift distribution tool was required. To estimate it and describe a number of parameters such as the total wing lift and lift slope, $C_{L_{\alpha w}}$, a lifting line tool was created utilizing the lifting line theory. This allowed for the design to proceed with data that is more accurate than simple statical relations. The main drawback of lifting line theory is that it cannot account for stall because of it's linear nature. To prevent inaccurate data, a check for near stall conditions was implemented. The process summarized below is adapted from *Aircraft Design A Systems Engineering Approach*[2].

The goal of the process is to obtain the lift coefficient at a finite number of points and, therefore, the lift distribution over the wing, as can be seen in Figure 5.7. To do so, the wing is first divided into a number of equally spaced segments, $n = 100$, as can be seen in Figure 5.7. Afterwards, Equation 5.7 (equation 5.40 from [2]) is used to obtain the intermediate unknowns. Linear twist is applied and root incidence is taken into account to calculate the effective angle of attack of each segment individually. Then using Equation 5.8 (equation 5.42 from [2]) the lift coefficients of each segment are calculated. The lift distribution of the wing can then be seen in Figure 5.8.
Having obtained the lift coefficients from Equation 5.8, the total lift coefficient of a wing can be obtained from Equation 5.9. Furthermore, using this equation and varying the angle of attack of the aircraft $C_{L_{\alpha w}}$ is obtained.

$$\frac{\bar{C}_i C_{l_\alpha}}{4\cdot b}(\alpha_0-\alpha_i)=\sum A_n \sin(n\theta)\left(1+\frac{\frac{\bar{C}_i C_{l_\alpha}}{4b}\cdot n}{\sin(\theta)}\right) \tag{5.7}$$

$$C_{L_i}=\frac{4b}{\bar{C}_i}\sum A_n \sin(n\theta) \tag{5.8}$$

$$C_{L_w}=\sum_i^n \bar{C}_i\cdot C_{L_i}\cdot\frac{b}{n} \tag{5.9}$$

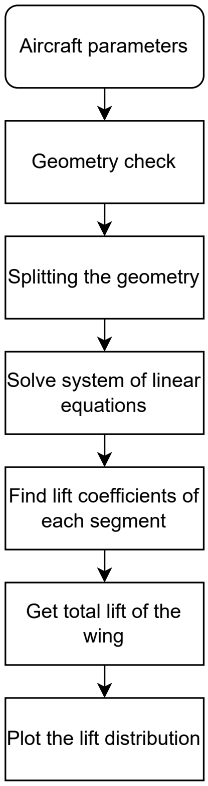

Figure 5.6: *Lifting line tool overview*

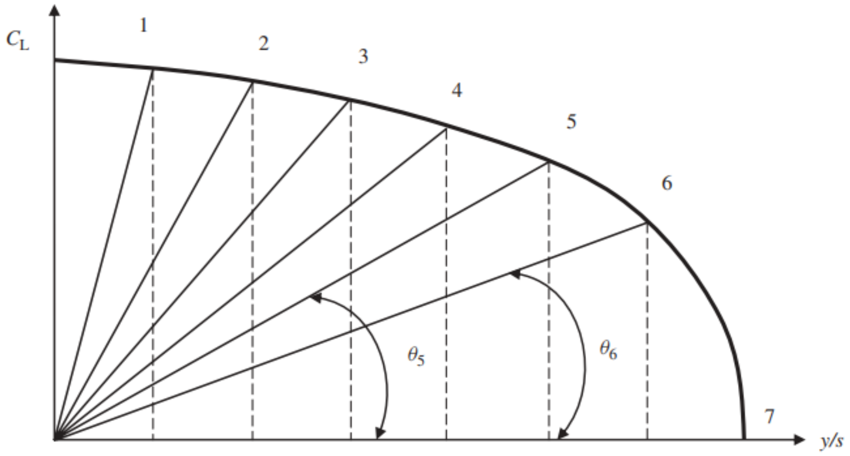

Figure 5.7: *Angles corresponding to each segment in lifting-line theory, reproduced from [2]*

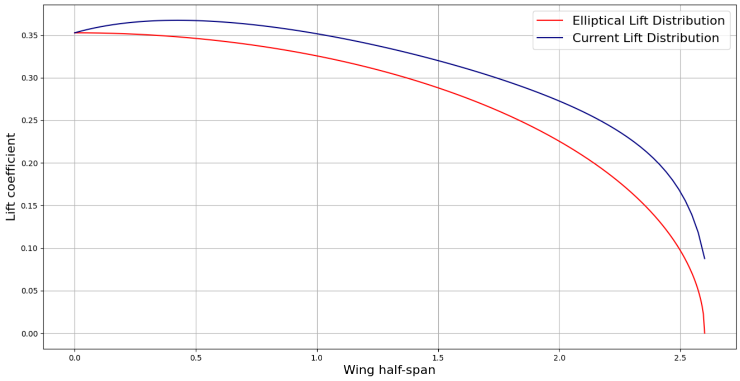

Figure 5.8: *Lift distribution over the wing*

5.2.5. Class 2 Weight Estimation

In order to size the wing to be capable of flying during cruise, sufficient lift is required to be in equilibrium with the weight of the aircraft. Therefore, the weight of the aircraft needs to be known in order to proceed with the design of the wing. A class 1 weight estimate has already been produced by Bolhuis et al.[10], and an initial weight estimate of 125 kg has been obtained. In this section, the process of obtaining the class 2 weight estimation will be explained.

The method for obtaining the class 2 estimate described here is adapted from *Aircraft Design A Systems Engineering Approach*[2]. The take-off weight of the aircraft is divided into 3 parts: empty weight, payload weight, and fuel weight, as can be seen in Equation 5.10 (equation 10.1 from [2]. The empty weight of the aircraft is divided into 3 further parts: structure weight, engine weight, and equipment weight, as given in Equation 5.11 (equation 10.2 form [2]). Finally, the structure of the aircraft is divided into the structural weights of the components of the aircraft: wing weight, fuselage weight, horizontal tail weight, vertical tail weight, landing gear weight, and, if applicable, the weight of the booms for an H-tail, as can be seen in Equation 5.12. An overview of the weight contributions and equations used to find them is given in Figure 5.9.

$$W_{TO} = W_E + W_P + W_F \tag{5.10}$$

$$W_E = W_S + W_{engine} + W_{eq} \tag{5.11}$$

$$W_S = W_W + W_{fus} + W_{ht} + W_{vt} + W_{LG} + W_{booms} \tag{5.12}$$

In order to estimate the weights of each of the components from Equation 5.12, specific equations from [2] were used. For the weight of the wing equation 10.3 from [2] was used. Similarly, the weights of the vertical and horizontal tail were obtained using equations 10.5 and 10.6 from [2]. The weight of the fuselage was obtained from equation 10.7 from [2]. Since no equation was available for estimating the weight of the booms, equation 10.7 from [2] was used, with parameters substituted for boom parameters. Finally, the weight of the landing gear was obtained from equation 10.8 from [2].

Table 5.3: *Coefficients used in equations 10.3-10.12 from [2]*

Coefficient	Value
K_ρ	0.0016
$K_{\rho HT}$	0.0335
$K_{\rho VT}$	0.094
$K_{\rho f}$	0.00235
K_L	1
K_{ret}	1.07
K_{LG}	0.5

The weight of the engine was obtained from equation 10.9 from [2], with the weight of the fuel system from equation 10.12 from [2]. The weight of the equipment was estimated to be equal to the weight of the installed avionics, the gun, and the gun motion mechanism, approximately 47 kg.

The weight of the payload is equal to the weight of the ammunition carried by the drone, and is estimated in Chapter 7, while the weight of the fuel was estimated in Chapter 10.

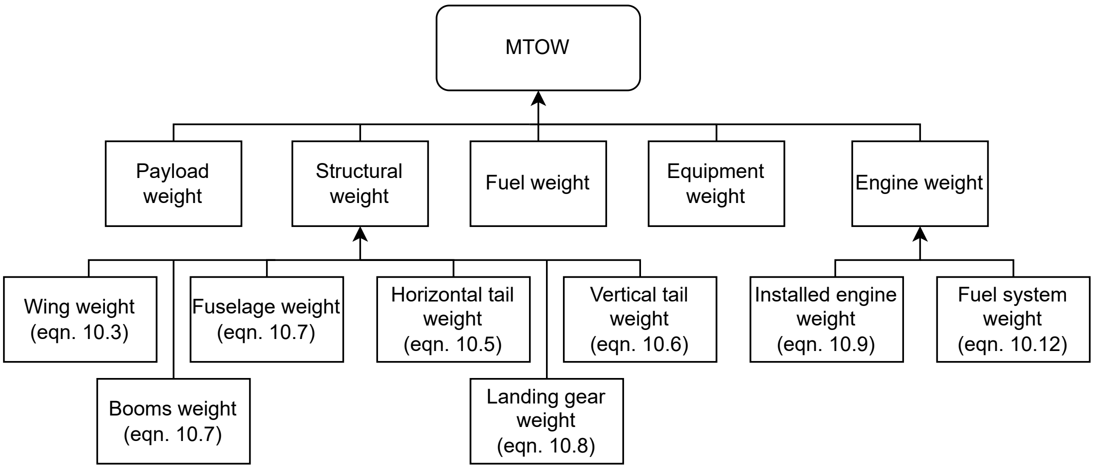

Figure 5.9: *Overview of weight contributions, all referenced equations from [2]*

5.2.6. Class 2 Drag Estimation

In order to estimate the drag of the aircraft, *Airplane Design Part VI*, chapter 4[1] was used. Due to the low speed required of the aircraft, the analysis of the drag was considerably simplified as only subsonic regime was considered. Furthermore, since the purpose of estimating the drag is to design the aircraft to minimize the drag during cruise, only clean cruise condition is considered. All the considered drag contributions are shown in Equation 5.13.

$$C_D = C_{D_{wing}} + C_{D_{fus}} + C_{D_{emp}} + C_{D_{boom}} \tag{5.13}$$

$$C_{D_{emp}} = C_{D_{HT}} + C_{D_{VT}} \tag{5.14}$$

In order to find the drag of the wing, the steps laid out in section 4.2.1[1] were followed. Similarly, to find the drag of the fuselage, section 4.3.1[1] was followed. It was assumed that the fuselage culminates in a point and therefore has no base area, and as such no base drag. The drag of the empennage consists of the drag of the horizontal and vertical tail, as can be seen in Equation 5.14. To find these, section 4.4.1[1] was followed.

For the purpose of finding the drag of the booms, they were assumed to be small fuselages. While this approach has its merits, as the shape of a boom and that of a typical fuselage are broadly similar, it does have two main drawbacks. First, the relationships described are usually statistical, and therefore not so accurate for areas as small as a boom. Second, this method does not account for the interference drag between the fuselage, the booms, and the engine. This is a major limitation of this method. Two possible solutions are proposed for future design work: CFD and wind tunnel testing. Both of these methods would allow for a more accurate understanding of the impact the booms of an aircraft have on the underlying drag, but they are unfortunately outside of the scope of this project.

5.2.7. High Lift Devices

A decision was made to use plain flaps only, due to their low cost and complexity. The presented method used to analyze the aircraft comes from *Airplane Design Part VI* sections 8.1.2 and 8.1.4[1].

First, the impact of the plain flap on the maximum lift of an airfoil needs to be understood. Equation 8.4[1] stipulates how this can be done for an arbitrary deflection, while equation 8.18[1] explains how this is done for the maximum deflection. Similarly, equation 8.27[1] discusses the wing lift increment, while equation 8.29[12] discusses the maximum wing lift increment.

Using the equations provided, the lift increment is found in two distinct ways. First, a new function is added to the lifting line tool (see Subsection 5.2.4) that allows for the lift distribution due to flap deflection to be computed. Second, equation 8.29[1] is used to find the maximum wing lift increment of the wing. The two values are compared to ensure the accuracy of the solution.

5.2.8. Ailerons

Ailerons primarily serve to enable the aircraft to roll, yet no clear military or civilian roll requirements exist for UAVs[13][14]. The closest two standards both have issues making their use impractical. *MIL-STD-1797A Flying Qualities of Piloted Aircraft*[13] is, as the name suggests, concerned with piloted aircraft, and *NATO STANDARD AEP-83 Light Unmanned Aircraft Systems Airworthiness Requirements*[14] has no specific roll requirements, with the closest requirement being:

"ER.2.1.2, UL47.3: The UA must be safely controllable and manoeuvrable in all FCS operating modes and in manual direct piloting mode (where applicable), in the most severe operating conditions as per UL.0, during all flight phases including: (...) level flight, including mission relevant special manoeuvres; (...)"[14]

Current loitering munitions and potential target systems have poor maneuverability (see Chapter 2), with usually no evasive maneuvers possible. Nevertheless, to ensure the system is future-proof and can perform its mission reliably, high maneuverability is desired. Therefore, the aircraft will be analyzed as if it was meant to meet the requirements set out by *MIL-STD-1797A*[13] for class 1 aircraft, with the understanding that failure to fulfill these requirements does not mean the aircraft is not airworthy. Furthermore, level 3 requirements are selected as no pilot is present and a computer is deemed to be capable of flying under high pilot load. According to *Flight Dynamics Principles*[15] the flight phase categories are as follows:

Category A: non-terminal flight phases that require rapid manoeuvring, precision tracking, or precise flight path control
Category B: non-terminal flight phases that require gradual manoeuvring, less precise tracking, and accurate flight path control
Category C: terminal flight phases that require gradual manoeuvring and precision flight path control

For the airborne part of the system, the flight phase categories can be seen in Table 5.4.

Table 5.4: *Aircraft speed categories*

	Category A	**Category B**	**Category C**
Speed [$\mathrm{m\,s^{-1}}$]	60-80	40-60	30-40

In order to estimate the effectiveness of the ailerons the method laid out in *Aircraft Design A System Engineering Approach* Section 12.4[2] was followed. An overview of the method is provided in Table 5.5. The steady-state roll rate was obtained using equation 12.37[2]. The aircraft drag in rolling motion, C_{D_R}, was estimated to be 0.95, and the average distance between the rolling drag center and the centerline of the aircraft, y_D, was estimated to be 40% of the semi-span of the wing in accordance with[2].

In order to find the time it takes for the aircraft to roll to an arbitrary angle, first, the mass moment of inertia of the aircraft needs to be estimated. To do so, the method laid out in *Aircraft Design A System Engineering Approach* Section 11.7[2] was followed. The wing, horizontal, and vertical tails were treated as rectangular prisms with the MAC of the respective surface acting as the chord. The fuselage and booms were treated as thin cylindrical shells. The engine and the gun were treated as solid cylinders. The propeller was treated as a slender rod. Finally, the avionics, fuel, fuel system, nose, and main landing gear were treated as point masses. Standard equations were used to find the mass moment of inertia for all components and parallel axis theorem was applied by utilizing the estimated center of gravity using Subsection 6.2.1.

Finally, the steady state roll rate, P_{ss}, was obtained from equation 12.37[2]. Then, the angle at which the aircraft enters the steady state roll and the time to roll to an arbitrary angle were obtained from equations 12.43[2] and 12.33[2], respectively. Using these values allowed for the analysis of the aircraft in roll. The final times it takes for the aircraft to roll to the angles set out by [13], for all three flight phase categories, can be seen in Table 5.10.

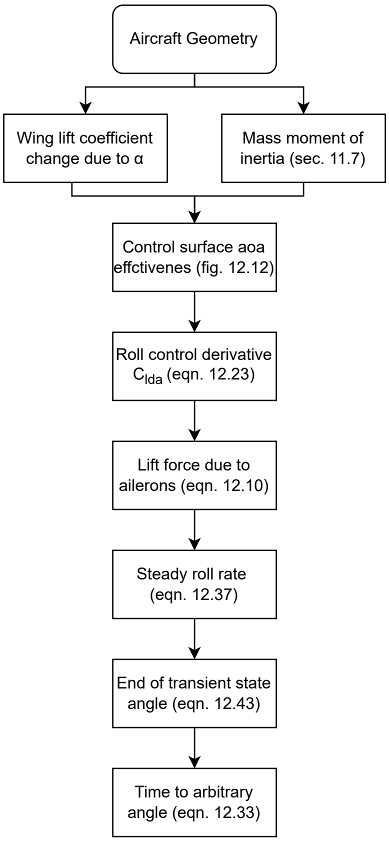

Table 5.5: *Method to obtain the roll rate overview, all references to [2]*

5.2.9. Optimization Methodology

In order to ensure an optimal design was reached, a new approach to the process of iteration was employed. The goal of the process, as explained in Subsection 5.2.1, is to minimize the drag and weight of the aircraft, while maintaining favorable flight characteristics. To that end, a multivariate global minimization algorithm with bounds was used. A total of 23 variables were optimized.

A SciPy[7] basinhopping algorithm was used due to its ability to find global minima, with a local minimization algorithm of 'L-BFGS-B', to allow for local optimizations. Due to the large number of parameters to be optimized, a multithreading algorithm was employed by splitting the bounds of the system among many cores. This drastically decreased the time it takes for the algorithm to compute the solution; however, it did remove some possible solutions from the option space, as all bounds were divided equally among the cores. This was mitigated afterwards by a human looking over the design and making changes to it based on engineering judgment.

A number of bounds were set-up to limit the possible option space, and therefore reduce the time the algorithm takes to run. While setting-up the bounds, care was taken to ensure they were not too restrictive, by looking at class 1[10] estimations and literature about drones of the same weight class. The bounds on the geometry of the aircraft can be seen in Table 5.6.

---

[7] URL `https://scipy.org/` [Cited 18 June 2025]

Table 5.6: *Bounds on Aircraft Geometry Parameters*

Component	Parameter	Min	Max
Wing	Root Chord [m]	0.5	1.5
	Tip Chord [m]	0.2	0.75
	Semispan [m]	1	3
	Twist [deg]	-5	5
	Root Incidence [deg]	0	10
	Distance Nose to $C_{1/4}$ [m]	1.3	3
	Dihedral [deg]	0	10
	Quarter Chord Sweep [deg]	0	15
HLD	Distance from Centerline [m]	0.3	1
	Length [m]	0.3	1
	Width [m]	0.1	0.4
Aileron	Distance from Centerline [m]	1	3
	Length [m]	0.3	1
	Width [m]	0.1	0.3
Fuselage	Length [m]	2	4
Horizontal Tail	$C_{1/4}$ to $C_{1/4}$ [m]	0.1	5
	Root Chord [m]	0.1	1
	Semispan [m]	0.1	1.5
	Height [m]	0	0.5
Vertical Tail	Tip Chord [m]	0.1	0.5
	Root Chord [m]	0.3	1
	Semispan [m]	0.5	2
	Quarter Chord Sweep [deg]	0	45

Having set-up the boundaries of the design, the cost function of the algorithm needed to be created. An overview of the cost function is presented in Figure 5.10. The cost function has been split into two main parts: goals and penalties. Goals are the parameters that the function is meant to minimize, but that should never go to zero, while penalties are meant to represent a suboptimal design. Initially, the penalties were set-up in a binary way, where either they were applied or not. This proved to be a suboptimal solution, as the function had a difficult time in converging to a minimum due to the lack of gradients. Afterwards, a change was made where the degree of non-compliance with the check dictated the level of penalty. This greatly improved the performance of the function.

The function (Figure 5.10) performed as follows. First, a new set of aircraft parameters was selected from within the bounds. A check was made for how much the geometries interfere; for example, if the aileron and the HLD occupy the same space, the rest of the analysis function was skipped to improve the speed of the program. A very small (on the order of 1 mm) degree of interference was allowed to not exclude solutions that had potential. If the interference check was passed, an analysis of the design began. The weight and the drag were computed using Subsection 5.2.5 and Subsection 5.2.6, respectively. Then, the aircraft stability derivatives were calculated as explained in Subsection 6.2.4. The roll performance of the aircraft was analyzed and compared to the requirements, as can be seen in Subsection 5.2.8. The effectiveness of the high lift devices was computed and compared to the assumed effectiveness as explained in Subsection 5.2.7. If the wing was not producing sufficient lift, another penalty was applied to ensure sufficient lift would be available during cruise. The vertical and horizontal tails would also be analyzed to ensure they fulfilled the requirements as stated in Chapter 6. Afterwards, a comparison was made to ensure that the tip chord was not greater than the root chord. Finally, the design was compared to the previous best

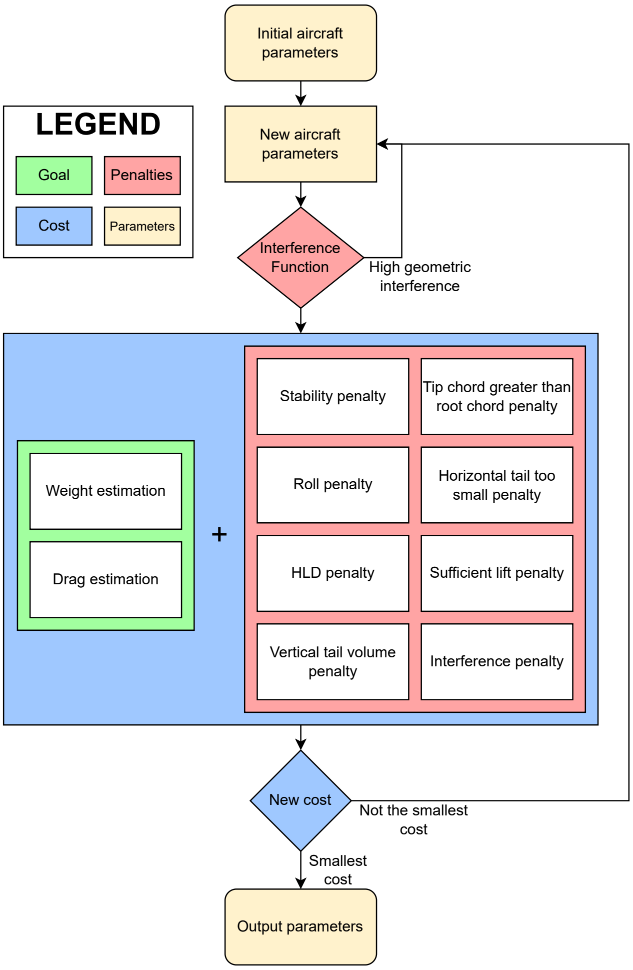

Figure 5.10: *Minimization function overview*

design and, if the cost function was lower, a new best design was set. This was done until the entire bounds area was covered.

5.3. Design Description

A mid-wing configuration was selected to allow for easy armaments integration, with the primary support of the gun being the front spar of the wingbox. This choice also had a positive impact on the aerodynamics of the aircraft, minimizing the drag. The final values of the geometry of the wing can be seen in Table 5.7, and that of the HLD and ailerons in Table 5.8 and Table 5.9, respectively. The roll performance of the aircraft can be seen in Table 5.10.

Table 5.7: *Final geometry values of the wing*

Parameter	Value
Root Chord [m]	0.7
Tip Chord [m]	0.5
Semispan [m]	2.6
Twist Angle [deg]	-3
Root Incidence [deg]	5
Distance Nose to $C_{1/4}$ [m]	2.3
Dihedral [deg]	0
Quarter Chord Sweep [deg]	0
Aspect Ratio [-]	8.67
Mean Aerodynamic Chord [m]	0.61
Surface Area [m^2]	3.12

Table 5.8: *Final geometry values of the HLD*

Parameter	Value
Distance from Centerline [m]	0.6
Length [m]	0.95
Width [m]	0.16
Max deflection [deg]	30

Table 5.9: *Final geometry values of the ailerons*

Parameter	Value
Distance from Centerline [m]	1.55
Length [m]	1
Width [m]	0.16
Max deflection [deg]	25

Table 5.10: *Roll performance of the aircraft*

Flight Phase Category	Angle	Required Time	Achieved Time
A	60	2.6	3.0
B	60	3.4	4.3
C	25	2.6	3.8

A final check was made on the airfoil and a new airfoil was selected by the code as optimal, NACA 63-210 airfoil. Nevertheless, the original airfoil was selected as the one to proceed with for two reasons. First, the drag bucket on NACA 63-210 is significantly smaller, as can be seen in Figure 5.11. Second, a reduction of the surface area of 0.3 m^2 once again indicates that NASA/Langley RC12-64C airfoil performs best. For these reasons, the final airfoil is NASA/Langley RC12-64C. The shape of the airfoil can be seen in Figure 5.5 and the polars are given n in Figure 5.4.

The booms connecting the empennage to the rest of the aircraft are also connected to the wing. Care was taken to ensure the booms do not interfere with the flaps and the propeller. The booms are described in greater detail in Subsection 6.3.1. Sufficient space for the fuel amount carried is present within the wing, as explained in Subsection 12.2.6.

Class 2 drag and weight estimation were performed on the final design of the aircraft, as explained in Subsection 5.2.6 and Subsection 5.2.5, respectively. The contributions of the components for the drag can be seen in Figure 5.12 and Table 5.11, and for the weight in Figure 5.13 and Table 5.12. The weight of the payload includes the weight of the gun, as well as the motion mechanism for it.

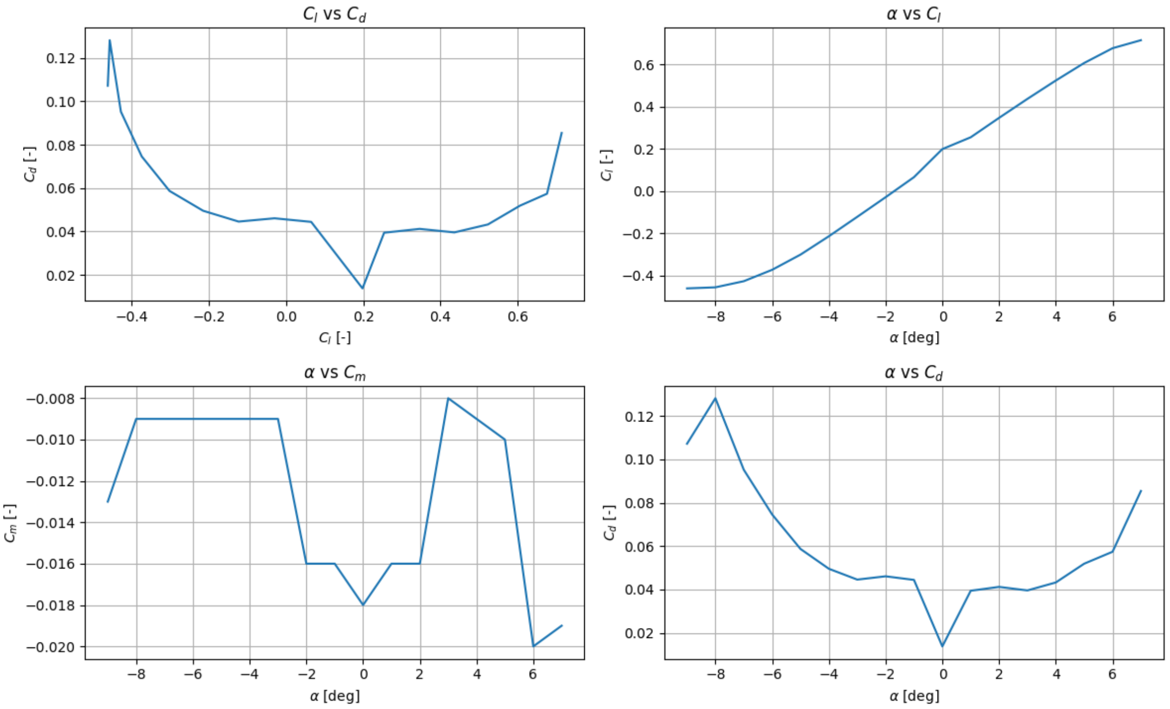

Figure 5.11: *Polars of NACA 63-210 airfoil*

Table 5.11: *Drag coefficients of aircraft parts*

Part	Cruise Drag Coefficient
Wings	0.009181
Fuselage	0.00735
Horizontal tail	0.00074
Vertical tails	0.0013
Booms	0.0031
Total	0.02178

Table 5.12: *Weight estimates of aircraft parts*

Part	Estimated Weight [N]
Wings	105.6
Fuselage	79.81
Horizontal tail	49.49
Vertical tails	31.68
Booms	8.49
Nose landing gear	2.44
Main landing gear	9.77
Avionics	98.1
Engine	378.16
Fuel	196.13
Fuel system	200.77
Payload (incl. armaments)	362.85
Total	1523.29

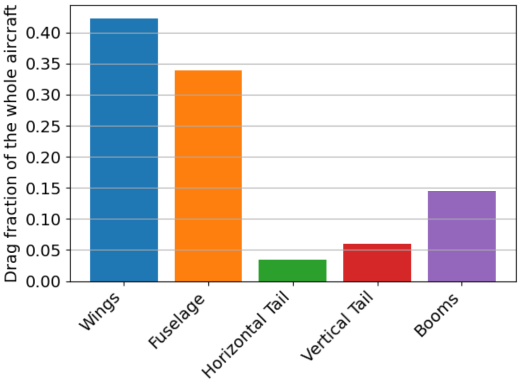

Figure 5.12: *Drag contribution of components of the aircraft*

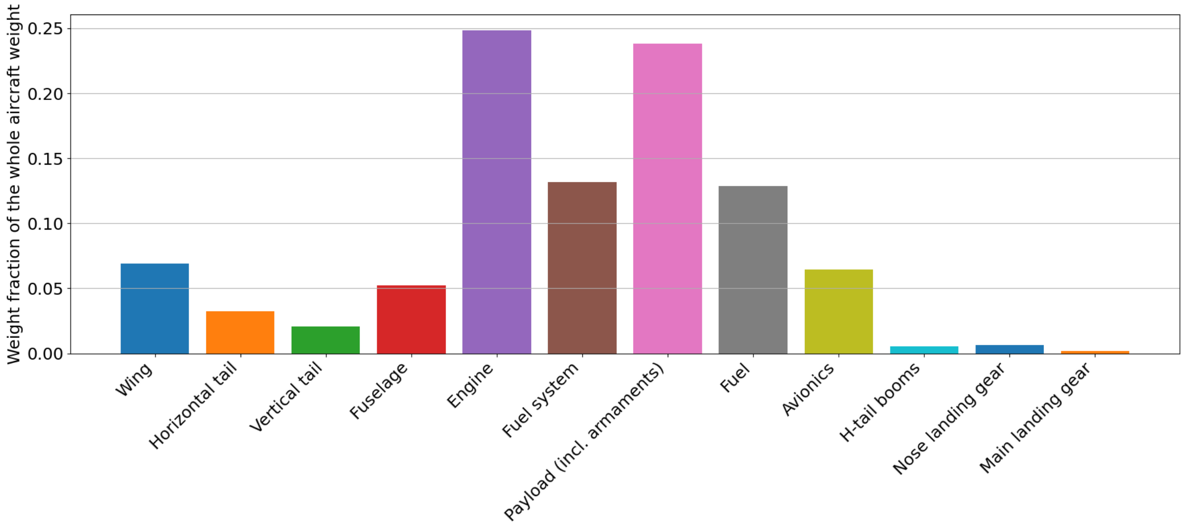

Figure 5.13: *Weight contribution of components of the aircraft*

5.4. Verification

In this section, the requirements compliance of the wing design will be presented. The requirement compliance matrix is visible in Table 12.12. As can be observed, SYS-01.19.188 and SUB-01.19.188.01 are not satisfied. The degree to which the requirements are not satisfied, however, means the design can proceed. As a recommendation for the future, a larger high lift device could be considered, or a more accurate method for estimating the landing distance could be used.

Table 5.13: *Requirements compliance for the wings*

Requirement Code	Condition	Result	Met?	How?
SUB-01.04.08.01	$C_L \geq 0.205$	0.975	Yes	Hand Calculations
SUB-01.04.09.01	$C_L \geq 0.876$	0.975	Yes	Hand Calculations
SUB-01.04.10.01	Available vol for fuel ≥ 16.08 L	64.182 L	Yes	Subsection 12.2.6
SUB-01.04.11.01	Available vol for fuel ≥ 16.08 L	64.182 L	Yes	Subsection 12.2.6
SUB-01.04.12.01	$C_L \geq 0.124$	0.975	Yes	Hand Calculations
SUB-01.07.19.01	Sufficient volume for structures	Sufficient volume	Yes	Subsection 12.2.6
SYS-01.07.22	Turn. radius ≤ 200 m	141.8 m	Yes	Equation 6.122[16]
SYS-01.07.23	Turn. rate ≥ $15\,^{\circ}\,\mathrm{s}^{-1}$	$29.7\,^{\circ}\,\mathrm{s}^{-1}$	Yes	Equation 6.123[16]
SYS-01.07.187	Military roll req.	No requirements	Yes	Subsection 5.2.8
SUB-01.19.187.01	No interference	No interference	Yes	Section 5.3
SYS-01.19.188	TO runway len. ≤ 1000 m	240 m	Yes	Equation 3.9[12]
SUB-01.19.188.01	$C_L \geq 0.98$	1.76	Yes	Equation 3.9[12]
SUB-01.19.188.02	No interference	No interference	Yes	Section 5.3
SYS-01.19.189	Land. runway len. ≤ 500 m	504.8	No	Equation 3.12[12]
SUB-01.19.189.01	$C_L \geq 1.8$	1.76	No	Equation 3.12[12]
SUB-01.19.189.02	No interference	No interference	Yes	Section 5.3

6

Empennage Design

In this chapter, the design of the empennage subsystem will be outlined. First, the requirements for the system will be presented in Section 6.1. Afterwards, the design process followed to size the horizontal and vertical stabilizers, the control surfaces, as well as to perform the dynamic analysis of the drone, will be explained in Section 6.2. Following this, the final design of the empennage, control surfaces, and dynamic analysis is outlined in Section 6.3. Lastly, the requirements will be verified against the design in Section 6.4.

6.1. Requirements

First, a number of requirements for the design of the empennage need to be defined. Here, a list of such requirements is presented.

- **SYS-01.04.15**: The airborne part of the system shall be controllable, in all operational environmental conditions, at all operational flight levels.
    - **SUB-01.04.15.01**: The rudder shall be capable of generating enough yawing moment to ensure recovery from a fully developed spin across the operational flight envelope.
    - **SUB-01.04.15.02**: The horizontal stabilizer shall ensure controllability at all operational altitudes and speeds.
- **SYS-09.19.78**: The launch system shall be capable of launching the airborne part of the system with side winds up to 9.6 $\mathrm{m\,s^{-1}}$ [13], with a reliability of at least 95%.
    - **SUB-09.19.78.01**: The empennage shall provide sufficient yaw stability and control authority to maintain directional control during take-off roll with sideslip angle up to 15°.

- **SYS-01.20.90**: The recovery system shall be capable of recovering the airborne part of the system with side winds up to 8.8 $\mathrm{m\,s^{-1}}$, with a reliability of at least 95%.
    - **SUB-01.20.90.01**: The empennage shall provide sufficient yaw stability and control authority to maintain directional control during landing with sideslip angle up to 15°.
- **SYS-01.22.117**: The airborne part of the system shall be capable of flight with a side wind up to 21 $\mathrm{m\,s^{-1}}$.
    - **SUB-01.22.117.01**: The empennage shall provide sufficient yaw stability and control authority to maintain directional control during cruise with sideslip angle up to 15°.

6.2. Design Process

In this section, the process to obtain the final empennage design will be explained. First, the method used to estimate the center of gravity and its range will be described. The remaining part will discuss the process used to obtain the horizontal stabilizer and elevator, the one used for the vertical stabilizer and rudder, and the one used to analyze the dynamic behavior of the CEDI drone.

6.2.1. Center of Gravity Estimation

With the weights of the components of aircraft estimated in Subsection 5.2.5 it is now possible to estimate the center of gravity of the aircraft and its range. Equation 6.1 was used to find the center of gravity of the entire aircraft on the x-axis. It was assumed that the aircraft is symmetric in the xz-plane, and that the center of gravity is on the centerline of the fuselage. The center of gravity of most components was known from the position of the respective system in the aircraft. The centers of gravity of the wing, horizontal, and vertical tail were assumed to be in the centroid of the trapezoid. The ones of the fuselage and booms were assumed to be halfway through their length.

$$x_{cg} = \frac{\sum m_i x_i}{\sum m_i} \tag{6.1}$$

The biggest issue in determining the aircraft's center of gravity was the landing gear position. According to *Airplane Design: A Systems Engineering Approach* the nose and main landing gear weights are directly proportional to the loads they support. However, a change in the distribution of weight of the landing gear will also affect the center of gravity of the aircraft. Therefore, an iterative loop, given in Figure 6.1, was performed. The primary purpose of the iteration loop is to find the center of gravity of the aircraft by adjusting the weights of the landing gear. The program ensures that the nose landing gear carries at least 8% of the total weight of the aircraft, and warns the user if this is not the case. Finally, the estimated weights of the nose and main landing gear are returned.

A preliminary analysis of the center of gravity revealed that having a pusher-prop engine after the tail of the aircraft was unfeasible: the center of gravity was very far aft of the MAC due to the high weight of the engine and the long force arm. Using a puller-prop engine was briefly considered; however, it was quickly rejected because of the positioning of the primary detection suite in the nose (see Chapter 9), as well as the interference with the bullet arc (see Chapter 7). Therefore, an H-tail configuration was selected, allowing for the engine to be moved much closer to the wing, with the propeller being in between wing mounted booms.

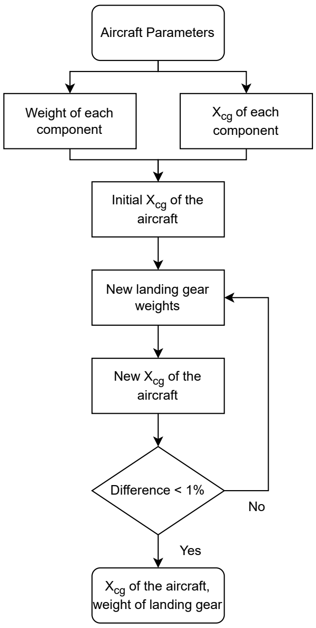

Figure 6.1: *Overview of center of gravity estimation*

The center of gravity contributions of each system can be seen in Figure 6.2.

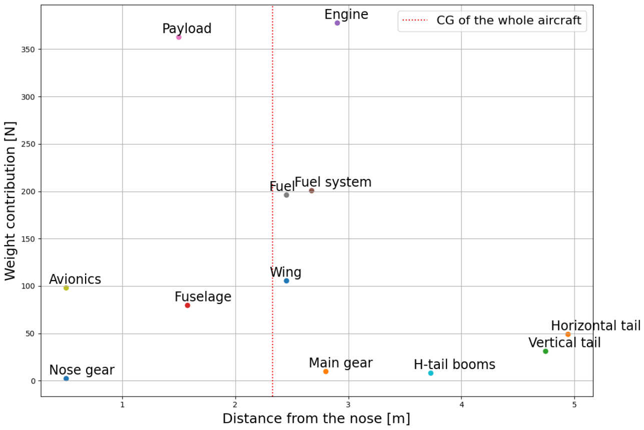

Figure 6.2: *Contributions of systems to the center of gravity*

6.2.2. Horizontal Stabilizer

In this subsection, the process and calculations used to determine the horizontal stabilizer design are presented. These are based on the static stability and controllability requirements of the aircraft. The stability line of the aircraft is given by Equation 6.2,

$$\bar{x}_{cg} = \bar{x}_{ac_{wf}} + \frac{C_{L_{\alpha_h}}}{C_{L_{\alpha_{A-h}}}}\left(1 - \frac{\delta\epsilon}{\delta\alpha}\right)\frac{S_h l_h}{S\bar{c}}\left(\frac{V_h}{V}\right)^2 - SM \tag{6.2}$$

where S_h/S is the ratio between the surface area of the horizontal stabilizer and the surface area of the wing, l_h is the distance from the quarter-chord point of the wing to the quarter-chord point of the horizontal stabilizer, $\bar{c}$ is the wing MAC, and V_h/V is the tail efficiency. A stability margin SM of zero was chosen, to allow for high maneuverability, prioritizing control authority over inherent stability.

The estimation of the aerodynamic center of the tail-less aircraft is given by Equation 6.3, with $\bar{x}_{ac_w}$ being estimated to be at the quarter point of the wing MAC, and $\bar{x}_{ac_f}$ being given by Equation 6.4,

$$\bar{x}_{ac_{wf}} = \bar{x}_{ac_w} + \bar{x}_{ac_f} \tag{6.3}$$

$$\bar{x}_{ac_f} = -\frac{\delta M}{\delta\alpha}\frac{1}{\bar{q}S\bar{c}C_{L_{\alpha_w}}} \quad \text{(eq. 8.85 from [1])} \tag{6.4}$$

where $\bar{q}$ is the dynamic pressure during cruise, $\bar{c}$ is the MAC of the wing, S is the wing surface, and $\delta M/\delta\alpha$ is the change is Mach number with changing angle of attack, given by equation 8.85 in[1]. For this, the fuselage had to be divided into segments and their average width and length had to be evaluated. Following *Airplane Design Part VI*, the fuselage was subdivided into 13 segments, as given in Figure 6.3. The first 5 segments are of equal length and are placed before the wing, and the final 6 segments are of equal length and are placed behind the wing. Segments 6 and 7 are of equal length and are placed so that they cover the wing.

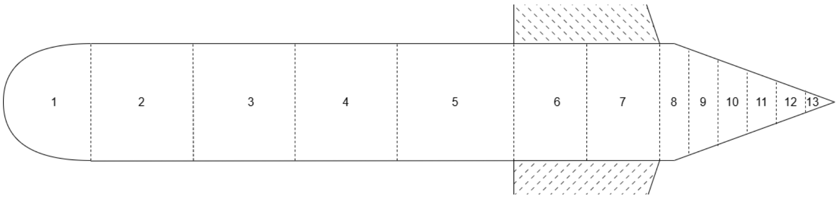

Figure 6.3: *Fuselage division into 13 segments; drawing not to scale.*

The lift coefficient slope of the horizontal stabilizer, $C_{L\alpha_h}$, is evaluated using the DATCOM method [17]:

$$C_{L_{\alpha_h}} = \frac{2\pi A_h}{2 + \sqrt{4 + \left(\frac{A_h\beta}{\eta}\right)^2\left(1 + \frac{\tan^2\Lambda_{0.5C_h}}{\beta^2}\right)}} \tag{6.5}$$

where A_h is the aspect ratio of the horizontal stabilizer, β is given in Equation 6.6, with M being the Mach number, η is the airfoil efficiency factor, assumed to be 0.95, and $\Lambda_{0.5C_h}$ is the sweep angle of the half-chord of the horizontal stabilizer.

$$\beta = \sqrt{1 - M^2} \tag{6.6}$$

The lift coefficient slope of the wing, $C_{L_{\alpha_w}}$, is obtained by the tool described in Subsection 5.2.4 and the one of the aircraft-less-tail, $C_{L_{\alpha_{A-h}}}$, is estimated by Equation 6.7 (equation 8.43 from [1]),

$$C_{L_{\alpha_{A-h}}} = K_{wf} C_{L_{\alpha_w}} \tag{6.7}$$

where K_{wf} is the wing-fuselage inference factor (given by equation 8.44 from [1]). Finally, $\delta\epsilon/\delta\alpha$ is calculated using Equation 6.8 (equation 8.45 from [1]),

$$\frac{\delta\epsilon}{\delta\alpha} = 4.44\left[K_A K_\lambda K_h (\cos\Lambda_{c/4})^{0.5}\right]^{1.19}\left[(C_{L_{\alpha_w}})_{atM}/(C_{L_{\alpha_w}})_{atM=0}\right] \tag{6.8}$$

with K_A, K_λ, and K_h being given by equations 8.46, 8.47, and 8.48 from [1], and $\left[(C_{L\alpha_w})_{atM}/(C_{L\alpha_w})_{atM=0}\right]$ by Equation 6.9:

$$\left[(C_{L_{\alpha_w}})_{atM}/(C_{L\alpha_w})_{atM=0}\right] = \frac{C_{L_{\alpha w}}}{\beta}\frac{1}{C_{L\alpha_w}} = \frac{1}{\beta} \tag{6.9}$$

Once the stability line is determined, the controllability line must be established. This is given by Equation 6.10:

$$\bar{x}_{cg} = \bar{x}_{ac_{wf}} - \frac{C_{m_{ac}}}{C_{L_{A-h}}} + \frac{C_{L_h}}{C_{L_{A-h}}}\frac{S_h l_h}{S\bar{c}}\left(\frac{V_h}{V}\right)^2 \tag{6.10}$$

where C_{L_h} is assumed to be -1 for a fully moving tail, -0.8 for an adjustable tail, and -0.35$A^{1/3}$ for a fixed tail, $C_{L_{A-h}}$ is given by assuming the weight to be equal to the lift during landing, and $C_{m_{ac}}$ is evaluated by Equation 6.11:

$$C_{m_{ac}} = C_{m_{ac_w}} + \Delta_{fus} C_{m_{ac_{fus}}} + \Delta_{flaps} C_{m_{ac_{flaps}}} \tag{6.11}$$

where $C_{m_{ac_w}}$ is the moment coefficient around the wing aerodynamic center (Equation 6.12), $\Delta_{fus} C_{m_{ac_{fus}}}$ is the influence of the fuselage (Equation 6.13), and $\Delta_{flaps} C_{m_{ac_{flaps}}}$ is the influence of deployed flaps, (Equation 6.13) [17].

$$C_{m_{ac_w}} = C_{m_{0airfoil}}\left(\frac{A\cos^2\Lambda}{A + 2\cos\Lambda}\right) \tag{6.12}$$

$$\Delta_{fus} C_{m_{ac_{fus}}} = -1.8\left(1 - \frac{2.5 b_f}{l_f}\right)\frac{\pi b_f h_f l_f}{4S\bar{c}}\frac{C_{L_0}}{C_{L_{\alpha_{A-h}}}} \tag{6.13}$$

$$\Delta_{flaps} C_{m_{ac_{flpas}}} = \left[x + 0.7\frac{A}{1+2/A}\mu_3 \Delta C_{l_{max}} \tan\Lambda_{c/4}\right] - C_L\left(0.25 - \frac{x_{ac}}{\bar{c}}\right) \tag{6.14}$$

with x given by:

$$x = \mu_2\left[-\mu_1 \Delta C_{l_{max}} - \frac{c'}{c} - \left[C_L + \Delta C_{l_{max}}\left(1 - \frac{S_{wf}}{S}\right)\right]\frac{1}{8}\frac{c'}{c}\left(\frac{c'}{c} - 1\right)\right] \tag{6.15}$$

In these equations, b_f is the width of the fuselage, h_f its height, and l_f its length; C_{L_0} is obtained from equation 8.32 from [1]; $\Delta C_{l_{max}}$ is the increase in airfoil lift coefficient generated by flaps, c'/c is the ratio between the chord of the airfoil with extended flaps and in clean configuration, and S_{wf}/S is the ratio between flapped wing area and reference wing area. The values of μ_1, μ_2, and μ_3 are determined using figure G-15, G-16, and G-16 from [18].

To determine the appropriate dimensions of the horizontal stabilizer, the mathematical relations governing its aerodynamic and stability contributions were implemented iteratively in code. These calculations inherently depend on the stabilizer's own properties, such as surface area, span, and aspect ratio; therefore, a loop-based approach was adopted to refine its geometry. The goal was to gradually increase the aspect ratio of the horizontal stabilizer, aiming for a value up to 4, which was set as a structural upper limit. The iteration halts if one of several constraints is met: the target aspect ratio of 4 is achieved; the stabilizer's span exceeds 2 meters; the stabilizer mean geometric chord becomes smaller than 15cm; or the tail arm distance exceeds 4 meters. The full decision flow and iteration logic are illustrated in Figure 6.4.

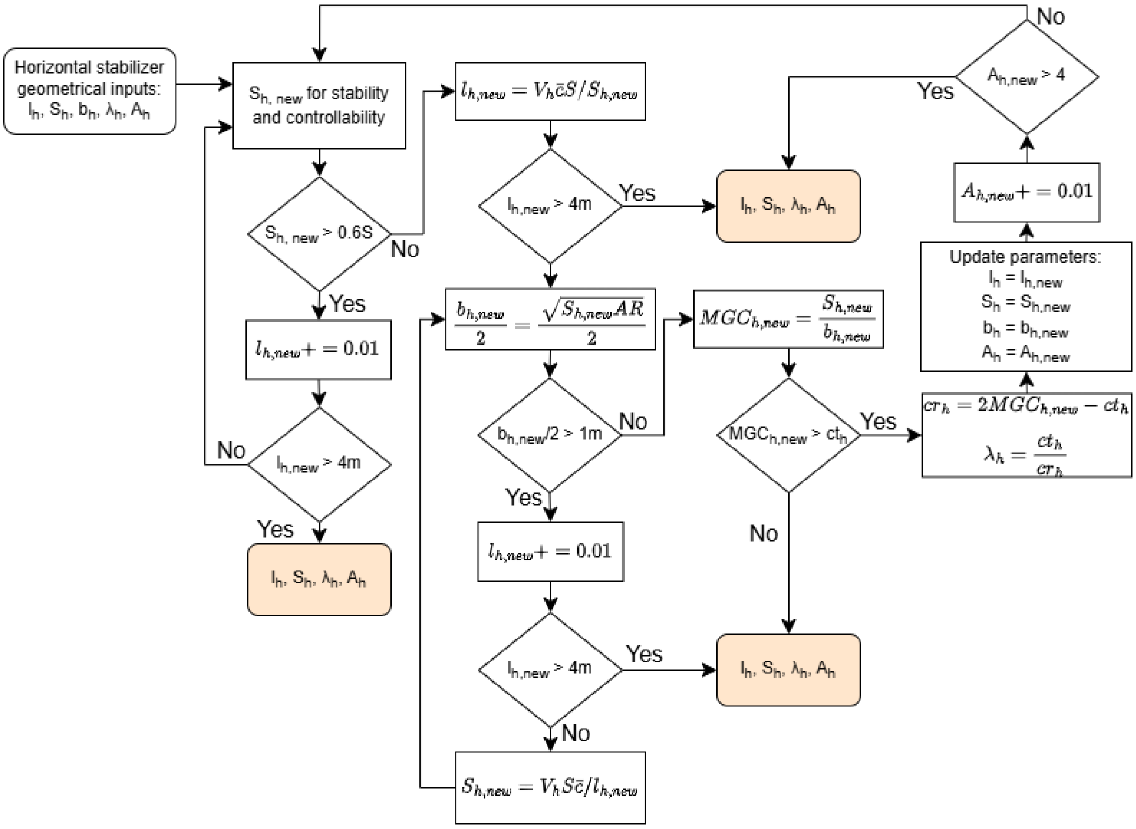

Figure 6.4: *Horizontal stabilizer geometry iteration logic*

6.2.3. Vertical Stabilizer

The sizing process of the vertical stabilizer began with an initial estimation based on values found in existing literature. A vertical tail volume coefficient of 0.06 was selected as a reference value [2]. Using this coefficient, along with the known wing reference area and the moment arm, which was assumed equal to the value previously established for the horizontal stabilizer, the surface area of the vertical tail was calculated. This provided a preliminary geometry. Following this, the vertical tail geometry was refined to incorporate the rudder.

The rudder itself was sized by evaluating the most demanding flight conditions that could affect yaw control. Three scenarios were considered: crosswind landing, spin recovery, and coordinated turning flight [2]. For each case, the required rudder deflection angle was estimated.

The rudder deflection required to safely land in crosswind conditions is found by solving the system of equations given by Equation 6.16 and 6.17.

$$\frac{1}{2}\rho V_T^2 S b\Big(C_{n_0} + C_{n_\beta}(\beta-\sigma) + C_{n_{\delta_r}}\delta_r\Big) + F_w d_c \cos\sigma = 0 \tag{6.16}$$

$$\frac{1}{2}\rho V_w^2 S_s C_{D_Y} - \frac{1}{2}\rho V_T^2 S\Big(C_{Y_0} + C_{Y_\beta}(\beta-\sigma) + C_{Y_{\delta_r}}\delta_r\Big) = 0 \tag{6.17}$$

where V_w is the crosswind speed, β the sideslip angle of 15 deg [13], C_{n_0} and C_{Y_0} are assumed to be zero, V_T is the aircraft total speed, given by Equation 6.18, F_w is given by equation 12.113 from [2],

d_c is the distance between the aircraft center of mass and the center of its projected side area, S_s is the projected side area, and C_{D_Y} is the aircraft side drag coefficient, estimated to be 0.8 [2]. The evaluation of the dynamic coefficients used in these calculations is given in Subsection 6.2.4.

$$V_T = \sqrt{V_w^2 + V_c^2} \tag{6.18}$$

The deflection needed to recover from a spin is determined by the needed yawing moment, evaluated using Equation 6.19:

$$N_{SR} = \left(\frac{I_{xx}I_{zz} - I_{xz}^2}{I_{xx}}\right)R_{SR} \tag{6.19}$$

where I_{xx}, I_{zz}, and I_{xz} are the respective moments of inertia of the aircraft, and R_{SR} is the yaw rate, set to $1.4\,\mathrm{rad\,s^{-2}}$ [2]. It should be noted that, because of the symmetry of the aircraft, I_{xz} was assumed to be zero.

The yawning moment may also be expressed by Equation 6.20, therefore allowing to determine δ_r:

$$N_{SR} = \frac{1}{2}\rho V_s^2 S b C_{n_{\delta_r}} \delta_r \tag{6.20}$$

where $C_{n_{\delta_r}}$ is calculated using the effective vertical tail area, effective rudder area, effective rudder span, and effective rudder chord. These values correspond to the portion of the vertical tail and rudder that are not subjected to the wave of the horizontal stabilizer during spin.

Finally, the rudder deflection needed to perform a coordinate turn is obtained by solving the system of equations given by Equation 6.21, 6.22, and 6.23.

$$\frac{1}{2}\rho V_c^2 S\left(C_{Y_\beta}\beta + C_{Y_r}\frac{rb}{2V_c} + C_{Y_{\delta_a}}\delta_a + C_{Y_{\delta_r}}\delta_r\right) = 0 \tag{6.21}$$

$$\frac{1}{2}\rho V_c^2 Sb\left(C_{l_\beta}\beta + C_{l_r}\frac{rb}{2V_c} + C_{l_{\delta_a}}\delta_a + C_{l_{\delta_r}}\delta_r\right) = (I_{zz} - I_{yy})rq \tag{6.22}$$

$$\frac{1}{2}\rho V_c^2 Sb\left(C_{n_\beta}\beta + C_{n_r}\frac{rb}{2V_c} + C_{n_{\delta_a}}\delta_a + C_{n_{\delta_r}}\delta_r\right) = I_{xz}rq \tag{6.23}$$

where r and q are the yaw and pitch rates and given by Equation 6.24 and Equation 6.25, respectively. Here, ϕ is the maximum roll angle achievable.

$$r = \frac{g\sin^2\phi}{V_c\cos\phi} \tag{6.24}$$

$$q = \frac{g\sin\phi}{V_c} \tag{6.25}$$

Once the rudder deflection angles required for the three critical flight scenarios are determined, the most demanding case is identified by selecting the deflection with the highest absolute value. This values was then compared against a predefined limit for rudder deflection, set at 30 degrees. If the required deflection exceeded this limit, the rudder span was incrementally increased to provide greater control authority. In cases where the larger rudder span risked interfering with the horizontal stabilizer, the vertical tail span was also increased to maintain sufficient geometric clearance. After each adjustment, the rudder deflection angles were re-evaluated based on the updated geometry. This iterative process continued until the required deflection fell within the allowable range.

6.2.4. Dynamic Analysis

This section describes the methodology used to determine the aircraft's stability and controllability characteristics. It outlines the process followed to compute the aerodynamic derivatives required for dynamic analysis, including stability and control coefficients. Additionally, it presents the formulation of the state-space model used to simulate the aircraft's dynamic response to control inputs and external disturbances.

Stability and control derivatives

The dynamic stability derivatives were calculated following *Airplane Design Part VI*, Section 10.2 [1]. It should be noted that following this approach sets the coefficients $C_{D_{\dot{\alpha}}}$, C_{D_q}, and $C_{Y_{\delta_a}}$ to zero. The following changes or estimations were applied to the evaluation of the other coefficients.

For all coefficient needing the lift coefficient of the wing, $C_{L_{\alpha_w}}$, the value obtained from the Lifting Line tool described in Subsection 5.2.4 was used.

In evaluating C_{D_u}, the derivative of the airplane drag coefficient with respect to the Mach number had to be evaluated. However, the drag estimation tool that was previously used was not suited for this purpose. Moreover, the change in drag coefficient was expected to be minimal, considering the low cruise speed. Therefore, this coefficient was set to zero.

A similar approach was taken in calculating the variation of the aerodynamic center with respect to Mach number, needed to estimate C_{m_u}. The aerodynamic center was calculated using Equation 6.26,

$$\bar{x}_{ac} = \left[\bar{x}_{ac_{wf}} C_{L_{\alpha_{A-h}}} + n_h C_{L_{\alpha_h}} \left(1 - \frac{\delta\epsilon}{\delta\alpha}\right)\left(\frac{S_h}{S}\right)\bar{x}_{ac_h}\right]\frac{1}{C_{L_\alpha}} \tag{6.26}$$

where $\bar{x}_{ac_{wf}}$ is given by Equation 6.3, $C_{L_{\alpha_{A-h}}}$ by Equation 6.7, $C_{L_{\alpha_h}}$ by Equation 6.5, $\delta\epsilon/\delta\alpha$ by Equation 6.8, $\bar{x}_{ac_h}$ is assumed to be located at the quarter-chord point of the horizontal stabilizer, C_{L_α} is calculated using Equation 6.27 and n_h is the dynamic pressure ratio given by equation 8.41 from [1].

$$C_{L_\alpha} = C_{L_{\alpha_{wf}}} + C_{L_{\alpha_h}} n_h \frac{S_h}{S}\left(1 - \frac{\delta\epsilon}{\delta\alpha}\right) \tag{6.27}$$

Equation 6.28 was used to estimate the drag-due-to-angle-of-attack derivative, as the chosen airfoil has parabolic drag polar [1]:

$$C_{D_\alpha} = \frac{2C_L}{\pi A e} C_{L_\alpha} \tag{6.28}$$

The value of C_{m_α} was calculated considering the most aft CG position, to account for the limiting case of stability. Moreover, the coefficients $C_{m_{\dot{\alpha}}}$ and $C_{L_{\dot{\alpha}}}$ were based on the assumption that the contribution of the horizontal stabilizer is the only important contribution to these derivatives [1].

C_{Y_β} was estimated for both single vertical tail, to be used if a conventional configuration is selected, and twin vertical tails, for H-tail configurations.

The control derivatives for ailerons, elevator, and rudder are estimated using the method explained in *Airplane Design Part VI* [1]. The following changes or estimations were applied to the evaluation.

The term α_{δ_e} is used in equations 10.93, 10.95, and 10.96 from [1] to obtain the elevator derivatives for drag, lift, and pitching moment, respectively. This term depends on three coefficients obtained from figures: k', $(c_{l\delta})_{theory}$, and $c_{l\delta}/(c_{l\delta})_{theory}$. However, these figures are based on the ratio c_i/c, which represents the chord of the control surface relative to the chord of the horizontal or vertical stabilizer. The maximum value shown in the figures for this ratio is 0.5. Since a fully moving elevator is used, this ratio is 1 for the sizing of the elevator. Although the value of k' was linearly extrapolated from the figure and the value of $c_{l\delta}/(c_{l\delta})_{theory}$ appears to have an upper limit of 1, the value of $(c_{l\delta})_{theory}$ cannot be estimated, as the behavior of the function beyond the graph is unknown. Consequently, the derivatives with respect to the elevator deflection, δ_e, are expected to be slightly underestimated.

Since dynamic analysis is carried out with respect to the stability reference frame, but the coefficients are calculated for the body reference frame, the transformations given by Equation 6.29 and

6.30 must be performed. Using small angle approximation, these become Equation 6.31 and 6.32,

$$C_Z = -C_L \cos\alpha - C_D \sin\alpha \tag{6.29}$$

$$C_X = C_L \sin\alpha - C_D \cos\alpha \tag{6.30}$$

$$C_Z = -C_L - C_D\alpha \tag{6.31}$$

$$C_X = C_L\alpha - C_D \tag{6.32}$$

where α is the cruise angle of attack.

State-space model

Having calculated all the parameters of the aircraft, the dynamic model is now constructed. The symmetric and asymmetric motions of the aircraft are assumed to be decoupled. This may not be the case in reality; however, since angles and rates are expected to be small, it proves a useful estimation of the dynamic behavior of the CEDI drone.

Here, the symmetric case will be considered, where the longitudinal response of the aircraft is analyzed. Equation 6.33 is the linear model for symmetric aircraft motion, when D_c is the differential operator given in Equation 6.34,

$$\begin{bmatrix} C_{x_u} - 2\mu_c D_c & C_{x_\alpha} & C_{Z_0} & C_{X_q} \\ C_{z_u} & C_{Z_\alpha} + \left(C_{Z_{\dot\alpha}} - 2\mu_c\right) D_c & -C_{X_0} & C_{Z_q} + 2\mu_c \\ 0 & 0 & -D_c & 1 \\ C_{m_u} & C_{m_\alpha} + C_{m_{\dot\alpha}} D_c & 0 & C_{m_q} - 2\mu_c K_{yy}^2 D_c \end{bmatrix} \begin{bmatrix} \hat{u} \\ \alpha \\ \theta \\ \frac{q\bar{c}}{V} \end{bmatrix} = \begin{bmatrix} -C_{X_\delta} \\ -C_{Z_\delta} \\ 0 \\ -C_{m_\delta} \end{bmatrix} \delta_e \tag{6.33}$$

$$D_c = \frac{\bar{c}}{V_c}\frac{d}{dt} \tag{6.34}$$

where V_c is the cruise speed of the CEDI drone, μ_c is the symmetric dimensionless mass, given by Equation 6.35, K_{YY} is the non-dimensional radius of gyration about the Y-axis, calculated using Equation 6.37, and μ_b is given by Equation 6.36:

$$\mu_c = \frac{m}{\rho S \bar{c}} \tag{6.35}$$

$$\mu_b = \frac{m}{\rho S b} \tag{6.36}$$

$$K_{yy}^2 = \frac{I_{yy}}{\rho S b^3}\frac{1}{\mu_b} \tag{6.37}$$

The state-space system is created by first applying Equation 6.38, where $\bar{u}$ is the input vector and $\bar{x}$ is the state vector. These are given by Equation 6.39,

$$C_1\dot{\bar{x}} + C_2\bar{x} + C_3\bar{u} = \bar{0} \tag{6.38}$$

$$\bar{u} = [\delta_e] \tag{6.39a}$$

$$\bar{x} = \begin{bmatrix} \hat{u} & \alpha & \theta & q \end{bmatrix}^T \tag{6.39b}$$

where $\hat{u}$ is the change in velocity, α is the angle of attack, θ is the pitch angle, and q the pitch rate. The input δ_e is the deflection angle of the elevator.

The model uses dimensionless parameters, while the measurements are dimension-having. Therefore, the model must be converted to the dimension-having version using Equation 6.40 and Equation 6.41. Additionally, the angles α and θ, and the pitch rate q are converted from radians to degrees. This leads to the matrices C1, given in Equation 6.42, C2, in Equation 6.43, and C3, in Equation 6.44.

$$\widehat{u} = \frac{V_t - V_c}{V_c} \tag{6.40}$$

$$\frac{q\bar{c}}{V} = q_{\text{meas}} \cdot \frac{\bar{c}}{V_c} \tag{6.41}$$

$$C1 = \begin{bmatrix} -2\mu_c \frac{\bar{c}}{V_c} & 0 & 0 & 0 \\ 0 & (C_{Z_{\dot{\alpha}}} - 2\mu_c)\frac{\bar{c}}{V_c}\frac{\pi}{180} & 0 & 0 \\ 0 & 0 & -\frac{\bar{c}}{V_c}\frac{\pi}{180} & 0 \\ 0 & C_{m_{\dot{\alpha}}}\frac{\bar{c}}{V_c}\frac{\pi}{180} & 0 & -2\mu_c K_{YY}^2 \frac{\bar{c}^2}{V_c^2}\frac{\pi}{180} \end{bmatrix} \tag{6.42}$$

$$C2 = \begin{bmatrix} C_{x_u}\frac{1}{V_c} & C_{x_\alpha}\frac{\pi}{180} & C_{Z_0}\frac{\pi}{180} & C_{X_q}\frac{\bar{c}}{V_c}\frac{\pi}{180} \\ C_{z_u}\frac{1}{V_c} & C_{z_\alpha}\frac{\pi}{180} & -C_{X_0}\frac{\pi}{180} & (C_{Z_q} + 2\mu_c)\frac{\bar{c}}{V_c}\frac{\pi}{180} \\ 0 & 0 & 0 & \frac{\bar{c}}{V_c}\frac{\pi}{180} \\ C_{m_u}\frac{1}{V_c} & C_{m_\alpha}\frac{\pi}{180} & 0 & C_{m_q}\frac{\bar{c}}{V_c}\frac{\pi}{180} \end{bmatrix} \tag{6.43}$$

$$C3 = \frac{\pi}{180}\begin{bmatrix} C_{X_\delta} \\ C_{Z_\delta} \\ 0 \\ C_{m_\delta} \end{bmatrix} \tag{6.44}$$

It is important to note that the measurements are calibrated with respect to the body axis system; therefore, they must transformed to the stability axis system. The transformations used for angle changes are given in Equation 6.45 and Equation 6.46.

$$\alpha_{\text{stab}} = \alpha_{\text{body}} - \alpha_0 \tag{6.45}$$

$$\theta_{\text{stab}} = \theta_{\text{body}} - \theta_0 \tag{6.46}$$

In analyzing the behavior of the drone, is important to take into account the gun recoil. Since the gun is placed on the centerline of the fuselage, it will not have significant lateral effects on the stability of the aircraft. However, its longitudinal impact must be estimated. The angular impulse is calculated using Equation 6.47, where J is the impulse and l is the arm length between the CG location and the quarter-chord point of the wing, where the force of the gun is applied (see Chapter 7). This is transformed in the initial pitch rate of the drone by applying Equation 6.48. A similar approach is applied to calculating the velocity change due to the gun recoil, given in Equation 6.49, where m is the mass of the drone. This approach assumes that the gun recoil does not impact the initial angle of attack and pitch angle.

$$H = J \cdot l \tag{6.47}$$

$$q = \frac{H}{I_{yy}} \tag{6.48}$$

$$\hat{u} = \frac{J}{m} \tag{6.49}$$

Similarly to the symmetric case, the asymmetric case, given in Equation 6.50, uses dimensionless parameters, with D_b being the differential operator given in Equation 6.51, μ_b given by Equation 6.36, and K_{xx}, K_{zz}, and K_{xz} following the logic given by Equation 6.37.

$$\begin{bmatrix} C_{Y_\beta} + \left(C_{Y_{\dot{\beta}}} - 2\mu_b\right) D_b & C_L & C_{Y_p} & C_{Y_r} - 4\mu_b \\ 0 & -\frac{1}{2}D_b & 1 & 0 \\ C_{\ell_\beta} & 0 & C_{\ell_p} - 4\mu_b K_{xx}^2 D_b & C_{\ell_r} + 4\mu_b K_{xz} D_b \\ C_{n_\beta} + C_{n_{\dot{\beta}}} D_b & 0 & C_{n_p} + 4\mu_b K_{xz} D_b & C_{n_r} - 4\mu_b K_{zz}^2 D_b \end{bmatrix} \begin{bmatrix} \beta \\ \phi \\ \frac{pb}{2V} \\ \frac{rb}{2V} \end{bmatrix} = \begin{bmatrix} -C_{y_{\delta_a}} \\ 0 \\ -C_{\ell_{\delta_a}} \\ -C_{n_{\delta_a}} \end{bmatrix} \delta_a + \begin{bmatrix} -C_{y_{\delta_r}} \\ 0 \\ -C_{\ell_{\delta_r}} \\ -C_{n_{\delta_r}} \end{bmatrix} \delta_r \tag{6.50}$$

$$D_b = \frac{b}{V_c}\frac{d}{dt} \tag{6.51}$$

For the asymmetric state-space representation, the input vector $\bar{u}$ and state vector $\bar{x}$ are given by Equation 6.52,

$$\bar{u} = \begin{bmatrix} \delta_a & \delta_r \end{bmatrix}^T \tag{6.52a}$$

$$\bar{x} = \begin{bmatrix} \beta & \phi & p & r \end{bmatrix}^T \tag{6.52b}$$

where β is the sideslip angle, ϕ is the roll angle, p is the roll rate, and r is the yaw rate. In the input vector, δ_a represents the deflection angle of the ailerons, while δ_r is the one of the rudder.

The parameters are converted using Equation 6.53 and Equation 6.54. Similarly to the symmetric case, the angles and angular rates are converted to degrees. This leads to the matrices C1, C2, and C3, given in Equation 6.55, Equation 6.56, and Equation 6.57.

$$\frac{pb}{2V} = p_{\text{meas}} \frac{b}{2V_c} \tag{6.53}$$

$$\frac{rb}{2V} = r_{\text{meas}} \frac{b}{2V_c} \tag{6.54}$$

$$C1 = \frac{\pi}{180} \begin{bmatrix} (C_{Y_{\dot{\beta}}} - 2\mu_b)\frac{b}{V_c} & 0 & 0 & 0 \\ 0 & -\frac{1}{2}\frac{b}{V_c} & 0 & 0 \\ 0 & 0 & -4\mu_b K_{XX}^2 \frac{b^2}{2V_c^2} & 4\mu_b K_{XZ} \frac{b^2}{2V_c^2} \\ C_{n_{\dot{\beta}}} \frac{b}{V_c} & 0 & 4\mu_b K_{XZ} \frac{b^2}{2V_c^2} & -4\mu_b K_{ZZ}^2 \frac{b^2}{2V_c^2} \end{bmatrix} \tag{6.55}$$

$$C2 = \frac{\pi}{180} \begin{bmatrix} C_{Y_\beta} & C_L & C_{Y_p} \frac{b}{2V_c} & (C_{Y_r} - 4\mu_b)\frac{b}{2V_c} \\ 0 & 0 & \frac{b}{2V_c} & 0 \\ C_{l_\beta} & 0 & C_{l_p} \frac{b}{2V_c} & C_{l_r} \frac{b}{2V_c} \\ C_{n_\beta} & 0 & C_{n_p} \frac{b}{2V_c} & C_{n_r} \frac{b}{2V_c} \end{bmatrix} \tag{6.56}$$

$$C3 = \frac{\pi}{180} \begin{bmatrix} C_{Y_{\delta_a}} & C_{Y_{\delta_r}} \\ 0 & 0 \\ C_{l_{\delta_a}} & C_{l_{\delta_r}} \\ C_{n_{\delta_a}} & C_{n_{\delta_r}} \end{bmatrix} \tag{6.57}$$

6.3. Design Description

In this section, the design of the horizontal and vertical stabilizers will be described. After this, the results of the dynamic analysis will be presented and analyzed.

6.3.1. Horizontal Stabilizer

The airfoil selection procedure followed the steps explained in Subsection 5.2.3, with the parameters changed to better fit the horizontal stabilizer. The ideal lift coefficient was set to 0 as the horizontal tail is ideally expected not to produce lift during cruise. The maximum lift coefficient was set to 1, with the understanding that -1 is the lift coefficient estimated for a fully moving tail. The selected airfoil was NPL 9660 airfoil. Its shape and polars can be seen in Figure 6.5 and Figure 6.6, respectively.

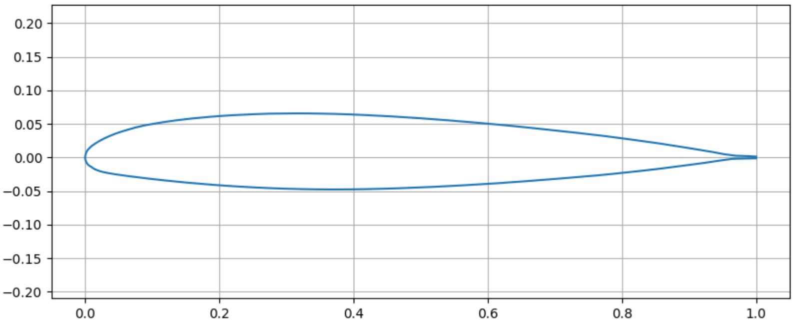

Figure 6.5: *Shape of the horizontal stabilizer airfoil (NPL 9660 airfoil)*

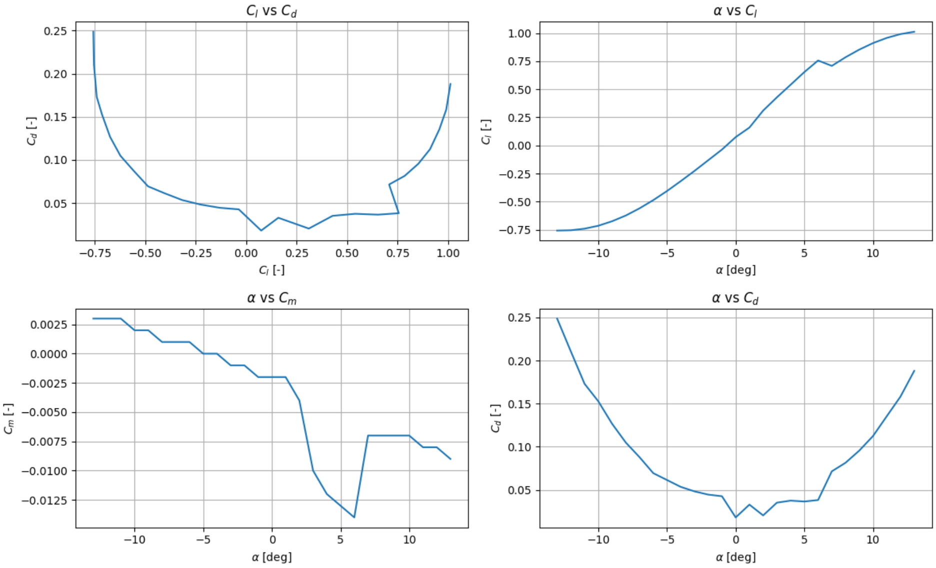

Figure 6.6: *Polars of the airfoil of the horizontal stabilizer (NPL 9660 airfoil)*

The scissor plot resulting form the stability analysis described in Subsection 6.2.2, including most forward and aft center of gravity locations, is given in Figure 6.7.

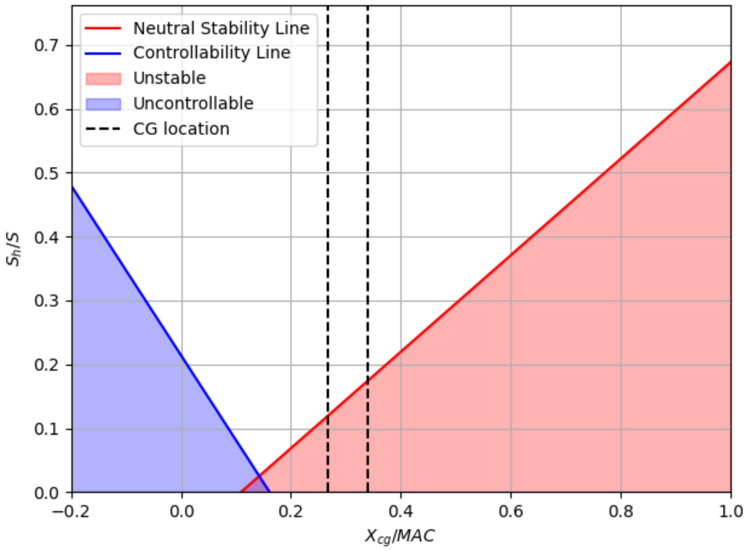

Figure 6.7: *Scissor plot*

It can be noted that the limiting case is given by the stability line. For a stable aircraft, the minimum ratio between horizontal stabilizer and wing surface areas is 0.175.

Since an H-tail configuration was selected, as described in Subsection 6.2.1, the taper ratio of the horizontal stabilizer is set to 1, ie. the horizontal stabilizer is rectangular. The aspect ratio, span, and surface area are determined by the iterative process given in Figure 6.4. It was decided to mount the horizontal stabilizer high on the vertical tail to avoid aerodynamic interference from the wing and to simplify the design space for spin recovery considerations during rudder sizing. This placement ensures cleaner airflow and more effective control during critical maneuvers. Additionally, a fully moving tail was chosen to enhance maneuverability. This configuration allows for more responsive pitch control, which is especially beneficial for agile flight and precise trajectory adjustments. Therefore, the geometrical properties of the horizontal stabilizer coincide with the ones of the elevator. These are given in Table 6.1.

Table 6.1: *Horizontal stabilizer and elevator geometrical properties*

Geometrical property	Value
Surface area [m^2]	0.616
Span [m]	1.1
Mean aerodynamic chord [m]	0.56
Distance from wing to tail quarter-chord [m]	2.6
Tail height from fuselage centerline [m]	0.66
Dihedral [deg]	0
Taper [-]	1
Aspect ratio [-]	1.96
Max deflection [deg]	25

These values give an S_h/S of 0.197, which is higher than the ratio needed for static stability of 0.175. Therefore, the drone is longitudinally statically stable.

The geometric properties of the horizontal stabilizer define some of the characteristics of the booms which connect the empennage to the rest of the aircraft. Since the booms should be located at the edges of the horizontal stabilizer, the distance between them shall not be less than the horizontal stabilizer span, equal to 1.1 m. Additionally, their length shall be high enough to allow for the proper distance between the horizontal tail and the wing. From this, it can be determined that the booms should be at least 2.5 meters long.

However, further analysis revealed that, with these parameters, the drone enters deep stall at an effective angle of attack of about 9°, which is lower than the stall angle of the wing of 14°. Therefore, it is suggested to iterate through the design of the empennage. Specifically, it is suggested to lower the horizontal stabilizer, and re-size the vertical tail, placing some of it below the booms.

6.3.2. Vertical Stabilizer

The airfoil selection procedure for the vertical tail followed the steps explained in Subsection 5.2.3, with the parameters changed to better fit the vertical stabilizer, namely ensuring that the airfoil is symmetric. The ideal lift coefficient was set to 0 as the vertical tail is ideally expected not to produce forces during nominal cruise. The maximum lift coefficient was set to 0.2. The selected airfoil was NACA-0009 airfoil. Its shape and polars can be seen in Figure 6.8 and Figure 6.9, respectively.

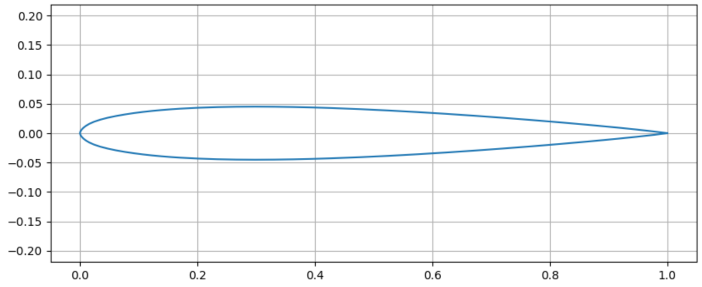

Figure 6.8: *Shape of the vertical stabilizer airfoil (NACA-0009 airfoil)*

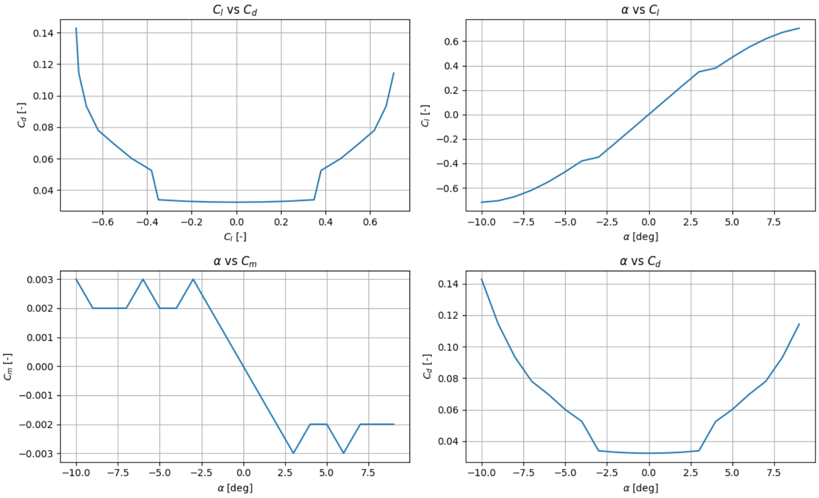

Figure 6.9: *Polars of the airfoil of the vertical stabilizer (NACA-0009 airfoil)*

The design process described in Subsection 6.2.3 leads to the geometrical properties given in Table 6.2 and Table 6.3 for the vertical stabilizer and rudder, respectively. It should be noted that the values given correspond to one vertical stabilizer; however, since an H-tail configuration was chosen, the drone will be equipped with two vertical stabilizers.

Table 6.2: *Geometrical properties of one vertical stabilizer*

Geometrical property	Value
Surface area [m^2]	0.277
Span [m]	0.71
Root chord [m]	0.5
Tip chord [m]	0.28
Mean aerodynamic chord [m]	0.40
Distance from wing to tail $c/4$ [m]	2.37
Quarter-chord sweep angle [deg]	13
Taper [-]	0.56
Aspect ratio [-]	1.82

Table 6.3: *Geometrical properties of one rudder*

Geometrical property	Value
Surface area [m^2]	0.125
Span [m]	0.5
Root chord [m]	0.30
Tip chord [m]	0.20
Mean aerodynamic chord [m]	0.25
$c_{\text{rudder}}/c_{\text{tail}}$ [-]	0.6
$b_{\text{rudder}}/b_{\text{tail}}$ [-]	0.70
$S_{\text{rudder}}/S_{\text{tail}}$ [-]	0.45
Distance from bottom of tail [m]	0.05
Max deflection [deg]	30

Since the horizontal stabilizer is mounted on top of the vertical tail, its wake will not interfere with the rudder during spin. Therefore, the effective area and span of both the vertical stabilizer and rudder are equal to the original ones. The design given above allows to satisfy the requirements for crosswind landing, spin recovery, and coordinated turn. The deflections of the rudder needed in these conditions are given in Table 6.4. In addition to this, the deflection needed to overcome crosswind during take-off and cruise are presented in Table 6.5:

Table 6.4: *Rudder deflection for critical conditions*

	Crosswind landing	Spin recovery	Coordinated turn
Rudder deflection [deg]	10.9	29.2	0.8

Table 6.5: *Rudder deflection for additional conditions*

	Crosswind take-off	**Crosswind cruise**
Rudder deflection [deg]	10.7	1.8

Although not critical, the rudder deflections for crosswind during take-off and cruise are evaluated to allow for requirement verification. The process of obtaining these values is the same as the one described for crosswind landing, with the substitution of the landing speed with the take-off and cruise speeds, respectively.

6.3.3. Dynamic Analysis

The stability and control derivative coefficients calculated using the method explained in Subsection 6.2.4 are summarized in Table 6.6.

Table 6.6: *Stability and control coefficients of the CEDI drone*

C_{X_0}	0.0	C_{Z_0}	0.123	C_{m_0}	-0.046	C_{Y_β}	-1.320	C_{n_β}	0.068	C_{l_β}	-0.018
C_{X_u}	0.0	C_{Z_u}	-0.031	C_{m_u}	0.017	C_{Y_p}	-0.311	C_{n_p}	-4.877e-04	C_{l_p}	-0.763
C_{X_α}	-0.102	C_{Z_α}	-5.918	C_{m_α}	-0.343	C_{Y_r}	0.238	C_{n_r}	-0.121	C_{l_r}	0.040
$C_{X_{\dot\alpha}}$	0.0	$C_{Z_{\dot\alpha}}$	-1.451	$C_{m_{\dot\alpha}}$	-5.978	$C_{Y_{\dot\beta}}$	0.004	$C_{n_{\dot\beta}}$	0.002		
C_{X_q}	0.0	C_{Z_q}	6.572	C_{m_q}	-20.817	$C_{Y_{\delta_a}}$	0.0	$C_{n_{\delta_a}}$	7.128e-06	$C_{l_{\delta_a}}$	0.046
$C_{X_{\delta_e}}$	-0.002	$C_{Z_{\delta_e}}$	-0.123	$C_{m_{\delta_e}}$	-0.509	$C_{Y_{\delta_r}}$	0.109	$C_{n_{\delta_r}}$	-0.048	$C_{l_{\delta_r}}$	0.007

The results of the dynamic analysis show that the aircraft exhibits stable lateral dynamic behavior. Specifically, the Dutch roll, aperiodic roll, and spiral motions are all dynamically stable, as illustrated by the response of the state variables in Figure 6.10, which depicts the Dutch roll as a representative case. The longitudinal dynamics reveal an slightly stable phugoid mode. This is also the case for the response to the recoil of the gun, given in Figure 6.11.

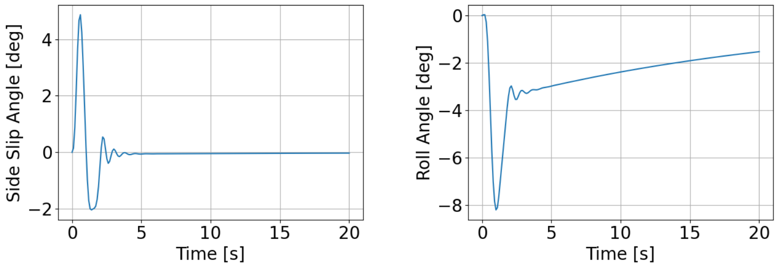

(a) *Sideslip angle vs time* **(b)** *Roll angle vs time*

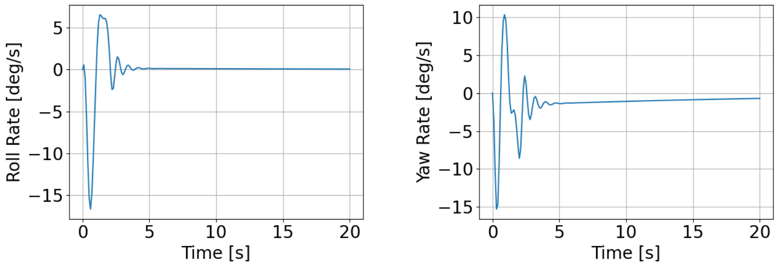

(c) *Roll rate vs time* **(d)** *Yaw rate vs time*

Figure 6.10: *System response to rudder pulse input: Dutch roll eigenmotion*

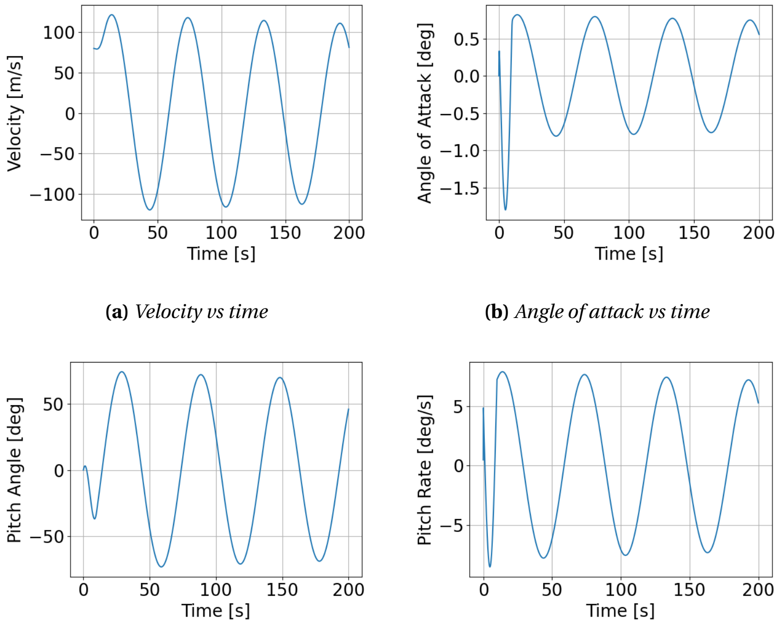

(a) *Velocity vs time* **(b)** *Angle of attack vs time*

(c) *Pitch angle vs time* **(d)** *Pitch rate vs time*

Figure 6.11: *System response to gun recoil as initial state*

As can be seen in Figure 6.11a and Figure 6.11c, the values obtained from this dynamic analysis are larger then expected and unrealistic. Therefore, the dynamic behavior of the aircraft cannot be approximated by linearized matrices. Nonetheless, the analysis provided useful qualitative data. Due to the drone's low inherent stability and slow response to disturbances, it struggles to correct its orientation effectively on its own. To ensure stable and reliable flight, the attitude must be actively controlled. An autopilot system should continuously monitor and adjust the drone's attitude to maintain optimal flight conditions and ensure it can consistently reach and hold the desired altitude.

6.4. Verification

The verification of the empennage design was carried out by assessing compliance with the requirements defined in Section 6.1. As the aircraft has not yet been manufactured and the design process is still ongoing, all requirements were verified through analytical methods. Each requirement was evaluated based on aerodynamic calculations and stability and control analyses. As shown in Table 6.7, all requirements were successfully met.

Table 6.7: *Empennage evaluation against requirements*

Requirement Code	Condition	Result	Met?	How?
SUB-01.04.15.01	δr_{spin}<30 deg	29.2 deg	Yes	Subsection 6.3.2
SUB-01.04.15.02	$S_h/S > S_h/S_{\text{controllability}}$	0.197	Yes	Subsection 6.3.1
SUB-09.19.78.01	$\delta r_{\text{crosswind}}$<30 deg	10.7 deg	Yes	Subsection 6.3.2
SUB-01.20.90.01	$\delta r_{\text{crosswind}}$<30 deg	10.9 deg	Yes	Subsection 6.3.2
SUB-01.22.117.01	$\delta r_{\text{crosswind}}$<30 deg	1.8 deg	Yes	Subsection 6.3.2

7

Armament Design

In this chapter the detailed design of the armament subsystem will be designed, first the requirements will be presented in Section 7.1 after which in Section 7.2 the specific gun system will be selected together with the corresponding 40 mm ammunition. Then the recoil and mounting system will be described in Section 7.3 followed by the compliance matrix described in Section 7.4

7.1. Requirements

The following requirements for the detection subsystem have been formulated in the baseline report[7]:

- **SYS-01.08.24:** The airborne part of the system shall be capable of eliminating the engaged target at a range of at least 50 m with a reliability of at least 95%.
  - **SUB-01.08.24.01**: The armament subsystem shall be able to neutralize targets with a reliability of at least 95%.
  - **SUB-01.08.24.02**: The armament subsystem shall be able to neutralize a target from a range of at least 50 m.
- **SYS-01.08.25:** The airborne part of the system shall be capable of eliminating the engaged target in a maximum time span of 240 s with a reliability of at least 95%.
- **SYS-01.08.30:** The airborne part of the system shall be capable of eliminating at least 5 enemy targets during a mission, with a reliability of at least 95%.
  - **SUB-01.08.30.01**: The armament subsystem shall be able to neutralize at least 5 targets per launch.
- **SYS-01.08.31:** The airborne part of the system shall be capable of eliminating targets with categories up to and including group 3 of the DoD UAS chart[1].
  - **SUB-01.08.31.1**: The armament subsystem shall be able to neutralize targets traveling at speeds of at least 130 knots.

7.2. Armament selection

In order to ensure the system can complete its mission and take down enemy targets, satisfying the requirements mentioned in Section 9.1, the drone will be outfitted with armaments. One of the most important mission phases is the engagement phase in which the enemy target is neutralized, as the ultimate goal of this design is to defend against enemy drones.

First, the type of armament system was selected, after which different specific weapon systems and ammunitions were evaluated. This led to the most suitable option for the mission considering all requirements. Cost, weight, kill reliability, and kill capacity were the main drivers behind the decisions made during this design process.

---

[1] URL `https://www.faa.gov/air_traffic/publications/atpubs/aim_html/chap11_section_3.html` [Cited 17 June 2025]

7.2.1. Weapon Selection

After the main trade-off, performed during the previous design phase, a lot of armament types were discarded, such as rocket propelled, kinetic impact, and air pressure based weapons. This led to the selection of projectile-based weapons as the primary armament option. Initially, four types of projectile weapons were researched and evaluated: high caliber explosive munition rifles, automatic shotguns, automatic machine guns, and automatic grenade launchers. These are briefly described below.

Automatic Shotgun

Shotguns were quickly identified as the least viable option by a long shot, mainly because of their limited range capabilities. Their use would require the vehicle to engage targets at very short distances, increasing intercept duration and posing close-proximity safety risks. More importantly, shotguns were unable to meet requirement SURQ-ARM-10, which mandates eliminating up to five enemy drones per flight without reloading. Given the need for multiple shells per target, especially for larger drones like the Shahed-136, and the 30-shell capacity of the largest drum magazines, this requirement could not be met. As a result, the shotgun was excluded as an armament option.

High Caliber Explosive Munition Rifle

The high-caliber explosive munition rifle was also discarded, primarily due to accuracy concerns when targeting moving aerial objects. Although this weapon offers high damage, requiring only a few hits to neutralize a target, achieving consistent accuracy mid-air is challenging. The selected ammunition, .50 caliber Raufoss Mk 211/NM140 rounds [2], are both heavy (43.09 g) and costly (approx. $95) per round, limiting the number of rounds the drone can carry. This results in fewer shots per target and makes each miss significantly more expensive. Given these constraints, especially in combination with the accuracy issue, this option was deemed unsuitable.

Automatic Machine Gun

The main advantage of a machine gun lies in the low cost and weight of its ammunition, allowing the drone to carry a large number of rounds and reducing the impact of missed shots. However, standard bullets deal relatively low damage, requiring multiple hits to neutralize larger drones, which is a limitation observed in Ukrainian battlefield use. Combined with likely inaccuracy, especially in automatic fire mode, this significantly increases the number of rounds needed per target. Additionally, automatic fire generates substantial recoil, which poses a serious challenge for airborne deployment. Unlike ground-based systems mounted on heavy, fixed platforms, the drone is light and airborne, making it highly susceptible to destabilization. This recoil-induced instability reduces accuracy and may require more ammunition than the drone can carry, given its limited payload capacity.

Automatic Grenade Launcher (Selected)

The automatic grenade launcher requires significantly fewer hits due to its high damage capability. Unlike the high-caliber explosive rifle, it demands much lower accuracy per shot, as the grenade's fragmentation allows effective damage without a direct hit and creates a relatively large damage area, improving effectiveness against drones. When comparing estimated ammunition per kill, the difference in cost and weight between machine gun bullets and the heavier, more expensive grenades is negligible. Additionally, the machine gun's need for continuous fire leads to cumulative recoil, whereas the grenade launcher can delay follow-up shots until recoil dissipates, simplifying recoil mitigation despite higher individual recoil forces. Finally, requiring only a few shots to neutralize a target reduces engagement duration and enables quicker interceptions. Based on this evaluation, the grenade launcher was deemed the most viable and effective weapon system option.

---

[2] URLhttps://warpigarmory.com/product/lake-ctiy-50-bmg-raufoss-mk-211-heiap-mk211/ [Cited 01 June 2025]

The specific grenade launcher that was selected because of weight, cost, range and kill capacity aspects is the Norinco LG5[3]. The weapon is shown in Figure 7.1. Although this automatic launcher, which is often referred to as a "sniper grenade launcher", has exceptional range (1000 m for point targets) and accuracy capabilities, it is also one of the relatively light and cheapest options on the market. Additionally, the modular magazine design is very preferable, with the biggest magazine storing 15 rounds.

Figure 7.1: *Norinco LG5 automatic grenade launcher (small magazine).*[4]

7.2.2. Ammunition Selection

After selecting the specific weapon system, the next step is picking out the best comparable ammunition. Two versions of the Norinco grenade launcher exist: the original version (QLU-11), used and designed by the Chinese military, and an export version (LG5), designed to fit NATO-caliber grenades (40x53 mm). Since the latter is exported to NATO countries, it was selected as the preferred version. A few of 40x53 mm caliber ammunition options exist[5], as listed:

- High-explosive, dual-purpose (HEDP) sniper grenade, 40×53 mm
- High-explosive precision grenade, 40×53 mm
- Programmable airburst grenade, 40×53 mm
- High-explosive incendiary grenade, 40×53 mm
- Incendiary grenade, 40×53 mm
- Training grenade, 40×53 mm

For the mission at hand, a programmable airburst grenade was deemed the most effective and was therefore selected as the ammunition to be used. More specifically, the 40x53mm HEDP-RF programmable airburst round by the Norwegian company Nammo was selected, its specifications being listed in Table 7.1. Citing Nammo[6]: "The HEDP Airburst ammunition is designed for use in any 40 mm AGL weapon. The HEDP-RF round provides airburst with pinpoint accuracy. The HEDP warhead provides fragmentation and penetration with high reliability. This allows for different target scenarios with only one type of 40 mm round."

---

[3] URL `https://odin.tradoc.army.mil/WEG/Asset/LG5_` [Cited 17 June 2025]

[5] URL `https://en.topwar.ru/164487-snajperskij-ruchnoj-granatomet-norinco-lg5.html` [Cited 16 June 2025]

[6] URL `https://www.nammo.com/product/our-products/ammunition/medium-caliber-ammunition/40-mm-products/40mm-x-53-hedp-rf/` [Cited 16 June 2025]

The rationale for choosing this type of grenade is that airburst grenades create a larger impact area compared to traditional high-explosive rounds, with all fragments propelled primarily forward, as illustrated in Figure 7.2. The mechanism involves detonating the projectile, which contains all fragments in the tip with a charge behind it, just before it reaches the target. This ensures that the fragments spread across the target's surface, increasing the effective hit area. Therefore, even if the projectile's trajectory narrowly misses, some fragments are likely to strike the enemy vehicle. This characteristic is especially favorable for neutralizing small UAVs, as a larger impact area increases the likelihood of disabling lift or control surfaces and damaging critical subsystems.

Table 7.1: *Nammo 40x53mm HEDP-RF airburst specifications*

Metric	**Value**[4]
Projectile weight	247 g
Muzzle velocity	240 m/s
Maximum dispersion	1.0 mils
Number of fragments	1200
Penetration	> 65 mm RHA
Airburst accuracy	1 ms resolution
Service temperature	-32°C to +63°C
Safety temperature	-46°C to +71°C

Figure 7.2: *Nammo airburst detonation.*

As mentioned previously, the Norinco LG5 allows for different types of magazines; the 15-round drum magazine was selected. Using the attack simulation tool as described in Section 3.4, it was determined that in order for the system to successfully achieve its mission, each individual vehicle shall be able to eliminate at least 5 targets per launch. Considering the damage capability of the selected airburst munition, a very conservative estimate, including occasional misses, is that an average of 3 rounds per kill is required. Therefore, each vehicle will need at least 15 rounds. Using the 15-round magazine plus 1 round in the chamber, totaling 16 rounds, will suffice conservatively.

7.3. Armaments Implementation/Integration Design

This section will discuss how the selected weapon system with its ammunition will be used during the mission. For the engagement phase of the interception a specific combat approach is designed, outlining exactly how the target will be engaged each time striving for the highest effectiveness possible with the chosen design. After which the integration of the armaments into the fuselage is explained, specifically explaining the way it is mounted and how the recoil from the weapon is mitigated using a spring-damper system.

7.3.1. Combat Approach Design

After selecting the armaments system, a certain way of approaching the targets must be designed to engage and eliminate the target implementing the armaments in the most effective and strategic way. The first thing to consider is the ideal interception: the enemy will come into the defended territory, after which the interceptor must cut off its path to close the distance. This is the fastest way to reach the target, but this also means that at the interception point, the two trajectories cross, resulting in high relative velocity difference. Eliminating the target during this small fly-by window is nearly impossible with the interceptor's current targeting and armament systems. Therefore, the interceptor will not simply let the target fly by. Just before interception, it will turn to align with the target's trajectory and adjust its speed to match. This maneuver positions the interceptor behind the target, tracking and following it from a safe distance. This approach provides more time to aim the weapon, improving the chances of eliminating the target. However, shooting loitering munitions directly from behind can be quite challenging due to the small target area visible from that angle, requiring very high accuracy. For this reason, the interceptor will climb to gain altitude relative to the target and engage from behind and above. Attacking at an angle greatly increases the projected strike area, making it significantly easier to hit the target, while also increasing the probability of damaging a critical surface or subsystem.

A drawback of shooting from behind, however, could be that if the target explodes, either because the warhead is hit or it is deliberately detonated as a defense mechanism, the interceptor itself could be damaged. To avoid harm from the blast or from flying into a cloud of shrapnel, the vertical distance between the interceptor and its target must exceed the fragmentation radius. Shrapnel from such an explosion can cause minor damage up to 46 m.[7] With this in mind, the interceptors are designed to fly at least 46 m above their target, ensuring safety from any potential airborne fragments. Due to the way the gun is mounted and integrated into the vehicle, it can be pointed down at a maximum angle of 32°, as explained in Subsection 7.3.3. To maximize the projected strike area, the gun will always be fired at this maximum depression. At this angle and with a vertical distance of 46 m, the horizontal distance from the target is 73.62 m. Therefore, the total firing range, which is the hypotenuse, will be 86.81 m. This is illustrated in Figure 7.3a below. Figure 7.3b next to that shows the projected dimensions of the main target (the Shahed-136) as seen by the interceptor's targeting system at the 32° firing angle. With a 1% accuracy, which will be explained in Subsection 9.2.3, the strike zone radius at a range of 86.81 m will be 0.8681 m. The strike zone in projected on the Shahed area as seen by the targeting system, the maximum off-set from the target is only 23 cm, and a direct hit probability of ≈ 90%.

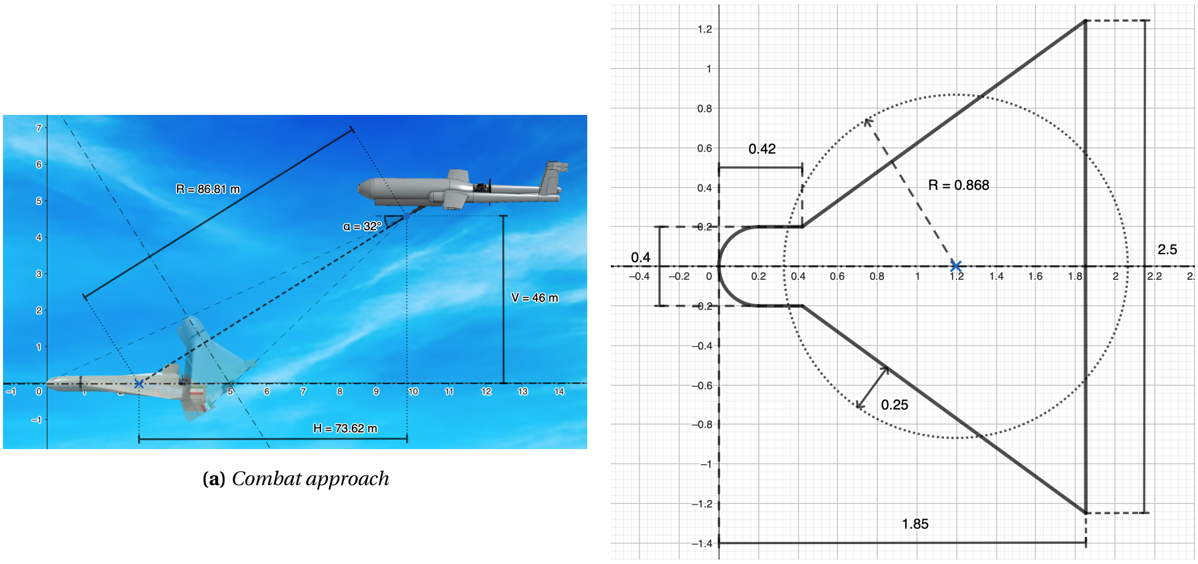

(a) *Combat approach*

(b) *Strike Zone*

Figure 7.3: *Combat approach (left) and Strike Zone (right).*

---

[7] URLhttps://isis-online.org/isis-reports/mobile/alabugas-shahed-136-geran-2-warheads-a-dangerous-escalation[Cited 16 June 2025]

7.3.2. Recoil System Design

The size and speed of the outgoing projectile will lead to significant recoil; therefore, a method of dealing with this recoil must be devised. The first step in this process is to model the forces caused by the shooting of the projectile on the gun. There are four known parameters: the mass of the projectile (247 g), the muzzle velocity of the projectile (240 m/s), the barrel length (0.6 m) and the barrel diameter (40 mm). The barrel length was found from visually inspecting pictures of the grenade launcher. With these known parameters, the starting pressure in the chamber (the pressure just after the propellant is detonated) can be found by assuming isentropic expansion and equating the work done by the expanding gas to the final kinetic energy of the projectile. This leads to the following equation:

$$P_0 = \frac{\frac{1}{2} m_{\text{proj}} V_{\text{muzzle}}^2 (\gamma - 1)}{A_{\text{bore}} \cdot L_{\text{chamber}} \left[1 - \left(\frac{A_{\text{bore}} \cdot L_{\text{chamber}}}{A_{\text{bore}} \cdot L_{\text{chamber}} + A_{\text{bore}} \cdot L_{\text{barrel}}} \right)^{\gamma - 1} \right]} \tag{7.1}$$

With γ taken as 1.2 [19] and L_{chamber} as 0.02, P_0 is found to be 113.94 Mpa. With this value and the other given parameters, the pressure, projectile acceleration and projectile velocity along the barrel, as well as resulting force over time, can be plotted, as given in Figure 7.4.

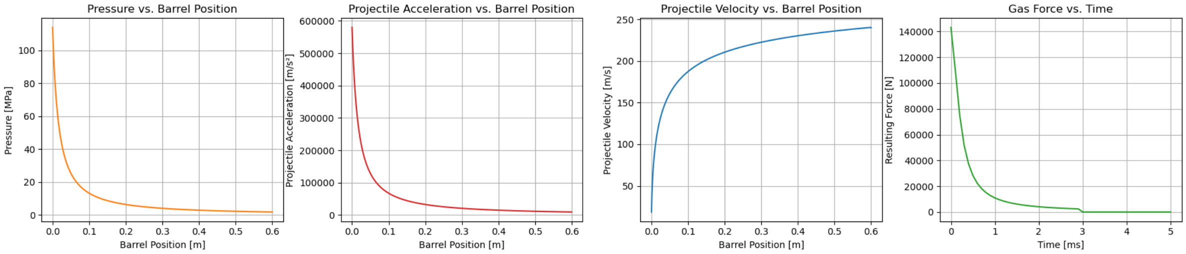

Figure 7.4: *Metrics of interest along the barrel and over time*

On the most right figure in Figure 7.4, it can be seen that the peak force is 140 kN. Although the duration of the peak force is short, its amplitude is very high and would significantly impact the design of the mounting points for the gun. Therefore, it was chosen to design a spring damper combination to reduce the peak force exerted. The system is modeled as two free masses, one for the drone and the other for the gun, with a spring and damper in between them, as can be seen in Figure 7.5.

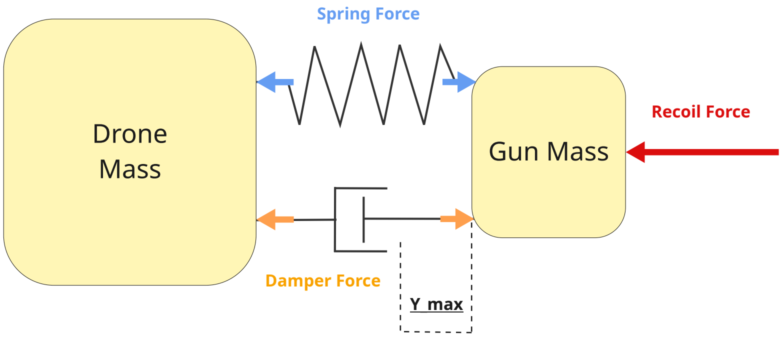

Figure 7.5: *Spring damper combination model*

This model results in four design parameters: the spring stiffness k_{eq}, the damping coefficient c_{eq}, the maximum allowed displacement y_{max}, and the pre-loaded delta δ, meaning how much the spring is pre-compressed. By setting y as the relative position between the two masses and limiting the forces to only the active regions of motion, the equations of motion become:

$$\begin{cases} m_G \ddot{x}_G(t) = F(t) - k_{\text{eq}} \cdot y(t) - c_{\text{eq}} \cdot \dot{y}(t), & \text{if } y(t) > 0 \\ m_A \ddot{x}_A(t) = k_{\text{eq}} \cdot y(t) + c_{\text{eq}} \cdot \dot{y}(t), & \text{if } y(t) > 0 \\ F_s = F_d = 0, & \text{otherwise} \end{cases} \tag{7.2}$$

$$y(t) = x_G(t) - x_A(t) - \delta \qquad \dot{y}(t) = \dot{x}_G(t) - \dot{x}_A(t) \tag{7.3}$$

Where x_G and x_A denote the positions of the gun and aircraft, respectively. The goal is to reduce the absolute value of the sum of the spring force F_s and the damper force F_d to their lowest possible value given the following constraints. The first constraint is y_{max}: the larger y_{max} is, the lower the absolute force, however, y_{max} is geometrically constrained by the aircraft geometry since a larger recoil 'stroke' would increase the length of the recoil system. A value of 0.3 m was chosen as a compromise between minimum absolute force and 'stroke' length. The second constraint is the damping ratio ζ: the damping ratio was set to 1, meaning the system is critically damped. This results in no overshoot and, therefore, the shortest time to return to the initial position. The third constraint is δ: the higher this value is, the more the gun is 'held' in the forward position. After a few iterations, this value was set at 0.2 m.

Using these constraints, a simulation can be run using the equations of motions and force input vector (Figure 7.4) mentioned above. The program then minimizes the absolute value of the sum of F_s and F_d by optimizing the values of k_{eq} and c_{eq} using a built in Python optimization algorithm.

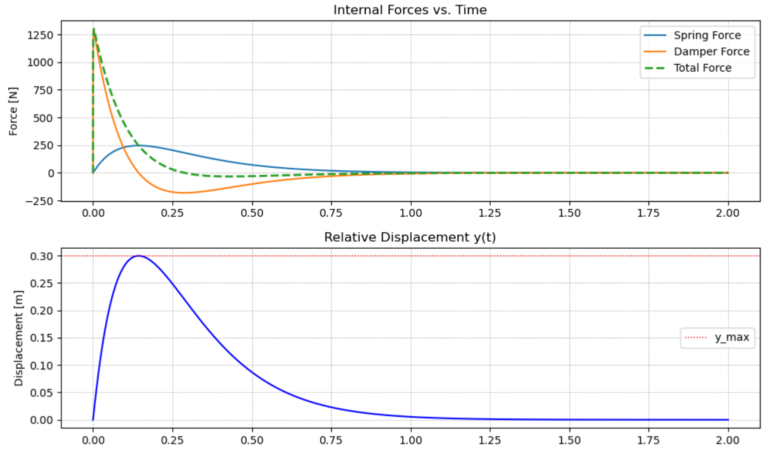

Figure 7.6: *Optimized recoil response*

Table 7.2: *Optimization results*

Parameter	**Value**
Optimal k_{eq} [$\mathrm{N\,m^{-1}}$]	822.0
c_{eq} [$\mathrm{N\,s\,m^{-1}}$]	235.9
Peak internal force [N]	1301.3
Max. relative disp. [m]	0.300

The final optimized values for k_{eq} and c_{eq} are given in Figure 7.2. As can be seen from the upper graph in Figure 7.6, the maximum absolute value of the sum of F_s and F_d is 1301.1 N. The lower graph shows the relative position of the drone and gun masses over time, it can be seen that the maximum 'stroke' is exactly 0.3 m and that there is no overshoot when returning to the initial position. The time to return to the initial position is about 1.25 s, meaning that, in principle, the maximum fire rate of the system would be 48 rounds per minute, which is more than sufficient to complete the mission.

7.3.3. Gun Mounting Design

Now that the optimal spring stiffness $k_{\text{eq,opt}}$ and damping coefficient $c_{\text{eq,opt}}$ have been found, the actual mounting system for the gun needs to be designed. It was decided that the point where the recoil force should be applied is the front of the wing box at the height of the quarter chord. In this way, the moment generated by the recoil is minimal as the moment arm towards the center of gravity is minimized. Furthermore, the wingbox is one of the strongest structures in the aircraft: applying the force to this structure directly negates the need for other (heavy) load path enabling structures.

It was decided that the gun would be mounted between two custom-made spring-damper combinations. Since the two springs and dampers are arranged in parallel, the effective spring stiffness and damping coefficient for each should be half of the desired overall values. Thus:

$$k_1 = k_2 = \frac{k_{\text{eq,opt}}}{2} = 411\,\text{N}\,\text{m}^{-1} \qquad c_1 = c_2 = \frac{c_{\text{eq,opt}}}{2} = 117.95\,\text{N}\,\text{s}\,\text{m}^{-1}$$

The spring damper combinations were conceptually designed in CAD, the main focus was to generate the overall dimensions and outline the working mechanism. The resulting parts could then be used to determine the interfaces with the rest of the aircraft. An exploded view of one spring damper combination can be seen in Figure 7.7.

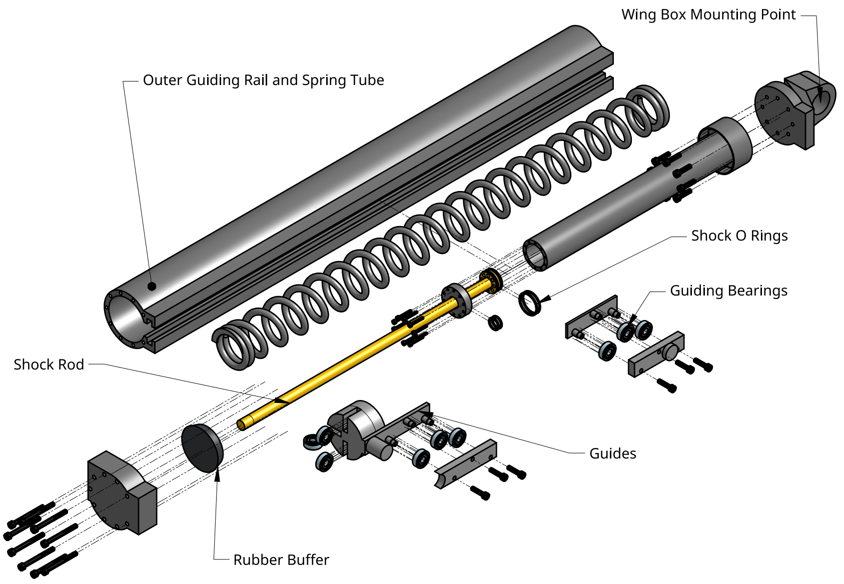

Figure 7.7: *Exploded view of spring damper combination*

It was chosen to make the gun retractable such that when it is not used it is safely stored in the fuselage. For this purpose, an extending mechanism needed to be design. It was chosen to use rails mounted to the inside of the fuselage together with worm and spur gears. This mechanism would then be powered by a stepper motor. An exploded view of the assembly can be seen in Figure 7.8.

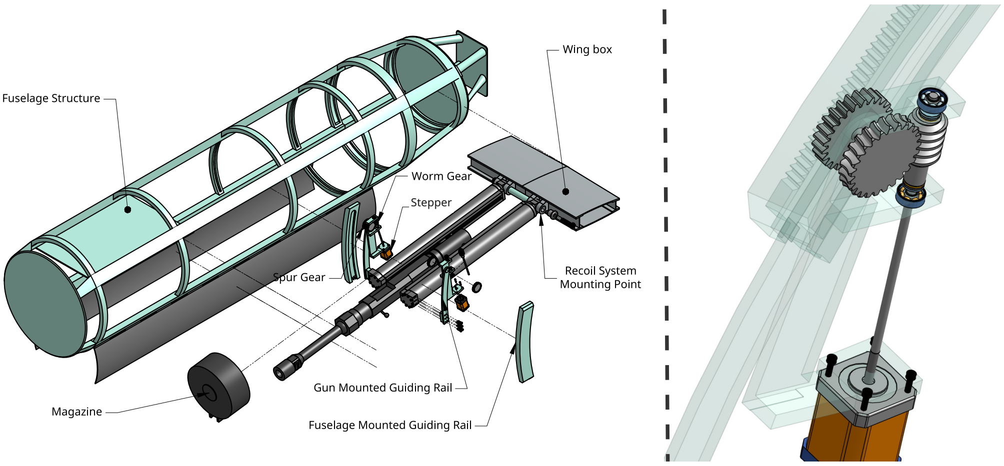

Figure 7.8: *Gun Mounting assembly exploded view and zoomed in view of gear mechanism*

The spring damper combinations are mounted to the wing box, where the rotation point of the gun is located. In this way, the line of action, and thus the moment arm of the recoil force, varies little with gun deflection. The gun rotates by the turning of the stepper motors, this then turns the worm gears, which are connected to spur gears that are paired to a rack inside the fuselage mounted guiding rail. The stepper motor is located downwards with respect to the top of the rail to allow the magazine to pass during the recoil 'stroke' of the gun. The worm and spur gears both have 25 teeth. This results in a gear ratio between worm and gear of 1:25: one turn of the stepper (and thus the worm) rotates the gear by 1/25 of a rotation. The 25 teeth of the spur gear together with the fuselage guiding rail geometry results in a gear ratio of 1:37.8. This means that for each rotation of the spur gear, the gun rotates 1/37.8 of a rotation about its mounting point on the wing box. The total gear ratio (GR) between the stepper and gun can be calculated as follows:

$$GR_{\text{total}} = GR_{\text{worm}} \cdot GR_{\text{spur}} = 25^{-1} \cdot 37.8^{-1} = 0.001058 \tag{7.4}$$

This means that for each turn of the stepper, the gun rotates with 0.001058 revolutions about its mounting point on the wingbox or, equivalently, 0.381°. The motor mount was sized for a NEMA 17[8] stepper motor. The average NEMA 17 has a step increment of 1.8° Therefore, considering the gear ratio between stepper and gun, the step increment for the gun is 0.0019°. This increment resolution was deemed more than sufficient. Assuming a stepper motor rotation of 1000 rpm, which is close to the lower bound of the available options, the resulting gun rotation speed is $6.35\,\deg s^{-1}$. While this is insufficient for dynamic targeting, the engagement protocol is based on a steady relative position between the attacker and defender, in which case the rotation speed is adequate. The maximum downward rotation limit is 32°, as seen in Figure 7.9.

---

[8] URL `https://www.mcmaster.com/products/electric-motors/stepper-motors-1~/` [Cited 17 June 2025]

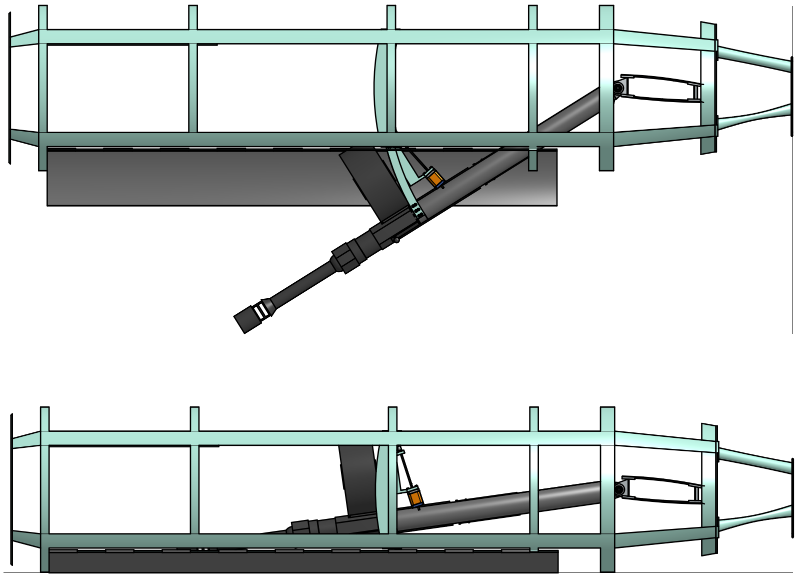

Figure 7.9: *Final rotation limits of the Gun*

7.4. Verification

Due to the limited availability of information on both weapon systems and ammunition, in combination with at this stage unknown factors, many of the requirements can not be verified. With more data on the effectiveness of airburst ammunition and on other subsystems relevant to the armament, such as control and detection, these requirements can be more thoroughly verified in future design stages. At this point, however, there is no indication that any of the specified requirements are infeasible. The current requirement verification is given in Table 7.3:

Table 7.3: *Requirements compliance for the armament subsystem*

Requirement Code	**Condition**	**Result**	**Met?**	**How?**
SUB-01.08.24.01	Elimination Reliability ≥ 95 %	NA	TBD	NA
SUB-01.08.24.02	Elimination range ≥ 50 m	180 m	Yes	Norinco LG5 specs
SYS-01.08.25	Engagement time ≤ 240s	Fire rate of 48rpm	TBD	Subsection 7.3.2
SYS-01.08.31	Tar. Size ≥ gr. 3 of the DoD UAS chart	NA	TBD	NA
SUB-01.08.30.01	Minimum number of eliminations ≥ 5	3 rounds per target	TBD	Norinco LG5 specs
SUB-01.08.31.1	Minimum target speed ≥ 130kts	NA	TBD	NA

8

Avionics Design

In this chapter, the avionics design will be outlined. First, the requirements for the system will be identified in Section 8.1. From these, the design process of the communication system, as well as the sizing of the servos, will be described in Section 8.2. Afterwards, the description of the avionics set, including communication, motors, and electrical integration, will be given in Section 8.3. Lastly, the requirement will be verified in Section 8.4.

8.1. Requirements

The following requirements for the avionics system have been formulated in the baseline report[7]. As the aircraft has not yet been fully designed and developed, some requirements are still left TBD.

- **SYS-01.06.18**: The airborne part of the system shall be capable of dynamic and static obstacle detection and recognition with sufficient time to avoid them at a reliability of **TBD**%.
- **MIS-01.14**: The airborne part of the system shall be able to navigate autonomously with the following specifications.
  - **SYS-01.14.47**: The airborne part of the system shall be capable of receiving GNSS signal.
  - **SYS-01.14.48**: The airborne part of the system shall be capable of autonomously following pre-specified points with a precision of at least **TBD** m, in ISA conditions, at all operational flight levels.
  - **SYS-01.14.49**: The airborne part of the system shall be capable of autonomously following pre-specified points with an accuracy of at least **TBD** m, in ISA conditions, at all operational flight levels.
  - **SYS-01.14.50**: The airborne part of the system shall be capable of autonomous loitering around a pre-specified point.
  - **SYS-01.14.51**: In the event that the GNSS signal is lost the airborne part of the system shall be capable of inertial navigation back to the launch location with a reliability of at least **TBD**%.
- **MIS-01.16**: The airborne part of the system shall be able to autonomously detect targets and obstacles and maneuver with the following specifications.
  - **SYS-01.16.61**: The airborne part of the system shall be able to autonomously avoid static obstacles, with a reliability of at least **TBD**%.
  - **SYS-01.16.62**: The airborne part of the system shall be able to autonomously avoid dynamic obstacles, with a reliability of at least **TBD**%.
  - **SYS-01.16.63**: The airborne part of the system shall be capable of autonomously tracking the engaged target, with a reliability of at least **TBD**%.
  - **SYS-01.16.64**: The airborne part of the system shall be capable of autonomously following the engaged target, with a reliability of at least **TBD**%.
  - **SYS-01.16.65**: In the event that the target is lost, the airborne part of the system shall be capable of autonomously following a search pattern.

  - **SYS-01.16.66**: In the event that the target is lost, the airborne part of the system shall be capable of autonomously returning to the point of last communication with the ground part of the system.
- **SYS-01.21.9**: The airborne part and the ground part of the system shall be capable of communicating between each other at a range of at least **230** km, in all operational environmental conditions, at all operational flight levels.
- **SYS-01.21.99**: The airborne part of the system shall be capable of communicating with the ground part of the system with a bitrate of at least **600** bit s^{-1}, in all operational environmental conditions.
- **SYS-01.21.101**: The airborne part of the system shall be capable of communicating with the ground part of the system with an error rate of no more than **TBD**%, in all operational environmental conditions.
- **SYS-01.21.103**: The airborne part of the system shall be capable of navigation, in all operational environmental conditions.
- **SYS-01.21.104**: The airborne part of the system shall have a redundant navigation subsystem.
- **SYS-01.21.105**: The airborne part of the system shall have a redundant communication subsystem.
- **SYS-15.21.107**: The communication system of the airborne part of the system shall comply with NATO STANAG 4586.
- **SYS-01.21.111**: The airborne part of the system shall be capable of returning to the launch location in the event that the communication signal is lost, with a reliability of at least **TBD**%.

8.2. Design Process

In this section, the design process for the antenna sizing, for both direct and satellite communication, as well as the sizing of the servos will be described.

8.2.1. Direct Communication Antenna Sizing

The sizing of the ground-vehicle communication system was carried out by performing a link budget between the potential antennas onboard the drone and the ground station. An omnidirectional antenna was selected for the onboard system. Although omnidirectional antennas typically offer lower gain compared to directional ones, they do not need to be pointed in a specific direction, which simplifies integration with the drone's configuration and reduces mechanical complexity.

Four different frequency bands were evaluated: UHF (200–450 MHz), low-band VHF (25–70 MHz), high-band VHF (108–137 MHz), and HF (3–23 MHz). These bands are all commonly used in military applications [20].

Ten different types of omnidirectional antennas were considered: whip, Rubber Duck, half-wave dipole, folded dipole, discone, loop, halo, helical, meander line, and spiral antennas. Their physical sizes were estimated based on the corresponding wavelength at each frequency band, considering typical antenna configurations, as given by Equation 8.1,

$$l_{\text{antenna}} = k\lambda = k\frac{c}{f} \tag{8.1}$$

where k is a parameter depending on the properties of the antenna, c is the speed of light, and f is the lowest frequency of the chosen bandwidth. For dipole, loop, halo, and spiral antennas this value correspond to the larger diameter. Gain values were also approximated based on standard antenna performance for each type, assuming optimal design and material use.

A summary of the estimated values is given in Table 8.1, where the size columns correspond to the largest dimension of the antenna if used in the specified frequency bands.

Table 8.1: *Dimension and gain of all considered omnidirectional antennas*

Antenna type	Configuration	Main dimension [m]				
		UHF	**High-band VHF**	**Low-band VHF**	**HF**	**Gain [dB]**
Whip	**1/4 wave**	0.38	0.69	3.00	24.79	8.0[1]
	1/2 wave	0.75	1.39	6.00	49.59	8.1
	5/8 wave	0.94	1.74	7.50	61.98	7.2
Rubber duck	-	0.23	0.11	0.48	3.97	2 [2]
Dipole	**1/2 wave**	0.24	0.44	1.91	15.78	2.2 [21]
	5/4 wave	0.60	1.11	4.77	39.46	5.2
Folded dipole [3]	-	0.12	0.22	0.95	7.89	2.2 [4]
Discone	-	0.26	0.49	2.10	17.36	2.0 [5]
Loop	**1/3 wave**	0.16	0.30	1.27	10.52	8.2 [22]
	1/4 wave	0.12	0.22	0.95	7.89	8.2 [22]
	1/2 wave	0.24	0.44	1.91	15.78	8.2 [22]
Halo	-	0.24	0.44	1.91	15.78	1.2
Helical [23]	-	3.00	5.56	24.00	198.35	15.4
Meander Line [6]	-	0.77	1.44	6.20	51.27	0.95 [24]
Spiral [7]	-	0.48	0.88	3.82	31.57	4.9 [8]

It is clear from the table above that the low VHF and HF bands are unfeasible, as the required dimensions for the on-board antenna are too high. Therefore, the rest of the design process will consider only the UHF and high VHF bands. Additionally, because of the limited space available on the CEDI drone, only the smaller antennas should be considered. Therefore, from this point onward, only the following types of antenna will be considered: quarter whip antenna, Rubber Duck antenna, half wavelength dipole antenna, folded dipole, discone antenna, the three types of loop antennas, and the halo antenna. The uplink and downlink budgets were evaluated using Equation 8.2 and Equation 8.3, respectively,

$$P_{rx} = P_{tx} + G_{tx} - L_{\text{path}} + G_{rx} + G_{LNA} - L_{LNA} + G_{\text{coding}} - SNR - M_{\text{fade}} \tag{8.2}$$

$$P_{rx} = P_{tx} + G_{tx} + G_{\text{amp}} - L_{\text{path}} + G_{rx} + G_{\text{coding}} - SNR - M_{\text{fade}} \tag{8.3}$$

where P_{rx} is the received power, P_{tx} is the transmitter power, G_{tx} and G_{rx} are the gains of the transmitter and receiver, respectively, G_{LNA} and L_{LNA} are the low-noise amplifier gain and noise loss, G_{coding} is the coding gain, SNR is the required Signal to Noise Ratio, and M_{fade} is the fade margin. L_{path} is the path loss given in Equation 8.4, where R is the distance between the two systems, λ is the wavelength of the signal, and γ_R is the specific atmospheric attenuation, assumed to be constant for all considered frequencies and equal to 0.4 dB/km [25].

---

[1] URL https://www.w8ji.com/VHF%20mobile%20vertical.htm [Cited 18 June 2025]

[2] URL https://www.nearson.com/antennas.php?page_id=67&0=1&1=25&display=list&sort=frequency&order=asc#sort [Cited 18 June 2025]

[3] URL https://radiance.ece.utoronto.ca/ece422/notes/13-folded.pdf [Cited 18 June 2025]

[4] URL https://www.antennaexperts.co/blog/what-is-a-folded-dipole-antenna [Cited 18 June 2025]

[5] URL https://www.mathworks.com/help/antenna/ug/discone-antenna-for-tv-broadcasting-system.html [Cited 18 June 2025]

[6] URL https://www.qsl.net/kk4obi/Meander%20Dipole.html [Cited 18 June 2025]

[7] URL https://www.antenna-theory.com/antennas/travelling/spiral.php [Cited 18 June 2025]

[8] URL https://www.steatite-antennas.co.uk/spiral-antennas/#spiral-antennas [Cited 18 June 2025]

$$L_{\text{path}}[dB] = L_{FS} + L_{\text{atm}} = 20\log_{10}\left(\frac{4\pi R}{\lambda}\right) + \gamma_R R \tag{8.4}$$

Although the link budget is usually performed by defining the distance between transmitter and receiver to obtain the signal margin as output, the calculations here are performed differently. Due to the need to satisfy NATO standard and seamlessly integrate with the existing infrastructure, the required values for SNR and minimum data rate are defined according to STANAG 4285 [26]. The required SNR depends on the data rate of the communication; therefore, it depends on the type, quality, and quantity of the information that is being transmitted. The required and assumed quantities for the link budget are summarized in Table 8.2 and Table 8.3, respectively.

Table 8.2: *Required values for link budgets*

	Downlink with video	**Downlink telemetry**	**Lowest possible downlink**
BER	1.00e-05	1.00e-05	1.00e-05
Data rate [bps] [26]	3600	600	75
Required SNR [dB] [26]	30	7	2
Encoding	BPSK	BPSK	BPSK

Table 8.3: *Assumed values for link budgets*

Parameter	**Value**
Fade margin [dB]	15 [9]
Coding gain [dB]	7 [27]
Ground antenna sensitivity [dBm]	-96 [28]
Ground antenna gain [dB]	7 [10]
Ground transmitting power [dBm]	50
Receiver amplifier gain [dB]	20
Receiver amplifier noise [dB]	3
Transmitting amplifier gain [dB]	20 [29]

Table 8.4: *Noise power for all frequency regimes*

Frequency regime	**Noise power [dBm]**
UHF	-120
High-band VHF	-129
Low-band VHF	-127
HF	-131

The link budget is applied to all considered antennas, and compared to the noise power of the specific frequency bands, calculated using Equation 8.5,

$$NP = 10\log_{10}(Bk_bT) \tag{8.5}$$

where, B is the bandwidth of the signal, k_b is the Boltzmann constant, and T is the system noise temperature, assumed to be 290 K. The noise temperatures for all considered frequency regimes are given in Table 8.4. The drone's flight altitude was set at 5 km. The maximum communication range for uplink communication is determined so that the power received by the drone is more than the noise power for that specific frequency bandwidth; these results are shown in Table 8.5. The maximum communication range for each type of transmission is determined by setting the maximum transmitter power at 100 W, and then ensuring that the received power at the ground station exceeds its sensitivity threshold; these results are presented in Table 8.6. It should be noted that the uplink communication does not require a SNR above 7, as only commands will be transmitted, and not videos.

URL `https://afar.net/rf-link-budget-calculator/#fade-margin` [cited 18 June 2025]

URL `https://www.trival-antennas-masts.com/antenna-products/ad-22-a-log-periodic-vhf-uhf-antenna-100-512-mhz-rev-a` [Cited 18 June 2025]

Table 8.5: *Maximum ranges for various uplink transmission SNR across possible frequency regimes*

SNR	7	2	7	2
	Range across UHF band [km]		**Range across high-band VHF [km]**	
1/4 wavelength whip antenna	145	162	188	205
Rubber duck	130	149	173	193
Half wavelength dipole	130	149	173	193
Folder dipole	130	149	173	193
Discone	130	149	173	193
Loop	145	163	188	207
Halo	130	148	173	191

Table 8.6: *Maximum ranges for various downlink transmission SNR across possible frequency regimes*

SNR	30	7	2	30	7	2
	Range across UHF band [km]			**Range across high-band VHF [km]**		
1/4 wavelength whip antenna	55	100	111	75	122	133
Rubber duck	45	88	98	63	109	120
Half wavelength dipole	45	88	98	63	110	120
Folder dipole	45	88	98	63	110	120
Discone	45	88	98	63	110	133
Loop	56	101	111	75	123	120
Halo	44	87	97	75	108	118

8.2.2. SATCOM Antenna Sizing

The inclusion of a satellite communication (SATCOM) system serves a critical role in ensuring communication redundancy and operational reliability. The primary communication system can experience degradation or complete loss due to atmospheric conditions, the vehicle moving out of range, interference such as jamming, or obstruction due to terrain. The SATCOM system provides an alternative communication pathway to enable continued monitoring and controllability of the fleet and to increase the probability of safe recovery of the system under adverse conditions.

To calculate the required size of the antenna, the required antenna gain (in a logarithmic scale) is first determined. This is done using Equation 8.6

$$G_{rx} + G_{tx} = P_{rx} - P_{tx} + L_{\text{path}} + L_{\text{misc}} \tag{8.6}$$

Where the path loss L_{path} is determined using Equation 8.4. However, it must be noted that the atmospheric attenuation within the equation is omitted, as this simplification does not hold for space communication. Additionally, to overcome atmospheric attenuation, the signal would require even more gain. As will be seen later in this section, this optimistic estimation still does not lead to a favorable size for the antenna. Within Equation 8.4, the range R is determined using Equation 8.7, calculating the slant range to the satellite based on the elevation angle θ, where R_E is the Earth radius and h is the altitude of the satellite:

$$R = \sqrt{(R_E + h)^2 - R_E^2 - \cos^2\theta} - R_E sin\theta \tag{8.7}$$

The power of the transmitter (vehicle), P_{tx}, is determined from the power budget, and the power required for the receiver (satellite), P_{rx}, is determined using Equation 8.3. The signal-to-noise ratio is based on the modulation type, encoding, and BER requirements. In this system, BPSK encoding and a 1/2 rate coding scheme are used. This leads to a required SNR of approximately 4.49.

Table 8.7: *Major characteristics of the SATCOM system*

Characteristic	Value
Signal frequency [GHz]	44.5
Min. elevation angle [deg]	20
Satellite altitude [km]	600
System noise temperature [K]	290
Transmitter power [W]	30
Data rate [Mbps]	0.5
Link margin [dB]	6

The initial design investigation focused on the traditional X-band (8-12 GHz) commonly used for (military) satellite communications. However, preliminary link budget analysis revealed significant challenges in meeting size constraints within this frequency range. To address these shortcomings, the frequency band was moved to a range of 43.5-45.5 GHz, a range already distinguished by NATO to be used for military satellite communications. Although the selection of a higher frequency aids in reducing the antenna size, it should be noted that it introduces additional design challenges such as increased atmospheric attenuation and more stringent pointing accuracy requirements. All of the characteristics of the data link used can be found in Table 8.7.

In total, three types of antenna were considered for sizing: a parabolic dish antenna, a microstrip patch array, and a helical antenna. However, due to form factor considerations, the helical antenna was abandoned early on. Based on the previously given values, the dimensions in Table 8.8 were found:

Table 8.8: *Comparison of Parabolic Dish Antenna and Microstrip Patch Array*

Aspect	Parabolic Dish Antenna	Microstrip Patch Array
Diameter / Array Size	Diameter: 73.8 cm	Array size: 59.9 × 59.9 cm
Beamwidth / Elements	Beamwidth: 0.3°	Number of elements: 16129

In Table 8.9, an overview for the entire range of frequencies is found:

Table 8.9: *Frequency comparison for various common frequency bands*

Frequency [GHz]	Required gain [dB]	Dish diameter [cm]	Array Size [cm]
8.0 (X-band)	42.0	155.6	128
12.0	42.8	142.0	115.4
18.0 (K-band)	44.6	116.0	94.4
27.0	46.3	94.7	76.9
43.5	49.8	87.9	71.4
45.5	50.0	85.9	69.6

Given these measurements and the dimensions of the fuselage, it can be argued that the antenna size obtained here is infeasible for this application. Even an increase in the power supply to 100 W leads to an antenna dish diameter of 54 cm. Therefore, it was decided to choose a commercial off-the-shelf option for the SATCOM system. The selected option is the Starlink Mini. This option was chosen as a placeholder; this was intended to show that systems with the Starlink Mini's characteristics, as shown in Table 8.10, are feasible.

The satellite communication system design process demonstrated significant challenges. While the 43.5-45.5 GHz frequency selection and system optimization (data rate reduction, power increase, and elevation angle optimization) provided substantial improvements over baseline X-band designs, the resulting antenna dimensions remained incompatible with integration requirements.

8.2.3. Servo sizing

To determine the size of the servo required, it is needed to have an idea of how much torque this servo has to provide. This will be calculated by assuming two forces on the control surface. The first one is caused by the dynamic pressure acting on the surface of the deflected control surface, and the second one is the resultant forces generated by changing the overall airfoil shape; the lateral force created by the rudder when deflected is an example of this. Gravitational forces due to their own weight will be ignored for now.

The total aerodynamic torque T_{total} is given by the sum of the torques caused by these two force components. The lateral force component is calculated using Equation 8.8 and the torque is then calculated using Equation 8.9, where the moment arm is at the quarter chord of the rudder.

$$F_{\text{side}} = \bar{q} S C_{y_{\delta_r}} \delta r \tag{8.8}$$

$$T_{\text{side}} = F_{\text{side}}(\bar{c}_{1/4}) \tag{8.9}$$

The flat plate approximation used for estimating drag follows from Jiang. H's, et al, research and is shown in Equation 8.10, where δ is the deflection of a flat plate, in this case, the rudder deflection [30]. The torque is then found by multiplying it by the moment arm, which will again be the quarter chord of the rudder.

$$C_D = 2\sin^2(\delta) \tag{8.10}$$

$$D = \bar{q} S C_{D_{rudder}} \tag{8.11}$$

Summing these two torques gives us the resultant torque that the servo must be able to deliver. The servo arm is connected to the rudder via a pushrod linkage. If the pushrod attachment point on the servo arm is positioned closer to the servo's rotation axis than the attachment point on the rudder horn, a mechanical advantage is achieved. This means a smaller torque is needed from the servo to produce the same force at the control surface.

From calculations in Chapter 6, it is determined that the case with the widest rudder deflection occurs under spin recovery conditions. This is a deflection of 29.2°, happening at stall conditions ($30\,\mathrm{m\,s^{-1}}$) and at altitude. Plugging these values into Equation 8.8 and Equation 8.9 allows the total torque required to be calculated. This is equal to 27.6 kg cm. Assuming that a mechanical advantage is gained by having a horn twice as large on the control surface means that only half this value is required. A margin of two will be taken to account for gust loads that might hit during this maneuver, bringing the total required torque back to 27.6 kg cm. The S9177SV Futaba servo is chosen due to its high torque capabilities and low weight.

The same code is run, but now with respect to ailerons, elevators, and flaps. The maximum deflection on the ailerons will happen at cruise speeds and altitude. This increased speed and area cause the torque to be much greater than for the rudder, almost double. Due to this, two servos will be placed per aileron. The flaps will only be active at take-off and landing, leading to a decrease in dynamic pressure drag, which leads to a decrease in the torque required. It was determined that one servo will be sufficient for this purpose.

The elevator will be the most critical control surface since it has to work during cruise conditions and is larger in size than the other surfaces due to it being the whole horizontal stabilizer. The calculation with the hinge line at the leading edge provided values that were an order of magnitude larger than the available servos. So the hinge line of the stabilizer will be located at 0.3 the chord of said surface. At this location, only two servos are required. This brings the total count of servos to 10 for the control surfaces.

An additional servo is required for firing the gun; this is just a trigger mechanism that requires a very low-torque servo. This will not be sized for.

8.3. Design Description

In this section, the hardware components used for the avionics are explained. The flight control unit is outlined in Subsection 8.3.1. On board processing in Subsection 8.3.2. Direct ground-to-vehicle communications in Subsection 8.3.3. IFF in Subsection 8.3.4. Satellite communication in Subsection 8.3.5. Motors in Subsection 8.3.6. Their inter connectivity are shown in Subsection 8.3.7.

8.3.1. Flight Control Unit (FCU)

The Flight Control Unit (FCU) selected for the interceptor drone is the Pixhawk Cube Orange+ [11], chosen for its reliability, low power consumption, and compatibility with other systems, allowing for easy integration. The Pixhawk Orange also has built-in IMU (3 for redundancy).

The FCU is responsible for receiving data from various onboard sensors, including its own built-in sensors, and then execute the flight commands specified. It directly commands the servos connected to the control surfaces and the throttle output of the engine. The FCU also accepts a dual GPS input for extra redundancy.

The Pixhawk Cube Orange+ receives a primary power input of 5.6 V at 2.5 A from the dedicated Pixhawk power module, resulting in a nominal power draw of approximately 14 W. As this is a mission-critical subsystem, an additional redundant power line is routed from the onboard generator, ensuring constant operation even in the event of battery failure.

8.3.2. Onboard Processing

The onboard processing unit selected for the interceptor drone is the NVIDIA Jetson Xavier NX, which serves as the core for real-time target detection. It processes incoming video streams using trained neural networks, enabling autonomous engagement decisions and intelligent tracking.

8.3.3. Direct Ground-to-Vehicle Communication

Following the design process described in Subsection 8.2.1, the design of the antenna is determined.

From Table 8.5 and Table 8.6 it can be determined that the best types of antennas for the mission are the quarter-wavelength antenna and the half-wavelength discone antenna.

From Table 8.1 one can obtain the main dimensions. Since the CEDI drone shall be able to communicate with the ground station using both UHF and high VHF bands, the quarter-wavelength whip antenna requires a length of at least 0.69 m, and the discone a diameter of at least 0.44 m. It should be noted that even although the length of the discone antenna is lower than the one of the whip antenna, its shape makes it inherently bulky and difficult to integrate into the compact structure of a UAV. In contrast, a quarter-ship antenna occupies significantly less volume, making it a more practical and space-efficient choice. Therefore, the quarter-wavelength whip antenna is selected for the design.

Using the quarter-wavelength whip antenna gain, given in Table 8.1, the uplink and downlink budgets can be determined. These are given in Figure 8.1.

---

[11] URL `https://docs.px4.io/main/en/flight_controller/cubepilot_cube_orange.html`. [Cited 17 June 2025]

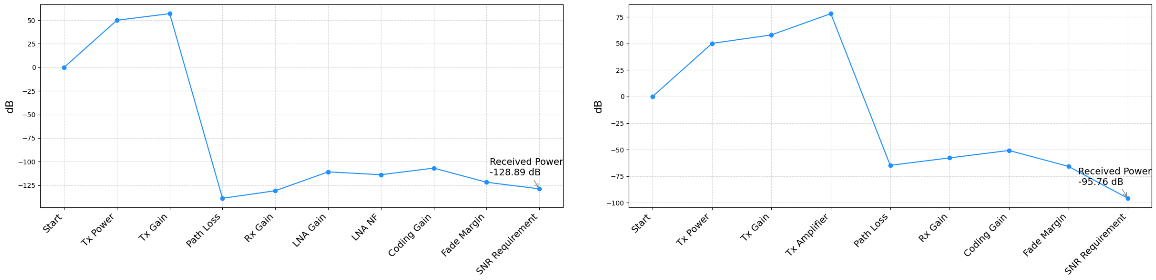

(a) *Uplink budget* **(b)** *Downlink budget at SNR of 30*

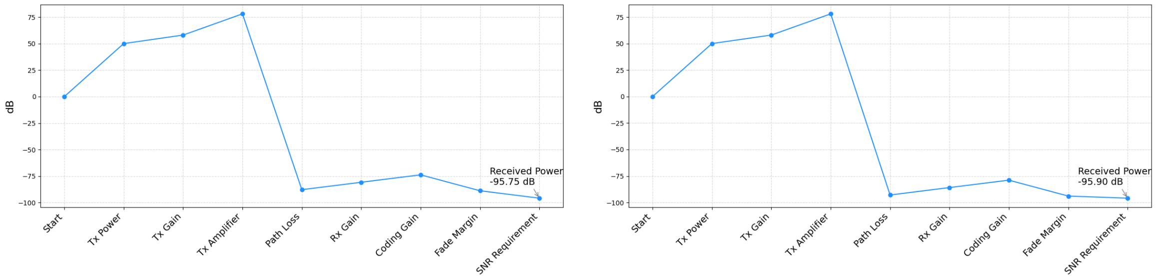

(c) *Downlink budget at SNR of 7* **(d)** *Downlink budget at SNR of 2*

Figure 8.1: *Link budgets for direct communication between ground system and vehicle*

8.3.4. Identification Friend or Foe (IFF)

IFF is standard in defense to avoid accidental engagement by friendly systems. Since the system developed consists of multiple defense drones, which should operate autonomously, friendly fire could be a risk that this component can mitigate. The IFF module selected is the uAvionix RT-2087/ZPX-1. This system weighs only 91 grams and has relatively low power usage, with a peak power of 6 W.

8.3.5. Satellite Communication

The selection of the Starlink Mini terminal provides a pragmatic solution that exceeds performance requirements while maintaining compatibility with aircraft size, weight, and power constraints. This COTS approach enables rapid deployment while providing proven reliability for the critical backup communication function. The decision validates the importance of considering commercial solutions alongside custom developments, particularly for subsystems where sizing constraints and the delivery time of the system are critical for the design.

Table 8.10: *Characteristics of the Starlink Mini*

Characteristic	Value
Size	289.5×259 mm
Weight Estimate	1.10 kg
Avg. Power Consumption	25–40 W
Input Rating	12–48 V, 60 W[12]

URL https://www.starlink.com/ [Cited 17 June 2025]

8.3.6. Motors

There are a number of systems that require motors to function, namely: rudders, ailerons, elevators, gun trigger, gun aiming mechanism, landing gears' retracting mechanism, and hatches that allow the landing gear to lower. A variety of motors will be used for this: stepper motors, servo motors and linear actuators. A brief description of what kind of motors will be used for the different subsystems is given in Table 8.11:

Table 8.11: *Motor selection for various mechanical subsystems*

Part	Motor Type	Reason
Rudder	Servo Motor	Requires precise angle control and real-time feedback
Aileron	Servo Motor	Continuous position adjustment during flight
Elevator	Servo Motor	Requires precise angle control and real-time feedback
Gun Trigger	Servo Motor	Quick actuation with position control
Gun Aiming Mechanism	Stepper Motor	Accurate, repeatable positioning over defined range. Low speed, high torque
Landing Gear Retraction	Linear Actuator	Linear motion with strong force and reliability

8.3.7. Electrical Integration

The inter connectivity between all the hardware components can be observed in Figure 8.2. They have been grouped by detection, communication, servos and motors and have been linked to the processing chip and the flight computer.

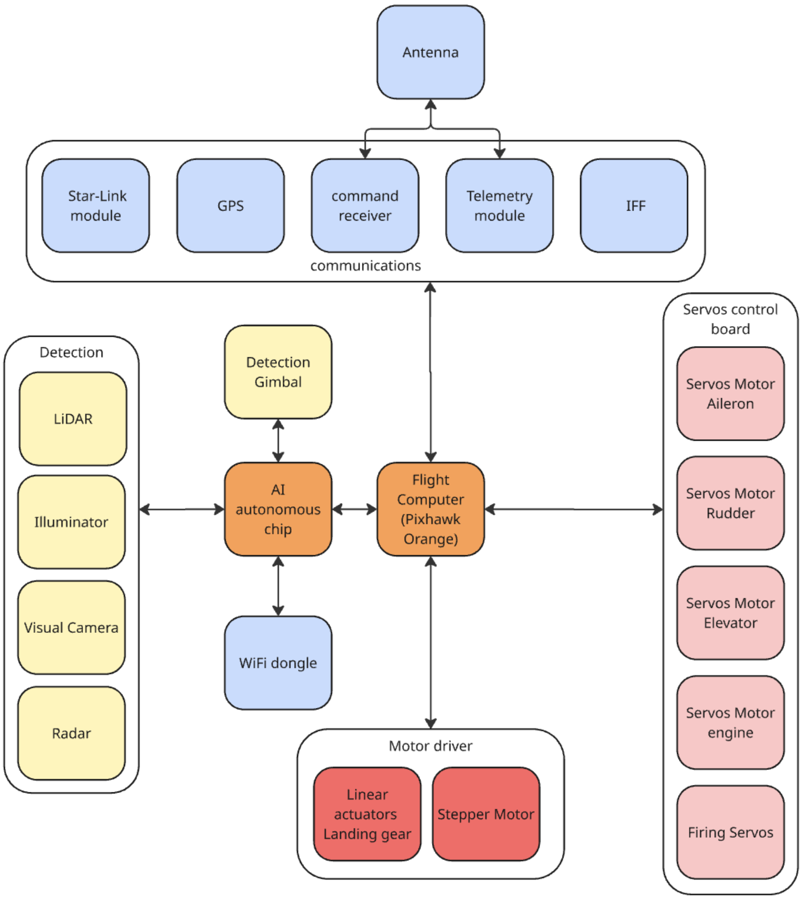

Figure 8.2: *Electrical block diagram showing the interconnections between the different components.*

8.4. Verification

The verification of the avionics design was carried out by assessing compliance with the requirements defined in Section 8.1. As the aircraft has not yet been manufactured and the design process is still ongoing, all requirements were verified through analytical methods. Due to the still ongoing design processes, some requirements could not yet been verified and have been left TBD. The results are shown in Table 8.12.

Table 8.12: *Requirements compliance for avionics*

Requirement Code	Condition	Result	Met?	How?
SYS-01.06.18	Dynamic and static obstacle detection and recognition	-	TBD	-
SYS-01.14.47	Receives GNSS signal	NA	Yes	Subsection 8.3.5
SYS-01.14.48	Follows pre-specified points (precision TBD)	-	TBD	-
SYS-01.14.49	Follows pre-specified points (accuracy TBD)	-	TBD	-
SYS-01.14.50	Loiter around pre-specified point	-	TBD	-
SYS-01.14.51	Inertial return on GNSS loss (reliability TBD)	-	TBD	-
SYS-01.16.61	Avoid static obstacles (reliability TBD)	-	TBD	-
SYS-01.16.62	Avoid dynamic obstacles (reliability TBD)	-	TBD	-
SYS-01.16.63	Track engaged target (reliability TBD)	-	TBD	-
SYS-01.16.64	Follow engaged target (reliability TBD)	-	TBD	-
SYS-01.16.65	Search pattern on target loss	NA	Yes	Subsection 8.3.5
SYS-01.16.66	Return to last communication point	NA	Yes	Subsection 8.3.2
SYS-01.21.9	Communicate over ≥ 230 km range	NA	Yes	Subsection 8.3.5
SYS-01.21.99	Communicate with bitrate ≥ 600 bps	0.5Mpa	Yes	Table 8.7
SYS-01.21.101	Communicate with error ≤ TBD%	-	TBD	-
SYS-01.21.103	Navigation in all conditions	NA	Yes	Subsection 8.3.5
SYS-01.21.104	Redundant navigation system	Dual setup	Yes	Subsection 8.3.1
SYS-01.21.105	Redundant communication system	Dual setup	Yes	Section 8.3
SYS-15.21.107	Comply with NATO STANAG 4586	NA	Yes	Subsection 8.2.1
SYS-01.21.111	Return to launch on comms loss (reliability TBD)	-	TBD	-

9

Detection Design

In this chapter the detection subsystem will be designed and discussed. The chapter starts with a list of the relevant requirements in Section 9.1. The design process is then discussed in Section 9.2 after which the final detection system is discussed in Section 9.3. The compliance with the requirements listed at the start of the chapter is then proved in Section 9.4.

9.1. Requirements

The following requirements for the detection subsystem have been formulated in the baseline report [7]:

- **SYS-01.06.17**: The airborne part of the system shall be capable of target detection and recognition from all directions with sufficient time to engage them, with a reliability of at least 95% in all operational environmental conditions.
    - **SUB-01.06.17.01**: The on-board detection subsystem shall be able to distinguish between targets and friendlies within the range specified in SUB-01.17.03.
    - **SUB-01.06.17.02**: The on-board detection subsystem shall have a FOV sufficient to identify the target in a single pass of the uncertainty volume of the ground-based radar.
    - **SUB-01.06.17.03**: The on-board detection subsystem shall be able to locate a target at a distance of 500 m.
    - **SUB-01.06.17.04**: The on-board detection subsystem shall be able to determine the relative speed of the target with respect to the detection subsystem within the range specified in SUB-01.17.03.
    - **SUB-01.06.17.05**: The on-board detection subsystem shall be able to detect the target under day and night conditions within the range specified in SUB-01.17.03.
    - **SUB-01.06.17.06**: The on-board detection subsystem shall have a refresh rate of 3 s^{-1}
    - **SUB-01.06.17.07**: The on-board detection subsystem shall be able to distinguish between 5 separate targets within the FOV specified in SUB-01.17.02 and within the range specified in SUB-01.17.03.
    - **SUB-01.06.17.08**: The on-board detection subsystem shall be able to detect the target under all weather conditions within the range specified in SUB-01.17.03
    - **SUB-01.06.17.09**: The on-board detection subsystem shall be able to provide the armament subsystem with target locations with 95 % accuracy .
    - **SUB-01.17.10** The on-board detection subsystem shall be able to identify if a target is destroyed.
    - **SUB-01.17.11** The on-board detection subsystem shall provide video to the on-board communication system.
- **SYS-01.06.18:** The airborne part of the system shall be capable of dynamic and static obstacle detection and recognition with sufficient time to avoid them at a reliability of 95% in all operational environmental conditions.

9.2. Design Process

The first step in eliminating a target is determining its location. Luckily, existing ground-based radar infrastructure can be used for battlefield management and guiding CEDI drones towards their targets. The accuracy of these radar systems at range is not sufficient to provide a firing solution; therefore, an onboard detection system must provide this capability. First, the onboard detection system must detect the targets, after which it should guide the CEDI drone towards it. At firing range, the onboard system must provide a firing solution. In addition to autonomous detection and targeting, the onboard detection system must provide a human operator with visuals to manually steer the CEDI drone and take out targets, as described by SUB-01.17.11.

The onboard detection system will be designed by first looking at the existing capabilities of ground-based radar infrastructure. Following the existing capabilities, the requirements for the onboard detection system can be completed. Different options to satisfy these requirements can then be explored, after which (a combination of) the best will be selected based of a trade-off.

9.2.1. Existing Ground-based Radar Infrastructure

Nations' radar capabilities are a closely guarded secret, which means that an estimate needs to be made to find the range at which the onboard detection system needs to take over. This estimate will be very conservative, such that it is certain that the onboard system can guide the CEDI drone towards its target. The range at which the onboard detection system needs to take over is determined by the uncertainty of the ground-based radar. The radar will 'ping' a target, which is the detected location of the target. This ping will have a certain uncertainty in range, elevation (vertical angle), and azimuth (horizontal angle). These uncertainties carve out a volume in which the target is present; therefore, the onboard system needs to find a target in this uncertainty volume. This uncertainty volume is a function of the range to the radar system, the radar system used, and the amount of radar systems that the target is in range of.

To conservatively estimate the uncertainty of ground-based infrastructure, a Python program was written. The radar systems of The Netherlands were analyzed. Mobile radar systems, like NATO Airborne Warning And Control System (AWACS) aircraft or navy vessels exist. However,their availability during wartime or a surprise attack is not always guaranteed, which means that a baseline radar system that is always available needs to be selected. The Thales GM200 MM/C radar is considered. The Netherlands currently has 16 in its inventory, with an option for another 2[1]. To detect airborne targets, it has a 400 km range[2], meaning that 16 units can easily cover an area the size of The Netherlands. Since this radar is primarily designed to detect larger targets like fighter jets or bombers, a conservative range of 250 km will be taken for detection of kamikaze UAVs like the Shahed-136. The radars will be assumed to be located at the airbases used for launching the CEDI drones, as described in Chapter 13. The accuracy for the GM200 MM/C is unfortunately not published. However, its bigger brother, the GM400, which uses the same radar type, has a reported accuracy of ±0.3° in elevation and azimuth and 50 m in range[3], so this accuracy will be taken. These accuracies represent the range in uncertainty of the reported value with respect to the true value and indicate the interval in which the true value lies with a stated probability. The recommended probability is 95%, which corresponds to two standard deviations of the mean for a normal (gaussian) distribution[4]. As the probability is not stated together with the accuracy specification, the 95% probability will be taken. The GM200 radar (previous generation) has a rotation speed of 3 s,

---

[1] URL https://connect.thalesgroup.com/nl/news/seven-additional-gm200-mm-c-radars-for-the-royal-netherlands-army [Cited 6 June 2025]

[2] URL https://www.thalesgroup.com/en/markets/defence-and-security/air-forces/ground-master-200-mmc [Cited 6 June 2025]

[3] URL https://www.radartutorial.eu/19.kartei/02.surv/karte016.en.html [Cited 6 June 2025]

[4] URL https://www.radartutorial.eu/01.basics/Radars%20Accuracy.en.html [Cited 6 June 2025]

meaning that a target is pinged at least every 3 seconds[5]. The GM200 MM/C is expected to improve upon this since it can generate multiple radar beams; however, 3 s will be used since the program is conservative.

The aim of the program is to reduce the overall uncertainty of the detected path points by combining the multiple radar measurements (of one point) and adding information from previous measurements. A flow chart of the program can be seen in Figure 9.1.

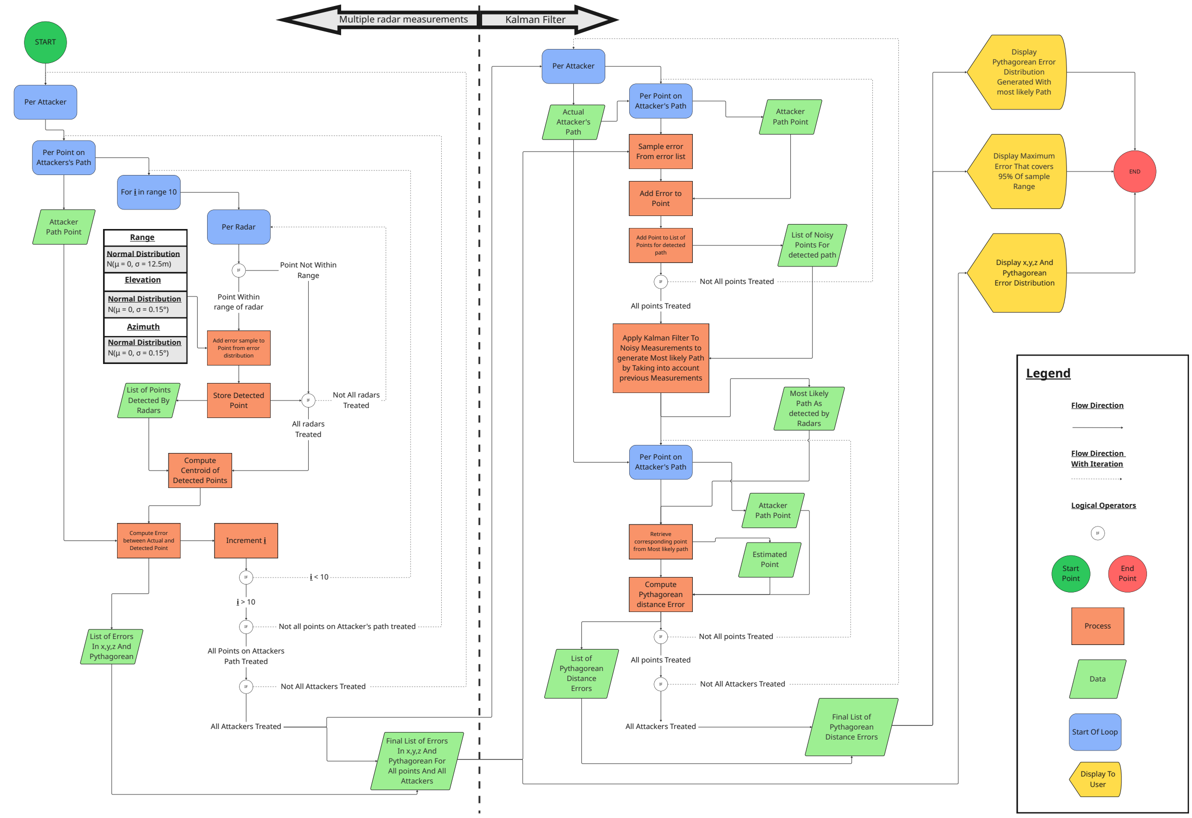

Figure 9.1: *Flow chart for radar error reduction program*

The program takes a statistical approach by considering all attackers and their corresponding paths. The third inner loop on the 'multiple radar measurements' side of the dashed line (blue box with 'For i in range 10') of the flow chart finds for one point on the attacker's path the error in x, y, z when multiple radar measurements are combined. The 'ping' for one radar is simulated by taking the actual attacker's path point and sampling an uncertainty from a 2 standard deviation normal (Gaussian) distribution which is appropriate for modeling the uncertainty as mentioned above. The exact distribution for each dimension can be seen in Figure 9.1. When all the 'pings' have been generated, the most likely actual point as detected by the radars is found. The maximum likelihood estimator of the true position as detected by the radars is the least squares solution of the detected points[6]. The global minimum of the least squares solution is given by the centroid[7]. This most likely actual point as detected by the radars is then compared to the actual path point to generate the errors in x, y, z. This process is repeated 10 times for each attackers path point and then for all points and all attackers to generate a statistical distribution of measurements errors.

---

[5] URL `https://www.thalesgroup.com/en/markets/defence-and-security/air-forces/airspace-protection/mid-range-radars/ground-master-200` [Cited 6 June 2025]

[6] URL `https://fmin.xyz/docs/applications/MLE.html` [Cited 16 June 2025]

[7] URL `https://math.stackexchange.com/questions/3019429/point-x-in-mathbbrn-that-minimizes-sum-of-distance-squares-sum-mathca` [Cited 16 June 2025]

This distribution can be seen in Figure 9.2.

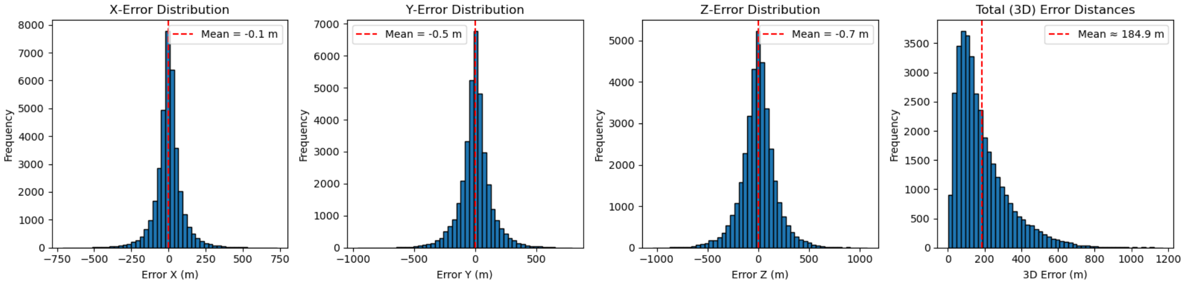

Figure 9.2: *Error distributions in x,y,z and Pythagorean from GM200 MM/C radar pings*

These errors can be further reduced when predicting the actual path as observed by the radars by considering previous measurements. This is done on the 'Kalman filter' side of Figure 9.1, per attacker the erroneous path as detected by the radar is created by sampling the error in x, y, z from the distributions created on the left side of Figure 9.1. Then, once the full erroneous path is created, a Kalman filter is applied to generate a better estimate. The Kalman filter is widely used in signal processing for smoothing out erroneous measurements by considering only previous measurements[8]. It is appropriate to use such a filter here, as it only considers previous measurements, and in the real world the radar's would only have access to these. The optimality of the Kalman filter in this application is difficult to quantify and beyond the scope of this discussion; the only purpose is to generate a better estimate by considering previous measurements. When the better estimate has been generated, each estimated point is compared to the corresponding actual point and the Pythagorean distance is calculated. This is done for all attackers, and the resulting distribution of the distance errors can be seen in Figure 9.3.

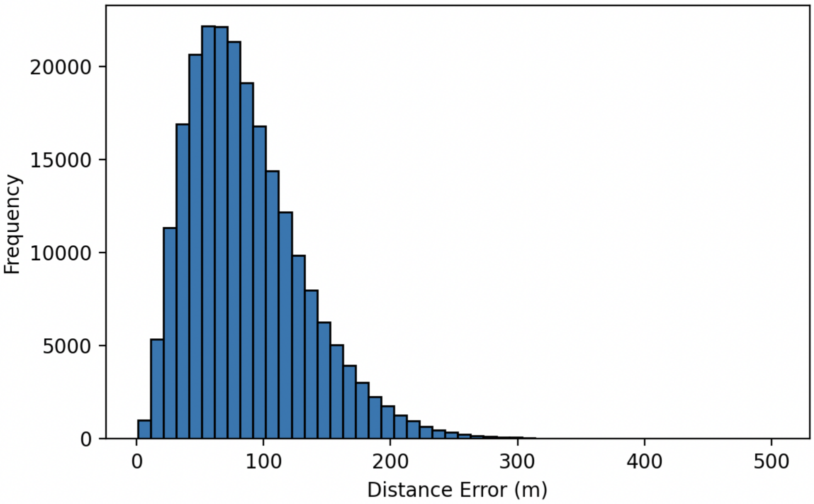

Figure 9.3: *Pythagorean error distribution from GM200 MM/C radar pings*

According to Figure 9.3, most targets will be accurate within 200 m, with all targets detected within 320 m. Correspondence with the head of command and control of the Royal Netherlands Air Force concluded that this is a very conservative estimate, with them estimating the capability at

---

[8] URL https://web.mit.edu/kirtley/kirtley/binlustuff/literature/control/Kalman%20filter.pdf [Cited 16 June 2025]

100 m error[9]. However the detection suite will be designed such that it can detect drones at a range of 500 m as a contingency. The range of SUB-01.06.17.03 was left TBD in the midterm, but can now be filled in to be 500 m.

9.2.2. Design Options

The following have been identified as design options for the detection suite. These forms of drone detection are later also found to be outlined in a literature study to the state-of-art of drone detection[31].

- **Optical Detection**: Passive method that looks for light signals, either visible light or on the infrared spectrum. Detection is done using optical features[10] or machine learning[32].
- **Radio Frequency Detection**: Passive method that listens for radio signals emitted by target drones. Localization is done using direction finding algorithms[33].
- **Acoustic Detection**: Passive method that listens for sound waves mainly generated by the propeller of the targets. Using beamforming[34] or triangulation[35] the direction of the target may be found.
- **Radar Detection**: Can be both passive or active. Active radars send their own signal, while passive radars use an external ’illuminator’ to illuminate the target. Both active and passive radars then look for the signal which reflects off the target.
- **LiDAR Detection**: Active method that works in a similar way to an active radar, however now with laser light. It emits laser pulses and measures the return time of a pulse. A cloud of points is created that accurately depicts the environment up to the reported range of the sensor.

9.2.3. Trade-off

The performance of each design option depends strongly on the chosen hardware. In addition to that, multiple design options are required to fulfill the requirements outlined in Section 9.1 as will be concluded later. Therefore, this trade-off will be done qualitatively to identify strengths and weaknesses of each option instead of assessing performance of hardware. This approach allows for adapting and layering of multiple design options. The criteria considered for the trade-off are Technology Readiness Level(TRL), price, detection range, accuracy, and robustness. TRL will be assessed using the definition set by the European Comission[11]. Price will be measured in the Euro currency and will only be concerned with the specific hardware required for each option. Integration of the hardware and labor are not considered here, but will be factored in for the final reported price of the total system.

Optical Detection

Optical detection and tracking of drones is a well researched subject, both using ground-based cameras[36] [37] and airborne[38]. Machine learning models offer the best performance; specifically, the YOLOv8 (You only Look Once version 8) model offers ground breaking performance[38] [3]. Its small network size allows running the model on mobile CPU-only devices, meaning the autonomous chip discussed in Chapter 8 is more then capable of handling the model. Since it is only proven in experiments, it is assigned a TRL level of 5.

The resolution of the images used to train the model is 1920x1080 pixels[38], therefore a camera of at least that resolution is required. To mitigate the limitations of the field of view of cameras and to add stabilization to increase accuracy and to aid in peace time operations, the camera could be placed on a 3 axis gimbal. Systems with sufficient resolution and on a stabilized gimbal like Siyi

---

[9] F. van Heck, personal correspondence, 11 June 2025

[10] A. Altena, personal correspondence, 23 May 2025

[11] URL `https://euraxess.ec.europa.eu/career-development/researchers/manual-scientific-entrepreneurship/major-steps/trl` [Cited 12 June 2025]

ZR10[12] and SkyDroid C12[13] which are specifically designed for airborne platforms cost around 500 Euro.

The accuracy achieved by an improved YOLOv8 model, as reported by Zhai et al [3], is 95% mean average precision (mAP). This model works by predicting a bounding box in which it thinks a drone is present. It also assigns a certainty score, meaning how certain the model is that the drone is contained within the bounding box. A limitation of the model is that it is trained on a dataset where there is always a drone present in the frame, meaning that it will always predict a bounding box even if no drone is present (although it will have a low certainty score). This limitation needs to be taken into account if this model is selected. In the context of detections, 95% mAP means that 95% of the predicted bounding boxes where correct, where a bounding box is correct if the intersection over union (IoU) is higher then 0.5. An IoU of 0.5 means that at least 50% of the bounding box intersects with the ground truth bounding box. Although this may seem a very low standard for classifying something as correct, the dataset used for this model is a set of images of drones at around 500 m away. The drones therefore occupy mostly around 1% of the image, with some others between 1 and 5% and outliers occupying between 5 and 10%. In Figure 9.4, taken from Zhai et al[39], some of the dataset images are plotted with the predicted bounding box and the certainty of the model. Due to the crucifix nature of drones, there is also a limit on the highest achievable IoU by a rectangular bounding box. Targets like the Shahed-136 are triangular, and therefore it is expected that 95% mAP can be achieved at a higher IoU. Although mAP cannot be directly translated to a distance accuracy, targeting a drone by shooting at the center of the bounding box is deemed excellent since in 95% of the cases at least 50% of the target is present within the bounding box. This means that the center of the bounding box will almost certainly coincide with the target.

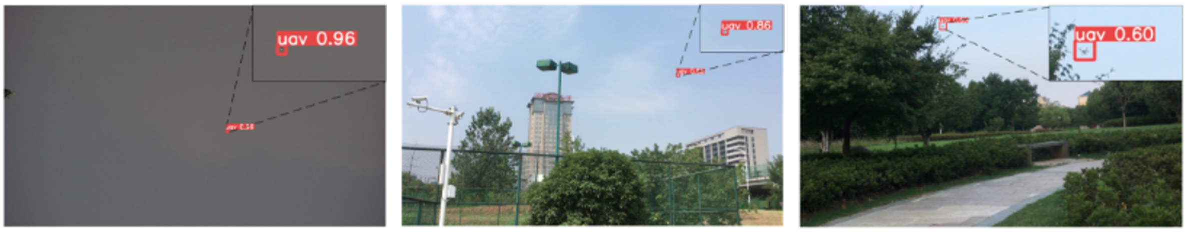

Figure 9.4: *Predicted bounding boxes at very long range, from Zhai et al[3]*

The range at which optical detection is able to detect a drone is highly dependent on weather and light conditions, as well as the angle at which the CEDI drone intercepts the target and needs to be determined by experiments. The theoretical upper limit can however be calculated. The YOLOv8 model has demonstrated its effectiveness at detecting drones when around 1% of the total pixels are a drone. The SkyDroid C12 camera is used as a reference camera with 2560 × 1440 resolution and 100 by 52 degrees FoV[14] and the Shahed-136 is used as a reference target. Assuming that the CEDI drone flies in the combat approach determined in Chapter 7, the target is 32° below the CEDI at a range of 86 m. The effective dimensions of the target are then 1.85 m in length and 2.5 m in width as reported in Chapter 7. The smallest dimension, 1.85 m in this case, should be taken up by the smallest amount of available pixels. The pixels required to be a target to be effectively classified as target is:

$$\text{pixels}_{\text{required}} = p_{\text{target}} \cdot \text{pixels}_{\text{available}} = 0.01 \cdot 1440 = 14.4 \tag{9.1}$$

Therefore at least 15 pixels should be a target for the YOLOv8 model to recognize it as a target.

---

[12] URL https://shop.siyi.biz/products/siyi-zr10-gimbal-camera [Cited 18 June 2025]
[13] URL https://www.worldronemarket.com/product/skydroid-c12/ [Cited 18 June 2025]
[14] URL https://www.worldronemarket.com/skydroid-c12-user-manual/ [Cited 18-June-2025]

The length each pixel should cover is then:

$$l_{\text{pixel}} = \frac{l_{\text{shahed}}}{\text{pixels}_{\text{required}}} = \frac{1.85}{15} = 0.123 \text{ [m]} \tag{9.2}$$

The smallest amount of pixels of the camera is in the vertical direction. The vertical field of view of the camera is 52°, the maximum range at which 0.123 m per pixel is achieved is then calculated by constructing a simple triangle where the horizontal leg is the range, the vertical leg the vertical distance, and the angle between the horizontal leg and the hypotenuse half the field of view angle. The vertical distance should be smaller than the amount of pixels available multiplied by the distance per pixel. Using geometric identities:

$$R \leq \frac{l_{\text{pixel}} \cdot \frac{\text{pixels}_{\text{vertical}}}{2}}{\tan(\frac{\kappa}{2})} = \frac{0.123 \cdot \frac{1440}{2}}{\tan(26)} = 181.6 \text{ [m]} \tag{9.3}$$

Therefore, the theoretical limit at which the reference camera can detect the reference target during combat approach is around 180 m. A zoom lens can be integrated to increase this range. The robustness of the system is deemed insufficient, since it is heavily influenced by weather and light conditions. Although mitigation methods exist, the robustness is still quite limiting for this design option.

Radio Frequency (RF)

Radio frequency works by listening for transmitted radio signals across different frequencies by the target drones. It has the advantage that it can be done using the existing antennas on the CEDI drone, therefore requiring no extra parts. The identified targets for the CEDI drone almost never transmit radio signals since they fly autonomously; therefore, this design method can already be disregarded.

Acoustic Detection

Acoustic detection of drones is a cheap and simple way of detecting drones, and is combat proven in the Russo-Ukrainian war[15]. The use of acoustics to detect drones has extensively been researched, meaning the basic principles are well known. At the time of writing, this method has only been used on a stationary platform, therefore the method needs to be adapted to function on an airborne platform. Personal correspondence with Anique Altena, researcher on acoustic detection of drones at the faculty of Aerospace Engineering of TU Delft, concluded that the main challenges of implementing acoustic detection on an airborne platform are the mitigation of wind noise and limiting the ego noise coming from mainly the propulsion system. Effective wind mitigation filters[39] exist and the array can be mounted on a boom in front of the CEDI drone to mitigate ego noise; however, the effect of these mitigation methods needs to be assessed and therefore acoustic detection will be assigned a TRL level of 1. Since this is an educational project, this is not marked as unacceptable.

Triangulation is one method of localizing a sound source. It works by placing at least four microphones out-of-plane with respect to each other and then measuring the time difference of arrival of a sound source. To implement acoustic triangulation, microphones need to be spaced in the order of meters apart, due to the speed of sound. A logical location would therefore be to place two microphones at both wing tips, and one other microphone out of plane; however, microphones can not be placed at the wing tips due to wing tip vortices and vibrations inducing to much noise into the system[16]. Therefore, multiple booms would be required to space the microphones. Considering these inefficiencies of implementing triangulation on an airborne of CEDI drone size is not feasible. Therefore, beamforming will be investigated.

---

[15] URL https://www.forbes.com/sites/sebastienroblin/2020/06/29/can-pocket-sized-radars-protect-us-from-drones-and-drone-collisions/ [Cited 12 June 2025]

[16] A. Altena, personal correspondence, 23 May 2025

Beamforming works by having multiple microphones on the same plane. This means that two of these arrays out of plane are necessary to pinpoint a target. A sound signal will hit the microphones at different times, meaning there is a phase difference between the signals measured by different microphones. By calculating the phase shift required to align the signals, the angle of the sound source with respect to the plane of the two microphones can be calculated. By doing this, for multiple pairs of microphones the source of a sound signal can be localized. Beamforming requires a significantly smaller microphone array. Microphone arrays like the ReSpeaker Mic Array v2.0 are used for the detection of drones using beamforming[34]. Arrays like the aforementioned are widely available and cost around 100 Euro. The detection range for beamforming methods on smaller FPV drones is between 100 m[34] and 450 m[4] (when using a slightly larger array). The accuracy is reported to be around 10°[34]. This corresponds to a distance error of around 15 m at the firing position described in Chapter 7.

The robustness of the system is unacceptable, since the system is not able to effectively track a drone when another sound source is present, as can been seen in Figure 9.5. The green line indicates the measured position of a drone, while the blue line represents the ground truth. When able to track, the accuracy is enough to guide the CEDI drone towards a target, but the track is deemed too unstable for the CEDI application. This can be seen in the graph in the timestamp around 400 seconds. There the acoustic tracking(green line) is very spotty. In the figure, a helicopter is present as a noise source, but in the CEDI scenario this can be another target drone which emits noise around the same frequency and intensity which is expected to make the track even less stable.

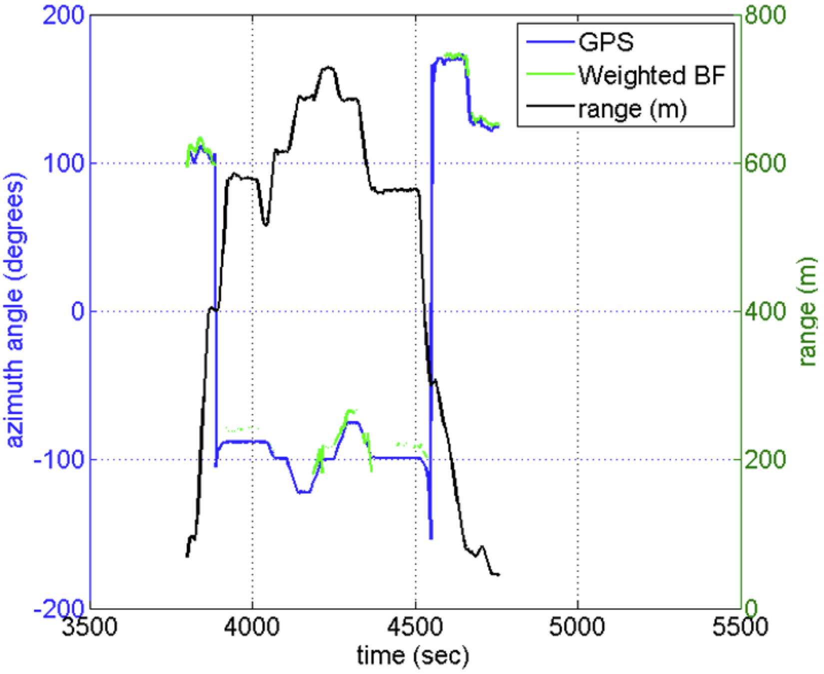

Figure 9.5: *Acoustic tracking in presence of another source. Figure and result from Benyamin et al(fig. 19 p.16)[4]*

Radar

Radar detection is very robust and offers the most range of all the design options. Radars work by emitting signals, which reflect of objects. The reflected signal is then measured by the same radar unit, making it an active method of drone detection. A lot of different types of radar exist, with each type having a different use case. Radar is widely implemented on airborne platforms like drones for obstacle avoidance, but also on larger commercial airframes for drone detection. Off-the-shelf solutions, like the echodyne echoflight[17], which fit the purpose of the CEDI drone, exists; therefore, it is assigned a TRL of 9.

The price of radar systems specifically for the tracking of other airborne vehicles is not available to the general public, since the typical customer for these type of systems is generally militaries or research institutes. However, the previously mentioned Echodyne Echoflight is reported by the institute of navigation to be $20,000[40], which converts to 17,400 Euro in June of 2025. The range for this radar for detecting large multi rotor aircraft is advertised to be 1.2 km. Since the typical targets of the CEDI drones are larger then these multi rotor aircraft and they don't utilize stealth technology, the range is expected to be better then 1.2 km but worse then the reported detection range for a human person(2 km. The accuracy is reported to be <1° in azimuth and <1.5° in elevation. This translates to about a 2.3 m accuracy at combat approach.

Possibly, the best part of a radar system is its robustness. While, for example, the optical system is influenced by the time of day and weather conditions, a radar always works if deployed properly. Heavy rain has some small performance penalty on it, since the signal is blocked by the rain droplets; however, this penalty is way smaller then for the other design options. This is why it is assigned a excellent score.

LiDAR

LiDAR is implemented in a lot of industrial applications, because of its very high accuracy. LiDAR is also already implemented on drone platforms, both for obstacle avoidance and mapping of areas. A tracking algorithm for rotary wing drones also exists, which is outlined by Abir et al[41]. As of 24 June 2025, no studies were found combining the LiDAR tracking of drones on an aerial platform, which is why this design option gets a TRL level of 5.

LiDAR's vary greatly in price, from 50 Euro obstacle avoidance sensors to 15,000 Euro mapping units. The range and power draw also change a lot depending on the intended application and price. Since the target track at which the CEDI drone will shoot should be as accurate as possible, the high accuracy of a LiDAR sensor can be exploited for this purpose. Therefore, the LiDAR options around 50 m to 100 m in range will be investigated. Options in that range cost around 300 Euro, such as the Benewake TFA300[18] and TinkerForge 2144[19]. The Benewake TFA300 was deemed especially interesting since it has a reported range of 300 m in a very small form factor and low power draw. It has a reported accuracy of 1% of the range[20], equating to 0.86 m at combat approach. LiDAR is also very robust, since it is not influenced by lighting conditions. LiDAR is however pretty significantly influenced by rain, since the rain droplets absorb and deflect the radiation. This could lead to a decrease in accuracy or false negatives/false positives in the detection. A study by Goodin et al[42] provides a mathematical model to estimate the effect of rain on the performance of automotive, which resulted in a decrease in range of about 30% at very heavy rain rates and a decrease in accuracy of 2%. The 2% decrease in accuracy decreases the accuracy to 0.88 m which has no significant effect on the performance of the CEDI system. The effect of the decrease in range on the CEDI system needs to be evaluated in future work.

---

[17] URL https://www.echodyne.com/radar-solutions/echoflight/ [Cited 23 June 2025]

[18] URL https://eu.robotshop.com/nl/products/benewake-uav-lidar-tfa300-w-ip67-protective-housing?gad_source=1&gad_campaignid=20156178605&gbraid=0AAAAAD_f_xxVbs1IJSZuDswAssGNUkWzf&gclid=CjwKCAjwmenCBhA4EiwAtVjzmmcN7kaawP94N9_9zCJAmj4zjEfKHx-1YyGLYM0tQtaxyM4v6htpBhoC5yQQAvD_BwE [Cited 24 June 2025]

[19] URL https://www.bol.com/nl/nl/p/tinkerforge-2144-laser-afstandsmeter-geschikt-voor-tinkerforge-1-stuk/9300000167221961/?Referrer=ADVNLGOO002027-S--9300000167221961-PMAX-C-22288392453&gad_source=1&gad_campaignid=22288424136&gbraid=0AAAAAD5OnmMH7vQF-Ba4QgrVZReNBtcCI&gclid=CjwKCAjwmenCBhA4EiwAtVjzmlgIqMc6SdPEdV3JYSRJlfoLC04z0tsSH8oKzMeQ_TukQg1tWnPNBRoCJUAQAvD_BwE [Cited 24 June 2025]

[20] URL https://en.benewake.com/TFA300/index.html [Cited 24 June 2025]

Trade-off

Now that all design options have been scored on the criteria, the graphical trade-off table can be constructed. The table is provided in Table 9.1. Please not that the accuracy is calculated taking the worst case accuracy in any direction reported by the source. Colors indicate unacceptable (red), bad (yellow), good (green), and excellent (blue).

Table 9.1: *Trade-off table for detection subsystem.*

Criteria	Acoustics	Radar	Optical	LiDAR
TRL [-]	Yellow 1	Blue 9	Green 5	Green 5
Price [EUR]	Blue 100	Yellow 8,700-17,400	Green 500	Green 300
Maximum range [m]	Yellow 100-450	Blue 1,200-2,000	Yellow 180	Yellow 300
Accuracy [-]	Yellow 8 m at combat approach	Green 2.3 m at combat approach	Blue 95% mAP	Blue 0.86 m at combat approach)
Robustness [-]	Red Unstable tracking when other noise sources are present	Blue Barely influenced by weather etc	Yellow Influenced by weather and light conditions	Green Gets slightly less accurate in rain

9.3. Design Description

From Table 9.1 it can be concluded that there is no clear winner. Therefore multiple design options are needed to accomplish the requirements outlined in Section 9.1. Therefore a suite of sensors is implemented. Radar will be used to close the distance between the 500 m error in ground-based radar pings and the target location. A radar was chosen since only radar and acoustics have the required range, but the radar is more reliable, accurate and has a higher TRL. However as concluded in Section 9.2 the accuracy of the radar is in the order of 2.3 m, which is not enough to shoot at the targets. Therefore a LiDAR sensor is integrated, which is used for the final stage targeting. As proved in Chapter 7, the accuracy is enough to fulfill the requirements. LiDAR is cheap, accurate and sufficiently developed such that no major research is needed to implement it for the CEDI use case. To fulfill SUB-01.17.11 also a visual light camera with thermal camera combination is implemented, complimented by the improved YOLOv8 targeting model outlined by Zhai et al[3].

The concept of sensor fusion is implemented to improve the detection suite. Sensor fusion in this setting means that the target location of multiple sensors are combined to acquire a more accurate and reliable target location. The overlap in range of the selected sensors makes this possible. Not only is this advantageous for the accuracy of the targeting but it also increases the robustness of the system. The robustness is increased since if one sensor fails to acquire a target, other sensors can fill the gap.

9.3.1. Component Selection

The components selected for the detection suite are listed in this subsection.

Radar

The echodyne echoguard[21] radar has been selected as the on-board long-range detection system. Its airborne version, echodyne echoflight[22], is practically the same radar but has 5 W lower power draw and in a smaller form factor. Because of the relatively small size of the echoguard and the available power from the generator, the ground based version is selected since it its reported to be around 8,700 euro[23] instead of 17,400 euro. The echoguard and echoflight radars were the the only radars found that fitted the CEDI mission profile. The radar has a hot standby mode, were it only draws 10 W. The range at which the echoguard can detect small fixed wing aircraft (Bayraktar TB2 used as reference for small fixed wing by manufacturer) is 2 km due to the higher power of the echoguard compared to echoflight. The FoV of the echoguard, 80° elevation and 120° azimuth, is sufficiently large to ensure the guaranteed detection of a target, since at 2 km distance only a FoV angle of 28° is needed to see the 500 m error distance of the ground based radar.

Optical Camera

The skydroid C12 optical camera and thermal imager combo was selected. It comes with a 3 axis stabilized gimbal, reducing the need for extra integration of the camera system with another gimbal. The thermal imager integrated in the camera housing increases the robustness of the system during night time or other low visibility environments. It is widely available and specifically made for airborne platforms. It is both linked to the YOLOv8 algorithm for targeting and the communications system to send video to ground operators.

LiDAR

The Benewake TFA300 LiDAR is selected because of its superior range, price and better connectivity to the avionics via its UART port. No better matching LiDAR was found. The TFA300 is integrated in the 3 axis stabilized gimbal from the skydroid C12. A limitation of this LiDAR is that it is not a scanning radar, meaning that it needs to be pointed at the target. The LiDAR can be used for both obstacle avoidance and targeting.

9.3.2. Targeting Logic

The targeting logic is visualized in Figure 9.6. It is a visualization of the logic behind the detection suite, not the mission profile. The true mission profile is outlined in the operational flow diagram provided in Chapter 13. The numbers P and Q in Figure 9.6 are determined by the Rules of Engagement(ROE) block 5-AV-3 in the operational flow diagram.

---

[21] URL `https://www.echodyne.com/radar-solutions/echoguard/` [Cited 18 June 2025]

[22] URL `https://www.echodyne.com/radar-solutions/echoflight/` [Cited 18 June 2025]

[23] URL `https://www.forbes.com/sites/sebastienroblin/2020/06/29/can-pocket-sized-radars-protect-us-from-drones-and-drone-collisions/` [Cited 24 June 2025]

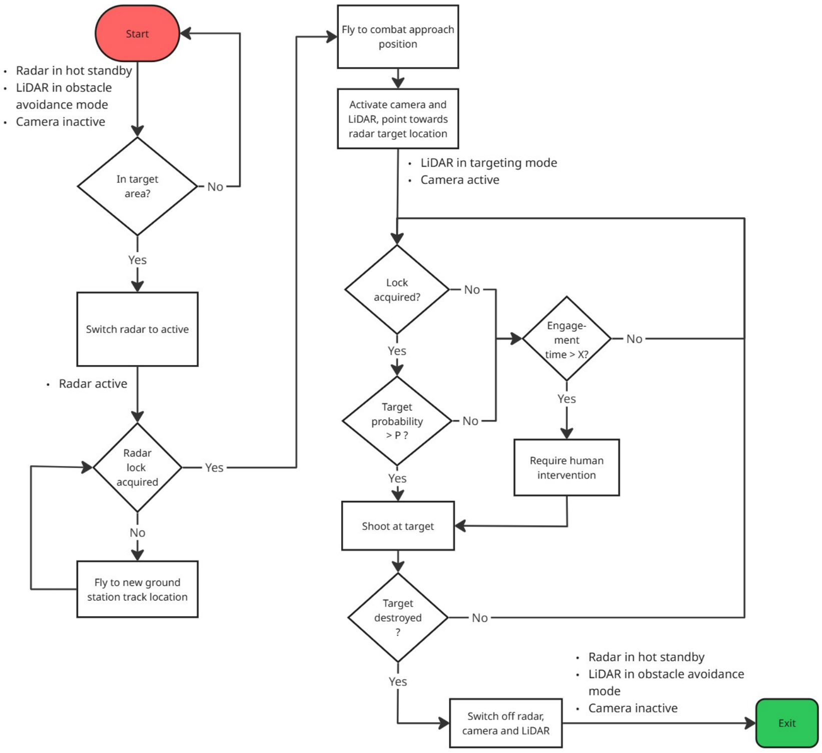

Figure 9.6: *Targeting logic*

9.4. Verification

To determine whether all requirements listed in Section 9.1 have been met, a compliance table can be set up. The table is provided in Table 9.2.

Table 9.2: *Requirements compliance for the detection subsystem*

Requirement Code	Condition	Result	Met?	How?
SUB-01.06.17.01	Perform IFF	NA	Yes	RT-2087/ZPX-1
SUB-01.06.17.02	Detect targets at a sufficient FOV	80°	Yes	Echoguard
SUB-01.06.17.03	Detect targets at 500 m	2000 m	Yes	Echoguard
SUB-01.06.17.04	Get target speed	NA	Yes	Echoguard
SUB-01.06.17.05	Identify target during day and night at 500 m	2000 m	Yes	Echoguard
SUB-01.06.17.06	Refresh rate $\geq 3\ \mathrm{s}^{-1}$	$10\ \mathrm{s}^{-1}$	Yes	Echoguard
SUB-01.06.17.07	Distinguish ≥ 5 targets at 500 m	20 targets	Yes	Echoguard
SUB-01.06.17.08	Detect under all weather conditions at 500 m	2000 m	Yes	Echoguard
SUB-01.06.17.09	Provide target location with 95% accuracy	100%	Yes	TFA300
SUB-01.06.17.10	Identify target elimination	NA	Yes	Skydroid C12
SUB-01.06.17.11	Provide video	NA	Yes	Skydroid C12
SYS-01.06.17	Target drone succesfully	NA	Yes	Sub req's met
SYS-01.06.18	Obstacle detection	NA	Yes	LiDAR

10

Propulsion Design

In this chapter, the propulsion subsystem will be designed and presented. First, the requirements for the cruise conditions are identified in Section 10.1. From these, an engine is selected that complies with the power required in Section 10.2. Afterwards, the propeller is sized and integrated into the design. This final design is thoroughly explained in Section 10.3 Lastly, final verification is carried out in Section 10.4

10.1. Requirements

- **SYS-01.04.08**: The airborne part of the system shall be capable of sustained flight up to an altitude of 5000 m, in ISA conditions.
  - **SUB-01.04.08.01**: The propulsion subsystem shall be able to provide the thrust needed to meet requirements under MIS-01.04 at altitudes up to 5000 m.
- **SYS-01.04.10**: The airborne part of the system shall have a range of no less than 460 km, in ISA conditions, at cruise altitude, at cruise speed.
- **SYS-01.04.11**: The airborne part of the system shall have an endurance of no less than 2 h, in ISA conditions, at cruise altitude, at cruise speed.
- **SYS-01.04.12**: The airborne part of the system shall have a cruise speed, when measured with respect to the ground, of more than 80 $\mathrm{m\,s^{-1}}$, in ISA conditions.
  - **SUB-01.04.12.01**: The propulsion subsystem shall support a continuous cruise speed of over 80 $\mathrm{m\,s^{-1}}$.
- **SYS-01.04.15**: The airborne part of the system shall be controllable, in all operational environmental conditions, at all operational flight levels.
  - **SUB-01.04.15.02**: The thrust setting of the propulsion subsystem shall be controllable.
- **SYS-01.10.34**: The airborne part of the system shall be capable of loitering for at least 2 h, in ISA conditions, at an altitude of no more than 5000 m.
  - **SUB-01.10.34.01**: The propulsion subsystem shall be able to sustain sufficient thrust for a duration of at least 2 h at the specified loitering speed.

10.2. Design Process

In this section, the propulsion design process will be explained and carried out. This includes the engine and the propeller.

10.2.1. Thrust and power needed

The first step in designing the propulsion subsystem is to determine the amount of thrust required to overcome drag at cruise. This is done assuming the thrust should be equal to the drag using Equation 10.1, with a density of $0.736\,\mathrm{kg\,m^{-3}}$ at altitude and a cruise velocity of $80\,\mathrm{m\,s^{-1}}$. The other parameters are iterated from the other subsystems. Since no specific requirements on climb rate or climb speed have been set, the climb profile will follow from the resulting cruise sizing. The power required at altitude is then Equation 10.2 assuming an initial efficiency $\eta = 0.8$. The values are shown in Table 10.1

$$T = D = \frac{1}{2}\rho V^2 S C_D \tag{10.1}$$

$$P = \frac{TV}{\eta} \tag{10.2}$$

Table 10.1: *Required thrust and power at cruise and sea level*

Metric	**Sea-level**	**Altitude** (5000m)
Thrust required	262.95 N	157.99 N
Power required	26.30 kW (35.26 HP)	15.56 kW (21.19 HP)

10.2.2. Engine Selection

Extensive market research was carried out to determine what the ideal engine would be. Turbojets, turboprops, and turbocharged piston engines were ruled out due to not meeting cost and weight requirements. This left piston engines and rotary engines. A distinction is made between two-stroke and four-stroke engines under the piston category.

Two-stroke engines are notoriously poor with regard to the environment; however, they provide a higher power-to-weight ratio, vital for a light UAV. Four-stroke engines are a lot more environmentally friendly at a cost of higher weight.

The two-stroke engine selected for the trade-off is the Limbach L275 EF [1]. Although this engine might not have the highest performance for this class, it is the one with the most widely available data, and it was chosen to sacrifice a bit of performance for a higher accuracy in results.

Finding four-stroke engines at this weight and power class proved to be quite hard. Four-stroke engines are the most common type used for mopeds and motorcycles with higher horsepower, typically around 15 HP and up. These, however, usually weigh too much, around twice as much as the respective two-stroke engine. The manufacturers also do not provide their power, torque, and specific fuel consumption (SFC) graphs. With this limited information, it is almost impossible to choose the correct engine and size a propeller, as the RPM over the whole flight envelope is needed. The chosen four-stroke engine is the paraglider engine EOS Quattro[2], as it is the only one with a high enough power-to-weight ratio.

Wankel engines are known for their compactness and smooth operation due to the low number of reciprocating parts. They have an excellent power-to-weight ratio, outperforming piston engines of similar mass, making them a great option for the CEDI drone. However, they tend to suffer from higher fuel consumption, particularly at high RPMs over extended periods. The Wankel engine selected for this trade-off is the AIE 225CS–40BHP [3], which is widely used in UAVs. Although more niche than conventional engines, it comes with well-documented specifications.

Table 10.2: *Parameter table for the engines*

	Weight [kg]	**Cost [€]**	**Power [HP]**	**Fuel Consumption [Lh^{-1}]**
Limbach L275 EF	7	9,000	25	10
EOS Quattro	17	2,500	30.6	2.8
AIE 225CS-40BHP	22	6,000*	40	[-]**

*Based on Wankel Engines with similar HP **Determined later in the report

Table 10.2 presents the main parameters of the three engine options considered. The AIE 225CS Wankel engine was selected, primarily due to the other two not meeting an updated power require-

---

[1] URL https://limflug.de/downloads/datasheets/L275-EF-datasheet-en.pdf [Cited 16 June 2025]

[2] URLhttps://www.eos-engine.com/index.php?lang=1&hID=71 [Cited 16 June 2025]

[3] URL https://www.aieuk.com/225cs-017-40bhp-gasoline-uav-propulsion-system/ [Cited 16 June 2025]

ment, but also due to the need for accurate performance data in a military context. Unlike the EOS Quattro, which lacked information such as power and torque curves, the AIE engine provides reliable performance metrics. Assuming a linear relationship between power, torque, and RPM would compromise the design's reliability [43]. To ensure accuracy in the estimation of the drone's capabilities, the AIE 225CS was chosen as the most suitable choice.

10.2.3. Power at altitude

A naturally aspirated engine will lose power as it climbs due to the decreasing density of air. Equation 10.3 is used to correct for this loss with $m = 0.9$, as stated by Saeedraey (2012) [2].

$$P = P_{\mathrm{SL}} \left(\frac{\rho}{\rho_0} \right)^m \tag{10.3}$$

The density at different heights is based on the ISA model. The power available against the altitude of the CEDI drone is plotted and shown in Figure 10.1. At the cruise altitude of 5000 m, CEDI has a maximum power available of 19.01 kW.

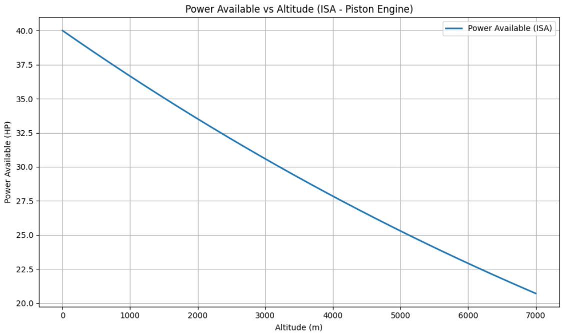

Figure 10.1: *Power available at different altitudes*

10.2.4. RPM matching

The engine manufacturer has included power and torque charts in their engine data sheet, which will be used to select an appropriate RPM to run at cruise, depending on the power required. These are portrayed in Figure 10.2. One thing to keep in mind is that this graph is obtained at sea level. So, an equivalent sea level value for the power required at cruise needs to be found. This is done by rearranging Equation 10.3 and using 15.8 kW for power at altitude. This gives an equivalent power at sea level of $P_{e_{\mathrm{SL}}} = 24.6$ kW.

Reading from the graph at the point where $P = 33.5$ HP gives an RPM of 6500 and a torque of 36 Nm. These values will be used for sizing the propeller accordingly.

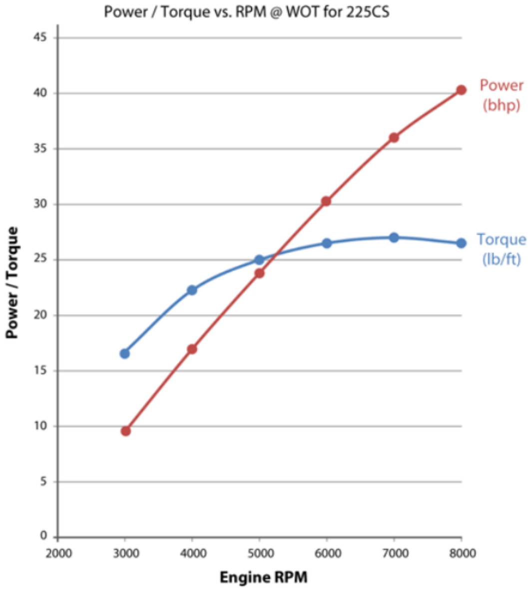

Figure 10.2: *Power and torque plot for the 225CS*[4]

10.2.5. Propeller Sizing

To get started on propeller sizing, all relevant parameters are listed in Table 10.3

---

[4] URL `https://www.aieuk.com/225cs-017-40bhp-gasoline-uav-propulsion-system/` [Cited 16 June 2025]

Table 10.3: *Cruise parameters for propeller sizing*

Metric	Value
Velocity	80 m/s
Thrust required	157.99 N
Power required (shaft, at altitude)	15.56 kW (21.19 HP)
Equivalent sea-level power	24.60 kW (33.51 HP)
Engine RPM	6500 RPM
Engine torque (sea-level)	36 N·m

The first parameter that limits the propeller design is its minimum diameter. This is determined based on fuselage width and how its obstruction affects propeller efficiency in a pusher configuration. Following Suprianto et al. [44], the obstruction can be quantified by the ratio shown in Equation 10.4.

$$B = \frac{D_{\text{fuselage}}}{D_{\text{propeller}}} \tag{10.4}$$

This ratio then defines a new efficiency factor shown in Figure 1 of Suprianto A. et al. [44]. This efficiency should be maximized; therefore, the size of the propeller should be maximized. The minimum value is limited by the diameter of the fuselage, which is 0.55 m.

The maximum propeller diameter is bound by the distance from the ground, the distance between the booms, and the propeller tip speed. The latter one should not exceed 0.85 Mach to prevent shockwave occurrence at the propeller tip [2]. Calculating the tip speed follows from basic dynamics principles and is shown in Equation 10.5, where $V_{\text{tip, static}}$ follows from Equation 10.6:

$$V_{\text{tip, cr}} = \sqrt{V_{\text{tip, st}}^2 + V_C^2} \tag{10.5}$$

$$V_{\text{tip, st}} = \frac{D_P}{2}\omega \tag{10.6}$$

At cruise altitude, the speed of sound is $320\,\mathrm{m\,s^{-1}}$. This gives a tip velocity limit of $272\,\mathrm{m\,s^{-1}}$. Setting this value for $V_{\text{tip, cruise}}$ and solving for D_p at 6500 RPM (highest torque) gives a value of 0.64 m. This is too small as it will give an effective diameter of 14 cm. The engine RPM will then be geared down to achieve a viable tip speed. The gear ratio will be determined based on the floor clearance at take-off as this is the limiting factor for maximum diameter. This value is given to be 0.822 m.

Using Equation 10.5 backwards, with a limit of $272\,\mathrm{m\,s^{-1}}$, leaves a maximum RPM of 6000. This should happen at engine maximum RPM, which is 8000; therefore, a gear ratio of 1.33 is used. At an engine speed of 6500 RPM, the propeller will spin at 4850 RPM.

10.2.6. JavaProp

When the diameter is selected, its time to move on to JavaProp. The initial step is to set the parameters. These are shown in Table 10.4

Metric	Value
Number of blades B [-]	2
RPM [min^{-1}]	4850
Diameter D [m]	0.822
Spinner diameter D_{sp} [m]	0.00
Velocity V [$\mathrm{m\,s^{-1}}$]	80
Thrust required T [N]	157

Table 10.4: *Inputs for JavaProp design*

The first iteration of the blade count was set at two to maximize propeller efficiency at cruise and minimize drag. Since this is a pusher configuration with no frontal airflow, the spinner diameter is set to zero. The thrust required to be generated by the propeller follows from Table 10.1 at cruise. It was also time to select an airfoil. While much consideration went into this initially, multiple sources mention that as long as an airfoil has reasonable drag characteristics, there is little gain from optimizing its 2-D properties [45]. For this reason, the Clark Y airfoil was chosen for its simplicity in manufacturing and common usage in propeller applications [46]. This was selected in JavaProp, which then generated the optimum blade geometry and computed the performance shown in Table 10.5.

This table shows that to generate 157 N of thrust, 14.78 kW of power is needed. This is less than what is shown in Table 10.1, therefore, it is sufficient. The advance ratio is another parameter that JavaProp calculates; this is how hard the propeller is working for a given RPM and diameter. With this, graphs for C_t and C_p against advance ratio are plotted in Figure 10.3a. These are useful to determine C_t and C_p at different altitudes, velocities, and RPM. These graphs were validated with experimental data found in a NASA report [47], and they match in a range of 5%, confirming our design. One last parameter to check is the required torque. Correcting the value for torque available from Figure 10.2, at 6500 RPM, due to the gear-ratio, it is determined that the available torque to the propeller is 47.88 N m. This means the propeller will be able to spin at the given conditions.

Table 10.5: *Propeller performance parameters*

Metric	Value
Advance ratio J [-]	1.204
Thrust T [N]	157
Power P [kW]	14.78
Torque Γ [N m]	29.1
Thrust coefficient C_t [-]	0.0715
Power coefficient C_p [-]	0.1013
Blade angle at 75 % R $\beta_{75\%R}$	33.1°
Pitch H [m]	1.26

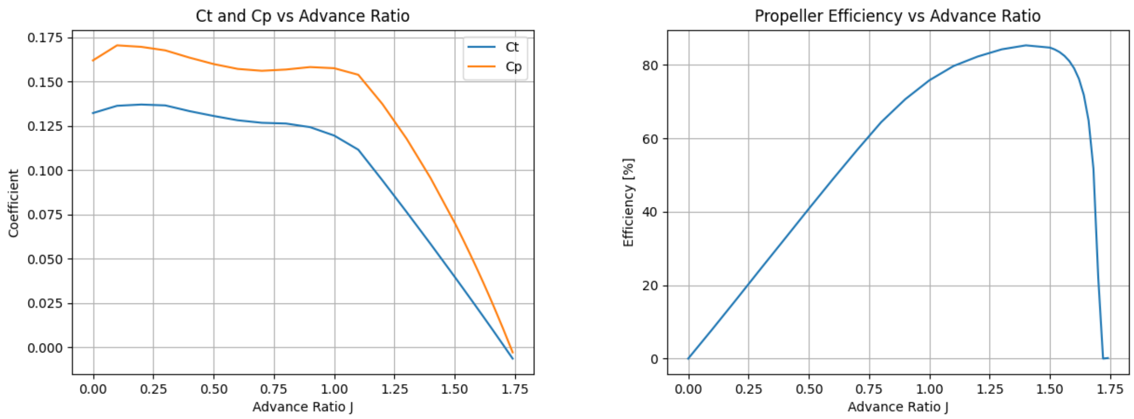

(a) *Thrust and power coefficients vs. advance ratio*

(b) *Efficiency vs advance ratio*

Figure 10.3: *(a) Coefficient curves; (b) Efficiency curve*

10.2.7. Climb

During climb, sea level altitude is assumed. Instead of relying on rate-of-climb requirements, this approach was done by fixing the climb rate to a moderate and realistic value, and then determining the climb airspeed that satisfies the power limits. The goal remains the same: to maintain a high enough propeller efficiency such that a fixed-pitch propeller is sufficient, avoiding the cost and complexity of a variable-pitch system.

A climb rate of $5\,\mathrm{m\,s^{-1}}$ at sea level is assumed, which offers a balance between climb performance and reasonable power demand. To ensure engine longevity and a high propeller efficiency, the available mechanical power is capped at 80% of maximum throttle. The power available for climb is then calculated using Equation 10.7.

$$P_{\text{avail}} = P_{\max} \cdot 0.8 = 30\,\text{kW} \cdot 0.8 = 24\,\text{kW} \tag{10.7}$$

With this available power, and fixing the climb rate $\dot{h}$ at $5\,\mathrm{m\,s^{-1}}$, the required airspeed for climb can be determined using the power balance, as can be seen in Equation 10.8.

$$\eta \cdot P_{\text{input}} = D_{\text{tot}} V + W_{TO} \cdot \dot{h} \tag{10.8}$$

Solving this equation for velocity at an input power of 24 kW, an efficiency of 0.8 and RoC of $5\,\mathrm{m\,s^{-1}}$ leads to a climb speed of $70\,\mathrm{m\,s^{-1}}$. Re-calculating the efficiency at this new speed from Figure 10.3b gives a value of 0.78.

10.2.8. Specific Fuel Consumption

The engine manufacturers did not provide a value for SFC; however, a paper published by SAE International describes a variety of tests performed on the 225CS-40BHP, which included determining its fuel consumption. The method used to determine the fuel consumption of a CEDI drone follows from this. [5]

The method outlined uses the engine brake mean effective pressure (BMEP) and plots a map of this against RPM. This is shown in Figure 10.4. The BMEP is calculated using Equation 10.9 (SAE Internaitonal [5]).

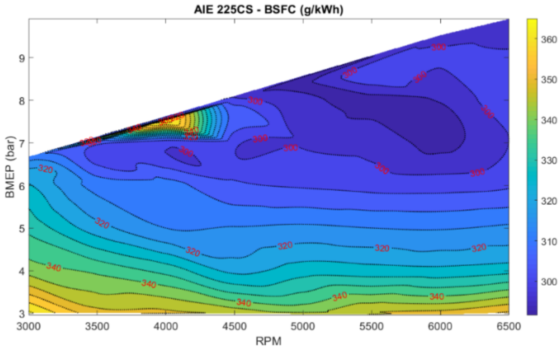

Figure 10.4: *SFC of the 225CS-40BHP at different torques and RPM [5]*

$$BMEP = \frac{2\pi \cdot \varepsilon \cdot \Gamma}{V_t} = \frac{2\pi \cdot \Gamma}{V_s} \tag{10.9}$$

where Γ is the total torque measured, V_s is the swept volume for a single flank (equal to $225 \times 10^{-6}\,\mathrm{m^3}$ for the AIE 225CS), V_t is the total swept volume displaced, equal to three times V_s, and ε is the number of crank revolutions per power stroke (equal to 3 for Wankel rotary engines).

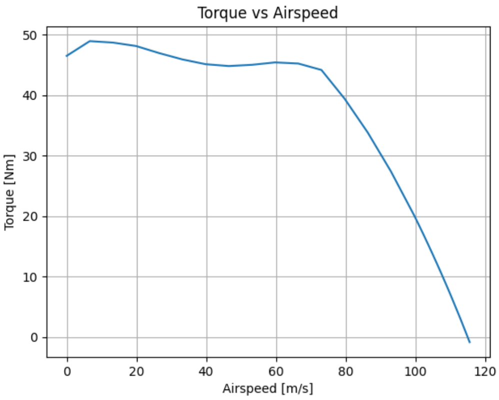

Figure 10.5: *Torque vs airspeed (at 6500 RPM)*

To determine the torque required by the propeller, a specific torque vs airspeed graph was plotted using JavaProp. This graph, shown in Figure 10.5, represents the torque required at 6500 RPM.

Between climb and cruise, the varying factor is airspeed; RPM and power remain constant, sacrificing some horizontal speed to enable climb. As the velocity changes, the torque requirement also shifts. These torque values are corrected by dividing by the gear ratio of 1.33 and are shown in Table 10.6.

Table 10.6: *Torque Results from graph*

Metric	**Cruise**	**Climb**
Advance Ratio J [-]	1.204	1.05
Torque Γ [N m]	30	33.84
BMEP [bar]	8.4	9.5
SFC (from Figure 10.4) [g/kWh]	305	300

10.3. Design Description

The final design for the propulsion subsystem will be summarized below. The British-made Wankel engine, AIE 225CS-40BHP, is the chosen engine. It is a rotary engine with a compression ratio of 9.6:1 and a total weight of 22 kg. It is capable of operating on multiple fuel types, providing flexibility in terms of fuel availability and logistics, especially in wartime. However, Jet A-1 was chosen as the primary fuel due to its widespread availability and compatibility with airbases. The engine's connection to the propeller is geared down by a ratio of 1.33, lowering the RPM at the propeller but increasing the torque it provides. The engine comes with a patented cooling system that utilizes pressurized gases from the combustion process as a medium for cooling in a sealed engine core. It is also fully controllable via an electrical control unit.

A two-blade propeller with the characteristics shown in Table 10.7 has been designed. The chosen airfoil is a Clark Y along the entire blade profile due to ease of manufacturing. A fixed-pitch propeller was chosen because the efficiency difference between climb and cruise conditions was only around 5%. This variation is small due to the high velocity during climb, so there was no need to include a more expensive and complex variable-pitch system, which would also require additional maintenance.

Table 10.7: *Propeller parameters*

Metric	**Value**
Max efficiency η	85.78%
Blade angle $\beta_{0.75R}$	33.1°
Pitch H [m]	1.26
Diameter D_P [m]	0.822

Portrayed below are the operational conditions of the CEDI during climb and during cruise. Both will run at 6500RPM. For climb, however, a bit of horizontal speed is sacrificed for a small climb rate. This makes sure the efficiency is kept as high as possible.

Table 10.8: *Engine and propeller parameters during climb and cruise*

Parameter	**Climb** (sea-level)	**Cruise** (5000 m)
Engine RPM	6500	6500
Power required P [kW]	24	24.60
Propeller efficiency η	77%	82%
Thrust T [N]	241	157
Advance ratio J	1.05	1.204
Airspeed V [$\mathrm{m\,s^{-1}}$]	70	80
Climb rate $\dot{h}$ [$\mathrm{m\,s^{-1}}$]	5	—
Fuel consumption (WOT) [g/kWh]	305	305

The maximum speed of the CEDI drone was calculated by determining the power available vs power required as a function of velocity and determining where they intersect, shown in Figure 10.6. The power available follows from Equation 10.10, where the efficiency changes with the advanced ratio, which changes with different velocities. This also takes into account the correction for a Wankel engine at altitudes. The power required is simply the drag multiplied by the velocity at a certain altitude. At the point where these equal, the maximum speed is found to be 88.48 $\mathrm{m\,s^{-1}}$.

$$P_{\text{avail}} = \eta(J) \cdot P_{\text{engine}_{altitude}} \tag{10.10}$$

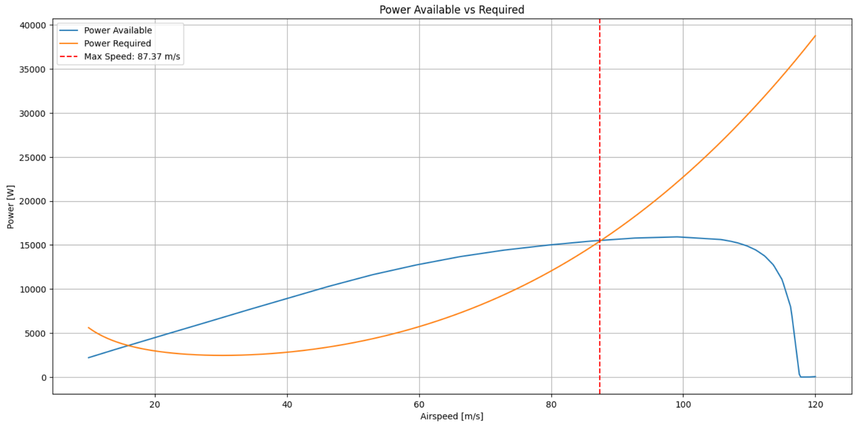

Figure 10.6: *Top speed of the CEDI drone*

The maximum range and endurance of the CEDI are calculated by finding the ideal power required for each case and determining the specific fuel consumption at those speeds. For maximum range, this corresponds to the point of maximum C_L/C_D, which graphically is where a straight line from the origin is tangent to the power required curve. This is the first contact point as the line rotates counterclockwise.

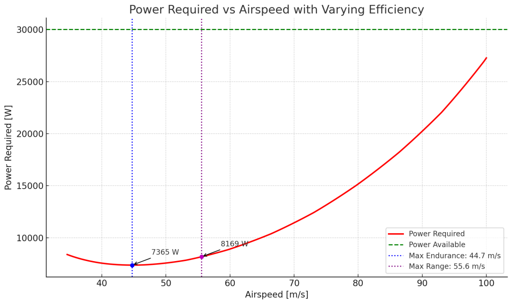

Figure 10.7: *Power for maximum range and endurance*

This is illustrated in Figure 10.7, where both the range and endurance points are shown. Minimum power corresponds to maximum endurance. The plot shows power required as a function of propeller efficiency, which varies with airspeed.

These two power values, along with the additional power required to charge the battery (conservatively estimated at a constant 2 kW), determine the total power demand during flight. Multiplying this power by the SFC gives the resultant fuel consumption in kilograms per hour. Since the nominal amount of fuel for a nominal mission was calculated to be 21.36 kg, this is the fuel that will be carried. An overview of these flights is portrayed in Table 10.9.

Table 10.9: *Fuel and propulsion parameters at nominal mission, max range and max endurance*

Parameter	Max Endurance	Max Range	Nominal Mission
Specific Fuel Consumption (SFC) [g/kWh]	305	305	305
Power Used P [kW]	9.37	10.17	24
Fuel Flow [$\mathrm{kg\,h^{-1}}$]	2.858	3.102	7.320
Airspeed V [$\mathrm{m\,s^{-1}}$]	44.7	55.6	80
Range R [km]	1202.6	1378	840
Endurance E [h]	7.47	6.89	2.92

10.4. Verification

These requirements were identified as the ones driving the propulsion subsystem design. These requirements are mainly concerned with operations at cruise condition and no climb requirements were provided by the user.

Table 10.10: *Requirements compliance for the propulsion subsystem*

Requirement Code	Condition	Result	Met?	How?
SYS-01.04.08	Sustain flight up to 5000 m	NA	Yes	Subsection 10.2.2
SUB-01.04.08.01	Thrust available at 5000 m	NA	Yes	Subsection 10.2.2
SYS-01.04.10	Range ≥ 460 km	840 km	Yes	Section 10.3
SYS-01.04.11	Endurance ≥ 2 h	2.9 h	Yes	Section 10.3
SYS-01.04.12	Cruise speed ≥ 80 m/s	80	Yes	Subsection 10.2.2
SUB-01.04.15.02	Thrust controllable	ECU	Yes	Subsection 10.2.2
SYS-01.10.34	Loiter ≥ 2 h below 5000 m	2.9 h	Yes	Subsection 10.2.2

11

Power Design

In this chapter the detailed design of the power subsystem will be presented. First, the requirements for the power system are identified in Section 11.1. Afterwards, the power usage per component will be assessed and batteries will be selected in Section 11.2. Then, a design description and electrical block diagram will be presented in Section 11.3. At last, the requirements will be verified in Section 11.4.

11.1. Requirements

- **SYS-01.01.1**: The system shall provide continuous and reliable electrical power to all onboard avionics during all mission phases.
  - **SUB-01.01.1.1**: The battery shall be able to provide sufficient power for all avionics.
  - **SUB-01.01.1.2**: The power system shall include redundancy such that failure of a single power path does not interrupt avionics operation.

11.2. Design Process

The main task of the power system is to manage the power distribution across the whole CEDI drone. The drone uses a lot of electrical systems, whether it is to control its movement or to track and attack target drones. These systems will be powered using a 6S Li-Po battery as opposed to a Li-Ion one. This is due to a two reasons: first, Li-Po batteries have much higher discharge currents; second, Li-Po batteries have a higher power-to-weight ratio.

Since the servos pull a particularly large current at maximum operational torque, a high discharge ratio is required to be able to power these and the remaining systems at the same time.

To size the battery, one must know how much power each system will consume and the duration of this consumption. Most of these are big assumptions since it will not be known for how long an aileron needs to be operated. However, this is the best that can be done at this stage in the design. For the elevator servos, the time is assumed as one hour since it is needed during climb and also to trim the aircraft. For the rest of the control surfaces, 5 minutes is estimated as they will only be powered during turns, take-off, and landing. The linear actuators will only be required during take-off and landing, so the time needed is low. Most of the flight control electronics are powered for the whole flight as they are needed for positioning, communication and attitude determination. The power usage and mission usage of all components are shown in Table 11.1.

Table 11.1: *Power usage per electrical component for a 2-hour mission*

Component	Power Usage	Mission usage (minutes)
Servo Motor (LA1)	5 A @ 7 V	5
Servo Motor (LA2)	5 A @ 7 V	5
Servo Motor (RA1)	5 A @ 7 V	5
Servo Motor (RA2)	5 A @ 7 V	5
Servo Motor (E1)	5 A @ 7 V	60
Servo Motor (E2)	5 A @ 7 V	60

Component	Power Usage	Mission usage (minutes)
Servo Motor (LR)	5 A @ 7 V	5
Servo Motor (RR)	5 A @ 7 V	5
Servo Motor (LF)	5 A @ 7 V	5
Servo Motor (RF)	5 A @ 7 V	5
Linear Actuator 1	7 A @ 12 V	2
Linear Actuator 2	7 A @ 12 V	2
Linear Actuator 3	7 A @ 12 V	2
Stepper Motor 1	4 A @ 12 V	20
Stepper Motor 2	4 A @ 12 V	20
Pixhawk FCU	2.5 A @ 5.6 V	120
Jetson Xavier NX	3.0 A @ 12 V	120
Radar (EchoGuard)	3.3 A @ 15 V	90
Camera	0.21 A @ 12 V	90
GPS Unit 1	0.05 A @ 5 V	120
GPS Unit 2	0.05 A @ 5 V	120
Starlink	3.3 A @ 12 V	30
IFF	0.5 A @ 5 V	120
LIDAR	0.75 A @ 5 V	120
Transmitting Power	100 W	120

This gives the whole system a total amount of energy used of 550 Wh. Applying a generous margin of 1.5, leaves a required energy of 825 Wh. This is the energy that will be needed for the nominal mission. Since the engine has a 2 kW, 28 V generator, not all this energy will have to be carried by the battery. A battery that can hold 500 Wh will be selected and the remaining power will be provided by the generator charging this battery. The battery chosen is the *Tattu G-Tech 6S 25000mAh 22.8V 10C High Voltage LiPo Battery*, weighing 2.5 kg. It is charged by the generator using a dedicated charger and battery management system. The energy to be provided by the generator is shown in Equation 11.1 with the power required being calculated in Equation 11.2.

$$E_{\text{generator}} = E_{\text{total}} - E_{\text{battery}} = 843 - 570 = 273\text{Wh} \tag{11.1}$$

$$P_{\text{required, avg}} = \frac{E_{\text{generator}}}{t} = \frac{273}{2} = 136.5\text{W} \tag{11.2}$$

This shows that the generator only needs to supply an average of approximately 137 W over the 2-hour mission to meet the total energy requirement. Given that the engine's generator is rated at 2 kW, this load represents less than 7% of its capacity, leaving room for charging under non-ideal conditions.

11.3. Design Description

To ensure that all systems of the CEDI drone receive the correct power, a clear overview of the power distribution is essential. For this reason, an electrical block diagram has been created, shown in Figure 11.1. This diagram shows how power flows from the sources to the various components. In this figure, the pink boxes indicate a power source. The voltage output of these power sources needs to be regulated and therefore multiple voltage regulators are considered, indicated in yellow. Then, the different components are grouped based on their voltage intake. The colored lines indicate different electrical potential levels, with red being high, yellow medium and green low voltage output.

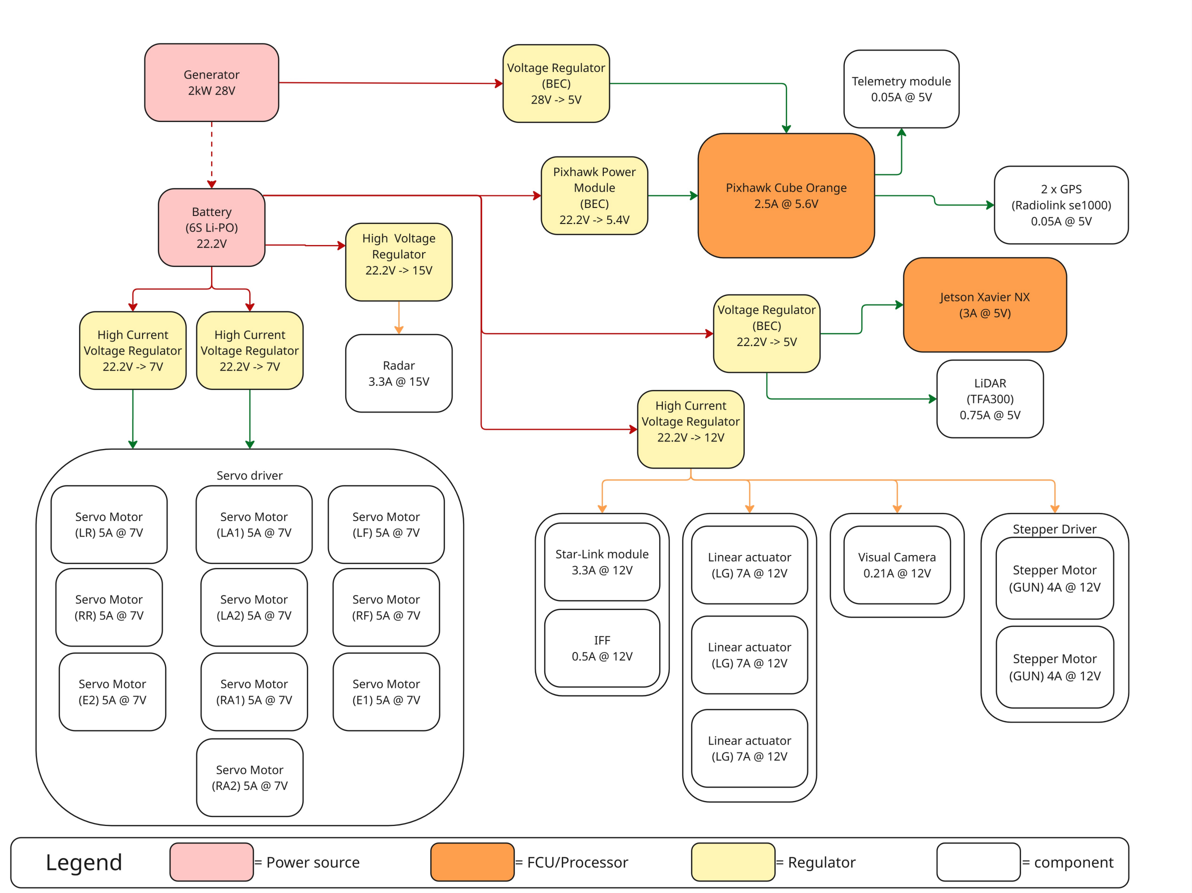

Figure 11.1: *The electrical block diagram for the avionics of the CEDI drone.*

11.4. Verification

The verification of the requirements have been assessed in Table 11.2.

Table 11.2: *Requirements compliance for the power system*

Requirement Code	Condition	Result	Met?	How?
SUB-01.01.1.1	$E \geq 843$Wh	$E_{max} = 1570$Wh	Yes	Hand calculation
SUB-01.01.1.2	nr power systems ≥ 2	nr= 2	Yes	Section 11.2
SYS-01.01.1	reliable & continuous power	NA	Yes	Section 11.2

12

Structural Design

In this chapter, the detailed design of the structures subsystem will be described. First, the requirements are identified in Section 12.1. Second, the design process of the wingboxes, fuselage, engine mounting and landing gear are explained in Section 12.2. Third, the main geometry of the wingboxes, fuselage and booms are presented in Section 12.3. Lastly, final verification of the requirements is carried out in Section 12.4.

12.1. Requirements

The following requirements for structures have been formulated in the baseline report and additional requirements have been added [7].

- **SYS-01.07.19**: The airborne part of the system shall be capable of withstanding without damage a load factor of at least 4, while maneuvering.
- **SYS-01.04.11**: The airborne part of the system shall have an endurance of no less than 2 h, in ISA conditions, at cruise altitude, at cruise speed.
  - **SUB-01.04.11.01**: The wing shall have sufficient fuel volume to fulfill.
- **SYS-01.22.122**: The airborne part of the system shall have sufficient structural integrity.
  - **SUB-0.1.22.122.1**: The structure of the wingbox shall be able to elastically sustain the internal shear loadings in the wing.
  - **SUB-0.1.22.122.2**: The structure of the wingbox shall be able to elastically sustain the internal bending loadings of the wing.
  - **SUB-0.1.22.122.3**: The structure of the wingbox shall be able to remain unbuckled until at least 503 MPa normal stress.
  - **SUB-0.1.22.122.4**: The structure of the wingbox shall be able to remain unbuckled until at least 251.5 MPa shear stress.
  - **SUB-0.1.22.122.5**: The structure of the fuselage shall be able to elastically sustain the internal bending and shear loading of the subsystems attached to it.
  - **SUB-0.1.22.122.6**: The structure of the fuselage shall be able to remain unbuckled under regular operation with a Margin Of Safety of at least 1.5.
  - **SUB-0.1.22.122.7**: The structure of the H-tail booms shall be able to elastically sustain the internal bending and shear loadings caused by the empennage.
  - **SUB-0.1.22.122.8**: The structures shall not interfere with needed control surface areas.
  - **SUB-0.1.22.122.9**: The wingbox shall have sufficient internal volume to house the needed servos.
  - **SUB-0.1.22.122.10**: The fuselage shall contain rails to allow movement of the armament subsystem
  - **SUB-0.1.22.122.11**: The fuselage shall contain frames to transfer loads from housed subsystems
  - **SUB-0.1.22.122.12**: The booms connecting the H-tail to the main wing shall be at least 2.5 meters long starting from the quarter-chord point of the main wing
  - **SUB-0.1.22.122.13**: The booms connecting the H-tail to the main wing shall be at most 75 millimeters wide.

12.2. Design Process & Assumptions

In this section the design process of the material selection, wing structure, empennage structure, fuselage and landing gear design will be outlined starting with a list of assumptions made during this process.

12.2.1. List of Assumptions

For the design process of the structural design, multiple assumptions have been made. These are all listed in the table below.

Table 12.1: *Assumptions made during requirement generation*

Label	**Assumption**	**Validity**
AS-STR-1	Wing structural and fuel load scales with cross-section of wingbox	The total structure is not yet known so this has been used as a first estimation.
AS-STR-2	The wingbox is assumed to be rectangular with the height of the smallest spar	This reduces the complexity of the design problem and the moment of inertia will always be smaller than the real wing box. So this is a conservative assumption
AS-STR-3	Thickness of skin and spar are assumed to be small in comparison with length	The thickness is going to be at least one order of magnitude smaller than the respective length. In this way the thin walled approximation can be used.
AS-STR-4	The stringers are assumed to be point areas	Since the stringer profile is not yet know this is an approximation
AS-STR-5	The stringer point areas are assumed to be one third of the boom areas of the plates of the beams	The total point area has to be divided over the plates and stringers and this ratio has been assumed reasonable
AS-STR-6	The maximum shear stress the structure can handle is assumed to be equal to the Tresca yield criterion	This criterion is an conservative approximation of the maximum shear stress
AS-STR-7	The required area moment of inertia is assumed to stem from the flexural formula (being driven by bending stresses)	Based on the maximum bending moment and the maximum normal stress the required moment of inertia are determined
AS-STR-8	The product moment of inertia around the centroid of the wingbox is assumed to be zero	This has been done to ignore asymmetrical bending, which is acceptable for preliminary design
AS-STR-9	The forces by the landing gear and tail are assumed to be point forces.	For preliminary design this approach is acceptable
AS-STR-10	The maximum loading factor is assumed to be ±4, with the ultimate loading factor being 1.5 times the maximum loading factor	A conservative estimation for the loading factor is considered, since no limiting CS regulations exist for drones
AS-STR-11	The cg of the wing is assumed to be equal to the cg of the wingbox.	Since the wingbox contains the most heavy structure of the wing, this assumption is deemed acceptable

AS-STR-12	For inertia and shear calculations, the empennage boom is assumed to be a hollow ellipse with constant dimensions of the tail end	The actual boom is slightly tapered, having larger dimensions near the root chord of the wing. However, a conservative dimension is taken to over-estimate the required thickness
AS-STR-13	The horizontal tail is assumed to be fixed at its ends	Since the horizontal tail is connected to the vertical tail, a type of constrained has to be chosen to analyze the internal loads
AS-STR-14	The lift distribution of the vertical stabilizer is assumed to be uniform	The lift distribution for this component could not be obtained and therefore a simplification was made

12.2.2. Material selection

The material the structure will be (primarily) made of has an immense impact not only on the performance of the structure, but also its weight, cost (both directly through acquiring the material and the further costs from manufacturing), complexity, and sustainability. As such, the material selection has to be well justified, taking all of these factors into account, and therefore a trade-off between feasible candidates will be performed. The materials selected for consideration were two aluminum alloys, namely Al-7075-T6 and Al-6061-T6, high strength steel AM350 (DA), Titanium alloy Ti-6Al-4V and a quasi-isotropic CFRP-based design.

Trade off Material Selection

To arrive at the most suitable material for the design of the interceptor, criteria will be defined, and their relative importance will be quantified. The criteria of which the trade-off constitutes are performance (weighing 50%), cost (weighing 30%) and sustainability (making up the remaining 20%).

The performance criterion further distinguishes between each material's properties and how well they are fit to specific load cases, as well as general properties. Firstly and most importantly, the yield strength of each material is divided by their density, to see which material provides the most elastic strength at the lowest weight penalty. A material that has a very high yield strength while weighing little is ideal, as it can be pushed to a high stress elastically (still returning to its original shape and not undergoing plastic deformation), allowing for smaller cross sections under the same loads due to the material's ability to bear higher stresses. Next, stiffer materials (in both normal stress - E - and shear stress - G) are preferred. Finally, each material's bending performance, in both beam bending and plate bending, is desired to be maximized, for which the $E^{1/2}/\rho$ and $E^{1/3}/\rho$ need to be maximized, respectively. The relative importance of these parameters has been placed at 40%, 15%, 10%, 10% and 25%.

Following the technical performance of each material, the sustainability is taken into account to directly influence the design. As mentioned in Chapter 15, a key aspect in which sustainability is taken into account is the material selection. The total eco-costs of each material from the IDEMAT database [1] are compared. This database compiles not just the CO_2-equivalent emissions of each material per kilogram, but also takes into account the environmental harm due to resource scarcity, as well as the burden on social sustainability through human toxicity released in the production of the material, for example.

Finally, the cost to purchase each material is also compiled and taken into account for the trade-off. As the end-goal is to produce a cost-effective system, minimizing material cost will naturally contribute to that objective, provided it is done without compromising on performance to an exceedingly high degree. The information used for the trade-off has been compiled in Table 12.2, with the sources listed.

---

[1] URL https://www.ecocostsvalue.com/data-tools-books/ [Cited 17 June 2025]

Table 12.2: *Properties of considered materials for the structural design*

Property \Material	**Al-7075-T6**[2]	Al-6061-T6[3]	**AM350 Steel**[4]	**Ti-6Al-4V**[5]	**CFRP**[6]
Density [$\mathrm{g\,cm^{-3}}$]	2.81	2.7	7.67	4.43	1.6
Yield Strength [MPa]	503	276	1100	880	105[7]
E-Modulus [GPa]	71.7	68.9	200	113.8	85
G-Modulus [GPa]	26.9	26	75	44	47
Plate Bending Perf. ($E^{1/3}/\rho$)	1.48	1.52	0.76	1.09	2.75
Beam Bending Perf. ($E^{1/2}/\rho$)	3.01	3.07	1.84	2.41	5.76
Tensile Perf. (E/ρ)	25.52	25.52	26.08	25.69	53.13
Shear Perf. (G/ρ)	9.57	9.63	9.78	9.93	29.38
Total Eco-Costs [€/kg]	2.28	2.18	2.21[8]	21.86	17.47
Purchasing Costs [$/kg]	3[9]	2.75[10]	14[11]	45[12]	85[13]

From this information, a trade-off was constructed, scoring each aspect on a normal scale, resulting in a final maximum weighted score of 6.61/10 for Al-7075, with the lowest scoring material being CFRP at a weighted score of 3.62. Following the trade-off, it was concluded that the material Al-7075-T6 was the most suitable material for this mission, including in the case of other materials' properties being under-estimated in performance and the winning material being over-estimated in performance.

12.2.3. Wing Structure Design

With the material selected and the wing planform geometry provided, the wingbox structure design was synthesized. Before the details of each step are given, a brief overview of the design process will be provided.

Overview of the Wing Box Design Process

Firstly, an analysis of the expected external and internal loads is conducted, to identify the magnitude of the internal loads the structure must bear. To aid in this, so-called (N)VM diagrams are constructed to find the spanwise positions of the largest magnitude of the shear and bending moment. Based on this critical load case, as well as a safety factor, a first estimate for the design is achieved

---

[2] Data from MatWeb URL`https://www.matweb.com/search/DataSheet.aspx?MatGUID=4f19a42be94546b686bbf43f79c51b7d` [Cited 17 June 2025]

[3] Data from MatWeb URL`https://asm.matweb.com/search/specificmaterial.asp?bassnum=ma6061t6` [Cited 17 June 2025]

[4] Data from ATI URL`https://www.atimaterials.com/Products/Documents/datasheets/stainless-specialty-steel/precipitationhardening/am_350_tds_en_v2.pdf` [Cited 17 June 2025]

[5] Data from MatWeb URL`https://asm.matweb.com/search/specificmaterial.asp?bassnum=mtp641` [Cited 17 June 2025]

[6] Data from Performance Composites URL`https://www.performance-composites.com/carbonfibre/mechanicalproperties_2.asp` [Cited 17 June 2025]

[7] Taken as 30% of the ultimate strength, to account for stress concentration factors when holes are introduced

[8] Taken as the closest match to AM350 in the IDEMAT database; X20Cr13 in this case

[9] Price from URL `https://www.calicometal.net/aluminium-7075-bar-sheet-plate-tube-fittings-manufacturer-supplier.html` [Cited 17 June 2025]

[10] Price from URL `https://www.tradewheel.com/p/aluminum-6061-t6-prices-per-kg-171794/` and URL `https://www.made-in-china.com/products-search/hot-china-products/Aluminium_6061_Price.html` [Cited 17 June 2025]

[11] Price from URL `https://www.onlinemetals.com/en/buy/aluminum/0-016-aluminum-sheet-6061-t6/pid/21563` [Cited 17 June 2025]

[12] Price from URL `https://am-material.com/news/introduction-to-ti-6al-4v-titanium-alloy/#elementor-toc__heading-anchor-8` [Cited 17 June 2025]

[13] Price from URL `https://www.infosys.com/engineering-services/white-papers/documents/carbon-composites-cost-effective.pdf` [Cited 17 June 2025]

by finding the required moment of inertia. At this stage of the design, nothing is decided yet, except the total area moment of inertia the structure must have, akin to what is seen in Figure 12.1a.

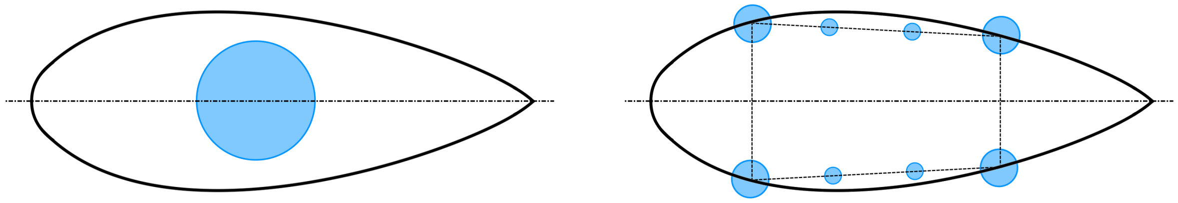

(a) *The first stage of the wing box design* **(b)** *The second stage of wing box design*

Figure 12.1: *Initial models of the wing box*

Shortly thereafter, based off of the wing geometry, boom areas shall be placed at the lowest possible height (thereby under-estimating the stiffness they provide, and over-estimating the required area to remain on the conservative side) according to the wing geometry, with the spars and skins receiving more represented area than stringers. The result of the next stage of the model can be seen in Figure 12.1b.

Once these boom areas have been determined, a shear distribution analysis can be carried out, albeit with idealized shear flows, refining the design further, as seen in Figure 12.2a.

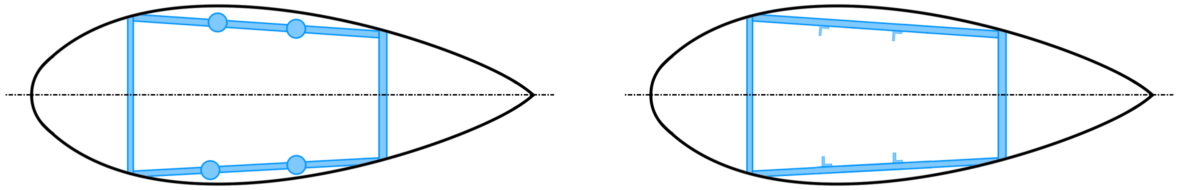

(a) *The third stage of the wing box design* **(b)** *The fourth stage of wing box design*

Figure 12.2: *Intermediate models of the wing box*

Finally, the buckling strength of the wing box is evaluated, for which the stringer geometry also becomes defined, which leads to a wing box design as seen in Figure 12.2b.

Finalized Wing Box Model

Before the design is elaborated on in further detail, a brief rundown of the design decisions and simplifications is illustrated in Figure 12.4.

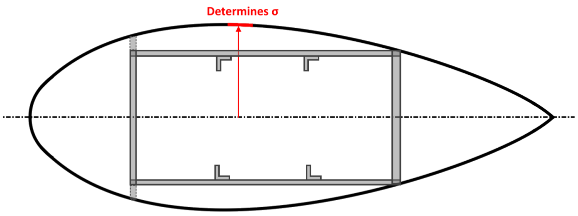

Figure 12.3: *The final wing-box as modelled for structural calculations*

Some key elements might immediately come to mind, like the wing box not following the airfoil contour, and being symmetrical. For the purpose of modeling the wing box structurally, this actually results in more stringent sizing requirements, as the moment of inertia scales with the distance to the neutral axis squared. Hence, to achieve the same moment of inertia with a lower distance, much more area, and therefore thickness and weight, is required. A critical reader might point to the fact that, while inertia scales with distance to the neutral axis, so does the stress, and taking the stress at a lower point would not be conservative. Therefore, to ensure the critical stress is not underestimated, the stress of the point furthest of the neutral axis is still taken for evaluation, despite not being "inside" the wing box. Once the design comes to realization and is manufactured, the wing box could follow the airfoil contour to enhance its stiffness even further.

Wing loading analysis

The first step in synthesizing the wingbox is to understand the different forces and loadings on the wing. The loads acting on the wing can be split into two categories: point loads and distributed loads. The point forces which are considered for the loading analysis are: the landing gear, which is positioned below the wing, and the tail boom, which is connected to the wing and connects the H-tail configuration to the rest of the aircraft's structure. A brief explanatory overview of the distributed forces acting on the wing has been provided in Figure 12.4, to be modeled in the next subsection.

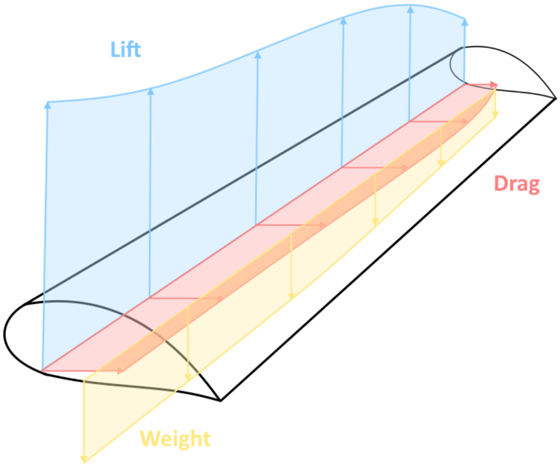

Figure 12.4: *A qualitative overview of the distributed forces acting on the wing*

The distributed forces consist of aerodynamic forces, as well as structural and fuel weights. From the aerodynamic analysis, the lift and drag distributions were obtained, which make up the aerodynamic distribution. These loads have been combined and corrected for the angle of attack to obtain the normal and axial forces acting on the wing. For the structural weight distribution, assumption AS-STR-1 has been considered, which states that the structural and fuel load scales with the cross-sectional area of the wingbox. To determine this weight distribution, $F_{\text{str}}(y)$, the following formula has been set up:

$$F_{\text{str}}(y) = \frac{0.5 \cdot W_{\text{wing}} \cdot A_{\text{cross}}(y)}{V_{\text{total}}} \tag{12.1}$$

where W_{wing} is the wing weight determined by the class 2 estimation, A_{cross} the cross-sectional area at location y, and V_{total} the total integrated cross-sectional area over the span. This approach has also been used to estimate the fuel weight distribution. However, first, the fuel volume needed to be calculated to determine the y span location of the end of the fuel tank. With this, the fuel weight distribution could be calculated over the length of the fuel tank. In the upper graph of Figure 12.6, the summation of the distributed load and the point forces can ben observed.

NVM analysis

Based on the total load obtained from the loading analysis, the internal shear and bending moment distributions can be computed. This is done in the y-z plane since this will be the critical case for the wing undergoing shear and bending. The analysis is essential to analyze the critical stresses, which will be evaluated in the next subsection. As a design choice, the maximum load factor has been set to ±4 as stated by AS-STR-10. Moreover, the density of sea-level conditions has been chosen, since this would give the most conservative force distributions. These choices will be used for the NVM analysis to discover the most critical loading.

When analyzing the shear and bending loads, a clear coordinate system has to be set up to avoid confusion related to the signage. The coordinate system and the positive directions of the loads which will be used for this analysis can be seen in Figure 12.5.

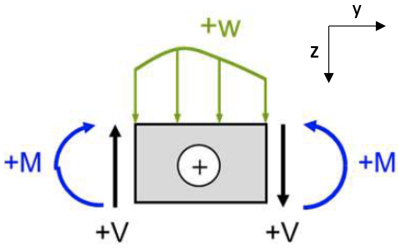

Figure 12.5: *Coordinate system used for the NVM analysis*[14].

The normal forces on the wing induces a shear force distribution. This relationship between distributed normal and shear force can be observed by the following equation:

$$\frac{dV_z(y)}{dy} = -w_z \tag{12.2}$$

where, $V_z(y)$ is the shear force as function of y along the span, and w_z the distributed load. The introduced point loads on the wing are related with shear as follows:

$$\Delta V_z = -P_z. \tag{12.3}$$

The internal shear force distribution is programmatically computed using the Euler integration method. The method partitions the half span of the wing into an array with step size $dy = 0.01$. To integrate the distributed load, an interpolation between two point was applied using the scipy interpolation function, allowing the function to be integrated using the scipy integration function. After the distributed load is integrated along the span, the shear force variations due to the point loads can be added. This approach introduces some inaccuracy due to the interpolation function; however, this small inaccuracy is deemed acceptable for this design stage. The total shear force over the span of the wing can be observed in Figure 12.6. From the shear force, the bending moment distribution can be derived. Since there are no point moments on the wing, only the distributed shear has to be related to the moment. This relationship can be seen in the following formula:

$$\frac{dM_x(y)}{dy} = V_z \tag{12.4}$$

Using the same integration approach as was done for the shear, the moment distribution is computed programmatically.

To investigate the shear flow and stresses in the structure, it is important to also analyze the torsional distribution along the span. This distribution was obtained by multiplying the lift distribution over the span by the respective length between the centroid and the aerodynamic center. To obtain this, AS-STR-11, which states that the centroid of the airfoil is concise with the centroid of the wingbox, is assumed. This respective length is, like the lift distribution, a function of y. Since the tail of the CEDI drone is connected to the main wing, this introduces a point torque. This change in torque is added to the distribution. A final torsional distribution along the half span of the wing can be observed in Figure 12.6.

---

[14] URL `https://brightspace.tudelft.nl/d2l/le/content/512120/viewContent/2875343/View` [Cited 12 June 2025].

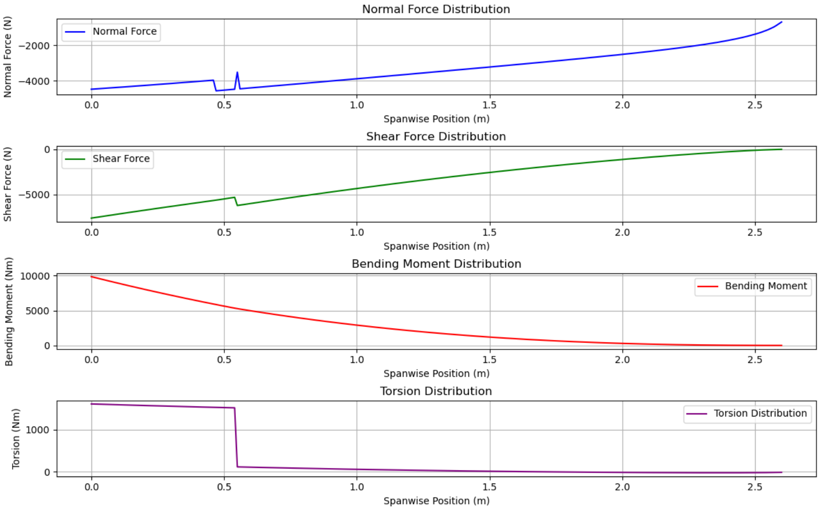

Figure 12.6: *NVM diagram of the main wing.*

Critical Stresses

To analyze the structural stresses an initial estimation for the spar locations was made. These were set at 30% and 60% of the wing chord. This choice is driven by the placement of the ailerons for which room needs to be saved.

To arrive at a wingbox design, it is necessary to derive the required moment of inertia. This is calculated from the flexural bending formula. The stress for which the moment of inertia is found is based on the yield strength of the selected material. For this stress, a safety factor of 1.5 is applied to get a lower maximum acceptable stress. The formula is shown below:

$$\sigma_{\text{safe}} = \frac{M_x \cdot z}{I_{xx}} \tag{12.5}$$

where σ_{safe} is the maximum acceptable stress, I_{xx} the moment of inertia around the x-axis, M_x the moment applied, and z the maximum distance from the neutral axis to the wingbox. By rearranging the formula, the minimum required moment of inertia can be calculated. This is done for the location with the highest bending load, which is located at the root of the wing; this is visualized in Figure 12.6. This results in a required moment of inertia of $2.36 \cdot 10^{-6}\text{m}^4$.

As already stated, to analyze the design for stresses, a conservative assumption was made to simplify the wingbox. Assumption AS-STR-2 states that the wingbox is assumed to be rectangular with the height of the smallest spar. This is a conservative assumption, since the respective distance from the neutral axis to calculate the moment of inertia is the smallest. The simplification is shown graphically in Figure 12.4.

With the simplified wingbox and the required moment of inertia, boom areas can be determined over the perimeter. This boom area can be computed by dividing the required moment of inertia by half of the height of the rear spar squared. This area needs to be distributed between the spars and the stringers. This is done by assigning two booms per spar at their ends. As a design choice, it was decided to use a total of four stringers. This decision is driven by the small tip chord and thus the small length of the wingbox at the tip. The ratio between the spar and stringer booms was set at 3 to 1. In Figure 12.1, the distribution of the boom areas can be observed.

Now that the boom areas have been positioned, a shear flow analysis can be performed. From this, an initial estimate of the required skin and web thicknesses can be made. The important loads for this analysis are the shear forces in z and x direction and the torsional load. Using Equation 12.6 and Equation 12.7, the shear flow can be calculated for the different sections between the boom areas.

$$q_1 = -\frac{\Gamma}{2A_m} [6] \tag{12.6}$$

$$q_{i+1,i} = q_i + \left[\frac{-V_z}{I_{xx}} Bz - \frac{V_x}{I_{zz}} Bx \right] [6] \tag{12.7}$$

with q_i the shear flow between section i, A_m the enclosed area, and B_i the boom area. However, since this is a simplified shear flow calculation due to the use of boom areas, it should be stated that the calculated shear flow of the sections does not fully follow the real shear flow. The simplified shear flow is actually an average of the actual shear flows. Therefore, a conservative safety factor of 3 has been applied to the critical shear flows. This factor has been deemed reasonable since for a linear distribution (when starting at zero) the average is at one third of the maximum. To go from shear flow to required thickness, a division is made with the maximum allowable shear stress, which is a material property. To arrive at this shear stress, the Tresca criterion is used on the maximum yield stress, which is given in Equation 12.8:

$$\tau = \frac{\sigma_y}{2} \tag{12.8}$$

Afterwards, a safety factor of 1.5 is applied to get the maximum allowable shear stress. From this, it is concluded that the most critical required thickness of the sections based on the shear flow is the thickness of the front spar web, which is required to be 1.25 mm. As the shear flow is clearly not limiting in the thickness of the web and skin, an initial thickness of 1.5 mm is assigned to start the buckling analysis.

Rib Spacing

To start the rib placement, which is dependent on buckling characteristics, some pre-determined ribs have been allocated. These can be seen in Figure 12.9, shown as the red lines.

The first two pre-determined ribs (0 and 12.5 cm from the root), have been placed due to the armament system inside the fuselage. This systems is placed against the front spar and can introduce large amounts of recoil. The next two ribs, placed at 49 cm and 61 cm, are placed to support the tail booms which also house the landing gear. The following rib (100 cm) has been placed for possible future armament extensions.

The rib spacing is analyzed based on three different buckling modes: skin buckling, web buckling, and column buckling of the stringers. Skin buckling occurs due to the large compressive stresses exerted by the bending moment analyzed in NVM Analysis. The equation to calculate the critical stress for buckling is given by Equation 12.9:

$$\sigma_{\text{crit}} = \frac{\pi^2 k_c E}{12(1-\nu^2)} \left(\frac{t}{b} \right)^2 \tag{12.9}$$

were, ν is the Poisson ration, E the Youngs modulus, b the length of the sheet, t the thickness, and k_c the buckling coefficient which is dependent on the plate's aspect ratio a/b. Values for k_c can be obtained from the graph plotted in Figure 12.7. To determine this coefficient, the fully clamped curve has been used (case D).

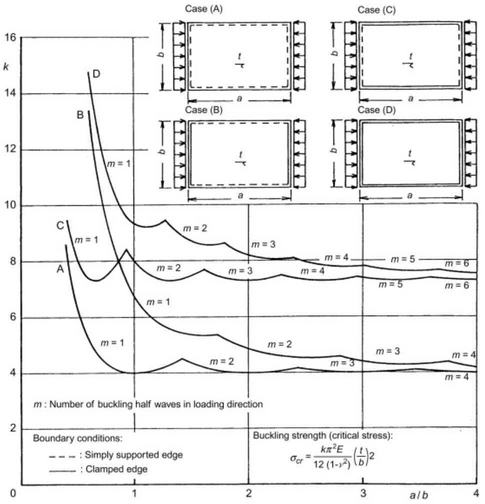

Figure 12.7: *Buckling coefficients for an isentropic flat plate under compressive stresses [6]*

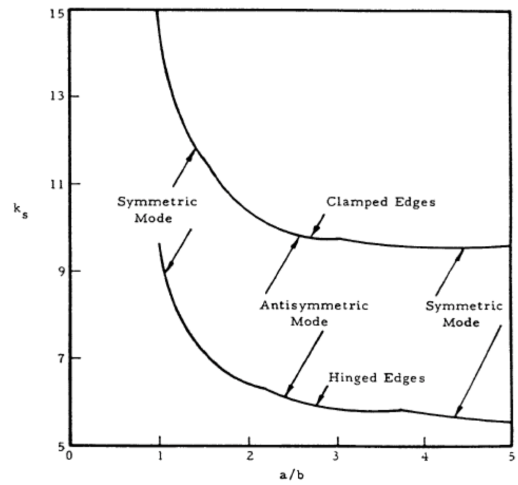

Figure 12.8: *Buckling coefficients for an isentropic flat plate under shear stresses [6]*

Web buckling in the spars can occur due to the shear forces analyzed in the NVM analysis. The critical shear stress can be calculated using Equation 12.10:

$$\tau_{\text{crit}} = \frac{\pi^2 k_s E}{12(1-\nu^2)}\left(\frac{t}{b}\right)^2 \tag{12.10}$$

where E, ν, b and t represent the same parameters as Equation 12.9. k_c is a buckling coefficient, again dependent on the plate's aspect ratio. Values for k_s can be obtained from the graph plotted in Figure 12.8, for which the fully clamped mode has been used as well.

The last buckling load is the column buckling of the stringers. To analyze this, first the dimensions of the stringers have to be determined from the critical stresses section. The required area for the stringers is 123.75 mm^2. As a design choice, an U-shape stringer was selected with all sides measuring 14 mm and a thickness of 3 mm due to the limited space in the wingbox at the tip. The critical stress for the column buckling can be calculated using Equation 12.11:

$$\sigma_{\text{crit}} = \frac{K\pi^2 E I_{xx}}{L^2 A} \tag{12.11}$$

where I_{xx} is the moment of inertia, A the cross-sectional area, and K the column buckling coefficient dependent on the end constrains. This coefficient equals 4 when both ends are clamped, which is the case for the stringers between the ribs.

Based on these three buckling modes, an algorithm was programmatically constructed to space the ribs. This was done by calculating the critical stresses between the pre-determined ribs. The stresses are then evaluated with σ_{safe} and τ_{safe}, which represent the yield stress and the maximum shear stress including a safety factor. If the critical stress is lower, an extra rib is placed in the center of the pre-determined ribs. This procedure is done until the critical stress becomes higher then the safety stresses. Since the buckling coefficients are dependent on the distance between the ribs, these have to be calculated every cycle a new rib is placed. This was done automatically by interpolating the graphs in the program.

With a thickness of 1.25 mm, the number of ribs needed to prevent sheet buckling became very large. Therefore, the decision was made to increase the skin thickness to 3 mm and the web to 2 mm. With this approach, the number of ribs per section was determined for the most critical buckling mode. The result of the rib spacing can be seen in Figure 12.9. In addition, rib number 9 (counter from the root chord) was shifted 3 cm towards the root. This was done to support the structure responsible for the rotation of the ailerons and the HLDs. With this small shift, the buckling requirements are still met. In Figure 12.10, the final cross-section of the wingbox of the wing is shown.

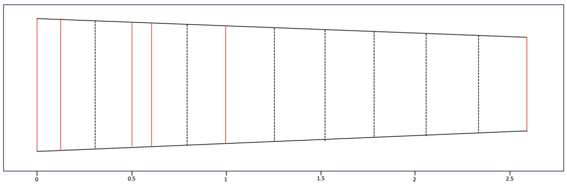

Figure 12.9: *The finalized rib placement with red being the pre-determined ribs and the dashed lines the assigned ribs.*

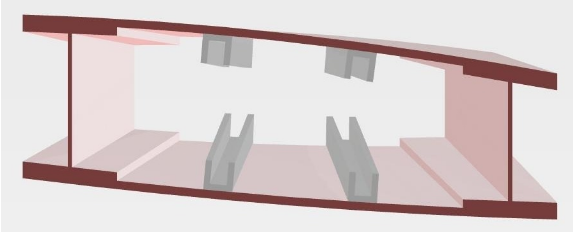

Figure 12.10: *The final wingbox cross-section design of the main wing.*

12.2.4. Empennage Structure Design

With the empennage-configuration of this aircraft being an H-tail, this poses some significant changes compared to conventional structural design. To start, booms will have to be designed to transfer the forces of the empennage to the main body. Besides that, conventionally, the fuselage will have to endure torques caused by the vertical stabilizer [48], though in this case that will no longer be required. Finally, the structure of the horizontal and vertical stabilizer themselves will need to be carried out.

Boom Sizing

As the main purpose of the booms is to transfer the load of the horizontal stabilizer to the main body. Since it is a long slender structure, the critical load is again expected to be the bending moment, in this case due to the downforce and structural weight of the empennage combined (acting in the same direction). This can be seen in Figure 12.11. To take into account the most critical scenario, the maximum downforce generated by the horizontal stabilizer, which would be at the dive speed, is taken. According to FAA Guidelines[49], the dive speed should be at most 1.25 times the maximum cruise speed; hence, 110 $\mathrm{m\,s^{-1}}$ was taken as the speed to design for. Additionally, the maximum negative lift coefficient of -1 of the horizontal stabilizer and the first estimated structural weight of 10 kg of the empennage are taken as loads to be transferred. The loads are transferred through two booms; hence, the total magnitude of the forces is divided by two.

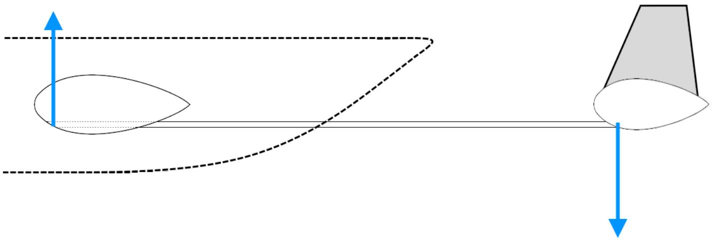

Figure 12.11: *The Free-Body Diagram of the booms used to connect the H-tail to the main fuselage.*

As such, to stiffen the booms against a bending moment in that direction, an elliptical boom is opted for, striking a compromise between structural efficiency, aerodynamics, and manufacturability. The area moment of inertia of an elliptical shape is calculated by Equation 12.12[50]:

$$I_x = \frac{\pi \cdot (a \cdot b^3 - a_i \cdot b_i^3)}{4} \tag{12.12}$$

with a being the semi-major axis and b the semi-minor axis of a horizontal thin walled ellipse (in case $b > a$, b becomes the semi major axis and a the semi minor axis). The thickness is assumed constant throughout, and equal to $a - a_i = b - b_i$. With this information and the free-body diagram, the thickness of the booms can be determined, again taking into account a safety margin of 1.5 on top of the highest load the tail is expected to generate during operation. The distance between booms is already set at its maximum to be able to integrate with the other subsystems (such as not intersecting with the propeller). In the end, this resulted in a boom of required stiffness of I_y (where the y axis corresponds to the global coordinate system) equal to $2.339 \cdot 10^6$ mm^4. A minimum width 75 mm and minimum height 180 mm boom (at the trailing edge) with thickness 2 mm throughout was chosen, providing a moment of inertia of $2.470 \cdot 10^6$ mm^4, thereby satisfying the minimum requirement. In reality, the boom will be tapered to be even bigger at the root; however, at this stage of the design, the boom is modeled as having the smaller dimensions throughout, thereby underestimating its stiffness at while still satisfying the requirement. Furthermore, a maximum deflection can be calculated with the following formula:

$$v_b = \frac{PL^3}{3EI} \tag{12.13}$$

Table 12.3: *Boom structural outcome*

Structural Parameter	Value
Maximum boom downward deflection [m]	0.1025
Maximum Downwards Force [N]	3485
Boom structural weight [kg]	5.54
Boom Length [m]	2.5
Critical Buckling Force [kN]	71

The result of the structural calculations of the booms can be found in Table 12.3, and all values have been deemed within the margin of safety.

Horizontal Stabilizer Wingbox Design

The wingbox of the horizontal stabilizer is design similarly to the one of the main wing. The loads acting on the surface include structural, lift, and drag distributed loads. No point forces are present for the horizontal tail. Based on the load distribution and using the same formulae presented in NVM analysis, the NVM diagram can be computed.

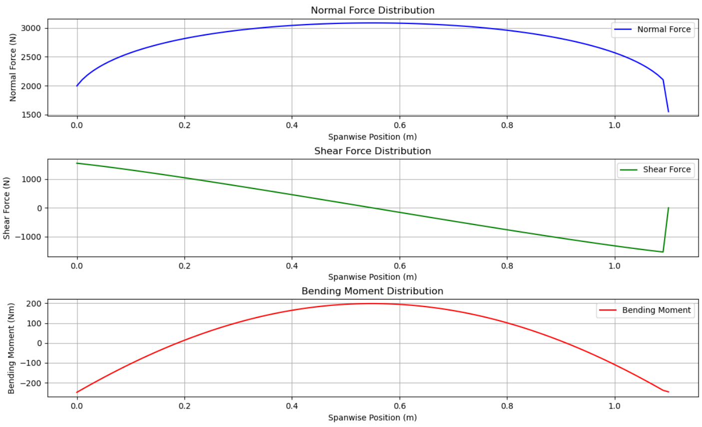

Figure 12.12: *The NVM diagram of the full span of the horizontal stabilizer.*

For this analysis, the full span was used to simulate the loads. Since the tips of the stabilizer are connected to the vertical stabilizer, a decision was made to assume that the wingtips have a fixed constraint (AS-STR-13). This assumption is necessary to determine the reaction moments at the tips. The standard formulae to determine these are presented in Equation 12.14 and 12.15[6].

$$M_A = \frac{1}{b_h^2}\int_0^{b_h} y(b_h - y)^2 f(x)\,dy \tag{12.14}$$

$$M_B = \frac{1}{b_h^2}\int_0^{b_h} y^2(b_h - y) f(y)\,dy \tag{12.15}$$

with b_h being the span of the horizontal stabilizer and $f(x)$ the load function. With these reaction moments determined, the NVM diagram can be computed. This is given in 12.12. The abrupt variation at the end is caused by the included reaction force.

As explained in Critical Stresses, the required moment of inertia, and consequently the required boom areas, could be computed. Based on this, the shear flow analysis could be performed. From this, the minimum critical thickness of 0.77 mm was found (including the correction factor of 3). This shows that shear flow is not the limiting factor. Therefore, for an initial thickness estimation for the buckling characteristics, a thickness of 1 mm was chosen. Using the same algorithm as presented in Rib Spacing, the ribs of the horizontal stabilizer can be spaced. To do this, a L stringer cross-section was chosen, since the required area of the stringers was significantly smaller, which made the dimensions less contained. Given the initial thickness, the required extra ribs in addition to the pre-determent ribs were determined to be 12, which was deemed too large of a number. Therefore, the thickness was increased to 2 mm. This resulted in a total amount of 6 extra ribs, which was accepted. In Figure 12.13 and Figure 12.14 the final wingbox of the horizontal stabilizer can be observed.

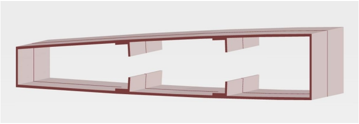

Figure 12.13: *Rib spacing overview of the model*

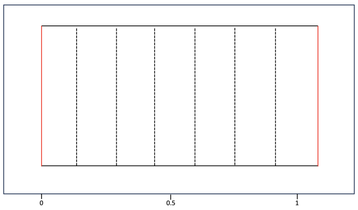

Figure 12.14: *The final rib spacing of the horizontal stabilizer*

Vertical Stabilizer Wingbox Design

For the vertical stabilizer, a different approach for the wing loading was taken. Since the stabilizer is positioned vertically, the structural load has no effect on the internal bending and shear load of the wing itself. Therefore, it was not included in the analysis. As for the lift distribution, a simplified model was assumed, since the actual lift distribution has not yet been obtained for this stage of the design. Therefore, AS-STR-14 assumes that the lift distribution over the vertical stabilizer is uniform and scales with the generated lift for the highest possible sideslip angle. The constraints for the wing tips were assumed to be fixed ends. Although this assumption does not represent the reality fully, it was deemed acceptable as it increases the bending loads at the tip, where the cross-section is smallest and therefore most critical. Following the steps taken in the previous wingbox sizing, the NVM diagrams were computed. These can be observed in Figure 12.15.

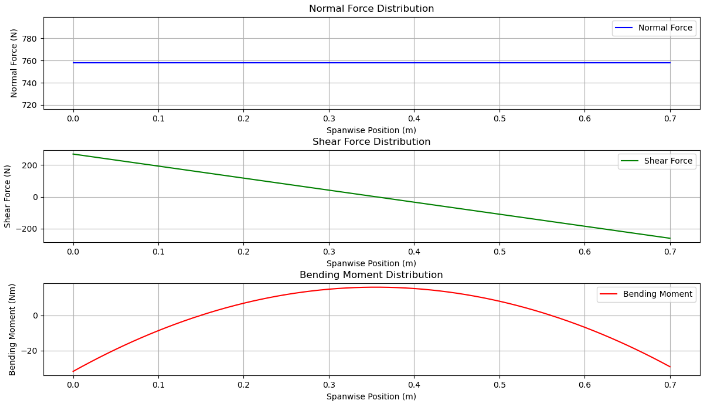

Figure 12.15: *NVM diagram for the vertical stabilizer.*

As a design decision, the spars were allocated a position of 0.1 y/c for the front spar and 0.35 y/c for the rear spar. This small range was necessary to leave space for the rudder, which has its extreme leading edge position at 0.4 y/c. In a similar manner to the previous two cases, the required moment of inertia and boom area were calculated and divided. However, it was decided to use two stringer in contrast to the other two wingbox designs. This choice involves the very small length of the wingbox at the tip. With these values obtained, the shearflow analysis was performed. As expected, this outcome is not limiting for the thicknesses of the skin and web. A similar initial thickness of 2 mm as in Table 12.2.4 was assigned for both the skin and the web.

Again, the same rib spacing algorithm was used. Pre-determined ribs were placed at the root and tip, but a rib was also placed at equal distance from the horizontal stabilizer as the wing tip rib. This spacing makes sure that the two stabilizers can be connected and leaves room for needed servos to control the horizontal stabilizer. The most critical spacing was selected of the 3 modes, and a rib spacing was obtained. This spacing is made graphical visible in Figure 12.16b, while the cross-section of the wingbox is given in Figure 12.16a.

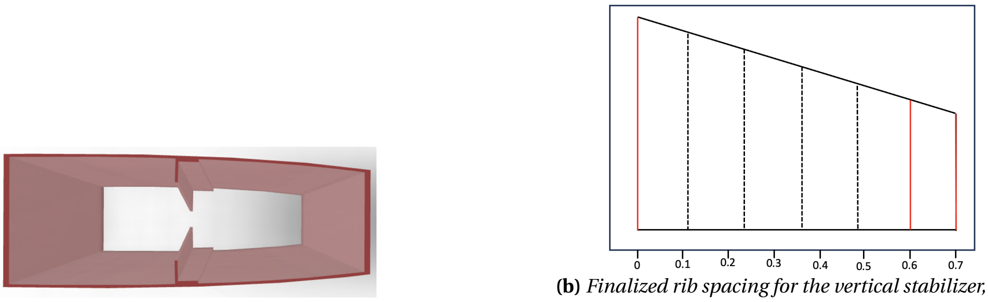

(a) *The cross-section of the wingbox of the vertical stabilizer.*

(b) *Finalized rib spacing for the vertical stabilizer, with in red the pre-determined ribs and dashed the required ribs.*

Figure 12.16: *Comparison of structural configurations for the vertical stabilizer.*

12.2.5. Fuselage Design

Similarly to the wing, the fuselage will be subjected to certain point and distributed loads. From the armaments and aerodynamics groups, the general outer dimensions of the fuselage have already been provided, as well as the application of 4 "rails" around the inside of the fuselage. As such, the fuselage skin thickness will need to be determined, based on the loading of the fuselage.

Fuselage loading

In static equilibrium, the fuselage is expected to be loaded by the weight of several subsystems (including the weight of their structural integration), the lift from the main wing, and finally its own weight. From this, the free-body-diagram of the fuselage was constructed, given in Figure 12.17, based on which the structural analysis is performed. In this case, the weights of the subsystems at the nose and tail of the fuselage are modeled as acting through the furthest point, thereby overestimating the bending moment they cause. On top of that, the mass of the nose landing gear was lumped with the detection suite, further solidifying the conservative nature of the estimate.

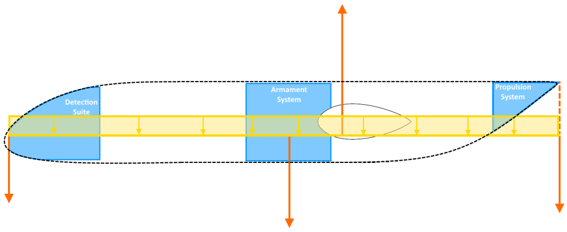

Figure 12.17: *Free-Body-Diagram of the Fuselage*

From the FBD, the peak moment in the fuselage can be found as described in NVM Analysis, with the peak moment occurring at the quarter chord point (where the lift force was approximated to act through), and the peak shear force also acting through this point (from the left limit), equal to 646 N m and 604 N, respectively.

Fuselage Stiffness Determination

From the peak moment and shear force, the stresses the fuselage must endure, and therefore the stiffness it must provide, can be determined. The bending moment is calculated using Equation 12.5, while shear is given by Equation 12.16.

$$\tau = \frac{VQ}{It} \tag{12.16}$$

From these formulae, it can be seen that the peak bending stress will occur at the furthermost point vertically from the neutral axis, while the peak shear stress will occur at the neutral axis (where Q is largest). In the case of the fuselage, if made to endure peak stress, utilizing all the strength of the material, a required inertia of $5.664 \cdot 10^5$ mm^4 is determined.

In addition to enduring bending and shear forces, the fuselage must also maintain its shape for aerodynamic purposes and provide stiffness for the integration of subsystems. This is achieved through adding longerons longitudinally and frames laterally. Due to the required presence of rails to move the armament subsystem throughout the fuselage, the function of the rail and longerons will be combined to offer further weight savings, as the rails already act like stiffeners, being distributed away from the neutral axis and attached to the fuselage skin. Finally, the placement of frames will be adjacent to important payloads or modules, such as to the rear of the detection suite, next to the armament system, and the landing gear.

In practice, due to the required presence of rails from the armament system, the longerons alone provide a stiffness of $305 \cdot 10^5$ mm^4 per longeron, with 4 of them present within the structure.

Following this large stiffness provided by the longerons, the fuselage's moment of inertia is approximated as coming solely from the longerons, neglecting the contribution of the skin (and therefore being conservative). With these values, the peak shear stress for a 1 mm outer shell is found to be 2.07 MPa (taking into account the skin contribution to the moment of area, but not the moment of inertia, thereby over-estimating the stress and still under-estimating the stiffness). Similarly, the peak normal stress due to the moment is found to be 2.34 MPa.

Table 12.4: *Buckling properties*

Structural Parameter	Value
Maximum frame distance [mm]	670
Clamping Condition	$SSSS$
Buckling Coefficient (C)	4
Skin Thickness [mm]	1
Maximum Compressive Stress [MPa]	2.336
Critical Buckling Stress [MPa]	3.526
Minimum Margin of Safety	1.509

Finally, the buckling strength of the fuselage must be considered. For this, it is assumed that the top part of the fuselage is "lumped" to the maximum height and bears the maximum stress as per the flexure formula, and be subjected to the buckling of a flat plate, governed by Equation 12.9. The structural parameters used for calculations are seen in Table 12.4. Due to the conservative nature of the calculation (with the compressive stress used for calculations already containing a safety factor of 1.5, before the MOS of the buckling is computed), the thickness is deemed sufficient with this margin of safety for the fuselage skin.

12.2.6. Fuel Tank Design

In this subsection, the design of the fuel tanks is described. The fuel used by the vehicle is fully stored in the wings. To determine if a sufficient volume is present in the wings, the internal volume of the wingbox was calculated using the values given in Table 12.5. As the cross-sectional area decreases linearly over the span, the calculation becomes straightforward, as can be seen in Equation 12.17.

$$V_{wingbox} = \frac{L}{2}(A_r + A_t) \tag{12.17}$$

Table 12.5: *Values used to Determine the Fuel Tank Design*

Characteristic	Value
Root Wingbox Cross-Sectional Area [m^2]	0.0165
Tip Wingbox Cross-Sectional Area	0.00842
Half-Span [m]	2.6
Wingbox Volume [L]	32.406
Required Fuel Mass[15] [kg]	20
Fuel Density (Jet-A1[16]) [gL^{-1}]	0.804
Required Fuel Volume per wing [L]	8.04

Looking at the values in Table 12.5, it can be concluded that the wingbox provides a sufficient volume for the fuel needed for the required performance. Given the required fuel volume, it can be determined that the fuel tank must be placed between the root and rib number 7, leading to a total available fuel tank volume of approximately 12.4 L per wing. It must be noted that a small volume loss is expected as a result of the stringers in the wingbox. However, since the volume of the tank is already rounded up due to placing the fuel tank in between the ribs, this is seen as a negligible contribution. The tank will be a fuel tank made of aluminum with a self-seal layer, often used in military applications to protect the fuel tanks from munitions[17].

---

[17] URL https://atlinc.com/industrial.html, Cited 22 June 2025

12.2.7. Engine Mounting Design

This subsection discusses the engine mounting design. The mount is designed to handle the weight, thrust, torque, and vibrations of the engine. The initial material selected for the mount is high-strength AM350 steel, as the engine has to apply high loads on a relatively small structure, for which a sufficiently strong material is needed. The structure connects each engine point to the firewall, using circular rods with a diameter of 5 mm.

The engine mount design process follows a two-stage optimization approach: first, the rod placement configuration if optimized; second, the structural dimensions for the selected configuration is optimized. The mount is attached to a firewall that is assumed to not move. The primary static loads include engine weight and maximum thrust. The torque is assumed to equally affect each mounting point, as these are placed equally around the center of gravity of the engine. The design constraints require that the stress on the mount is lower than the yield stress, divided by a safety factor of 1.5. The buckling constraint is found by determining the critical load for Euler buckling. For vibrations, the natural frequency of the mount is determined. To avoid resonance, the natural frequency should be larger than the excitation frequency, multiplied by a safety factor of 2.0. The connections are optimized by setting up a global stiffness matrix, and determining the stress on the mount for various configurations of engine-firewall point connections. After this process, the values displayed in Table 12.6, Table 12.7, and Table 12.8 were found. As can be seen from the values presented, the structure can withstand the torque, and the axial and vibrational loads applied by the engine.

Table 12.6: *Stress Analysis*

Max Stress [MPa]	5.05
Yield Stress [MPa]	1100

Table 12.7: *Frequency Analysis*

First Natural Freq. [Hz]	902.21
Actuation Freq. [Hz]	108.33

Table 12.8: *Maximum Displacements*

Disp. x (thrust) [mm]	0.001
Disp. y [mm]	0.004
Disp. z (weight) [mm]	0.008
Rotation x [deg]	0.026
Rotation y [deg]	0.005
Rotation z [deg]	0.115

12.2.8. Landing Gear Design

This section will discuss the design process and justifications for the landing gear, which will be based on comparable vehicles and most importantly this vehicle's specific dimensions and characteristics. A fully retractable tricycle landing gear configuration was chosen for this design: it consists of two main landing gear (MLG) struts located aft of the CG, retracting forwards, and one nose landing gear (NLG) strut located forward and slightly offset from the centerline, retracting backwards.

Additionally, the landing gear is designed assuming that taxiing, take-off, and landing will solely take place on paved runways. Potential later iterations can integrate bigger tires to adjust to more rough terrain.

Positioning

Once the drone's configuration with its preliminary longitudinal dimensions, as well as wing and tail sizing, are known, the design process of the landing gear is initiated. First, the main landing gear positioning is determined by looking at the configuration of the vehicle, and where it was already most structurally strong, so the use of unnecessary additional structures can be avoided. The location of the wing is inherently one of the design's most strong places because of the wing spars, wing boxes, and stringers. It is important to ensure that there is enough distance between the CG and the MLG, which must be aft of the CG, to prevent tipping back. Therefore, the MLG is positioned at the most aft location under the wing, at the trailing edge, 2.8 m from the nose. It was decided to place the MLG where the booms cross the wing. Locating the MLG to align with the booms comes with additional structural benefit and provides storage room for the MLG when retracted. Therefore, the MLG is positioned 0.55 m from the centerline of the fuselage, which is enough to ensure lateral stability on the ground.

To ensure longitudinal stability on the ground, the nose landing gear is positioned as far forward as allowed by the fuselage design. This is just aft of the detection suite, at 0.5 m from the nose. However, this is also where the armament system is located. Therefore, because of the barrel lying on the centerline of the fuselage, not enough space is available to store the nose landing gear during flight. To account for this problem, a simple solution was offered: namely, placing the nose landing gear with a slight offset of 115 mm from the centerline. Therefore, when retracted, the NLG lies right besides the barrel of the gun, as seen in Figure 12.18.

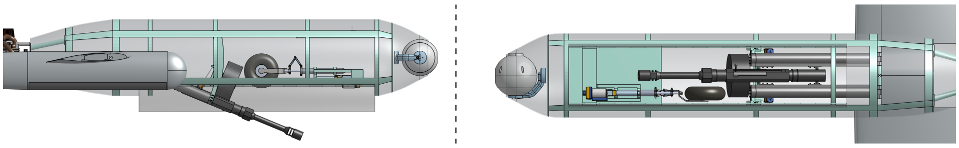

Figure 12.18: *Landing gear position when retracted. (Note: detection system substitute is displayed)*

12.2.9. Sizing

The next step in this design is to size the landing gear using the positioning determined in the previous subsection. The technical drawing shown in Figure 12.19 is constructed by plugging all dimensions obtained from previous design steps into a 3D model. The critical condition is given at take-off. During this phase, 90% of maximum C_L should be provided to obtain maximum lift, with a margin to avoid premature stall. Using the C_{L_α} curve (provided by Equation 6.27), the needed rotation angle is determined to be 11°. Using this angle, the lowest points are projected on the technical drawing below, from which it follows that the tail will be the critical point for a potential tail strike, rather than the propellor. This is preferable, as a sudden increase in rotation angle would result in damage to the tail instead of the propeller.

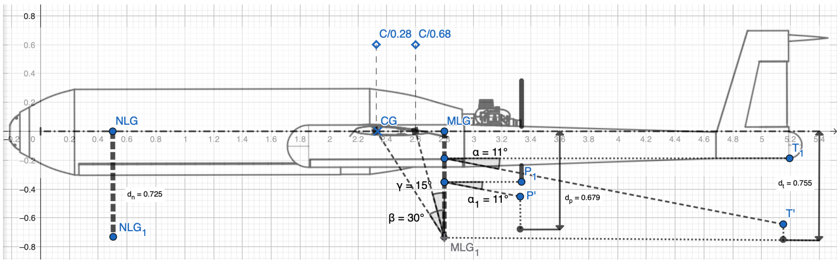

Figure 12.19: *Technical drawing landing gear sizing (dimensions in m).*

The figure above shows the technical drawing plugged into the Geogebra calculator tool[18], which was used to size the landing gear. For all calculations and measurements, the origin of the figure is considered to be the nose of the aircraft. Although this tool does sometimes induce small rounding errors, everything was rounded conservatively. Using this tool, the distance from the centerline to the lowest points of the vehicle in full rotation (α) were projected. The most critical points were determined to be the bottom of the propellor (P_1) and the tip of the tail (T_1). Their lowest possible position projections are indicated with P' and T'. To ensure the propellor is never scraped during landing and take-off, a standard ground clearance of 9 inches is needed.[19] Rounding off conservatively, a clearance of 23 cm is implemented. This results in a minimal landing gear size of $d_p = 0.74$

---

[18] URL https://www.geogebra.org/calculator [Cited 15 June 2025]

[19] URL http://www.ae.metu.edu.tr/~ae451/landing_gear.pdf [Cited 15 June 2025]

m. The tail is more critical, however; implementing a clearance of 10 yields a minimal landing gear size of $d_t = 0.755$ m. Conventionally a tail clearence of 15 is required for UAV's [20]. However, 10 is deemed enough clearance for this design considering the the landing gear is sized without wheels and the actual rotation angle will be slightly less then the angle of attack in reality. This is done to simplify conservatively, the 10 drawn in Figure 12.19 is more than . The minimal MLG length as a result of this (0.755 m) is its final size as measured, from the center line to the wheel axis conservatively. Should the rotation angle increase, the clarence dictated by the tail would increase more then the one dictated by the propeller, which means the propeller can under no circumstance be scraped on the ground.

With the MLG size known the tip-back angle of 13.36° can be obtained from the sketch, this is the maximum nose-up rotation of an aircraft at which the tail first contacts the ground, occurring with the landing-gear strut fully extended. The angle between the main wheel's vertical and the center of gravity must be greater than the tip back angle, or 15°, whichever is larger. In this case, an angle of 15°is larger: this yields the most aft CG limit at 0.68C. A CG located aft of this limit would cause the drone to tip back. Similarly, the the most aft CG point possible follows from the projected line at an angle of 30°crossing the center line at 0.28C. A CG in front of this location would cause porpoising and an unachievable elevator input would be necessary to achieve the desired rotation angle. As can be seen in the figure above, the CG is located just within the range, very close to the forward limit. A CG aft of 25°would be preferred during take off to limit porpoising; however, this proved to be unattainable with the current design. Nonetheless, the current design is capable of providing great pitch inputs as a result of the large elevator. This design feature should mitigate the porpoising caused by the CG being aft of the preferred range [21].

The NLG is sized at 0.725 m measured from the centerline of the fuselage to the wheel axis. It is designed to be 3 cm shorter than the MLG. This is because of the limited space in the front of the fuselage, which also hosts the gun bay, and to further prevent tipping back.

Mounting and Design

At this stage in the design only an indication of the mounts and actuator mechanism is given. The struts will use an oleo damper to act as suspension. The landing gear will be actuated by an electrical linear actuator[22], which will act as an additional strut during the deployed state of the landing gear. The current positioning and mounting methods can be seen in Figure 12.20.

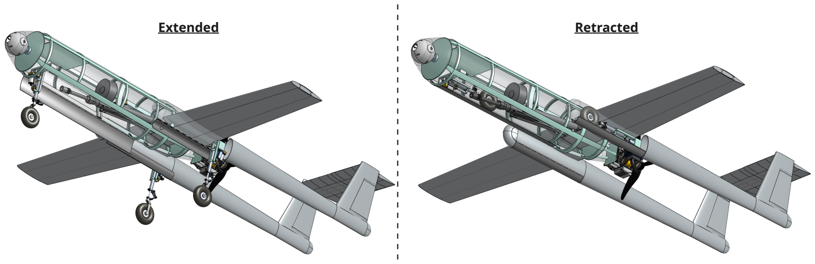

Figure 12.20: *Preliminary design of the landing gear. (Note: detection system substitute is displayed)*

12.3. Design Description

The finalized geometry outlined during the design process Section 12.2 is summarized in the table below.

---

[20] URLhttps://aviation.stackexchange.com/questions/7444/does-the-predator-drones-design-make-a-tail-strike-more-likely-on-takeoff-and-l? [Cited 16 June 2025]

[21] URL http://www.ae.metu.edu.tr/~ae451/landing_gear.pdf [Cited 15 June 2025]

[22] URL https://www.mcmaster.com/products/linear-motion-actuators/electric-actuators-1~/ [Cited 16 June 2025]

Table 12.9: *Finalized wingbox design geometry - All Components*

Main Wing

Property	Value
Front spar x/c	0.3
Rear spar x/c	0.6
Web t [mm]	2
Skin t [mm]	3
Cap t [mm]	4
Cap len [mm]	45
Str len [mm]	14
Str t [mm]	3
Str nr	4
Type	hat

Horizontal Tail

Property	Value
Front spar x/c	0.3
Rear spar x/c	0.7
Web t [mm]	2
Skin t [mm]	2
Str len [mm]	11
Str t [mm]	1.5
str nr	4
Type	L

Vertical Tail

Property	Value
Front spar x/c	0.1
Rear spar x/c	0.35
Web t [mm]	2
Skin t [mm]	2
Str len [mm]	8
Str t [mm]	1
str nr	2
Type	L

Table 12.10: *Finalized fuselage design geometry*

Geometrical property	Value
Skin thickness [mm]	1
Longeron nr	4
Longeron t [mm]	4
Longeron A [mm^2]	1005

Table 12.11: *Finalized boom geometry*

Geometrical property	Value
Height [mm]	180
Width [mm]	75
Thickness [mm]	2

12.4. Verification

An overview of each requirement and the details of how they are met is found in Table 12.12.

Table 12.12: *Requirements compliance for the structure*

Requirement Code	Condition	Result	Met?	How?
SYS-01.07.19	$n = 4$	Structural integrity	Yes	Subsection 12.2.3
SUB-01.4.11.01	Fuel vol≥1608	248	Yes	Subsection 12.2.6
SUB-0.1.22.122.1	Sufficient structural integrity	Structural integrity	Yes	Section 12.2
SUB-0.1.22.122.2	Sufficient structural integrity	Structural integrity	Yes	Subsection 12.2.3
SUB-0.1.22.122.3	$\sigma_{]\text{crit}} \geq 503$ [MPa]	$\sigma_{crit} \geq 503$ [MPa]	Yes	Subsection 12.2.3
SUB-0.1.22.122.4	$\tau_{\text{crit}} \geq 251.5$ [MPa]	$\tau_{crit} \geq 251.5$ [MPa]	Yes	Subsection 12.2.3
SUB-0.1.22.122.5	$\sigma, \tau \leq \sigma_y, \tau_y$	N/A	Yes	Hand Calculations
SUB-0.1.22.122.6	Sufficient buckling performance	N/A	Yes	Hand Calculations
SUB-0.1.22.122.7	$\sigma, \tau \leq \sigma_y, \tau_y$	N/A	Yes	Hand Calculations
SUB-0.1.22.122.8	x position rear span ≤ 0.65 x/c	0.6 [x/c]	Yes	Subsection 12.2.3
SUB-0.1.22.122.9	vol ≥ 5 [L]	29 [L]	Yes	Hand Calculations
SUB-0.1.22.122.10	Required rails	N/A	Yes	Subsection 12.2.5
SUB-0.1.22.122.11	Required frames	N/A	Yes	Subsection 12.2.5
SUB-0.1.22.122.12	L≥ 2.5 [m]	L≥ 2.5 [m]	Yes	Hand Calculations
SUB-0.1.22.122.13	d≤ 75 [mm]	d≤ 75 [mm]	Yes	Hand Calculations

13

Logistics & Operations Concept

In this chapter, the operations and logistics of the system will be described. First, the system's structure will be outlined in Section 13.2, along with the distribution of hardware throughout the Netherlands. The nominal mission profile will then be described in Section 13.3, along with the system's potential applications for other purposes, including peacetime uses. Then, a RAMS analysis will be performed in Section 13.4. Lastly, the logistic support that enables reliable operation will be described in Section 13.5.

13.1. Requirements

The following requirements for logistics & operations have been formulated in the baseline report and additional requirements have been added [7].

- **SYS-10.19.71**: The airborne part of the system shall be capable of being launched in less than 5 minutes from target recognition.
- **SYS-09.19.76**: The reliability of the launch system shall be greater than 90%, in all operational environmental conditions.
- **SYS-10.20.85**: The airborne part of the system shall be capable of being recovered in less than 10 minutes, from end of descent, to a refuelable state.
- **SYS-09.20.88**: The reliability of the recovery system shall be greater than 90%, in all operational environmental conditions.
- **SYS-16.21.109**: The ground communication system shall be capable of communicating with at least 6 airborne systems.
- **SYS-16.21.110**: The ground part of the system shall be capable of data integration and sharing with the military structure of the user.
- **MIS-19.28**: The system shall be safe during all pre-mission, mission, and post-mission phases.
- **MIS-14.33**: The manufacturability and maintainability of the system shall be performed using standard industrial or military equipment and shall comply with the following specifications.
    - **SYS-22.33.175**: All line-replaceable units shall be replaceable by field personnel using basic hand tools.
    - **SYS-22.33.176**: Subsystems such as the propulsion subsystem, avionics bay, or landing gear shall be replaceable at military maintenance depots using standard military workshop equipment.
    - **SYS-22.33.177**: Repairs requiring structural restoration shall be performed in the manufacturer's facilities.
    - **SYS-14.33.178**: All structural materials shall be readily available through global suppliers with lead times under 2 weeks.

13.2. System Composition

For any defense project, it is not sufficient to design a stand-alone system. The real power lies in integrating into a wider defense network, enabling systems to communicate and complement one another. In the case of CEDI, the decision was made not to try to tackle the complex task of airspace surveillance and detection with the system itself. Very complex systems already exist for this task that would outperform anything within CEDI's budget anyway. Blending into the existing infrastructure allows access to this high-quality targeting data basically for free. The CEDI system can also contribute to the system by providing sensor data from unique locations. In NATO, the requirements for this interoperability capability for unmanned aircraft are specified in NATO AEP-84 VolII(A)(1) [14]. To comply with NATO standards, the prescribed structure will be followed, as shown in Figure 13.1; it includes:

- **C4I**: Command, Control, Communications, Computer, and Intelligence
- **AV**: Air Vehicle
- **UCS**: UAV Control System
- **LRR**: Launch, Recovery & Replenishment

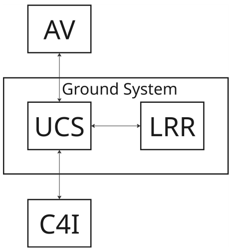

Figure 13.1: *System Functional Architecture*

The **C4I** is the central Command & Control system, which is part of the existing NATO infrastructure. It provides target information, tracking, mission definition, and Common Operational Picture (**COP**).

The **UCS** is the system that ties all segments together. It controls the **AV**, provides a human-machine interface for operator input, receives telemetry and payload data, processes it, and displays it to the operator, communicates with other systems, and sends useful information back to **C4I**.

The **AV** is the interceptor itself. It performs the physical part of the mission, specifically the interception and destruction of enemy attack munitions. Its sensors also provide battlefield intelligence, which is fed into **C4I** via the **UCS**.

The **LRR** is the ground system at the operating bases. It provides launch, recovery, and replenishment capabilities to the **AV**. Depending on the mission and alert level, the provided launch time may be as short as 5 minutes. Also, an **ICT** (Integrated Combat Turnaround) can be performed. This is a quick refueling and rearmament procedure for when the **AV** needs to get back in the air quickly during a prolonged attack.

13.2.1. Ground System Design

The **AV** has already been described extensively in the rest of this report; the **C4I** is only a system that needs to be interfaced with. That leaves the **UCS** and **LRR**. As these systems are only supporting operation, the level of detail in design is less than for the **AV**. However, some explanation is still provided.

13.2.2. UAV Control System

The **UCS** is most importantly responsible for commanding and controlling the Air Vehicles. It further communicates with the **LRR** system and **C4I** to coordinate its operations with what is happening on the rest of the battlefield. As there is significant autonomous capability in all flight phases, including detection, tracking, and engagement, one **UCS** can be used to control multiple **AV**'s. The elements are illustrated graphically in Figure 13.2.

- Core UCS computer
- HCI (Human Computer Interface)
- UCS - AV interface
- UCS - C4I interface
- UCS - LRR interface

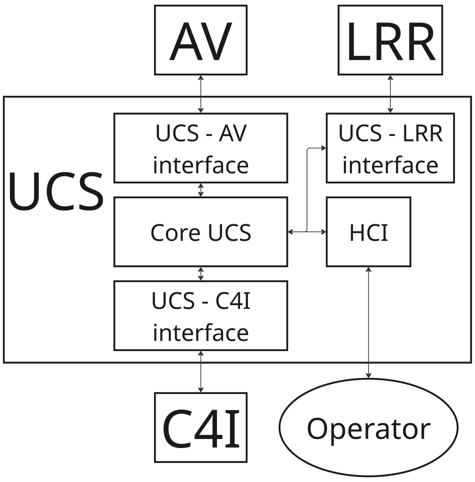

Figure 13.2: *UCS architecture*

The **UCS** will take the physical form of a 20 ft standard container. Depending on the **ROE**. All elements of the **UCS** will be included as shown in Figure 13.3.

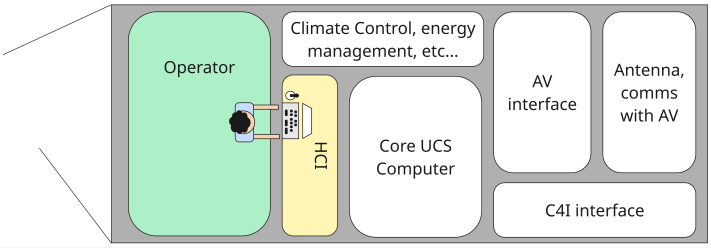

Figure 13.3: *Preliminary UCS layout*

13.2.3. LRR

The LRR is responsible for getting the vehicle ready for flight, launch, recovery, and replenishment of Consumables. At each airfield, an **LRR** system is present. The storage hangar of the **AV** is included in the **LRR**, located near the runway to ensure scramble times of less than 5 minutes. For launch and recovery, a paved runway will be used. The replenishment consists of both refueling and replenishing the armament. A mobile cart is present that can refuel the air vehicle next to the runway during an integrated combat turnaround. This cart will also hold spare, pre-loaded magazines that can be quickly loaded into the drone during refueling.

13.2.4. Defense of Dutch Airspace

The system is designed based on a case study of Dutch airspace defense. In this case, the entire system consists of units stationed at 10 airfields spread over the Netherlands, as shown in Figure 13.4.

Figure 13.4: *Base Locations*

At each airfield, multiple interceptors are stationed along with supporting ground equipment. Ground equipment on each base is **LRR** hardware and a **UCS** system, as the direct communication antenna is integrated into the **UCS**, which then gives a good data and video link during takeoff and landing.

The distribution of defenders is based on the attack simulation described in Section 3.4. A manual optimization was performed to determine the optimal distribution of operating bases nationwide, along with the number of interceptors stationed at each base.

The number of interceptors here refers to the number of Fully Mission Capable (**FMC**) interceptors, which are interceptors that are not in maintenance, being upgraded, or used for training. Historically, the **FMC** rate for military aircraft is 75 % [51], a more exact number for this has to be determined at a later stage when more detail is available. This brings the minimum total amount of interceptors at the bases with 4 **FMC** interceptors to 6 ($4 \div 0.75 = 5.33$), and at bases with 3 **FMC** interceptors to 4 ($3 \div 0.75 = 4$).

Table 13.1: *Air Vehicle System Composition*

Base	**FMC interceptors**	**Total interceptors**
Rotterdam The Hague Airport (EHRD)	4	6
Eindhoven Airport (EHEH)	4	6
Volkel Air Base (EHVK)	4	6
Teuge Airport (EHTE)	4	6
Groningen Airport Eelde (EHGG)	4	6
Vliegbasis Leeuwarden (EHLW)	4	6
Amsterdam Airport Schiphol (EHAM)	3	4
Vliegbasis Gilze-Rijen (EHGR)	3	4
Enschede Airport Twente (EHTW)	3	4
Lelystad Airport (EHLE)	3	4
Total	36	52

13.3. Mission Profiles

In this section, multiple mission profiles will be described, with the main one being the design mission profile for air defense.

13.3.1. Air Defense

The **AV** is being designed for the primary mission of air defense, targeting inexpensive, long-range attack munitions. Although the exact mission profile is dependent on the incoming threat, many operations are still predetermined for this mission. The standard defense mission profile is displayed using two different figures. An Operational Flow Diagram, and an N2 Chart describing continuous communications that do not fit into a discrete step diagram.

Operational Flow Diagram

The OFD shows the mission in discrete steps and decisions. All necessary discrete steps, decisions, and communication between **C4I**, **UCS**, **AV**, and **LRR** are shown. It is divided horizontally into four main segments, as shown in Figure 13.1. The mission is also divided into distinct phases that occur during its execution.

The nominal wartime air defense mission starts with **AV**'s standing on Quick Reaction Alert with a scramble time of less than 5 minutes. They are constantly communicating with the **UCS** to send updates on their system health. The **UCS**, in turn, compiles all this data and updates **C4I** on the total system health and readiness. The flight mission begins with the detection of an enemy attack by a sensor connected to the **C4I** system. Based on information about the attack and the system health, **C4I** can decide to order the deployment of the CEDI system.

The CEDI system will then jump into the next phase, where it receives the scramble command. **AV**'s are woken up from their neutral state and pushed to the runway by operators. While this is happening, the **UCS** receives target information, Rules of Engagement (**ROE**), and the Common Operational Picture (**COP**). This is passed onto the **AV**'s. The **AV**'s take off, climb, and initiate their cruise phase towards the intercept area. As discussed in Chapter 9, the **C4I** network will be able to guide the **AV** towards the target with an uncertainty of 500 m.

Then the most interesting phase starts: the targeting. When the **AV** approaches this target area, it descends to 500 m below the expected target location. As a result, the target is then above the **AV** for sure; the on-board radar is not affected by ground clutter but gets a clear visual of the target against the sky. When target detection and lock are achieved by the **AV** on-board sensors, the **AV** starts to close the distance, opens its weapon bay doors, and moves into the engagement position described in Subsection 7.3.1. The **AV** performs **IFF** (Identification Friend or Foe) using both the hardware described in Subsection 8.3.4 and the onboard computer-vision AI to avoid destroying friendly airborne systems. The **AV** simultaneously checks the **ROE** to check whether it is allowed to decide on engaging itself. Depending on the **ROE** and how sure it is about its **IFF**, it can send a visual - either a video feed or still image, depending on the data link - to the operator in the **UCS** to ask for permission to engage. The **UCS** and operator can decide to pass the decision up the chain of command to **C4I** depending on the **ROE** and their own judgement.

When the decision is made to engage, the grenade launcher shoots. Afterwards, the camera system performs **BDA** (Battle Damage Assessment) to assess the effect of the weapon on the target. Depending on the ammunition status and **BDA** results, the **AV** either tries to re-engage or asks for further commands.

When the decision is made to return to base, the **AV** returns to cruise altitude, cruises back, and approaches the **LRR**. During this, the **LRR** prepares to receive the **AV**. An approach and landing is coordinated, and the **AV** lands.

When an **ICT** (Integrated Combat Turnaround) is to be performed, the AV is received by the **LRR** next to the runway where a refueling and rearmament cart is present. Refueling is initiated by opening the wing tank and filling it up. The rearmament is performed by rotating the gun down; the landing gear is tall enough to leave sufficient ground clearance. An operator can now reach the magazine and replace it; there is sufficient clearance to allow this access.

Continuous Communications N2 Chart

An N2 chart was made that describes the continuous communication between the different systems involved. This is given in Figure 13.5. This allows for mission updates, like aborting or being directed towards a new target.

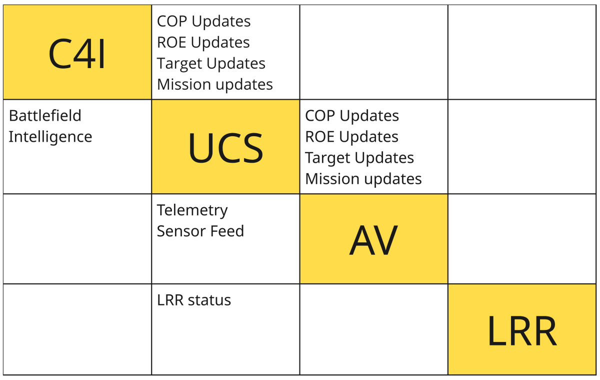

C4I	COP Updates ROE Updates Target Updates Mission updates		
Battlefield Intelligence	UCS	COP Updates ROE Updates Target Updates Mission updates	
	Telemetry Sensor Feed	AV	
	LRR status		LRR

Figure 13.5: *N2 chart displaying continuous communication between different segments*

13.3.2. Peacetime operations

The **AV** is designed primarily for air defense, and an integrated gun is utilized for this purpose. The vehicle can, however, still be applicable during peacetime. A wide range of situations exists where it may be helpful to have a cheap airborne platform with good imaging capability on board. This can be the case in search and rescue operations, surveillance of a secured area or a large event, police operations, or in the monitoring of wildfires using the IR imaging capability. The advantage of the design is that it aims to achieve a low cost per vehicle and low operational costs. Where a high-performance military drone might be overqualified and too expensive to use in such cases, the deployment of CEDI is a cost-effective way to help in these situations while maintaining the operational readiness of the system itself and its crew.

13.4. RAMS Analysis

To ensure the Reliability, Availability, Maintainability, and Safety of the system, it must be analyzed on (and designed for) these qualities. This section analyzes these RAMS characteristics, addressing the expected reliability and availability, an outline of scheduled and unscheduled maintenance activities, and the safety-critical functions within the system.

13.4.1. Safety Analysis

Ensuring the safety of the CEDI system is essential, due to its autonomous operation in hostile environments. The system must be robust against both internal failures and external threats, to ensure that it can continue fulfilling its mission. Because of this, several safety-critical systems have been identified:

- The primary flight controls must maintain full functionality under all nominal and contingency conditions to ensure the aircraft can maintain controllable. Redundant actuators and fault-tolerant flight control algorithms should be implemented to mitigate the risk of loss-of-control incidents.
- A robust collision avoidance system is vital to prevent mid-air collisions during missions, as adversaries may attempt ramming attacks, or the vehicle may encounter other aircraft or obstacles such as towers when flying at low altitude.
- In the event of a communication failure, the autonomous flight system must rapidly and seamlessly assume control to maintain safe operation. This includes the ability to return to base, hold a safe loiter pattern, or continue the mission based on pre-programmed logic, depending on the severity and context of the failure.

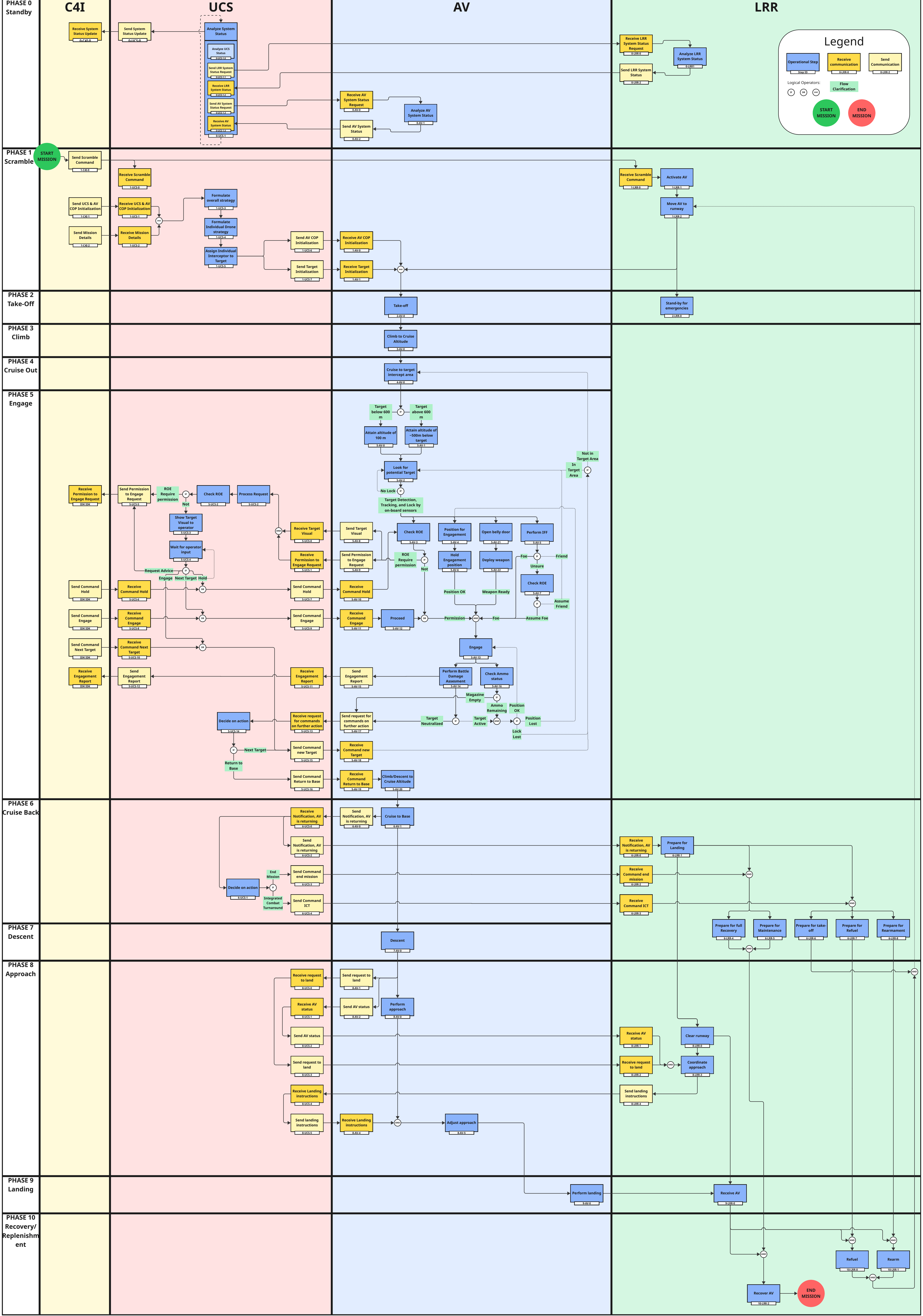
C4I
UCS
AV
LRR
PHASE 0 Standby
PHASE 1 Scramble
PHASE 2 Take-Off
PHASE 3 Climb
PHASE 4 Cruise Out
PHASE 5 Engage
PHASE 6 Cruise Back
PHASE 7 Descent
PHASE 8 Approach
PHASE 9 Landing
PHASE 10 Recovery/ Replenishment
Legend
Operational Step
Step ID
Receive communication
0-LRR-0
Send Communication
0-LRR-2
Logical Operators:
IF
OR
AND
Flow Clarification
START MISSION
END MISSION
Receive System Status Update
0-C4I-0
Send System Status Update
0-UCS-0
Analyze System Status
Analyze UCS Status
0-UCS-1.0
Send LRR System Status Request
0-UCS-1.1
Receive LRR System Status
0-UCS-1.2
Send AV System Status Request
0-UCS-1.3
Receive AV System Status
0-UCS-1.4
0-UCS-1
Receive AV System Status Request
0-AV-0
Analyze AV System Status
0-AV-1
Send AV System Status
0-AV-2
Receive LRR System Status Request
0-LRR-0
Analyze LRR System Status
0-LRR1
Send LRR System Status
0-LRR-2
START MISSION
Send Scramble Command
1-C4I-0
Receive Scramble Command
1-UCS-0
Send UCS & AV COP Initialization
1-C4I-1
Receive UCS & AV COP Initialization
1-UCS-1
Send Mission Details
1-C4I-2
Receive Mission Details
1-UCS-2
AND
Formulate overall strategy
1-UCS-3
Formulate Individual Drone strategy
1-UCS-4
Assign Individual Interceptor to Target
1-UCS-5
Send AV COP Initialization
1-UCS-6
Send Target Initialization
1-UCS-7
Receive AV COP Initialization
1-AV-0
Receive Target Initialization
1-AV-1
AND
Receive Scramble Command
1-LRR-0
Activate AV
1-LRR-1
Move AV to runway
1-LRR-2
Take-off
2-AV-0
Stand-by for emergencies
2-LRR-0
Climb to Cruise Altitude
3-AV-0
Cruise to target intercept area
4-AV-0
Target below 600 m
IF
Target above 600 m
Attain altitude of 100 m
5-AV-0
Attain altitude of ~500m below target
5-AV-1
Look for potential Target
5-AV-2
No Lock
IF
Target Detection, Tracking, and Lock by on-board sensors
Not in Target Area
In Target Area
IF
Check ROE
5-AV-3
Position for Engagement
5-AV-4
Open belly door
5-AV-21
Perform IFF
5-AV-5
ROE Require permission
IF
Not
Hold Engagement position
5-AV-6
Deploy weapon
5-AV-22
Foe
IF
Friend
Unsure
Check ROE
5-AV-7
IF
Assume Friend
Position OK
Weapon Ready
Send Target Visual
5-AV-8
Send Permission to Engage Request
5-AV-9
Receive Command Hold
5-AV-10
Receive Command Engage
5-AV-11
Proceed
5-AV-12
OR
Permission
AND
Foe
Assume Foe
Engage
5-AV-13
Perform Battle Damage Assesment
5-AV-14
Check Ammo status
5-AV-16
Send Engagement Report
5-AV-15
Magazine Empty
IF
Ammo Remaining
Position OK
Target Neutralized
IF
Target Active
AND
IF
Position Lost
Lock Lost
Send request for commands on further action
5-AV-17
Receive Command new Target
5-AV-18
Receive Command Return to Base
5-AV-19
Climb/Descent to Cruise Altitude
5-AV-20
Receive Permission to Engage Request
IDK IDK
Send Permission to Engage Request
5-UCS-5
ROE Require permission
IF
Not
Check ROE
5-UCS-2
Process Request
5-UCS-2
Show Target Visual to operator
5-UCS-3
Wait for operator input
5-UCS-4
Request Advice
IF
Engage
Next Target
Hold
AND
Receive Target Visual
5-UCS-0
Receive Permission to Engage Request
5-UCS-1
Send Command Hold
IDK IDK
Receive Command Hold
5-UCS-6
OR
Send Command Hold
5-UCS-7
Send Command Engage
IDK IDK
Receive Command Engage
5-UCS-8
OR
Send Command Engage
5-UCS-9
Send Command Next Target
IDK IDK
Receive Command Next Target
5-UCS-10
OR
Receive Engagement Report
IDK IDK
Send Engagement Report
5-UCS-12
Receive Engagement Report
5-UCS-11
Decide on action
5-UCS-14
Receive request for commands on further action
5-UCS-13
IF
Next Target
Return to Base
Send Command new Target
5-UCS-15
Send Command Return to Base
5-UCS-16
Receive Notification, AV is returning
6-UCS-0
Send Notification, AV is returning
6-UCS-2
Decide on action
6-UCS-1
IF
End Mission
Integrated Combat Turnaround
Send Command end mission
6-UCS-3
Send Command ICT
6-UCS-4
Send Notification, AV is returning
6-AV-0
Cruise to Base
6-AV-1
Receive Notification, AV is returning
6-LRR-0
Prepare for Landing
6-LRR-1
Receive Command end mission
6-LRR-2
Receive Command ICT
6-LRR-3
AND
AND
Prepare for full Recovery
6-LRR-4
Prepare for Maintenance
6-LRR-5
Prepare for take-off
6-LRR-6
Prepare for Refuel
6-LRR-7
Prepare for Rearmament
6-LRR-8
AND
AND
Descent
7-AV-0
Receive request to land
8-UCS-0
Receive AV status
8-UCS-1
Send AV status
8-UCS-2
Send request to land
8-UCS-3
Receive Landing instructions
8-UCS-4
Send landing instructions
8-UCS-5
Send request to land
8-AV-1
Send AV status
8-AV-2
Perform approach
8-AV-0
Receive Landing instructions
8-AV-4
AND
Adjust approach
8-AV-5
Receive AV status
8-LRR-1
Clear runway
8-LRR-0
Receive request to land
8-LRR-2
AND
Coordinate approach
8-LRR-3
Send landing instructions
8-LRR-4
Perform landing
9-AV-0
Receive AV
9-LRR-0
AND
AND
AND
Refuel
10-LRR-0
Rearm
10-LRR-1
AND
Recover AV
10-LRR-2
END MISSION

- The GPS system is crucial to navigate and coordinate properly with each vehicle. To ensure resilience against spoofing and jamming, the GPS signal should be checked against inertial backup navigation systems, and use signal validation techniques if possible.
- The weapons arming-disarming system is a critical safety barrier against unintended firing of munition. The system must be designed with rigorous fail-safe logic to ensure that arming can only occur under strict authorization and environmental criteria, with disarming protocols always taking precedence under uncertain or degraded conditions.

It is recommended to perform rigorous testing under simulated failure scenarios to validate system behavior and compliance with established safety standards.

13.4.2. Fault Tree Analysis

The following section presents the fault tree analysis for the system, identifying potential failure modes and their causal relationships. This structured breakdown provides insight into the root causes of system-level failures, supporting risk assessment and mitigation planning. The faults are broken down hierarchically, with lower-level faults being causes for higher-level failures.

13.4.3. Subsystem Redundancy

Within the design of the CEDI drone, redundancy for critical hardware is included to ensure the continuous operability of each vehicle. The flight computer, as mentioned in Subsection 8.3.1, is fitted with 3 IMU's, 2 gyroscopes, and 2 barometric pressure sensors. Additionally, each vehicle is fitted with 2 GPS sensors. Lastly, the communication system is designed to be redundant through the vehicle having both a direct communication link and a satellite link, as described in Subsection 8.3.3 and Subsection 8.3.5.

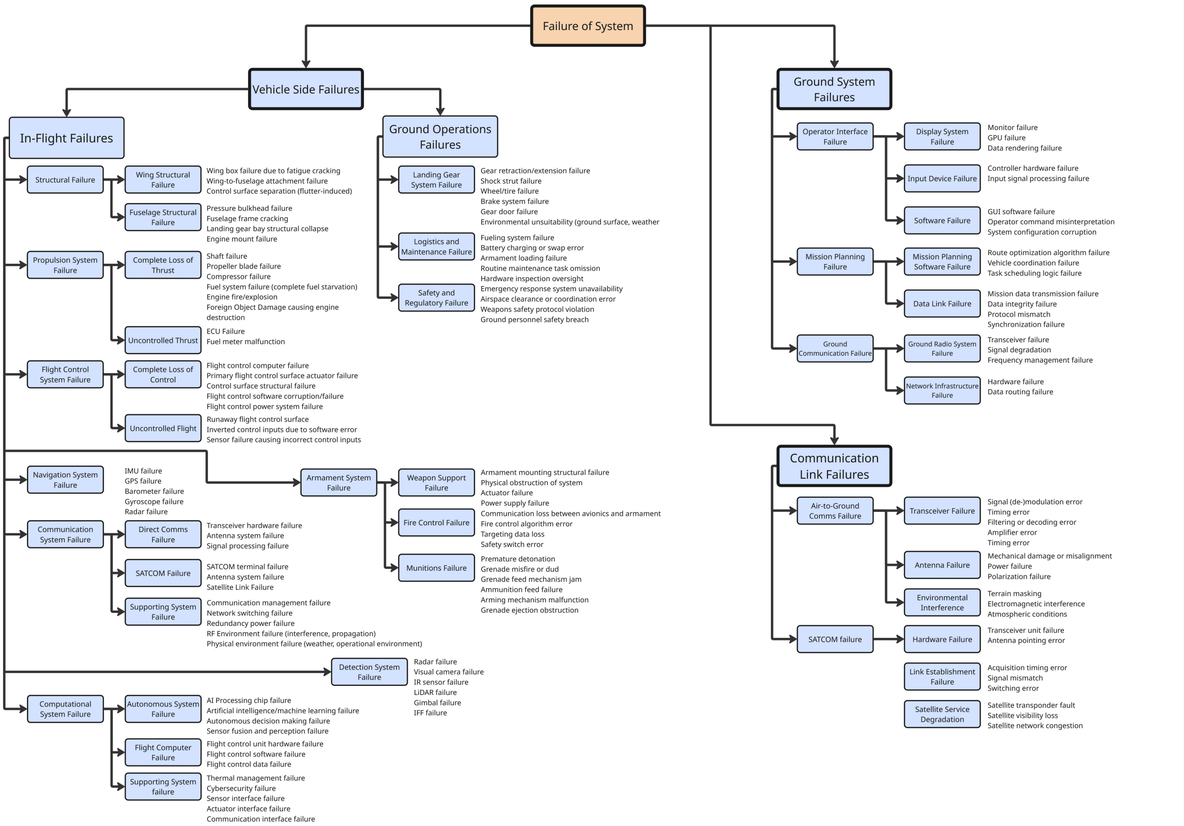

Figure 13.6: *Fault Tree Analysis of the CEDI System*

13.4.4. Fleet Redundancy

In the deployment of the CEDI fleet, both the coverage of the desired area and the reliability by which this coverage can be achieved must be taken into account. To ensure the system as a whole is fully mission capable, a redundant number of vehicles is needed at all times, to take into account several factors: downtime due to servicing of vehicles; loss of vehicles due to the elimination of vehicles during missions; communication failures or navigation errors that render certain vehicles temporarily or permanently inoperable; and environmental disturbances such as adverse weather conditions; signal interference; or unexpected terrain challenges. This redundancy ensures that even in the presence of individual unit failures, the fleet can still provide continuous and complete coverage of the designated area. As described in Subsection 13.2.4, a fleet of 52 vehicles is needed to ensure that 36 vehicles are available at all times. This contingency is based on the FMC standards for aircraft in the US military [51]. However, it is recommended to assess whether this goal is sufficient for the CEDI system, as factors such as the vehicles's autonomous capabilities, the vehicle's resistance to damage, and the ability of the system to respond to local failures. Simulation-based testing, more detailed structural analysis and historical failure rate data from similar autonomous systems can provide a more accurate estimate of the required number of operational reserves.

13.4.5. Maintenance

For the maintenance of the system, operations were divided into three categories: regular inspection and maintenance on base; less common component repairs for which components may need to be ordered; and complete overhauls and upgrades to the system. The list below is intended to be a comprehensive overview, and not an exhaustive list of all maintenance operations.

Organizational Level (Base Operations, Regular Support)

- Daily Inspections: Pre-flight and post-flight aircraft condition checks.
- Basic Maintenance: Fluid servicing, battery maintenance, minor component replacement.
- System Diagnostics: Fault isolation and troubleshooting.
- Scheduled Maintenance: regular inspection moments after a certain amount of flight hours.

Intermediate Level Interventions and Repairs (Regional Support)

- Component Repairs: Avionics, actuator, and sensor repair and calibration.
- Engine Maintenance: Engine inspections and minor repairs (e.g. seal replacement).
- Structural Repairs: Primary and secondary structure maintenance.
- Software Updates: Mission software and flight control system updates.

Complete Overhauls (Manufacturer Support)

- Design changes and capability upgrades.
- Complete replacement of critical systems (e.g. engine replacement).
- Technology Refresh: Avionics and systems technology updates.

13.5. Logistic Support

The logistical support framework for the CEDI system leverages existing military base infrastructure while introducing specialized support equipment and procedures for the system. The CEDI system is designed for rapid deployment and sustained operations with a minimal logistical footprint. In this section, the required support infrastructure, equipment, and components are described and categorized into various aspects of support logistics.

First, taxiing is performed by operators, moving the **AV** to the start of the runway by hand. The Air Vehicles are relatively lightweight, making it easy for the operators to push them to their start positions. For take-off and landing procedures, it is assumed that the system can be used with existing runway infrastructure and air traffic control procedures. Additionally, the airbase should house a dedicated hangar space designed for both long-term aircraft storage and daily operational readiness. The layout should accommodate maintenance bays equipped with tooling and diagnostic systems for regular maintenance and inspections.

The airbase should also support multiple fuel delivery configurations to meet both high-tempo operations and routine servicing. Standard military refueling stations would provide fuel dispensing using the existing Jet-A fueling infrastructure and can accommodate multiple aircraft simultaneously. For rapid deployment scenarios, a mobile fuel cart system would be used to enable quick turnaround. In parallel, the base supports battery charging and electrical energy management. A centralized charging station is equipped to service **AV** batteries with fast-charge capability, thermal management, and charge monitoring. Surge-protected power lines and backup generators should ensure continuous availability, while battery health diagnostics support preventative maintenance and safety compliance.

Finally, rearming the system is designed to be a simple and efficient manual process, minimizing ground time and personnel requirements. The primary armament consists of a grenade launcher with detachable magazines, each pre-loaded with a set number of grenades. Rearmament is accomplished by manually removing the spent magazine and replacing it with new units. As the landing gear provides clearance under the fuselage, and the magazine is removable when the armament system is deployed, it is possible to reload the system on the ground without using auxiliary equipment.

13.6. Verification

An overview of each requirement and the details of how they are met is found in Table 13.2

Table 13.2: *Requirements compliance for the logsistics & operations*

Requirement Code	Condition	Result	Met?	How?
SYS-10.19.71	$t_{launch} \leq 5$min	unknown, likely w/in limits	-	-
SYS-09.19.76	Reliability ≥ 90%	unknown, high	-	-
SYS-10.20.85	$t_{recovery} \leq 10$min	unknown, likely w/in limits	-	-
SYS-09.20.88	Reliability ≥ 90%	unknown, high	-	-
SYS-16.21.109	$n_{vehicles} \geq 6$	8	Yes	Subsection 13.2.1
SYS-16.21.109	Data integration capability	N/A	Yes	Subsection 13.2.1
MIS-19.28	Safe state	N/A	Yes	Chapter 13
MIS-14.33	Standard equipment used	N/A	Yes	Subsection 13.4.5
SYS-22.33.175	Component replacement on base	N/A	Yes	Subsection 13.4.5
SYS-22.33.176	Subsystems replaceable at depots	N/A	Yes	Subsection 13.4.5
SYS-22.33.177	Major repairs at manufacturer	N/A	Yes	Subsection 13.4.5
SYS-22.33.178	Materials available	N/A	Yes	Subsection 13.4.5

14

Technical Risk Assessment

The technical risk assessment, conducted by the team in the midterm report, has been extended for the different components designed in this phase [10]. The risks are assessed using qualitative levels for both likelihood and consequences, as it is difficult to accurately quantify the probability of a risk occurring or the exact severity of its impact. Extremely unlikely refers to an event that is not expected to occur under any foreseeable circumstances, while almost certain refers to a risk that is expected to occur if nothing is done to prevent it. Similarly, negligible impact refers to a risk that leads to no noticeable effect on cost, schedule, or performance, while mission failure means the risk will prevent the project from meeting its primary objectives. This qualitative approach enables clear prioritization of risks without requiring exact numerical data. Risks which became irrelevant during the process have been removed.

14.1. Identification of Technical Risks

Development Phase

TR-DEV-2 **Overly ambitious system requirements**: This risk refers to requirements exceeding what is feasible; drivers include lack of technical experience and optimism bias; impacts include the inability to meet performance targets withing time and/or the allocated budget.
Probability: 2 - Feasibility analysis and supervisory input reduce the likelihood of it happening.
Impact: 4 - Leads to a system design that cannot be fully developed within the given limits.

TR-DEV-3 **Selected concept too complex to implement**: The concept may exceed the team's ability to design and implement; drivers include over-engineering and underestimating complexity; impacts include wasted effort and inability to complete the design development.
Probability: 2 - Concept selection is guided by a feasibility analysis and design trade-off, reducing the chance of choosing an unmanageable design.
Impact: 4 - Overcomplexity may prevent completion within the given time limit.

TR-DEV-4 **Concept lacks modularity**: The system cannot be developed in parallel; the main driver is monolithic design choices; the main impacts include delays due to tight integration dependencies and difficulty in performing design modifications.
Probability: 2 - Even though modularity is considered in the design, integration planning may be overlooked.
Impact: 3 - It can delay development and integration, while also impacting future applications and modifications.

TR-DEV-5 **Poor documentation of design choices**: Key design decisions may not be properly recorded or justifies, making it unclear why certain paths were taken; drivers include lack of responsibility for documentation, time pressure, and prioritizing implementation over record-keeping; impacts include difficulty in retracing reasoning, reduced project credibility, and potential repetition of past mistakes.
Probability: 3 - Documentation is often deprioritized in fast-paced projects.
Impact: 2 - While it may hinder traceability and cause inefficiencies, it does not directly threaten project success.

TR-DEV-6 **Subsystems lack well-defined interfaces**: Subsystems may not connect or communicate properly; the main driver is unclear interface specifications; impacts include delays during integration and potential need for redesign.

Probability: 3 - Teams often work in parallel with loose coordination and lack of proper communication.

Impact: 4 - Could prevent the subsystems from working together, leading to a partial failure.

TR-DEV-7 **Overlooking tolerances and clearances**: The risk leads to mechanical parts not fitting or clashing with each other; drivers include the lack of Design for Manufacturability and a rushed design phase; impacts include physical interference and the inability to assemble the system.

Probability: 3 - Precision is often neglected in the early stages of the design.

Impact: 4 - Can halt the assembly process or lead to a mechanical failure of the system.

TR-DEV-9 **Inaccurate recoil modeling during design phase**: The recoil of the machine gun on the drone may not be properly modeled. Drivers for this could be that too simplified models have been used, which do not grasp the real world dynamics.

Probability: 2 - Might be overlooked in early stage.

Impact: 4 - Flight instability which reduces accuracy could result in mission failure.

TR-DEV-10 **Incorrect load estimations**: The load exerted on the structure could differ from reality; drivers include incorrecty load modelling.

Probability: 2 - Small mistakes can be made.

Impact: 3 - The system can be either over- or under-designed.

Manufacturing Phase

TR-MAN-1 **Long lead time or unavailable components or materials**: Parts may not arrive on time; drivers include late ordering and suppliers issues; impacts include blocked development or rushed integration, delaying schedule.

Probability: 4 - Very likely with short timelines and external suppliers.

Impact: 4 - Can stall the entire project and force suboptimal substitutions.

TR-MAN-4 **Subsystems don't integrate**: Subsystems may be found to be incompatible during assembly; drivers are unclear interfaces and asynchronous development; impact includes time loss and debugging bottlenecks.

Probability: 4 - May happen if interface work isn't rigorously followed.

Impact: 5 - Can prevent the system from working entirely.

TR-MAN-5 **Test environment doesn't match demo conditions**: The demonstration conditions may differ from the real-world environment in which the system operates; drivers include weather and environmental changes and limited testing scenarios; impacts include the system failing in live conditions despite passing tests.

Probability: 2 - Less likely if demo is well scoped and designed.

Impact: 4 - Could lead to failure during operation even if tests were passed.

TR-MAN-6 **Misalignment of gun mounting during assembly**: Slight errors (angular or positional) can arise when installing the automatic gun mount. This could affect accuracy and/or induce vibrations during firing.

Probability: 3 - Manual assembly risk, can be prevented with precision jigs.

Impact: 4 - Results in lower firing accuracy or mechanical failure.

TR-MAN-7 **Improper ammo feed system tolerances**: Precise clearances are important for a belt-fed ammunition system in order to function properly. Clearances can deviate because as a result of machining, material warping, or misaligned guides during assembly. Incorrect clearances can lead to jamming when firing.

Probability: 3 - Small margin of error, low-cost builds.

Impact: 4 - Requires disassembly.

Operating Phase

TR-OPS-2 **Maintenance performed too late**: The necessary maintenance may be postponed; the drivers for this may be that in war time there is limited amount of time for maintenance and the system has to be continuously active; the impact of this will be that the performance of the system will lack the requirements.
Probability: 2 - Maintenance is standard procedure however in wartime it could be that time is limited.
Impact: 3 - Degraded performance of the system.

TR-OPS-3 **Insufficient training of the operators**: The operators might not be trained sufficiently to operate the system; drivers for this risk might be compressed training time due to wartime urgency or the lack of standardized procedures; the impact of this could be improper system setup, calibration or transportation; impacts include system damage, collateral damage and mission failure
Probability: 1 - Training gaps are unlikely since during peace time training operations frequently performed.
Impact: 4 - Untrained personnel results in misuse of the system.

TR-OPS-4 **Severe weather conditions**: Missions could be operated in severe weather conditions; impacts include that the weather conditions are such that it will pass the requirements for which the system has been designed.
Probability: 2 - Very severe weather is unlikely in Europe.
Impact: 4 - The system is not designed for these conditions and the mission might fail.

TR-OPS-5 **Overly ambiguous assumptions for the mission requirements**: The assumptions made for the mission requirements might differ too much from real conditions; drivers for this include overly optimistic or rushed estimates; the impact is that the system's performance may fall short of the required standards.
Probability: 4 - Assumptions tend to be too optimistic.
Impact: 4 - The design can lead to poor mission fit.

TR-OPS-6 **Overheating**: The system might fail due to overheating; drivers include high ambient temperatures combined with insufficient cooling and high processor loads or barrel heat; the impact is that the vehicle catastrophically fail.
Probability: 3 - Overheating is a realistic concern in small high performance systems.
Impact: 5 - Overheating means that the system will crash, which will lead to mission failure.

TR-OPS-7 **Armament jamming:** The armament system might jam due to mechanical reasons; drivers for this include the use of older launcher systems or environmental exposure; the impact is that the vehicle is unable to eliminate targets.
Probability: 1 - Launcher jamming is a rare occurrence.
Impact: 4 - Target cannot be eliminated.

TR-OPS-8 **Misalignment sensors due to vibrations**: The vibrations caused by the piston engine and the machine gun create can gradually cause misalignment of the sensors; the drivers include extended use without re-calibration.
Probability: 3 - Likely over long missions or after multiple deployments.
Impact: 4 - May lead to mission failure.

TR-OPS-9 **Servos on a control surface area seize**: The servos could break which will result in unusable control surface areas.
Probability: 2 - High quality reliable servos are used.
Impact: 4 - The system could crash if it is not controllable.

TR-OPS-10 **Insufficient AI training**: Too little available training data can cause mis-detection.
Probability: 2 - A lot of data of the Shahed (and other potential targets) is available since it is a frequently used drone.
Impact: 4 - Mis-detection will results in less eliminated drones.

TR-OPS-11 **Failing actuators**: The landing gear could get stuck because of a failure in the actuators.
Probability: 2 - Failing actuators is a rare occurrence.
Impact: 4 - Landing without landing gear can cause meaningful of structural damage.

Countermeasures

TR-CMS-1 **Evasive manoeuvres**: Countermeasures, like evasive maneuvers, can be implemented by the enemy; the impact will be that the CEDI drone is unable to eliminate the drones because they are more difficult to hit.
Probability: 4 - Countermeasures are very likely to be implemented.
Impact: 3 - The targets are more difficult to hit and will take longer to eliminate.

TR-CMS-3 **Faster flying drones**: There is the risk that new developed drones fly faster than the reference drones the system is designed for; the impact for this would be that the enemy drones are much harder to intercept and probably will reduce the kill rate.
Probability: 3 - countermeasures like this are very common in a war. However, developing this is harder than CMS-1.
Impact: 3 - Target becomes harder to intercept, which could reduce kill rate.

TR-CMS-4 **Compromised security**: A vehicle could be captured by the enemy, which may obtain valuable information; drivers for this are a crashed vehicle being captured or one being intercepted by the enemy; impacts include that the technical information can be used by the enemy to develop a system that responds to the current level of technology.
Probability: 3 - Downed vehicle could be recovered by the enemy.
Impact: 3 - Critical design features may be revealed. However, outdated technology would be of limited value.

14.1.1. Risk Mitigation and Contingency Plan

This section outlines the mitigation strategies developed for the key risks previously identified in the project. For each risk, both the probability and the impact have been reassessed after the implementation of appropriate mitigation measures. These updated values, along with corresponding contingency plans, are presented in Table 14.1. The contingency plans ensure that, should the risks materialize, effective and timely actions are in place to manage their consequences. The risks are ranked based on a scale from 1 to 5, and quantified based on engineering judgment.

Table 14.1: *Technical Risk Assessment with Mitigation and Contingency plan*

ID	Responsible	Mitigation type	Mitigation	Pre-mitig.	Post-mitig.	Contingency
TR-DEV-2	Maciej	Probability	Early feasibility assessment, peer and supervisor reviews of initial requirements.	2	1	Revise requirements and adjust where possible
		Impact	None	4	4	
TR-DEV-3	Nico	Probability	Prioritizing simplicity during trade-off, including implementation readiness as selection criteria.	2	1	Revise trade-off and prioritize simplicity. Do not over-engineer
		Impact	Decomposition of design into manageable subsystems, planning of design reviews.	4	3	
TR-DEV-4	Douwe	Probability	Promoting modularity from earl stages.	2	2	Assign team to separate modules.
		Impact	Using interface control documents.	3	1	
TR-DEV-5	Stijn	Probability	Assign documentation responsibilities, using templates to track decisions.	3	2	Discuss within team and prevent happening

ID	Responsible	Mitigation type	Mitigation	Pre-mitig.	Post-mitig.	Contingency
		Impact	None	2	2	
TR-DEV-6	Tim	Probability	Ensure proper system engineering practices, regularly checking interface compatibility.	3	2	Revise design chooses and analyze how the system still can be integrated
		Impact	Include integration testing in development timeline.	4	3	
TR-DEV-7	Nico	Probability	Conduct design-for-manufacture reviews.	3	2	Revise safety factors and design flaws
		Impact	Allocate time for physical prototyping.	4	2	
TR-DEV-9	Vincent	Probability	Make sure the system is properly validated	2	1	Revise validation procedure and re-integrate armaments.
		Impact	Apply safety margins to drone design	4	3	
TR-DEV-10	Vincent	Probability	Make sure the system is properly validated	2	1	Revise validation procedure and redesign
		Impact	Apply safety margins to drone design	3	2	
TR-MAN-1	Vincent	Probability	Identify and order long-lead items early, conduct supplier risk assessment.	4	3	Consider multiple suppliers when this happens.
		Impact	Maintain buffer in the schedule for delays.	4	3	
TR-MAN-4	Douwe	Probability	Conduct interface checks prior manufacturing, conduct integration rehearsals with dummy parts.	4	2	Analyze in what way the system still can be integrated
		Impact	Maintain subsystem modularity, keep interface log with version updates.	5	3	
TR-MAN-5	Ariele	Probability	Define test cases based on worse-case scenario.	2	1	Stop further deployment until issue is further analyzed.
		Impact	Add test margins to performance requirements.	4	3	
TR-MAN-6	Ariele	Probability	Test accuracy before mission	3	1	Analyze alignment mounting
		Impact	None	4	4	
TR-MAN-7	Anna	Probability	Validate performance with tests	3	1	Revise testing protocols and replace parts
		Impact	Make sure that the design allows for easy access to gun parts	4	3	
TR-OPS-2	Anna	Probability	Prioritizing simplicity during the trade-off	2	1	Revise procedure
		Impact	None	3	3	
TR-OPS-3	Jan Paul	Probability	-	1	1	Operators should contact experienced operator if system used wrongly
		Impact	A more autonomous design will result in less dependency on operators and therefore less training is needed.	4	3	
TR-OPS-4	Vincent	Probability	None	2	2	If weather is too severe, system has to stop to prevent damage.
		Impact	The system will be designed to sustain severe weather environment till a certain level	4	3	
TR-OPS-5	Maciej	Probability	Be conservative with the assumptions and discuss them with the entire team.	4	2	Discuss effects and decide on the design.
		Impact	None	4	4	

ID	Respon-sible	Mitigation type	Mitigation	Pre-mitig.	Post-mitig.	Contingency
TR-OPS-6	Vincent	Probability	Optimizing internal airflow using airducts	3	2	Retrieve the crashed system since it might be possible to repair.
		Impact	Program the system in a way it will shut down non-critical subsystems first (like sensors)	5	3	
TR-OPS-7	Tim	Probability	Check gun functionality before every mission	1	1	Vehicle should return to base ASAP for check
		Impact	None	4	4	
TR-OPS-8	Vincent	Probability	Perform re-calibration after every mission	3	1	Revise dampening strategy
		Impact	Include vibration dampeners	4	2	
TR-OPS-9	Vincent	Probability	Couple servos for redundancy	2	1	Enter stable glide to land
		Impact	-	4	4	
TR-OPS-10	Vincent	Probability	Implement validation protocols for detection	2	1	Train AI model with recent data.
		Impact	Communication with ground to proceed elimination	4	2	
TR-OPS-11	Vincent	Probability	-	2	2	check actuators
		Impact	Communicate to land on low risk surface.	4	3	
TR-CMS-1	Douwe	Probability	None	4	4	Revision of attack strategy
		Impact	Algorithms which can predict movement target	3	2	
TR-CMS-3	Anna	Probability	Design speed should consider possible countermeasures	3	1	
		Impact	None	3	3	
TR-CMS-4	Anna	Probability	Usage encrypted storage and short data retention. Usage system within the border Netherlands.	3	1	Track the system to recapture it
		Impact	Usage of redundant security layers and proper planning of design obsolescence, ensuring critical features are quickly outdated or remotely invalidated.	3	2	

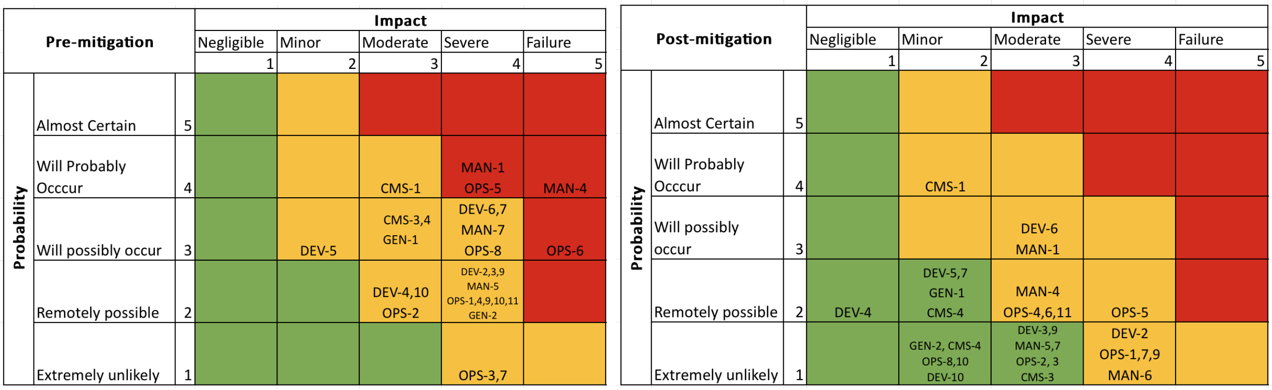

Pre-mitigation			Impact				
			Negligible	Minor	Moderate	Severe	Failure
			1	2	3	4	5
Probability	Almost Certain	5	🟩	🟧	🟥	🟥	🟥
	Will Probably Occcur	4	🟩	🟧	🟧 CMS-1	🟥 MAN-1 OPS-5	🟥 MAN-4
	Will possibly occur	3	🟩	🟧 DEV-5	🟧 CMS-3,4 GEN-1	🟧 DEV-6,7 MAN-7 OPS-8	🟥 OPS-6
	Remotely possible	2	🟩	🟩	🟧 DEV-4,10 OPS-2	🟧 DEV-2,3,9 MAN-5 OPS-1,4,9,10,11 GEN-2	🟥
	Extremely unlikely	1	🟩	🟩	🟩	🟧 OPS-3,7	🟧

(a) *Pre-mitigation risk map*

Post-mitigation			Impact				
			Negligible	Minor	Moderate	Severe	Failure
			1	2	3	4	5
Probability	Almost Certain	5	🟩	🟧	🟥	🟥	🟥
	Will Probably Occcur	4	🟩	🟧 CMS-1	🟧	🟥	🟥
	Will possibly occur	3	🟩	🟧	🟧 DEV-6 MAN-1	🟧	🟥
	Remotely possible	2	🟩 DEV-4	🟩 DEV-5,7 GEN-1 CMS-4	🟧 MAN-4 OPS-4,6,11	🟧 OPS-5	🟥
	Extremely unlikely	1	🟩	🟩 GEN-2, CMS-4 OPS-8,10 DEV-10	🟩 DEV-3,9 MAN-5,7 OPS-2, 3 CMS-3	🟧 DEV-2 OPS-1,7,9 MAN-6	🟧

(b) *Post-mitigation risk map*

Figure 14.1: *Risk map of technical risk pre- and post-mitigation, with unacceptable in red, correctable in orange and acceptable in green*

15

Sustainable Development

In this chapter the sustainability considerations during the design process will be described, first the environmental sustainability will be described in Section 15.1 followed by the social sustainability in Section 15.2 and finally the economic sustainability in Section 15.3.

15.1. Environmental Sustainability

In Aerospace projects, environmental sustainability has become of paramount concern in recent years. The designers can utilize many tools to improve the ecological sustainability of their designs, and many of these are applied in this project. Firstly and most importantly, for ecological sustainability (but also economic as will be discussed hereafter), the aircraft shall be reusable. While many attack drones in the weight class of the CEDI are one-use only, the CEDI shall be a reusable drone, contributing tremendously to its sustainability.

Next, a sustainable material has to be selected of which the aircraft will primarily consist. For this, the eco-costs of the material is minimized. This way all ecological aspects of the manufacture of a material are taken into account, not merely the carbon emissions, which could leave a blind spot to human toxicity in manufacturing, for example. In the end, an aluminum alloy was selected for the design of the CEDI, which, besides having a low eco-cost, is a highly recyclable material, further contributing to the sustainability of the aircraft. Additionally, the fuel consumption of the CEDI shall be minimized by selecting an efficient propulsion system, taking into account that a heavier subsystem will have negative drag consequences. From a back of the envelope perspective, having the CEDI-system available to neutralize an enemy attack could also act as a deterrent, potentially preventing enemy attacks altogether, therefore not only preventing more expensive (and polluting) defense systems being deployed, but also the attack from happening in the first place, which would further reduce negative ecological effects.

15.2. Social Sustainability

In recent years, the global stage has become much less secure, so the social acceptability of a defensive system like the CEDI is expected to become greater and greater. Consequentially, social sustainability is being pursued by having a highly effective defense system against the threat of Shaheds, even acting as a deterrent (as mentioned in Section 15.1), ensuring the system doesn't have to be used too often. By promoting safety in areas deploying the system, which citizens are expected to value highly, this increases the social acceptability (and therefore also social sustainability) of the system.

15.3. Economic Sustainability

To ensure economic sustainability, the cost of the aircraft and its operation needs to be estimated and minimized. Several budget requirements were taken into consideration during the design of the system (USER-BUD-2, USER-BUD-3, and USER-BUD-4). To ensure the design's success, these requirements must be met. To that end, the costs of obtaining, maintaining, and flying, as well as the cost per elimination, were estimated.

The cost of a singular airborne system was computed using a bottom-up approach. The cost of all components purchased off the shelf was compiled, and their integration costs were estimated. The table and diagram of the costs for each system can be seen in Figure 4.3. The final cost of a single unit is estimated to be approximately €82,000, and the total cost of acquiring all 52 Air Vehicles described in Table 13.1 is approximately €4,264,000.

The operational cost is meant to reflect the cost to keep the system operational by including the maintenance and flight operations costs. Both of the costs were estimated separately and their sum was taken as the estimate for the yearly operational cost. A standard metric of 7.5% of the initial cost is assigned to maintenance and yearly repair costs [52]. This value excludes the armament maintenance, which is assigned a different value based on its specification: 15% of initial pricing for a rifle [1]. For the flight operations cost, the required number of pilots is taken as a baseline. The salary of a military drone pilot was estimated to be approximately 40,000 Euro[2], due to the usually lower earnings in the military sector when compared to the civil aviation sector. Furthermore, the 'pilot utilization factor' was estimated based on the predicted level of automation and the expected amount of drones a single pilot can control in parallel. The minimum number of pilots per base of operations was set to 4, assuming an 8 hour shift and allowing for some flexibility in case a pilot e.g. befalls illness. The greater number of the two was then taken as a minimum number of pilots and this number was multiplied by 40,000 to obtain the personnel cost. The total yearly operation costs of the system were estimated to be approximately €3,950,000.

Finally, the marginal cost per kill was estimated to be approximately €900. With a cost of a grenade of approximately €300, it was estimated that, conservatively, it takes approximately 3 grenades to take down an enemy target.

With the costs estimated it is clear that the system is capable of meeting the budget requirements.

---

[1] URL `https://www.westcoastarmory.com/common-gunsmithing-services`, [Cited 20 May, 2025]

[2] URL `https://www.aviationjobsearch.com/career-hub/articles/career-advice/salary-and-benefits/drone-pilot-salary-guide`, [Cited 20 May 2025]

16

Future Outlook

This chapter presents a comprehensive roadmap for transitioning the design of the CEDI system from its current preliminary phase to full operational deployment. Building upon the technical design described in the previous chapters, this future outlook provides a framework for the evaluation of the project timeline and the implementation of the design. The transition from conceptual design to operations encapsulates a large time span containing many phases. To help structure the timeline, several phases are described and broken down into sub-processes in the project design & development logic contained in Section 16.1, visualized as a flow diagram and a Gantt chart. The production plan is described in further detail in Section 16.2

16.1. Project Design & Development Logic

The project design and development plan establishes the technical pathway from preliminary design to operational deployment, encompassing all engineering disciplines required for the successful realization of the system. This section details the systematic approach to transform the conceptual design into flight-qualified hardware and software systems.

The first step to determining the timeline for further development of the system is to assess the time available until deployment. In real-life situations, this deadline is frequently imposed by other parties; in this project, the deadline was determined based on the typical duration of military technology projects, which, depending on the scope of the project, is usually not longer than one year. Therefore, the duration of the post-DSE duration of the project was selected to be 52 weeks. The flow of activities in these 52 weeks is displayed in Post-DSE Flowchart. This flow is additionally displayed in a Gantt chart.

The post-DSE workflow is divided into the following phases:

1. **Detailed design & architecture**: refining the design of the aircraft and ground system, refining the network architecture, and writing detailed flight procedures.
2. **Prototyping & initial testing**: developing a prototype aircraft and testing components in the laboratory and on the ground.
3. **Setup of supply chain & manufacturing planning**: designing the production process, determining quality control procedures, procuring required tooling and equipment, and planning the supply chain.
4. **Flight testing & validation**: validating the functionality of the aircraft, control system, communication system, armaments, testing coordination of the vehicles, and determining the functionality of the system under different conditions.
5. **Full-scale production & integration**: producing the aircraft and ground systems, integration of the system, and quality control of each unit.
6. **Certification & approval**: ensuring airworthiness & compliance with military regulations.
7. **Deployment & operations**: setting up each base by installing infrastructure and training personnel, deploying the system, validating the system in situ and entering units into operation.
8. **Life cycle management**: designing maintenance schedules, planning for future functionality, and planning for end-of-life disposal of the system.

16.2. Production Plan

The production plan, given in Figure 16.1, outlines a comprehensive manufacturing strategy required to deliver an operational system within the specified timeline and quality standards. This section constructs the timeline of all the activities required for the production of CEDI, from the sourcing of components and materials to the integration of the entire system.

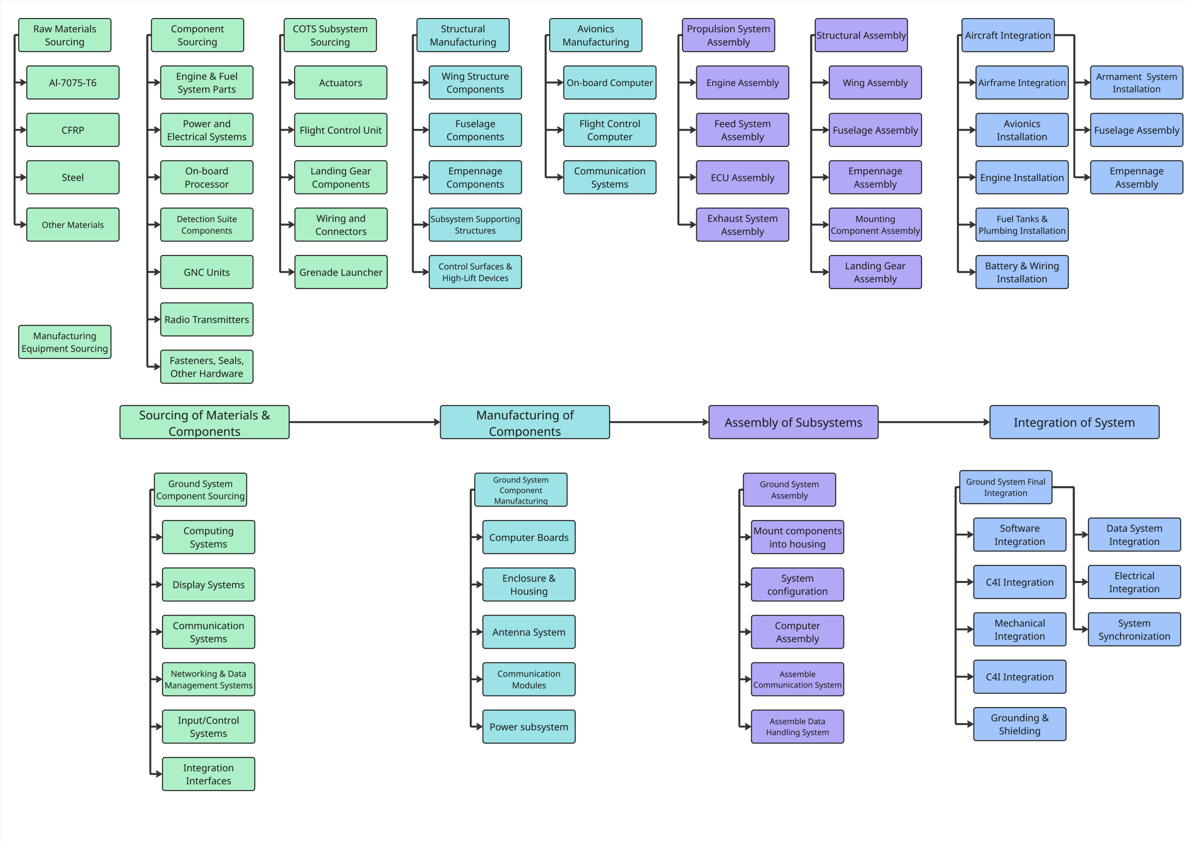

Figure 16.1: *Production plan for the CEDI system*

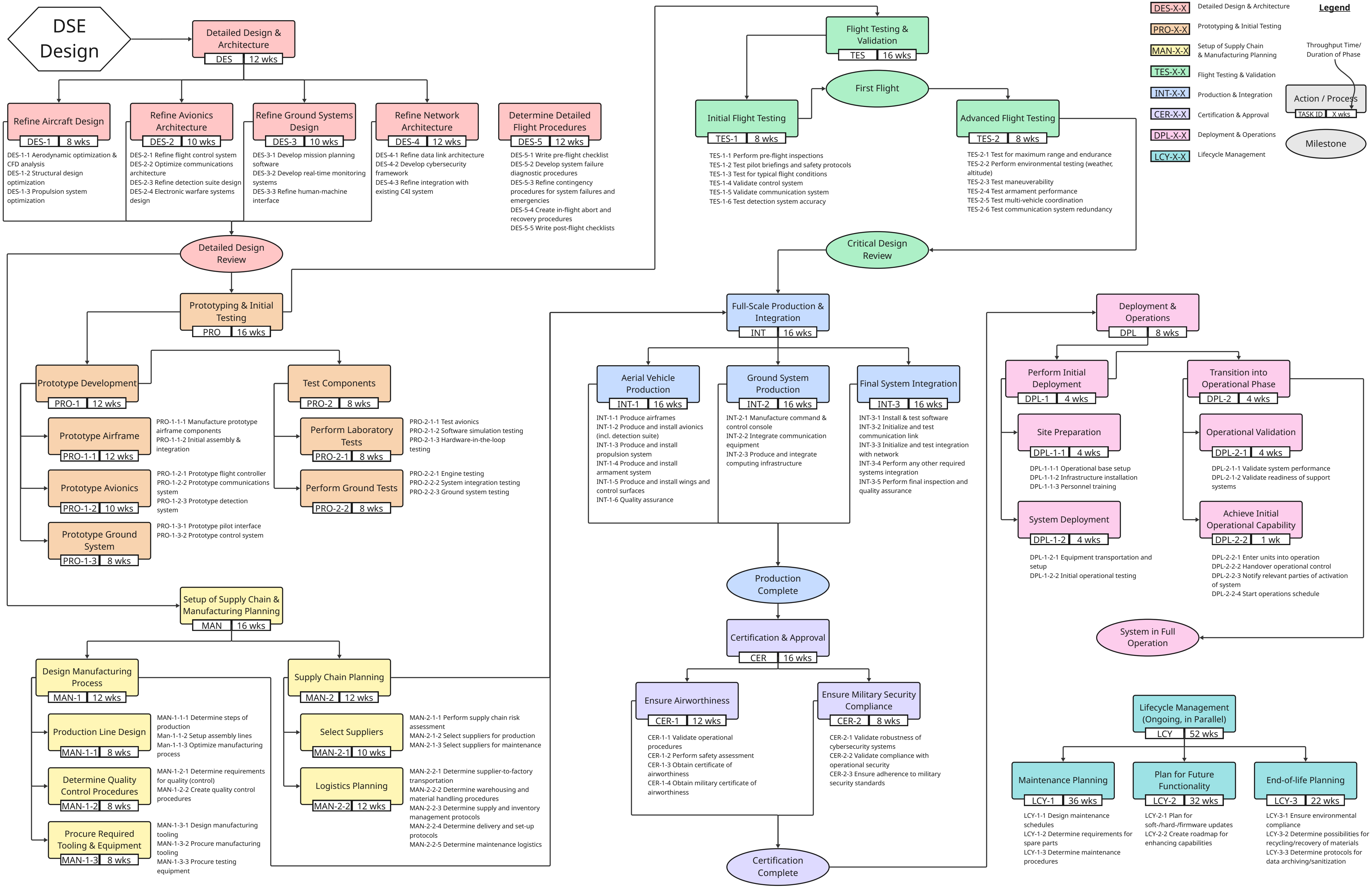

DSE Design

Detailed Design & Architecture
DES 12 wks

Refine Aircraft Design
DES-1 8 wks
DES-1-1 Aerodynamic optimization & CFD analysis
DES-1-2 Structural design optimization
DES-1-3 Propulsion system optimization

Refine Avionics Architecture
DES-2 10 wks
DES-2-1 Refine flight control system
DES-2-2 Optimize communications architecture
DES-2-3 Refine detection suite design
DES-2-4 Electronic warfare systems design

Refine Ground Systems Design
DES-3 10 wks
DES-3-1 Develop mission planning software
DES-3-2 Develop real-time monitoring systems
DES-3-3 Refine human-machine interface

Refine Network Architecture
DES-4 12 wks
DES-4-1 Refine data link architecture
DES-4-2 Develop cybersecurity framework
DES-4-3 Refine integration with existing C4I system

Determine Detailed Flight Procedures
DES-5 12 wks
DES-5-1 Write pre-flight checklist
DES-5-2 Develop system failure diagnostic procedures
DES-5-3 Refine contingency procedures for system failures and emergencies
DES-5-4 Create in-flight abort and recovery procedures
DES-5-5 Write post-flight checklists

Detailed Design Review

Prototyping & Initial Testing
PRO 16 wks

Prototype Development
PRO-1 12 wks

Prototype Airframe
PRO-1-1 12 wks
PRO-1-1-1 Manufacture prototype airframe components
PRO-1-1-2 Initial assembly & integration

Prototype Avionics
PRO-1-2 10 wks
PRO-1-2-1 Prototype flight controller
PRO-1-2-2 Prototype communications system
PRO-1-2-3 Prototype detection system

Prototype Ground System
PRO-1-3 8 wks
PRO-1-3-1 Prototype pilot interface
PRO-1-3-2 Prototype control system

Test Components
PRO-2 8 wks

Perform Laboratory Tests
PRO-2-1 8 wks
PRO-2-1-1 Test avionics
PRO-2-1-2 Software simulation testing
PRO-2-1-3 Hardware-in-the-loop testing

Perform Ground Tests
PRO-2-2 8 wks
PRO-2-2-1 Engine testing
PRO-2-2-2 System integration testing
PRO-2-2-3 Ground system testing

Setup of Supply Chain & Manufacturing Planning
MAN 16 wks

Design Manufacturing Process
MAN-1 12 wks

Production Line Design
MAN-1-1 8 wks
MAN-1-1-1 Determine steps of production
Man-1-1-2 Setup assembly lines
Man-1-1-3 Optimize manufacturing process

Determine Quality Control Procedures
MAN-1-2 8 wks
MAN-1-2-1 Determine requirements for quality (control)
MAN-1-2-2 Create quality control procedures

Procure Required Tooling & Equipment
MAN-1-3 8 wks
MAN-1-3-1 Design manufacturing tooling
MAN-1-3-2 Procure manufacturing tooling
MAN-1-3-3 Procure testing equipment

Supply Chain Planning
MAN-2 12 wks

Select Suppliers
MAN-2-1 10 wks
MAN-2-1-1 Perform supply chain risk assessment
MAN-2-1-2 Select suppliers for production
MAN-2-1-3 Select suppliers for maintenance

Logistics Planning
MAN-2-2 12 wks
MAN-2-2-1 Determine supplier-to-factory transportation
MAN-2-2-2 Determine warehousing and material handling procedures
MAN-2-2-3 Determine supply and inventory management protocols
MAN-2-2-4 Determine delivery and set-up protocols
MAN-2-2-5 Determine maintenance logistics

Flight Testing & Validation
TES 16 wks

Initial Flight Testing
TES-1 8 wks
TES-1-1 Perform pre-flight inspections
TES-1-2 Test pilot briefings and safety protocols
TES-1-3 Test for typical flight conditions
TES-1-4 Validate control system
TES-1-5 Validate communication system
TES-1-6 Test detection system accuracy

First Flight

Advanced Flight Testing
TES-2 8 wks
TES-2-1 Test for maximum range and endurance
TES-2-2 Perform environmental testing (weather, altitude)
TES-2-3 Test maneuverability
TES-2-4 Test armament performance
TES-2-5 Test multi-vehicle coordination
TES-2-6 Test communication system redundancy

Critical Design Review

Full-Scale Production & Integration
INT 16 wks

Aerial Vehicle Production
INT-1 16 wks
INT-1-1 Produce airframes
INT-1-2 Produce and install avionics (incl. detection suite)
INT-1-3 Produce and install propulsion system
INT-1-4 Produce and install armament system
INT-1-5 Produce and install wings and control surfaces
INT-1-6 Quality assurance

Ground System Production
INT-2 16 wks
INT-2-1 Manufacture command & control console
INT-2-2 Integrate communication equipment
INT-2-3 Produce and integrate computing infrastructure

Final System Integration
INT-3 16 wks
INT-3-1 Install & test software
INT-3-2 Initialize and test communication link
INT-3-3 Initialize and test integration with network
INT-3-4 Perform any other required systems integration
INT-3-5 Perform final inspection and quality assurance

Production Complete

Certification & Approval
CER 16 wks

Ensure Airworthiness
CER-1 12 wks
CER-1-1 Validate operational procedures
CER-1-2 Perform safety assessment
CER-1-3 Obtain certificate of airworthiness
CER-1-4 Obtain military certificate of airworthiness

Ensure Military Security Compliance
CER-2 8 wks
CER-2-1 Validate robustness of cybersecurity systems
CER-2-2 Validate compliance with operational security
CER-2-3 Ensure adherence to military security standards

Certification Complete

Deployment & Operations
DPL 8 wks

Perform Initial Deployment
DPL-1 4 wks

Site Preparation
DPL-1-1 4 wks
DPL-1-1-1 Operational base setup
DPL-1-1-2 Infrastructure installation
DPL-1-1-3 Personnel training

System Deployment
DPL-1-2 4 wks
DPL-1-2-1 Equipment transportation and setup
DPL-1-2-2 Initial operational testing

Transition into Operational Phase
DPL-2 4 wks

Operational Validation
DPL-2-1 4 wks
DPL-2-1-1 Validate system performance
DPL-2-1-2 Validate readiness of support systems

Achieve Initial Operational Capability
DPL-2-2 1 wk
DPL-2-2-1 Enter units into operation
DPL-2-2-2 Handover operational control
DPL-2-2-3 Notify relevant parties of activation of system
DPL-2-2-4 Start operations schedule

System in Full Operation

Lifecycle Management (Ongoing, in Parallel)
LCY 52 wks

Maintenance Planning
LCY-1 36 wks
LCY-1-1 Design maintenance schedules
LCY-1-2 Determine requirements for spare parts
LCY-1-3 Determine maintenance procedures

Plan for Future Functionality
LCY-2 32 wks
LCY-2-1 Plan for soft-/hard-/firmware updates
LCY-2-2 Create roadmap for enhancing capabilities

End-of-life Planning
LCY-3 22 wks
LCY-3-1 Ensure environmental compliance
LCY-3-2 Determine possibilities for recycling/recovery of materials
LCY-3-3 Determine protocols for data archiving/sanitization

Legend

DES-X-X Detailed Design & Architecture
PRO-X-X Prototyping & Initial Testing
MAN-X-X Setup of Supply Chain & Manufacturing Planning
TES-X-X Flight Testing & Validation
INT-X-X Production & Integration
CER-X-X Certification & Approval
DPL-X-X Deployment & Operations
LCY-X-X Lifecycle Management

Throughput Time/ Duration of Phase
Action / Process
TASK ID X wks
Milestone

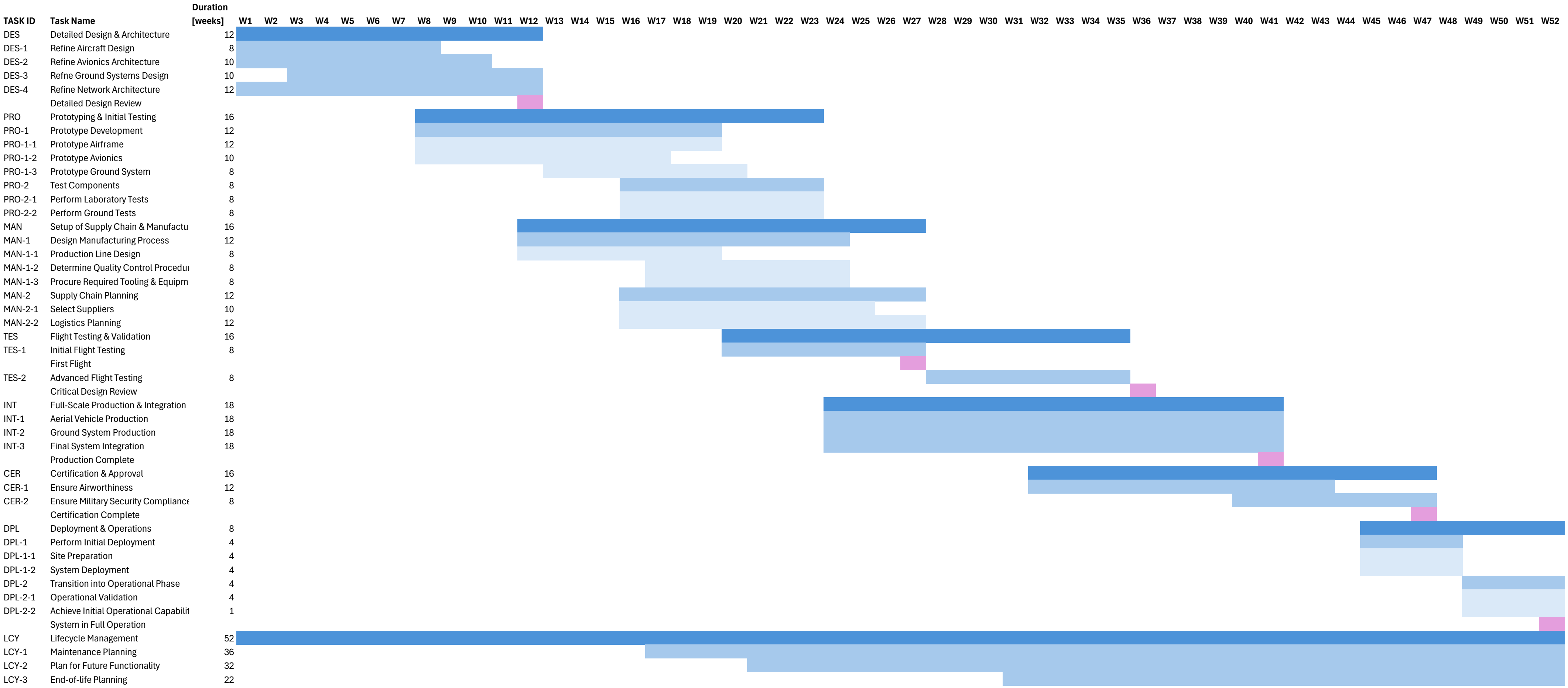

TASK ID	Task Name	Duration [weeks]
DES	Detailed Design & Architecture	12
DES-1	Refine Aircraft Design	8
DES-2	Refine Avionics Architecture	10
DES-3	Refne Ground Systems Design	10
DES-4	Refine Network Architecture	12
	Detailed Design Review	
PRO	Prototyping & Initial Testing	16
PRO-1	Prototype Development	12
PRO-1-1	Prototype Airframe	12
PRO-1-2	Prototype Avionics	10
PRO-1-3	Prototype Ground System	8
PRO-2	Test Components	8
PRO-2-1	Perform Laboratory Tests	8
PRO-2-2	Perform Ground Tests	8
MAN	Setup of Supply Chain & Manufactu	16
MAN-1	Design Manufacturing Process	12
MAN-1-1	Production Line Design	8
MAN-1-2	Determine Quality Control Procedu	8
MAN-1-3	Procure Required Tooling & Equipm	8
MAN-2	Supply Chain Planning	12
MAN-2-1	Select Suppliers	10
MAN-2-2	Logistics Planning	12
TES	Flight Testing & Validation	16
TES-1	Initial Flight Testing	8
	First Flight	
TES-2	Advanced Flight Testing	8
	Critical Design Review	
INT	Full-Scale Production & Integration	18
INT-1	Aerial Vehicle Production	18
INT-2	Ground System Production	18
INT-3	Final System Integration	18
	Production Complete	
CER	Certification & Approval	16
CER-1	Ensure Airworthiness	12
CER-2	Ensure Military Security Compliance	8
	Certification Complete	
DPL	Deployment & Operations	8
DPL-1	Perform Initial Deployment	4
DPL-1-1	Site Preparation	4
DPL-1-2	System Deployment	4
DPL-2	Transition into Operational Phase	4
DPL-2-1	Operational Validation	4
DPL-2-2	Achieve Initial Operational Capabilit	1
	System in Full Operation	
LCY	Lifecycle Management	52
LCY-1	Maintenance Planning	36
LCY-2	Plan for Future Functionality	32
LCY-3	End-of-life Planning	22

16.3. Recommendations

This section presents a set of actionable recommendations based on the findings and analysis conducted in the preceding sections. The proposed measures aim to improve the performance of the system, address identified limitations, and guide future development or implementation efforts.

Building on the work presented in this report, several actions can be taken to further develop and refine the system. First, it is recommended to verify the validity of using a large fixed-wing drone with the YOLOv8 object detection model, as most existing literature and datasets target small rotary drones. Additionally, the empennage design should be iterated upon to avoid deep stall of the horizontal stabilizer. Further work should also include further analysis of the aircraft's response to gun recoil, as this could significantly affect stability and control. From a systems perspective, planning and analyzing the routing of data logs for the various avionics components is crucial for both mission performance and post-mission diagnostics. The effect of rain on the effectiveness of the detection suite should also be assessed.

Some of the required developments will demand more extensive work and analysis. It is particularly important to explore the possibility of using non-commercial satellite communication systems to avoid reliance on infrastructure controlled by potentially hostile nations or organizations. Similarly, further analysis should be carried out on jamming threats, including identification of weak points of the system and the development of possible countermeasures. From a mission flexibility standpoint, the system should be investigated for potential modifications that would support peacetime applications. For example, this could include replacing the weapon system with a different payload and reevaluating mission parameters such as fuel requirements, sensor types, and payload capacity. If the mission demands it and feasibility studies support the decision, a more powerful engine may also be considered. Additionally, the noise level of the vehicle should be evaluated and its consequences analyzed.

Finally, extensive testing and manufacturing steps will be required to validate and finalize the design. The structural model of the aircraft must be updated to include cutouts, followed by an investigation of resulting stress concentrations, including the effects of rivets and bolts. A full FEM analysis of the modified structure is essential for ensuring safety and integrity. In parallel, CFD simulations should be conducted on both the aircraft body and the propeller, and followed by wind tunnel testing and physical structural tests (such as a whiffle-tree) after manufacturing to validate aerodynamic performance. The propeller should also be prototyped and tested independently to assess efficiency and structural soundness. Lastly, the weapon system must undergo rigorous testing, both standalone and in conjunction with the automation mechanism, and finally integrated into the aircraft to assess the complete system performance.

17

Conclusion

At the end of this Design Synthesis Exercise, a complete interceptor drone system that meets the requirements for defending the Netherlands against large-scale drone attacks has been developed. Building on the design laid out during the baseline and midterm phases, Concept 4, the Cost-Effective Gun Drone, was selected and refined into a full design. The final system concept consists of 52 air vehicles spread out between ten airbases around the Netherlands.

The final vehicle design features a conventional fixed-wing UAV with a pusher configuration. The central fuselage houses the main avionics, power electronics, and weapon system, while the Jet-A1 fuel is housed in the wing. The gun is mounted on the wing spar and controlled by a guiding rail movable on the vertical axis. Two booms span out from the wings and support the H-tail empennage configuration. Target detection is fully autonomous, using a nose-mounted radar and gimbal camera. Sensor data is processed onboard by the Jetson Xavier NX, which identifies and tracks threats in real time. The chip then sends commands to the flight control unit to maneuver the drone and align the gun for interception.

The system itself meets all top-level requirements: a system capable of launching within 5 minutes, eliminating threats at less than €1,000 per kill, and operating for over 2 hours on a single flight. The UAV has been designed to be manufacturable and maintainable, ensuring it fits into NATO's operational systems with minimal logistical challenges. The autonomous operation of the system reduces the need for skilled operators and supports scalability in the event of high-volume attacks.

To advance the system, next steps include validating the use of the object detection models on fixed-wing platforms, further analyzing gun recoil effects, and optimizing avionics data handling. Additionally, critical areas such as communication resilience, jamming countermeasures, structural integrity, aerodynamic performance, and full-system weapon integration must be addressed through extensive testing and simulation.

17.1. Acknowledgment

We would like to extend a special thanks to Paul Roling, our principal tutor, for his continuous support and guidance throughout the entire Design Synthesis Exercise. To our coaches, Shreyas Anand and Marguerite Arvis, whose expertise and feedback were essential in shaping our technical work and helping us stay on track. We are also grateful to Mark Voskuijl and Anique Altena for their expert advice and valuable input during key stages of the design. Lastly, we would like to thank Eunkyung Cho, our teaching assistant, for feedback on our report writing and help provided.

Bibliography

[1] J. Roskam, *Airplane Design Part VI: Preliminary Calculation of Aerodynamic, Thrust and Power Characteristics.* 2004.

[2] H. S. Mohammad, *Aircraft Design A Systems Engineering Approach John Wiley &amp Sons (2012).* 2012.

[3] X. Zhai, Z. Huang, T. Li, H. Liu, and S. Wang, "YOLO-Drone: An Optimized YOLOv8 Network for Tiny UAV Object Detection," *Electronics 2023, Vol. 12, Page 3664*, vol. 12, p. 3664, 8 2023.

[4] M. Benyamin and G. H. Goldman, "Acoustic Detection and Tracking of a Class I UAS with a Small Tetrahedral Microphone Array," 9 2014.

[5] G. Vorraro, J. W. Turner, and S. Akehurst, "Testing of a Modern Wankel Rotary Engine - Part III: Firing Condition Analysis," 3 2022.

[6] G. Maddux, "Stress Analysis Manual," pp. 1–6, 1969.

[7] A. Bolhuis, S. Cuppers, D. d. Jong, M. Grajda, V. Maan, A. Malugani, B. Paulis, J. P. Peters, N. R. Dfouni, and T. Uijlenhoet, "Baseline Report," tech. rep., Delft University of Technology, Delft, 5 2025.

[8] M. Voskuijl, T. Dekkers, and R. Savelsberg, "Flight Performance Analysis of the Samad Attack Drones Operated by Houthi Armed Forces," *Science & Global Security*, vol. 28, pp. 113–134, 9 2020.

[9] M. Voskuijl, "Performance analysis and design of loitering munitions: A comprehensive technical survey of recent developments," *Defence Technology*, vol. 18, pp. 325–343, 3 2022.

[10] A. Bolhuis, S. Cuppers, D. de Jong, M. Grajda, V. Maan, A. Malugani, B. Paulis, J. P. Peters, N. R. Dfouni, and T. Uijlenhoet, "Midterm Report," tech. rep., Delft University of Technology, Delft, 5 2025.

[11] W. Edwards and F. Barron, "SMARTS and SMARTER: Improved Simple Methods for Multiattribute Utility Measurement," *Organizational Behavior and Human Decision Processes*, vol. 60, pp. 306–325, 12 1994.

[12] J. Roskam, *Airplane Design Part I: Preliminary Sizing of Airplanes.* 1985.

[13] "MIL-STD-1797A Flying Qualities of Piloted Aircraft."

[14] "NATO STANDARD AEP-83."

[15] M. V. Cook, *Flight Dynamics Principles.* Elsevier, 2 ed., 2007.

[16] J. D. J. Anderson, *Introduction to Flight.* eighth ed., 2012.

[17] F. Oliviero, "AE3211-I Systems Engineering and Aerospace Design - Requriment Analysis and Deisng principles for A/C stability & control," 2025.

[18] E. Torenbeek, "Synthesis of Subsonic Airplane Design," pp. 541–542, 1982.

[19] W. Hatch, *Interior ballistics of Guns.* New York: Wiley, 1963.

[20] S. Speretta, "AE 2111-II Aerospace Design and Systems Engineering Elements II - Spacecraft Telecommunications," 2023.

[21] J. D. Kraus, *Antennas.* McGraw-Hill Inc., second edition ed., 1997.

[22] A. Khaleghi and I. Balasingham, "Low-Profile and High-Gain Linear Polarized Loop Antenna," in *2020 14th European Conference on Antennas and Propagation (EuCAP)*, pp. 1–4, IEEE, 3 2020.

[23] A. Djordjević, A. Zajić, M. Ilić, and G. Stüber, "Optimization of Helical Antennas," *IEEE Antennas and Propagation Magazine*, vol. 48, pp. 107–116, 12 2006.

[24] M. Ma and K. Deng, "The study and implementation of Meander-line antenna for an integrated transceiver design," *Univerisity of Gavle*, 2 2010.

[25] International Telecommunication Union, "Attenuation by atmospheric gases and related effects," tech. rep., ITU-R, 2022.

[26] "STANAG 4285," 1989.

[27] G. Forney, "Introduction to convolutional codes," 2003.

[28] ICAO, "UAT System Performance Simulation Results ," 2005.

[29] D. M. Dobkin, "UHF RFID Readers," in *The RF in RFID*, pp. 103–188, Elsevier, second edition ed., 2013.

[30] H. B. Jiang, Y. R. Li, and Z. Q. Cheng, "Relations of lift and drag coefficients of flow around flat plate," *Applied Mechanics and Materials*, vol. 518, pp. 161–164, 2014.

[31] V. Semenyuk, I. Kurmashev, A. Lupidi, D. Alyoshin, L. Kurmasheva, and A. Cantelli-Forti, "Advances in UAV detection: integrating multi-sensor systems and AI for enhanced accuracy and efficiency," *International Journal of Critical Infrastructure Protection*, vol. 49, p. 100744, 7 2025.

[32] B. K. S. Isaac-Medina, M. Poyser, D. Organisciak, C. G. Willcocks, T. P. Breckon, and H. P. H. Shum, "Unmanned Aerial Vehicle Visual Detection and Tracking using Deep Neural Networks: A Performance Benchmark," *Proceedings of the IEEE International Conference on Computer Vision*, vol. 2021-October, pp. 1223–1232, 3 2021.

[33] A. Martian, C. Paleacu, I. M. Marcu, and C. Vladeanu, "Direction-finding for unmanned aerial vehicles using radio frequency methods," *Measurement*, vol. 235, p. 114883, 8 2024.

[34] B. Blekemolen, *Tracking drones with small microphone arrays.* PhD thesis, Delft University of Technology, Delft, 5 2025.

[35] F. Christnacher, S. Hengy, M. Laurenzis, A. Matwyschuk, P. Naz, S. Schertzer, and G. Schmitt French-German, "Optical and acoustical UAV detection," *https://doi.org/10.1117/12.2240752*, vol. 9988, pp. 83–95, 10 2016.

[36] M. Elsayed, M. Reda, A. S. Mashaly, and A. S. Amein, "Review on Real-Time Drone Detection Based on Visual Band Electro-Optical (EO) Sensor," *Proceedings - 2021 IEEE 10th International Conference on Intelligent Computing and Information Systems, ICICIS 2021*, pp. 57–65, 2021.

[37] J. Park, D. H. Kim, Y. S. Shin, and S. H. Lee, "A comparison of convolutional object detectors for real-time drone tracking using a PTZ camera," *International Conference on Control, Automation and Systems*, vol. 2017-October, pp. 696–699, 12 2017.

[38] H. Hao, Y. Peng, Z. Ye, B. Han, X. Zhang, W. Tang, W. Kang, and Q. Li, "A High Performance Air-to-Air Unmanned Aerial Vehicle Target Detection Model," *Drones 2025, Vol. 9, Page 154*, vol. 9, p. 154, 2 2025.

[39] S. Zhao, M. Dabin, E. Cheng, X. Qiu, I. Burnett, J. Chia-chun Liu, and J. Express Lett, “Mitigating wind noise with a spherical microphone array,” *The Journal of the Acoustical Society of America*, vol. 144, pp. 3211–3220, 12 2018.

[40] W. A. Lies, L. Narula, P. A. Iannuci, and T. E. Humphreys, “Low SWaP-C Radar for Urban Air Mobility,” in *IEEE/ION Plan 2025*, (Salt Lake City), 4 2025.

[41] T. A. Abir, P. S. Gupta, M. Islam, V. Le, A. Copley, R. Han, E. Kuantama, J. Dawes, and P. Nguyen, “Detection and Tracking of Drone Swarms using LiDAR,” tech. rep., University of Texas at Arlington, Anaheim, 6 2025.

[42] C. Goodin, D. Carruth, M. Doude, and C. Hudson, “Predicting the Influence of Rain on LIDAR in ADAS,” *Electronics 2019, Vol. 8, Page 89*, vol. 8, p. 89, 1 2019.

[43] M. Rizwan, “Lab Report No.07 | PDF | Horsepower | Engines,” tech. rep., National University of Sciences and Technology, 4 2024.

[44] A. Suprianto, F. Hartono, D. Herdiana, D. Tresnoningrum, and N. Pramana, “Pusher Propeller Performance Investigation on Lightweight Medium Range UAV,” *Engineering Journal*, vol. 28, pp. 11–24, 9 2024.

[45] O. Gur, *Propeller Design.* American Institute of Aeronautics & Astronautics, 1 ed., 2024.

[46] J. Gordon Leishman, *Introduction to Aerospace Flight Vehicles.* 2025.

[47] E. P. Hartman and D. Biermann, “NATIONAL ADVISORY COMMITTEE FOR AERONAUTICS THE AERODYNAMIC CHARACTERISTICS OF FULL-SCALE PROPELLERS HAVING 2, 3, AND 4 BLADES OF CLARK Y AND R. A. F. 6 AIRFOIL SECTIONS,” tech. rep., 1938.

[48] R. Alderliesten, *Introduction to Aerospace Structures and Materials.* TU Delft OPEN Publishing, 2018.

[49] Federal Aviation Administration, “Design Dive Speed,” tech. rep., 2000.

[50] R. Abbott, *ANALYSIS AND DESIGN OF COMPOSITE AND METALLIC FLIGHT VEHICLE STRUCTURES.* 2019.

[51] B. L. COL James Kays LTC William B Carlton MAJ Mark M Lee CPT William L Ratliff, “Analysis of Operational Readiness Rates DEPARTMENT OF SYSTEMS ENGINEERING AND OPERATIONS RESEARCH CENTER TECHNICAL REPORT,” tech. rep., 1998.

[52] J. Jackson, K. Ladino, G. Abdulai, and A. Engineering, “AEN-160: Decision Aid for Estimating the Cost of Using a Drone in Production Agriculture,” tech. rep., 5 2021.